Development of an Active Magnetic Attitude Determination and Control System for Picosatellites on highly inclined circular Low Earth Orbits

A thesis submitted in fulfilment of the requirements for the degree
Master of Engineering by Research

Jens Gießelmann
Dipl.-Ing. (FH)

School of Aerospace, Mechanical and
Manufacturing Engineering
Science, Engineering and Technology Portfolio
RMIT University
June 2006

Declaration

I certify that except where due acknowledgement has been made, the work is that of the author alone; the work has not been submitted previously, in whole or in part, to qualify for any other academic award; the content of the thesis is the result of work which has been carried out since the official commencement date of the approved research program; and, any editorial work, paid or unpaid, carried out by a third party is acknowledged.

Jens Gießelmann
03/28/2006

Abstract

Small satellites are becoming increasingly important to the aerospace industry mainly due to their significantly reduced development and launch cost as well as shorter development time frames. In order to meet the requirements imposed by critically limited resources of very small satellites, e.g. picosatellites, innovative approaches have to be taken in the design of effective subsystem technologies. This thesis presents the design of an active attitude determination and control system for flight testing on-board the picosatellite 'Compass-1' of the Univerity of Applied Sciences Aachen, Germany. The spacecraft of the CubeSat class with a net spacecraft mass of only 1kg uses magnetic coils as the only means of actuation in order to satisfy operational requirements imposed by its imagery payload placed on a circular and polar Low Earth Orbit. The control system is capable of autonomously dissipating the tumbling rates of the spacecraft after launch interface separation and aligning the boresight of the payload into the desired nadir direction within a pointing error of approximately 10°. This nadir-pointing control is achieved by a full-state feedback Linear Quadratic Regulator which drives the attitude quaternion and their respective rates of change into the desired reference. The state of the spacecraft is determined by a static statistical QUEST attitude estimator processing readings of a three-axis magnetometer and a set of five sun sensors. Linear Floquet theory is applied to quantify the stability of the controller and a non-linear dynamics simulation is used to confirm that the attitude asymptotically converges to the reference in the absence of environmental disturbances. In the presence of disturbances the system under control suffers from fundamental underactuaction typical for purely magnetic attitude control but maintains satisfactory alignment accuracies within operational boundaries.

Keywords: CubeSat, Compass-1, picosatellite, active magnetic attitude control, attitude determination, Linear Quadratic Regulator.

Acknowledgements

I would like to take the opportunity to express my thanks to the people who have made my studies an exciting experience of professional and cultural discovery.

Firstly I would like to thank my senior supervisor Professor S. Abanteriba for his support and for giving me the opportunity to pursue my postgraduate studies at the Royal Melbourne Institute of Technology, Australia.

My appreciation also belongs to the faculty of the aerospace engineering department at my home institution, the University of Applied Sciences Aachen, Germany, for their growing engagement and support and conviction that the ambitious endeavour of University satellite development will result in a measureable success. I extend my special thanks to my second supervisor Prof. Dr. rer. nat. H.-J. Blome for his kind support professionally and personally and to Prof. Dr.-Ing. W. Ley who just as well never hesitated to offer his guidance during my studies.

The grand project of satellite engineering cannot succeed without funding. I would like to thank the German Aerospace Centre for their financial support and for expressing their trust in my skills and the skills of the entire project team.

I appreciate the commitment and the endurance of every student involved in whatever part of the grand project. Thanks to you all for the exciting time we shared.

In particular, I would like to thank my mate and Compass-1 project manager Artur Scholz for his warm leadership and for sharing his vision with me. My thanks also to Alexander Weiß for lending me his competent ears whenever needed.

Last but not least, I want to express my gratitude to my parents. Without their love and support I would not have been able to pursue my passion for challenging the seemingly impossible and choose a career in space engineering. Thank you for believing in and encouraging me. This thesis is dedicated to you.

Contents

List of Figures

List of Tables

Acronyms and Abbreviations

µC	Microcontroller
A/D	Analog-to-Digital
AC	Alternating Current
ADC	Analog-to-Digital Converter
ADCS	Attitude Determination and Control System
AGS	Aachen Ground Segment
AMR	Anisotropic Magnetoresistive
BJT	Bi-Junction Transistor
BOL	Begin of Life
bps	bits per second
CAD	Computer Aided Design
CDHS	Command and Data Handling System
CG	Centre of Gravity
CMOS	Complementary Metal-Oxid Semiconductor
COM	Communications Subsystem
COTS	Commercial-off-the-shelf
CP	Centre of Pressure
CPU	Central Processor Unit
CS	Coordinate System
CW	Continuous Wave
DC	Direct Current
DCM	Direction Cosine Matrix
DTMF	Dual-Tone Multi-Frequency
DTU	Denmark Technical University
DUT	Device under Test
EEPROM	Electrically Erasable Read Only Memory
EKF	Extended Kalman Filter
EPS	Electric Power System
FOV	Field of View
FSF	Full State Feedback
FSK	Frequency Shift Keying
GPS	Global Positioning System
I/O	Input/Output
I²C	Inter-Integrated Circuit
IAGA	International Association of Geomagnetism and Aeronomy
IGRF	International Geomagnetic Reference Field
IUGG	International Union of Geodesy and Geophysics
JAXA	Japan Aerospace Exploration Agency
KB	Kilobyte
LEO	Low Earth Orbit
LQR	Linear Quadratic Regulator
LSB	Least Significant Bit

MEMS	Micro-Electro-Mechanical System
MOEMS	Micro-Opto-Electro-Mechanical System
MOSFET	Metal-Oxid Semiconductor Field Effect Transistor
NOAA	National Oceanic and Atmospheric Administration
OBC	On-bard Computer
OLE	One Line Element
PCB	Printed Circuit Board
PEEK	Polyetheretherketone
PLL	Phase Locked Loop
PTFE	Polytetrafluorethylene
PWM	Pulse Width Modulation
QVGA	Quarter Video Graphics Array
RAAN	right ascension of the ascending node
RAM	Random Access Memory
RF	Radio Frequency
RMIT	Royal Melbourne Institute of Technology
ROM	Read Only Memory
rpm	revolutions per minute
RTOS	Real Time Operating System
SAR	Succesive Approximation Register
SEC	Space Environment Center
SGP	Simplified General Pertubations
SQUID	Superconducting Quantum Interference Device
SSETI	Student Space Exploration and Technology Initiative
STR	Structures and Mechanisms
P-POD	Poly-Picosatellite Orbital Deployer
TCS	Thermal Control System
TLE	Two Line Element
T-POD	Test-Picosatellite Orbital Deployer
UASA	University of Applied Sciences Aachen
UHF	Ultra High Frequency
VGA	Video Graphics Array
VHF	Very High Frequency
VLSI	Very Large Scale Integration
w.r.t.	with respect to
WMM	World Magnetic Model

Notation

Reference Frames

$F_i = \{\hat{i}_1, \hat{i}_2, \hat{i}_3\}$	inertial reference frame
$F_o = \{\hat{o}_1, \hat{o}_2, \hat{o}_3\}$	orbit reference frame
$F_b = \{\hat{b}_1, \hat{b}_2, \hat{b}_3\}$	body reference frame
$F_c = \{\hat{c}_1, \hat{c}_2, \hat{c}_3\}$	control reference frame
$F_{ECI} = \{\hat{\imath}_{ECI}, \hat{\jmath}_{ECI}, \hat{k}_{ECI}\}$	Earth-centred inertial frame
$F_{ECEF} = \{\hat{\imath}_{ECEF}, \hat{\jmath}_{ECEF}, \hat{k}_{ECEF}\}$	Earth-fixed frame

Vectors and Matrices

a, b, v, R	vectors appear in normal type with capital letters usually reserved for matrices. The context distuingishes vectors from scalars.
E	Identity Matrix
${}^{o}v$	vector v expressed in the orbit frame
$\text{diag}([a_1\ a_2\ \ldots\ a_n]^T)$	diagonal matrix with components on diagonal corresponding to $[a_1\ a_2\ \ldots\ a_n]^T$ and zero off-diagonal components

Symbols

t_{JD}	Julian Date
ω_b^{bo}	rotational rate of the body frame w.r.t. the orbit frame
P_n^m	Schmidt-normalized Legendre functions
a_w	wire cross sectional area
$\bar{q}^{bo} = (q^T q_4)^T$	attitude quaternion representing a rotation of the body frame w.r.t. the orbit CS
θ'_m, ϕ'_m	coelevation and east longitude of the magnetic dipole
g_n^m, h_n^m	IGRF model coefficients
a	euler axis
A	plant system matrix
B	local geomagnetic flux density
C	circumference
c_D	coefficient of drag
D	residual magnetic dipole
E	electric field

F	Plant system matrix
f_p	pitch frequency
G	Control Input Matrix
h	angular momentum
H(jω)	transfer function
i	angle of incidence, inclination, current
I	inertia tensor
I_1, I_2, I_3	pincipal moments of inertia (in the control frame)
J	infinite linear quadratic cost functional
J	principal inertia (for one-dimensional problems)
K	LQR gain
k_φ	torsional stiffness
m	magnetic moment
N	number of turns
q	electrical charge
R	range
r	reflectance factor
T	torque, period, temperature
t_0	epoch
u	control input vector
v	velocity
x	state vector
α	general angle
θ	colatitude/coelevation
θ, φ, ψ	pitch, roll, yaw
λ_m	magnetic latitude
ρ	density
σ	inertia parameter
τ	time constant
φ, λ	longitude, latitude
Ψ	monodromy matrix
Φ	principal euler angle, state transition matrix

Constants

AU	average earth-sun distance	149,597,870.691 km
R_E	Earth equatorial radius	6378.135 km
M	Earth magnetic dipole moment	$7.79 \cdot 10^{24}$ nTm^3
B_0	equatorial magnetic flux @ sea level	30036.74 nTR_E^3
μ_0	magnetic permeability of vacuum	$4\pi \cdot 10^{-7}$ N/A²
Φ_0	magnetic flux quantum	$2{,}0678 \cdot 10^{-15}$ Wb
$\omega_\oplus$	Earth's angular velocity	$7.29211585538 \cdot 10^{-5}$ rad/s
S_0	Mean Solar Constant	1371 W/m²
c	Speed of Light	$3 \cdot 10^8$ m/s

Chapter 1

Introduction

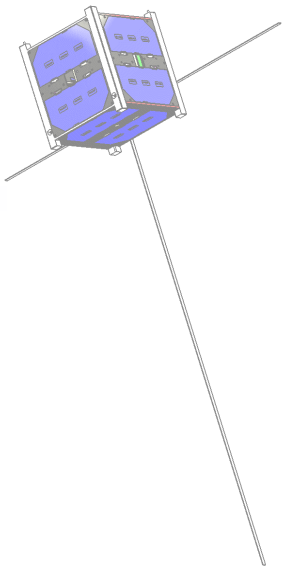

1.1 Microsatellites

While a relatively small number of highly capable and complex spacecrafts were in the focus of interest for the space market and space science a decade ago, microsatellites are becoming increasingly important to the aerospace industry in recent times. Although there does not exist a binding definition of satellite classes, a microsatellite is commonly agreed to have a lift-off weight of less than 100kg, e.g. Microsat-70; in astronautical circles every space vehicle lighter than one metric ton is considered “small”. With the emergence of an increasing number of microsatellites, finer subdivisions have been de facto introduced: a nanosatellite is a spacecraft of less than 10kg mass, e.g. SNAP, a picosatellite is a lightweight vehicle of less than only 1kg, e.g. Stensat, and is currently the smallest conceived satellite class.

The main advantage of microsatellites is the dramatically reduced development and launch cost as well as shorter development time frames. Projects usually take 5 months to 2.5 years from idea to launch; a fact which satisfies spontaneously emerging infrastructural or scientific needs more immediately. Another less obvious implication of the reduced development time frames is the fact that small satellites are more likely to integrate up-to-date technology or newly developed systems; for example, a large satellite system which is ten years in the making may end up essentially consisting of decade-old technology unless costly design changes have been undertaken at an advanced stage of the system development. This is a phenomenon virtually unknown to small satellite developers and a direct consequence is that the spacecraft design is often close to its maximum achievable effectiveness while also allowing a calculated risk of implemening novel, i.e. untested and unmatured, system solutions. The costs for such spacecraft are in the range of tens to hundreds of thousands of Euros, due to lower cost for launch, hardware, transportation and integration testing in smaller, less expensive to operate test facilities. Launch costs are effectively reduced by sharing the launch vehicle with a primary, usually the heavier, payload. In this cost-sharing scenario, commonly referred to as a “piggyback launch”, the operators of the secondary payload waiver the freedom of selecting the target orbit and delays of the primary payload‘s launch readiness delay the launch of the microsatellite but not vise versa. However, the cost for the launch is a mere fraction of the total launch cost and

is on the order of 30,000 €/kg depending on the launch vehicle. This enables universities, small companies and developing countries to participate in the international business of space technology.

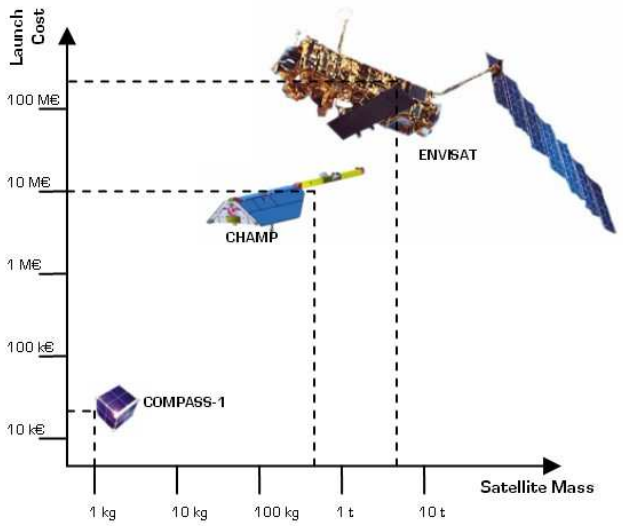

Figure 1.1: Relationship between spacecraft mass and launch cost

From the current perspective, limited space, power and mass clearly restricts the selection of payloads. However, very small satellites are a rapidly evolving technology branch since these miniature satellites fill specific niches and at the same time open new fields of application. Today, microsatellites are employed in the form of low-cost realizations of traditional mission objectives, such as Earth observation, communication and science, e.g. BIRD [2]. Examples for potential future microsatellite applications are loose or tight swarms and constellations to enable distributed, redundant and flexible mission scenarios for space and Earth observation and communication which are prohibitively expensive to attempt with convential spacecraft, or as supplementing elements to conventional missions by servicing and monitoring bigger spacecrafts and space stations. An interesting commercial exploitation of micro- or picosatellites could be as a test-bed for new technologies or components, with competitive costs compared to laboratory testing facilities for µgravity, radiation, long-term vacuum exposure, thermal cycling, etc.

Until most of the above mentioned mission scenarios can be realized with picosatellites, a number of technological challenges have to be faced; the main areas of unexplored subsystem capabilities on picosatellites are certainly in communication, data processing, attitude control and propulsion. A substantial obstacle to the picosatellite system design is that many systems and concepts of conventional satellites cannot be simply implemented, because the key system components are currently unavailable and thus need to be entirely built from scratch.

1.2 The CubeSat Standard

Picosatellite developments also suffered partly from the lack of a unified design standard. The latter problem has been addressed by the California Polytechnic State University at San Luis Obispo, referred to as CalPoly, and Stanford University, which combined efforts to develop a new class of standard spacecraft, called 'CubeSat' [1]. This standard defines a cubic structural bus with the dimensions of (10x10x10)cm³ and a maximum mass of only 1kg, hence requiring extremely light-weight and power efficient systems; a cell-covered cube of this size provides an average electrical power of between 1 and 2 Watts electrical, depending on the quality of the solar generators. These figures put considerable constraints on the design of a CubeSat. Despite this fact, the CubeSat concept attracts growing attention, in particular from universities; an estimated number of around 40 international universities are involved in designing CubeSats primarily for technology demonstration purposes while sharing their experiences and ideas with the CubeSat community in the academic spirit at workshops and via the internet. Many of the key technologies required to enable highly efficient picosatellite missions are not yet developed but space companies begin to derive an interest in investing into miniaturized spacecraft components from the market situation. In the meanwhile, universities can afford to fill the niche of exploring novel technologies and at the same time deliver high-quality education and training to their students.

Figure 1.2: The Poly Picosatellite Orbital Deployer (P-POD) in exploded view (left) and normal view (right)

An important component of the CubeSat standard has been the development of the Poly Picosatellite Orbital Deployer (P-POD), the common interface between a launch vehicle and up to three CubeSats [3]. The P-POD, shown in figure 1.2, was built to greatly simplify the integration between the CubeSats and any launch vehicle. Its small and modular design allows it to fit into under-utilized spaces inside the launch vehicle's payload fairing. The current P-POD is capable of containing and subsequently deploying three single CubeSats, a double plus a single CubeSat, or one triple CubeSat, such as the earthquake finder Quakesat [58].

California Polytechnic State University negotiates yearly launch opportunities on the Russian launch vehicle DNEPR and the German/Russian vehicle Rockot. Currently, a total of 8 picosatellites of the CubeSat class populates the Low Earth Orbit (LEO). The first series of 5 CubeSats (plus one triple CubeSat) was launched on the 30th of June 2003, 14:15:26 UTC from the Russian Cosmodrome in Plesetsk on a Rockot launch vehicle, a former SS-19 ballistic missile. Three more CubeSats were released from the European student satellite SSETI-Express on the 27th of October 2005.

On the 26th of July 2006 at 7:43 pm UTC a Dnepr launch vehicle lifted off from the Baikonur Cosmodrome in Kazakhstan, carrying a total of 18 small spacecraft including 14 CubeSat type satellites from 10 different universities and 1 private company, in an attempt to expand the LEO single CubeSat population from a mere 8 to 21. Unfortunately, the converted SS-18 Intercontinental Ballistic Missile operated as a civil launch vehicle since 1999, suffered a first stage engine failure less than 2 minutes into the ascent, causing a premature engine shut-off and preventing staging. The wreckage of the launch vehicle as well as five P-PODs meant to release 13 single and 1 double CubeSat was found 150km south of Baikonur where the diverted launch trajectory came to its tragic end. The CubeSats that were lost as a result of the failed launch attempt are: AeroCube-1, CP-1 and 2, ICE Cube-1 and 2, ION, HAUSAT-1, KUTESat, MEROPE, nCube-1, RINCON, SACRED, SEEDS and Voyager.

The following sections present a brief overview over the eight previous and current CubeSat spacecraft launched in June 2003 and October 2005 and their respective missions.

1.3 First CubeSat Launch

AAUSat

The mission objectives of the satellite AAUSat which was developed by students of Aalborg University in Denmark were to take visual range images of the Earth with a high resolution imager (1280 by 1024, 24bit color depth) and to demonstrate three-axis attitude control. The spacecraft body was, alike every other launched CubeSat to date, made from aerospace grade aluminium alloy and a small number of structural members from titanium. AAUSat was powered by high-efficiency triple-junction photovoltaic generators mounted on five of the six cube faces and four Lithium-Polymer battery cells. Computing power was provided by a Siemens Infineon C616 central processor. AAUSat carried active magnetic three-axis attitude control; the control system consisted of three square magnetorquers, five sun sensors and a 3-axis magnetometer. The Danish spacecraft experienced two and a half months of severely limited operation; due to limited data it has not been possible to fully establish the cause. The official cause for the limited success were problems with the communications transmitter and/or power supply system.

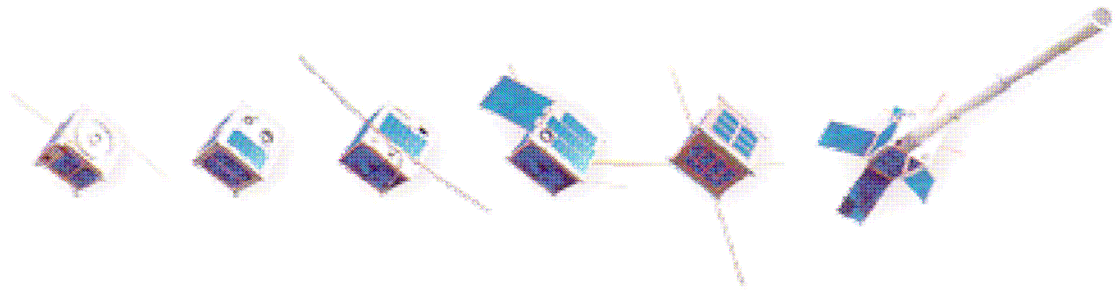

Figure 1.3: Artistic impression of the CubeSats of the first launch campaign in 2003; from left to right: AAUSat, CanX-1, XI-IV, CUTE-1, DTUSat, QuakeSat (illustration taken from [10])

CanX-1

The Canadian Advanced Nanospace eXperiment [4] developed by the Space Flight Laboratory of the Institute for Aerospace Studies at the University of Toronto carried a color CMOS imager for taking Earth images, and a monochrome CMOS imager to test the feasibility of tracking star fields, the moon and the Earth's horizon as a potential spacecraft attitude sensor on future picosatellite missions. A further technology demonstration was the determination of the orbital position using a miniature GPS receiver. The computational core was provided by an ARM7 central processor which was sufficiently powerful for the satellite's attitude stabilization algorithms in the form of angular momentum dumping using only magnetorquers and a COTS magnetometer. As with DTUSat, no signals have been received from CanX-1 since deployment from the P-POD interface.

DTUSat

The second Danish CubeSat on the 2003-launch was DTUSat, developed by more than 70 students of the Technical University of Denmark (DTU). The mission goals were to perform an in-orbit software upload and to demonstrate three-axis attitude control. In addition the spacecraft was supposed to take images of the Earth using a custom-developed camera module; however, delays in the completion of the lens system forced the spacecraft developers to implement a dummy in place of the camera. Another ambitious mission objective was the deployment of a 450m electrodynamic tether for the reduction of the orbital semi-major axis after the operational period has expired. DTUSat generated its electrical power through triple-junction solar cells on four of the six cube faces. A 32-bit RISC central processor provided sufficient computational power for system operation and the satellite's attitude control algorithms. Similar to AAUSat, the attitude control system utilized five sun sensors, three magnetorquers and a redundant custom-designed 4-axis magnetometer. Unfortunately, no transmissions have been received from the spacecraft after release from the P-POD launch system.

The 2003 Rockot launch vehicle carried only 2 P-PODs, one of which was reserved for the commercial triple-CubeSat QuakeSat, leaving 3 slots for the three single-Cubes described above. The two remaining spacecrafts, both developed at different Tokyo Institutes, launched in a launch pod known as the T-POD (Tokyo-Picosatellite Orbital Deployer) developed by the University of Tokyo. Apart from the different allocation space, the internal design of the T-POD is identical to the P-POD, such that any spacecraft built according to the CubeSat standard could be launched in a T-POD.

XI-IV
The Intelligent Space Systems Laboratory of the University of Tokyo has built the second Japanese CubeSat on the first ever CubeSat launch in 2003, called XI-IV (X-Factor Investigator-IV; "sai-four"). Its mission objectives are to establish communication with the satellite, to take and transmit low resolution images (128 by 120 pixels) of the Earth and outer space and to in-orbit verify the use of COTS components on a picosatellite platform. The cube is powered by monocrystaline solar cells and Lithium-Ion secondary batteries. The transceiver allows a downlink data rate of 1K2bps using the AX.25 packet radio protocol and CW uplink. The satellite carries passive magnetic attitude control in the form of a permanent magnet and hysteresis elements. XI-IV's mission is considered an advanced success, as it is, alike CUTE-1, still operational and several hundred images have been received.

CUTE-1
The Cubical Titech Engineering Satellite CUTE-1 is a Japanese CubeSat developed by 16 graduate and undergraduate students at the Tokyo Institute of Technology, Laboratory for Space Systems [13]. The primary mission goals were to test two different implementations of downlink communication protocols, the deployment of additional solar arrays for extended power generation and on-board attitude determination. Power was provided by moderate-efficiency monocrystaline silicon solar cells; an 8-bit central processor served as the on-board computer (OBC). Attitude determination was achieved by a piezoelectric vibration gyroscope, a 2-axis accelerometer and a CMOS array sunsensor. The spacecraft is operational since its launch in June 2003 with advanced mission success for more than 2 years and counting.

1.4 Second CubeSat Launch

For almost two and a half years, the above presented picosatellites were the only CubeSat type spacecraft in LEO. This changed with the Cosmos-3M launch of the European student satellite SSETI-Express as a secondary payload on the 27th of October 2005 which contained three CubeSats to test an in-orbit release of smaller spacecraft from a larger mothership. The CubeSats carried on-board in the Tokyo T-PODs are labeled UWE-1, XI-V and NCube-2. Out of the three CubeSats, two are fully functional until now.

UWE-1
The overall project objective of the Universität Würzburg's Experimentalsatellit-1 [5] is to test adaptations of internet protocols such as TCP (Transmission Control Protocol), UDP (User Datagram Protocol), STCP (Stream Control Transmission Protocol) and HTTP (HyperText Transfer Protocol) to the space environment, characterized by significant signal propagation delays due to the large distances and much higher noise levels compared to terrestrial links. Sufficient power for satellite operation is generated by triple-junction solar generators and stored in 2 Lithium Ion battery cells. The spacecraft is equipped with a UHV transmitter that allows transmission at either 1K2 or 9K6bps. A µLinux operating system is implemented in a Hitachi H8S-2674R microprocessor. Attitude control is achieved in a passive magnetic manner. The spacecraft is operating nominally.

XI-V

The XI-V (X-Factor Investigator-V) CubeSat is a follow-on mission to the XI-IV mission launched in 2003. Originally, XI-V was developed as a flight-spare model of XI-IV. Now, XI-V is being used as an upgraded CubeSat with the same basic design as XI-IV. The modified mission goals are to test radiation tolerant CIGS [$Cu(In,Ga)Se_2$] solar cells in orbit, developed by JAXA. XI-V carries the same CMOS camera as flown on XI-IV; however, with a considerably improved control software. A major improvement is the obtained image resolution; it is now enlarged to 320 x 240 pixels corresponding to QVGA size. The camera software interface now also supports taking a series of images of up to five frames per second; the spacecraft developers intend to use the data to extract information about the body rotation rates in order to better resolve a problem experienced with the passive magnetic attitude control of XI-IV; the attitude control subsystem is identical to XI-V. The improved message transmission service is via morse-coded CW signals and FSK packets at 1200bps. The spacecraft is operating nominally.

NCube-2

NCube [6] is a collaborative project of four Norwegian universities and educational institutes; these are: Narvik University College (HIN), Norwegian University of Science and Technology (NTNU), Trondheim, Agricultural University of Norway (NLH), and the University of Oslo. The overall mission objective of NCube-2 is the same as that of NCube-1, lost in the failed launch attempt in July 2006, namely to demonstrate ship traffic surveillance and reindeer tracking from a spaceborne platform using the maritime AIS (Automatic Identification System) communication concept. The spacecraft is equipped with monocrystalline solar cells and one Li-Ion battery cell; it carries downlink transmitters in the UHF and S bands. In order to support the active magnetic attitude control system, with attitude information being derived from EKF filtered coarse sun sensor (solar cell currents) and COTS magnetometer measurements, a 1.5m gravity gradient boom can be deployed upon telecommand. Unfortunately, no signals have been received from the CubeSat yet and the reported cause may be that the spacecraft was never released from the SSETI mothership; whether this was due to a premature antenna release or a malfunction of the T-POD is impossible to ascertain.

1.5 Australian CubeSat Development: CASSat

The Centre of Excellence for Autonomous Systems (CAS) in Sydney is currently working on a pico-satellite mission called CASsat as an educational project in various space-related fields. The primary mission objectives are to provide a dynamic and realistic learning environment for undergraduates, graduates and staff and to establish locally, within CAS, the skills and processes necessary for the development of small satellite technology. The focus of the design activities which are largely in their initial stages is on picosatellite attitude control, including technologies such as target-pointing in loose formations. The satellite is intended to carry a radiometric payload.

All the above picosatellite developments have in common a focus on subsystem technologies rather than scientific payloads. The ambitious technology demonstrations targeted by CubeSat developers around the world are one by one creating the key technologies required to enable productive missions in the future.

1.6 Introduction to Compass-1

Compass-1 is the name of a picosatellite platform being developed in strict accordance with the CubeSat specifications by students of the University of Applied Sciences Aachen, Germany, in association with the Royal Melbourne Institute of Technology, Australia [11]. Since its initiation in October 2003 this ambitious project is managed and carried out by students of the astronautical engineering department, with a majority being undergraduate students. The project aims at a multitude of objectives; firstly the students will gain essential hands-on experience in realizing a complex research and development project in an autonomously organised environment from preliminary design to launch and operation of the completed satellite. The project also envisions to create a capable infrastructure that inspires further space engineering activities to take place at the participating universities. Besides these programmatic goals, the technical objective is to demonstrate the functionality and feasibility of a very small and lightweight and at the same time sophisticated satellite bus and its potential for future applications. This thesis constitutes a contribution towards these efforts.

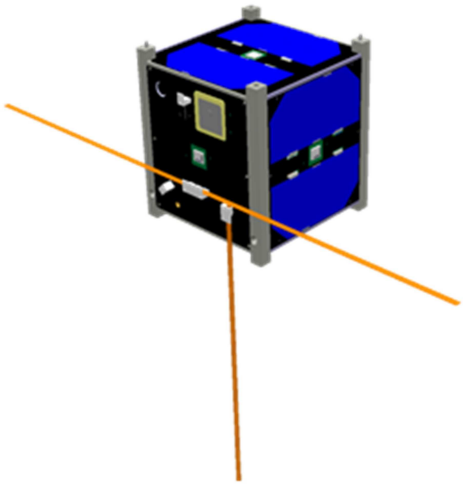

Figure 1.4: CAD rendering of Compass-1; the monopole antenna is not shown in full size

Mission

Compass-1 will conduct a combined Earth observation / technology demonstration mission. During its six months design life time, it will orbit the Earth on a sun-synchronous Low Earth Orbit (LEO) with an inclination and altitude of approximately 98° and 800km, respectively. Built mainly from **c**ommercial-**o**f-**t**he-**s**helf (COTS) CMOS microtechnology, it will take images of the Earth in the visual electromagnetic range and demonstrate novel technologies and miniaturized subsystems specifically designed or adapted for use on picosatellite platforms.

Payload

The primary payload of Compass-1 is a highly integrated color camera module which enables the Earth observation mission. The module consists of a lens system and a light sensitive CMOS array which generates VGA images with a resolution of 640 by 480 pixels.

The module has not been specifically designed for the use in space, but already achieved some space-heritage when the Japanese XI-IV CubeSat demonstrated the functionality of a predecessor module in orbit. The field of view of 54° results in a ground swath size of 614 by 460 km assuming a nominal orbit altitude of 800km. A camera is a simple payload with limited scientific outcome, but it requires a complex host infrastructure and is therefore an ideal choice for the technology demonstation objective of the mission. Each image has a relatively large size of approximately 300KB (2,457,600 bits); with a pass duration of less than 10 minutes and the requirement of transferring an image during a single pass, this yields an ambitious demand for the downlink data rate. In that sense, the camera can be considered as a place-holder for future technological or scientific payloads, once the functionality of the spacecraft bus is validated under space environment conditions. Not only does the camera module generate large quatities of data, as any potential scientific sensor would, but it does so in a way that is intuitively accessible by a general audience, thus enabling the operations team to share payload data with the public. Less intuitive quantities of data are generated by the secondary technology demonstration payload of Compass-1, the Phoenix GPS receiver [12]. The Phoenix receiver is a COTS, small outline, 12-channel, single-frequency GPS receiver with modified software to cope with the high-dynamics environment of a picosatellite in LEO. Upon telecommand, navigation solutions are recorded and dumped to the Aachen Ground Station (AGS) for non-real-time performance analysis.

Communications Subsystem

Coping with the relatively large amounts of payload data requires a transmitter which supports high data rates. While most previous CubeSats used a downlink speed of 1200kbits per second (1K2bps), Compass-1 attempts downlink rates of 9K6bps, which should enable an (for a CubeSat mission) unprecedented full VGA image dump during a single overflight. The highly integrated transceiver supports three channels of information exchange: (i) the frequency-shift-keying (FSK) modulated downlink in the 437.405MHz UHF frequency band, (ii) a morse-coded 437.275MHz continous-wave (CW) beacon signal and (iii) a VHF dual-tone-multi-frequency (DTMF) uplink. A digital controller external to the transceiver circuits is responsible for modulating and demodulating the signals and conforms the downlink data stream with the wide-spread AX.25 amateur packet radio protocol. The FSK packet downlink is accomplished through two 175mm dipole antennae and contains payload data and comprehensive housekeeping information; the CW beacon shares the dipole antenna, while the command and data uplink is received by a 500mm monopole antenna

Electrical Power System / Thermal Control

The Compass-1 spacecraft is powered by cutting-edge triple-junction solar generators manufactured by RWE Space Solar Power [7]. Triple junction cells consist of three layers of different partially transparent semiconductor compound materials (Gallium-Indium-Phosphorus/Gallium-Arsenide/Germanium) with a titanium-oxide antireflective coating; this advanced cell structure yields an average BOL efficiency of 27%. Five of the six CubeSat faces are covered with a total of 10 single cells which produce an electrical power of $3.34W_{BOL}$ during full sunlight. The power subsystem manages the charging procedure of the battery during daylight and regulates the power bus voltages of 3.3V and 5V. Excess power is stored in a pack of two Lithium-Polymer secondary batteries which have a combined capacity of 2400mAh. These novel batteries are characterised by a very high volumetric and

gravimetric power density but require careful thermal management. This is the reason why the electric power system (EPS) and the thermal control system (TCS) are concatenated to form a combined subsytem. Active thermal control is achieved through electrically heating the batteries such that their monitored temperature never falls below the freezing point at which the batteries may show unpredictable and suboptimal behavior. The rest of the spacecraft is passively controlled by choosing a spacecraft coating with adequate emission and absorption characteristics. The EPS/TCS periodically compiles basic status and health data in the form of battery voltages and temperatures which are directly transferred to the communication subsystem for transmission through the CW downlink channel. In this way, COM and EPS/TCS form a minimal system which provides basic status data even if all other subsystems fail.

Command and Data Handling System

The Command and Data Handling System (CDHS) manages the internal system modes of the spacecraft and its subsystems [8]. It receives telecommands from the groundstation through the communications system to trigger a mode-switch and periodically gathers detailed system status data which is too comprehensive for the morse-coded CW beacon stream. In addition, the CDHS is the only direct interface to the camera payload; it initiates the imaging process, which may be timed, buffers the image data in dedicated on-system Flash memory slots and transmits them selectively upon reception of the appropriate telecommand. The CDHS also serves as a GPS telemetry data buffer before the data is dumped to the ground station. The Flash unit has a capacity of 32MB enabling storage of app. 50 images plus engineering and housekeeping data. In terms of the overall configuration, the CDHS is considered a ‘mother-board’ onto which all other subsystems are card-slotted, much like the main-board of a personal computer. This implies that the CDHS contains a printed bus structure through which all inserted subsystems are connected to the power and data bus lines.

Structures and Mechanisms

The structure of a CubeSat has to survive a range of mechanical launch loads without impairment; it comprises all load bearing parts, mounting components as well as the mechanisms which are required by the CubeSat specification document [10]. The main body of the Compass-1 spacecraft consists of a separatable cubic frame structure [9] made from a dedicated aerospace aluminium alloy Al 6061-T6 with a similar thermal expansion coefficient as the PTFE impregnated, hard-anodized Al 7075 T-73 structure of the P-POD. This high-stiffness “frame-beam” type structure provides mounting provisions for two of three mechanisms as well as for the six laser-cut sheet metal panels which form the cube faces; these provide mounting positions for various system components such as the communication antennae and the antenna release mechanism. All structural members are made from the same aluminum alloy and all members which are outward-facing are hard-anodized for proper thermo-optical behavior as well as avoidance of cold-welding during the launch inside the P-POD container.

The three mechanisms, (i) the kill-switches, (ii) the separation springs and (iii) the antenna release mechanism, satisfy standard regulations as well as operational requirements. The kill-switch ensures that the spacecraft is completely passive during launch until ejection from the

launch container; the separation springs are required in order to compensate cumulative manufacturing tolerances of all three CubeSats sharing a P-POD container as well as assuring a minimum safety clearence between the three satellites. The antenna release mechanism is required due to space constraints inside the P-POD; during launch the antenna system is stowed and after a certain time after release from the launcher the antennae made from spring steel are deployed using a "burn-wire" type method.

It is not only the responsibility of the structures group to design and verify a suitable CubeSat structure and reliable mechanisms but also to define and iteratively control all mass properties of the spacecraft (position of the center of mass, moments and products of inertia, etc.), elaborate solutions for the wiring of harness components and for the actual integration procedure of the tiny spacecraft. Most of these tasks can only be reasonably accomplished by carefully maintaining a detailed CAD model of the spacecraft which serves as a top-level reference for every subsystem.

Attitude Determination and Control System

The objective of the Attitude Determination and Control System (ADCS) is twofold; firstly it shall stabilize the spacecraft's body rotation rates and angular momentum upon completion of the impulsive P-POD and antenna release sequences in the initial mission stage; and secondly, during nominal operation, it shall stabilize the desired attitude against all attitude disturbing influences resulting from the LEO environment in order to point the imager payload towards the surface of the Earth within a specified margin of error. These goals must be achieved within stringently limited mass, power and size.

Table 1.1: Technical Resources allocated to the Attitude Determination and Control System (ADCS)

Mass:	no more than 200g
Power:	no more than 400mW$_{el}$ nominal
	no more than 1600mW$_{el}$ peak for short durations
Size/Volume:	no more than 20% of the total CubeSat volume

Power shall be primarily drawn from the 3.3 Volts power bus line; however, a 5V bus line is available to the ADCS in the nominal operation mode, during which the spacecraft shall maintain a nadir-pointing attitude, i.e. an orientation in which the camera boresight always points to the center of the Earth. In doing so, the ADCS shall be accurate to 10 degrees maximum total deviation from the reference nadir attitude under nominal conditions.

It is a common goal among CubeSat developers to create systems of high autonomy; Compass-1 carries this idea further by introducing the concept of modularity to the spacecraft design. Contrary to the top-level design philosophy of most of the other CubeSat architectures, which incorporates a single central OBC for all computational tasks, the idea of a decentralized command and data handling is applied on Compass-1. This implies that all computational processes, e.g. signal processing and execution of algorithms, are performed on the subsystem level on a dedicated processor. The advantage of this architecture is that the interfaces between the subsystems may be kept very simple, since only high level data is exchanged. Also, processes may truly run in parallel on distributed processors.

Disadvantages are higher power consumption and more complexity on the subsystem level, requiring slightly longer development times. A derived requirement from the statements made above is that the ADCS shall have the capability of running autonomously for the longest part of the mission; intervention from the ground segment shall be minimized.

This thesis comprehensively presents the design of the novel active magnetic attitude control system which satisfies the above requirements. The system is dedicated for picosatellites on highly inclined circular LEO orbits for first flight-testing on the Compass-1 spacecraft in 2007.

1.7 Contributions of this Work

In the past few years a number of authors have considered active magnetic control for three-axis stabilization, and the more relevant works are listed in the bibliography and referred to in the text. While the main objective of the grand research project is to, based on previously elaborated control theory, develop a practical solution to the attitude control problem for first in-orbit verification aboard a picosatellite, the objective of this thesis document is to (i) supplement the current body of knowledge in the specific field of magnetic attitude control and to (ii) serve as a comprehensive reference for future picosatellite system developers attempting to implement this novel approach to attitude control.

The main original contributions are identified as:

- The linear spacecraft dynamics in state space are modeled in quaternions throughout. Previous authors derived a plant system in a mixed quaternion / body rate state variable vector [17,19,20,21]. It is believed that the switch from a mixed notation to a complete quaternion notation will simplify the implementation for spacecrafts without rate sensors in their attitude determination sensor suit.

- Establishment of an analytical simplification of the Linear Quadratic Regulator (LQR) attitude controller synthesis process. In order to enable the application of classical LQR controller design methods, the periodic system must be transferred to a system with constant coefficients. An analytical solution to the problem of averaging the periodic part of the state space model in time has been found based on a direct geomagnetic dipole field approximation. This simplifies the synthesis process considerably for satellites with circular target orbits.

- Simulation of controller implementation considering realistic operational conditions. This work, for the first time, presents a multitude of simulation scenarios for both ideal and realistic implementation conditions, i.e discretization of the control loop, discrete magnetorquer operation, magnetometer readings subject to noise and drift and a multiplexed measurement/control sequence. Operational assumptions have been made on the basis of the Compass-1 system design, but are deemed characteristic for many CubeSat designs.

Owing to the factual nature of the project, various presentations have been given at conferences, national space agencies and institutes in the context of the Compass-1 spacecraft development. A published co-authored paper concerned with system-level design aspects for CubeSats following the example of Compass-1 is „CubeSat – Technical Aspects“, which has been held in 2004 at the 55th International Astronautical Congress in Vancouver, Canada.

1.8 Overview over Thesis

- Chapter 1 has established the context of technology development for picosatellites by presenting an overview of past CubeSats and the mission goals set for the near-future CubeSat Compass-1. In addition, the top-level requirements and the overall design architecture of the attitude control system for first flight-testing in 2006 have been defined.

- Chapter 2 presents models of the rigid spacecraft dynamics and kinematics. The concept of gravity gradient stability will be established and the equations of motion will be linearized in the desired nadir pointing attitude state.

- Chapter 3 presents the environment of a spacecraft in LEO, with emphasis on the dynamic disturbance enviroment. In addition the topology of the geomagnetic main field as the driving resource for the magnetic attitude control concept will be presented including a model for its accurate representation.

- Chapter 4 deals with the description of hardware component selection of the developed attitude control system and the implications for the performance of the overall system.

- Chapter 5 presents the theory of magnetic attitude control. This includes both the well-known detumbling controller and the controller for nominal nadir-pointing control. The LQR controller and its application to the magnetic attitude control problem is elaborated in order the arrive at a systematic controller synthesis methodology. The main result of Floquet's theory for linear periodic systems will be applied in order to verify the stability of the system under LQR control.

- Chapter 6 presents details of the attitude estimation process for full-state LQR feedback. This process includes the generation of reference information as well as the actual estimation of the spacecraft attitude in 3D space for a given set of input information.

- Chapter 7 ties all the above together by validating the performance of the designed controllers in a realistic dynamics simulation environment. Results are given for both the ideal implementation conditions and for more realistic conditions including hardware performance models.

- Finally, chapter 8 summarizes the results of the thesis and presents recommendations for future work as well as an outlook on the Compass-1 launch.

Chapter 2

Spacecraft Model

The discipline of attitude dynamics involves the analytical study of the rotational motion of a near torque-free body in three-dimensional space while being virtually decoupled from its translational state. This chapter concisely presents important mathematical background for the parametrization and kinematics of the attitude of a general rigid body in space, as well as the non-linear dynamic and kinematic equations of motion. This chapter will also present the gravity gradient as a supporting environmental torque and its effect on flight stability. A crucial result of this chapter will be the derivation of the linear state-space model of the satellite dynamics which will be used for the synthesis of the attitude controller in chapter 5. To start with, the spacecraft-centered frames of reference used for the attitude dynamics of Compass-1 are presented in the following; Earth-centered coordinated systems (CS) are presented in chapter 6 in the context of attitude determination.

2.1 Spacecraft-Centred Reference System Definition

The reference frames useful in general spaceflight dynamics are composed of a triad of orthogonal unit base vectors, generalized as $F = \{\hat{\imath}, \hat{\jmath}, \hat{k}\}$. A limited set of meaningful and intuitive reference systems has been established which appear throughout literature and form a common base for the representation of space flight dynamics. All coordinate systems considered in this thesis are so-called right-handed frames, i.e. $\hat{\imath} \times \hat{\jmath} = \hat{k}$.

Four spacecraft-centered coordinate systems, i.e. reference frames with their origins coinciding with the spacecraft center of gravity (CG), provide a sufficient base for many occurring attitude tasks and are probably the most important frames to the spacecraft control engineer. These references are called the *inertial frame*, the *orbit frame*, the *body frame* and the *control frame*. Three of these four frames are depicted in figure 2.1, which shows Compass-1 in a generalized attitude with respect to the reference frames.

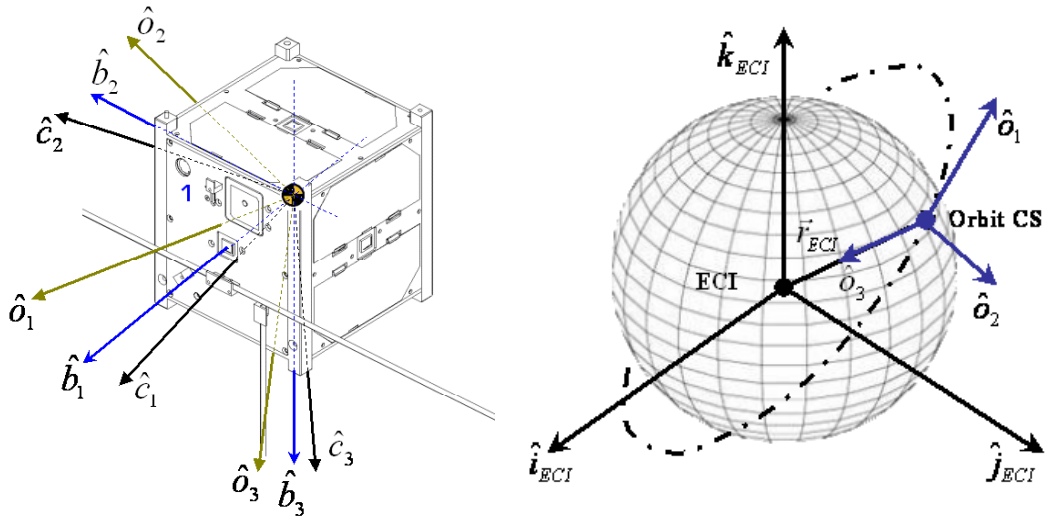

Figure 2.1: Three important spacecraft centered frames of reference: The control frame (black) and the body frame (blue) and their relation to the orbit frame (green) and to each other in the left illustration; the right illustration shows the orientation of the orbit frame of reference w.r.t. the inertial frame ('ECI')

Inertial Frame

The $\hat{\imath}_3$ axis of the inertial frame $F_i = \{\hat{\imath}_1, \hat{\imath}_2, \hat{\imath}_3\}$ joins the poles of the spacecraft-centered celestial sphere and is parallel to the axis of rotation of the Earth, which is (almost) inertially fixed. The $\hat{\imath}_1$ axis is the line joining the spacecraft CG with the south-to-north intersection of the ecliptic plane and the celestial equator of the spacecraft centered celestial sphere. In other terms, the direction parallel to the sun-to-Earth line on the first day of spring (w.r.t. the northern hemisphere). This direction is historically called the spring equinox, or *vernal equinox* ♈. The $\hat{\imath}_2$ axis completes the right-hand orthogonal cartesian coordinate system.

Orbit Frame

For the nadir-pointing attitude stabilization problem this important frame defines the attitude reference of the spacecraft. The $\hat{o}_3$ axis of the orbit[1] frame $F_o = \{\hat{o}_1, \hat{o}_2, \hat{o}_3\}$ points towards the Earth's centroid and the $\hat{o}_2$ axis is anti-parallel to the normal of the orbital plane. The $\hat{o}_1$ axis completes the right-handed cartesian coordinate system and it coincides with the satellite's vector of velocity if the orbit is perfectly circular. On any closed orbit about a single primary, the orbit frame rotates once about the orbital $\hat{o}_2$ axis with respect to the inertial frame; on a circular orbit, the rate of rotation or the "mean motion", labeled ω_0, is constant.

Body Frame

A meaningful definition of the body frame $F_b = \{\hat{b}_1, \hat{b}_2, \hat{b}_3\}$ can be based on the satellite's geometric properties or alternatively on payload pointing geometries; in either case, the decision is made by the control engineer. For the general case of a CubeSat which is characterized by a cubic structural bus, the body axes are most intuitively defined as being parallel to the edges of the cube, or equivalently being normal to the sideplates. In the specific case of Compass-1, $\hat{b}_1$ points through the antenna system panel (Side 1) and $\hat{b}_3$ points along the camera boresight. The ordering of the body frame axes has its original roots in the discipline of aeronautics where x-z-y was defined as '*forward-down-over the right wing plane*', respectively.

Control Frame

In real-world satellite structures the inertia tensor aligned with the body frame contains non-zero products of inertia. In many situations system equations can be substantially simplified if the dynamics problem is expressed in a frame, in which the off-diagonal terms of the positive definite inertia matrix are zero. The frame, in which this is the case, is referred to as the principal frame, or control frame $F_c = \{\hat{c}_1, \hat{c}_2, \hat{c}_3\}$. The diagonal elements of the new inertia tensor ${}^{c}I = diag(I_1,I_2,I_3)$ are found by evaluation of a linear eigenvalue problem, i.e.

$$\det\left[\mathrm{I} - \lambda \cdot \mathrm{E}\right] = 0 \quad \text{with } \lambda_i > 0 \quad \text{and} \quad \lambda_i \in \mathbf{R} \tag{2.1}$$

The eigenvalues are the principal moments of inertia and the corresponding eigenvectors $\hat{c}_1$, $\hat{c}_2$ and $\hat{c}_3$ are the base vectors of the control frame expressed in the body frame, i.e. the eigenvectors can be used to construct the Direction Cosine Matrix which transforms the body frame into the control frame. On Compass-1 every effort is undertaken in terms of equipment/subsystem placement in order to align the principal axes with the body frame, such that the assumption of $F_c = F_b$ is reasonable and will be used throughout this thesis.

[1] the orbit frame is also commonly referred to as 'Local Vertical / Local Horizontal' frame, because the two defining axes are indeed vertical and horizontal to the Earth's surface at the location of the spacecraft.

2.2 Attitude Parametrization

It is often necessary to perform transformations between different coordinate frames, for instance in order to express a vector in a different frame. The above discussion of the control frame-body frame relationship has introduced the very practical need to be able to express one CS in relation to another. This is the very essence of attitude parametrization; following the orientation of a reference frame is completely equivalent to following the orientation of a rigid body. In the following, three of the most common methods for doing so are presented; these are the Direction Cosine Matrix, Euler angles and quaternions.

2.2.1 Direction Cosine Matrix

The most straight-forward way to transform one set of base vectors into another is by matrix transformation. For instance, a matrix R^{bo} may be used to transform vectors expressed in F_o into F_b such that

$$^{b}v = R^{bo} \cdot {}^{o}v \tag{2.2}$$

Since these transformations have the property of being *orthonormal*, the reverse transformation from F_b into F_o is achieved by the transpose of the matrix R^{bo}

$$^{o}v = R^{ob} \cdot {}^{b}v \tag{2.3}$$

$$R^{ob} = R^{bo^{-1}} = R^{bo^{T}} \tag{2.4}$$

A transformation matrix of this type is called a Direction Cosine Matrix (DCM) owing to the fact that it is composed of the direction cosines of the angles between respective base vectors,

$$R_{ij} = \hat{o}_i \cdot \hat{b}_j = \cos\alpha_{ij} \tag{2.5}$$

which, in the case of (2.5), represents a scalar projection of the body axes onto the orbit frame base vectors.

2.2.2 Euler Angles

The most easily accessible way of constructing a DCM for the purpose of rotating coordinate frames and expressing the attitude of a vehicle is by defining any general rotation as a sequence of three simple rotations about the body base vectors. It is common to parametrize the deviation of F_b with respect to F_o in terms of a set of three Tait-Bryan angles, or Cardan angles, pitch (θ), roll (φ) and yaw (ψ); these terms originate from the discipline of aeronautical flight mechanics which historically forms the notational framework for spacecraft flight dynamics.

The standard definition of an aircraft body frame

$$F_b = \{\hat{b}_1,\ \hat{b}_2,\ \hat{b}_3\}$$

is 'forward, over the right wing plane, down' direction-wise or 'roll, pitch, yaw' axis-wise, respectively. For 3-axis stabilized spacecraft, a 3-2-1 rotation sequence is often used. This means that the original body triad

$$^0\{\hat{b}_1,\ \hat{b}_2,\ \hat{b}_3\} = \{\hat{o}_1, \hat{o}_2, \hat{o}_3\}$$

first undergoes an angular yaw rotation ψ about the $^0\hat{b}_3$ body axis which yields a new frame

$$^1\{\hat{b}_1,\ \hat{b}_2,\ \hat{b}_3\}$$

The next rotation will be about the $^1\hat{b}_2$ axis by the pitch angle θ to form $^2\{\hat{b}_1,\ \hat{b}_2,\ \hat{b}_3\}$, and finally the new frame is rotated about $^2\hat{b}_1$ by the roll angle φ.

Mathematically, that is

$$^b v = R_1(\phi)\cdot R_2(\theta)\cdot R_3(\psi)\cdot {}^o v \tag{2.6.a}$$

or

$$^b v = \begin{bmatrix} 1 & 0 & 0 \\ 0 & \cos\phi & \sin\phi \\ 0 & -\sin\phi & \cos\phi \end{bmatrix}\cdot\begin{bmatrix} \cos\theta & 0 & -\sin\theta \\ 0 & 1 & 0 \\ \sin\theta & 0 & \cos\theta \end{bmatrix}\cdot\begin{bmatrix} \cos\psi & \sin\psi & 0 \\ -\sin\psi & \cos\psi & 0 \\ 0 & 0 & 1 \end{bmatrix}\cdot {}^o v \tag{2.6.b}$$

The three individual rotations yield the DCM for the absolute orientation of F_b with respect to F_o. In (2.7), c and s denote the cosine and the sine function, respectively.

$$\mathrm{R}^{\mathrm{bo}} = \begin{bmatrix} \mathrm{c}\theta\cdot\mathrm{c}\psi & \mathrm{c}\theta\cdot\mathrm{s}\psi & -\mathrm{s}\theta \\ \mathrm{s}\phi\cdot\mathrm{s}\theta\cdot\mathrm{c}\psi - \mathrm{c}\phi\cdot\mathrm{s}\psi & \mathrm{s}\phi\cdot\mathrm{s}\theta\cdot\mathrm{s}\psi + \mathrm{c}\phi\cdot\mathrm{c}\psi & \mathrm{s}\phi\cdot\mathrm{c}\theta \\ \mathrm{c}\phi\cdot\mathrm{s}\theta\cdot\mathrm{c}\psi + \mathrm{s}\phi\cdot\mathrm{s}\psi & \mathrm{c}\phi\cdot\mathrm{s}\theta\cdot\mathrm{s}\psi - \mathrm{s}\phi\cdot\mathrm{c}\psi & \mathrm{c}\phi\cdot\mathrm{c}\theta \end{bmatrix} \tag{2.7}$$

Small angle approximation ($\sin\alpha \approx \alpha$ for small α) is a common assumption for the linearization of dynamic systems as shown later in this chapter. The linearized DCM for a 3-2-1 rotation sequence is

$$R^{bo} = \begin{bmatrix} 1 & \psi & -\theta \\ -\psi & 1 & \phi \\ \theta & -\phi & 1 \end{bmatrix} \tag{2.8}$$

Note, that there are 3 axes to choose from for the first rotation, 2 for the second and 2 for the third, yielding 3x2x2 = 12 possible rotation sequences, of which 6 are formed by a symmetric euler angle set, e.g. 3-1-3. Note also, that unlike rotations defined by a DCM, rotations in terms of euler angles require adherence to a consistent definition of the rotation sequence. Hence, euler angles without reference to the sequence convention yield ambiguous attitude information. However, the main problems associated with euler angles to construct a DCM are the occurrence of singularities and the computational burden imposed by the evaluation of 6 trigonometric functions, 4 additions and 16 multiplications. Alternative kinematic representations exist, which are celebrated for various superiorities over euler rotations. Certainly the most important method of attitude parametrization is achieved by the use of so called *quaternions*.

2.2.3 Quaternions

After the discovery of the complex number system $\mathbb{C}$ many mathematicians wondered if there were any number systems of even higher dimension. After a long and frustrating period without success in this field of research it transpired that the natural successor to $\mathbb{C}$ actually exists in not three but *four* dimensions; the set of these non-commutative numbers, called quaternions, is labeled $\mathbb{H}$ in honor of their discoverer, Irish physicist and mathematician Sir William Rowan Hamilton (1805 – 1865) [18]. His famous fundamental quaternion equations are preserved in a stone of the Brougham Bridge over the Royal Canal in Dublin onto which he carved his sudden strike of genius with a pocket knife.

Quaternions prove to be an elegant way of expressing the orientation of a body in euclidean space, utilizing the concept of Euler parameters which are a consequence of Euler's Rotation Theorem; this states that the most general motion of a rigid body with a fixed point is a rotation about a fixed axis. Hence, the Euler parameters **a** ('Euler axis') and Φ ('Euler principal angle') suffice to fully describe any general vehicle attitude. The Euler parameters are used to form the elements of a quaternionic number

$$\bar{q} = q_1 \cdot i + q_2 \cdot j + q_3 \cdot k + q_4 \cdot 1 = \begin{bmatrix} q^T & q_4 \end{bmatrix}^T$$

as

$$q_1 = a_1 \cdot \sin\left(\Phi/2\right) \tag{2.9.a}$$

$$q_2 = a_2 \cdot \sin\left(\Phi/2\right) \tag{2.9.b}$$

$$q_3 = a_3 \cdot \sin\left(\Phi/2\right) \tag{2.9.c}$$

$$q_4 = \cos\left(\Phi/2\right) \tag{2.9.d}$$

generally satisfying $i^2 = j^2 = k^2 = ijk = -1$ and specifically (for 3D rotations) being subjet to a normalization constraint

$$\bar{q}^T \cdot \bar{q} = 1 \tag{2.10}$$

to account for the fact, that a general angular displacement has only three degrees of freedom. Of course it is possible to convert attitude information from one parametrization, e.g. quaternions, to another form, e.g. DCM.

$$R = (q_4^2 - q^T q)E + 2qq^T - 2q_4 q^{\times} \tag{2.11}$$

where q^x is the skew-symmetric matrix of the vector part of the quaternion. Skew-symmetric matrices are matrices which obey the form shown in (2.12) and may be simply used as a convenient way of reformulating a vector cross product into a matrix representation, i.e

$$a \times b = a^{\times} \cdot b$$

$$a^{\times} = \begin{bmatrix} 0 & -a_3 & a_2 \\ a_3 & 0 & -a_1 \\ -a_2 & a_1 & 0 \end{bmatrix} \tag{2.12}$$

While quaternions also provide a means to perform unlimited sequences of rotation, the main advantage of quaternions is the provision of a singularity-free and efficient attitude parametrization. A given quaternion always defines a corresponding attitude in an unambiguous manner without the need for additional conventions as in the case of euler angles, and much more compact than by a DCM. However, care must be taken since a given attitude does not unambiguously relate to a unique quaternion, because

$$\bar{q} = -\bar{q} \tag{2.13}$$

2.3 Kinematic Equation of Motion

Unambiguously resolving the time history of the attitude of a rigid body is a process involving two stages of integration. First the dynamic equations of motion are integrated in order to relate a torque acting on a spacecraft structure with a history of angular velocity, starting from known body rotational rates. The second step relates the history of body angular velocity with the attitude of the body with known initial orientation, by integration of the kinematic equations of motion.

Since the attitude of Compass-1 is parametrized in terms of quaternions, the kinematic equation of motion of choice is as shown in (2.14)

$$\dot{\bar{q}} = \frac{1}{2}\Omega \cdot \bar{q} = \frac{1}{2} \cdot \begin{bmatrix} q^{\times} + q_4 \cdot E \\ -q^T \end{bmatrix} \cdot \vec{\omega} \tag{2.14}$$

$$\Omega = \begin{bmatrix} 0 & \omega_3 & -\omega_2 & \omega_1 \\ -\omega_3 & 0 & \omega_1 & \omega_2 \\ \omega_2 & -\omega_1 & 0 & \omega_3 \\ -\omega_1 & -\omega_2 & -\omega_3 & 0 \end{bmatrix} \tag{2.15}$$

Note that the kinematic equation of motion (2.14) consists of 2 linear differential equations. However, their variable coefficients preclude closed-form solutions.

When dealing with nadir-pointing satellites like Compass-1, the attitude with respect to the orbital reference frame is of foremost interest. So to be of any practical use the kinematics model in (2.14) must yield attitude information in the orbit frame. Since the dynamic equations of motion resolve the body rates w.r.t. the inertial frame, as will be shown soon, two options of implementing (2.14) in a numerical simulation environment are conceivable: (i) the kinematics are evaluated in the inertial frame and subsequently transformed into the orbit frame, or (ii) the inertial body rates are transformed into the orbit frame which is itself rotating with respect to the inertial world and then integrated by (2.14). Either way, coordinate transformation is required. The MATLAB/Simulink simulation software developed to analyse the performance of the control laws (see chapter 7) synthesized in chapter 5 uses the latter method for attitude integration. The following reasoning is used to derive the orbital body rates from the inertial rates.

Angular velocities add if expressed in a common frame.

$$\omega_b^{bi} = \omega_b^{bo} + \omega_b^{oi} \tag{2.16}$$

Starting from (2.16) the relationship for the angular rates of the body frame w.r.t. the orbit frame, expressed in the body CS (ω_b^{bo}) can be established as follows.

$$\omega_b^{bo} = \omega_b^{bi} - \omega_b^{oi} \tag{2.17.a}$$
$$\omega_b^{oi} = R^{bi} \cdot \omega_i^{oi} \tag{2.17.b}$$
$$\omega_i^{oi} = -\omega_0 \cdot \hat{o}_2 \tag{2.17.c}$$
$$R^{bi} = R^{bo} \cdot R^{oi} \tag{2.17.d}$$
$$\omega_b^{bo} = \omega_b^{bi} - R^{bo} \cdot R^{oi} \cdot (-\omega_0 \cdot \hat{o}_2) \tag{2.17.e}$$

Although not used for the purpose of attitude kinematics on Compass-1 the kinematic equations of motion in terms of 3-2-1 euler angles yield some useful equations for system linearization.

$$p = \omega_{b,1}^{bo} = \dot{\phi} - \dot{\psi} \sin\theta \tag{2.18.a}$$
$$q = \omega_{b,2}^{bo} = \dot{\theta} \cos\phi + \dot{\psi} \cos\theta \sin\phi \tag{2.18.b}$$
$$r = \omega_{b,3}^{bo} = \dot{\psi} \cos\theta \cos\phi - \dot{\theta} \sin\phi \tag{2.18.c}$$

Applying the small angle approximation on (2.18.a,b,c) yields the simple relationships

$$\omega_{b,1}^{bo} \approx \dot{\phi} \tag{2.19.a}$$

$$\omega_{b,2}^{bo} \approx \dot{\theta} \tag{2.19.b}$$

$$\omega_{b,3}^{bo} \approx \dot{\psi} \tag{2.19.c}$$

Solving (2.18.a,b,c) for the rates in roll, pitch and yaw, i.e. $\dot{\phi}$, $\dot{\theta}$ and $\dot{\psi}$, results in

$$\dot{\phi} = p + (q\sin\phi + r\cos\phi)\cdot\tan\theta \tag{2.20.a}$$

$$\dot{\theta} = q\cos\phi - r\sin\phi \tag{2.20.b}$$

$$\dot{\psi} = (q\sin\phi + r\cos\phi)\cdot\sec\theta \tag{2.20.c}$$

which shows a simple way of obtaining attitude information (w.r.t. to the inertial reference system) in terms of euler angles by integration of (inertial) body rate measurements (p, q, r) from a known initial condition. These rate measurements may be obtained by a variety of inertial rate sensors, e.g. gyros. Equations (2.20.a,b,c) also illustrate one of the major disadvantages of euler angle attitude parametrization: for this specific rotation sequence, a singularity exists at $\theta = \pi/2$. In some gyroscopic inertial systems, as a practical example, this abstract singularity might cause a phenomenon called g*imbal lock*, i.e. a situation in which the cardanic suspension frame hits hard-stop type limits of the measurement space.

2.4 Dynamic Equation of Motion

Since Compass-1 is modeled as a rigid body, Euler's law yields a more direct approach to finding the dynamic equation of motion than Newton's second law, which would be the method of choice for non-rigid, flexible spacecraft structures. In the inertial frame Euler's Law relates the net applied torque about the CG with the rate of change of the body's angular momentum about the CG. Spinning spacecraft and gyroscopic instruments utilize this relation in order to passively stabilize the spin axis inertially.

$$^{i}\dot{h} = {}^{b}T \tag{2.21}$$

The angular momentum is defined as

$$h = I\omega \tag{2.22}$$

The inertia tensor of a rigid body is constant in the body frame F_b. Hence, it is common to express the dynamics of the body w.r.t. a body-fixed CS, e.g. the body frame; here, the angular momentum is defined as

$$\begin{aligned} {}^{b}h &= I\cdot\omega_{b}^{bi} \\ I &= const. \end{aligned} \tag{2.23.a}$$

and

$$ {}^{b}\dot{h} = I \cdot \dot{\omega}_b^{bi} \tag{2.23.b} $$

It is noteworthy to observe from (2.23.a) that the angular momentum and angular velocity will only be aligned when the body rotates about one of the principal axes, i.e. in the control frame the inertia tensor is diagonal and only one element of ω_c^{ci} is non-zero.

Applying the general rule of the derivative of vectors in rotating coordinate frames

$$ \frac{d}{dt} a \Big|_i = \frac{d}{dt} a \Big|_b + \omega_b^{bi} \times {}^{b}a \tag{2.24} $$

eqn. (2.22) can be rewritten in the body frame

$$ {}^{i}\dot{h} = {}^{b}\dot{h} + \omega_b^{bi} \times {}^{b}h = {}^{b}T \tag{2.25} $$

Inserting (2.23.a) and (2.23.b) and solving for $\dot{\omega}_b^{bi}$ yields

$$ \dot{\omega}_b^{bi} = -I^{-1}\omega_b^{bi} \times I\omega_b^{bi} + I^{-1}\,{}^{b}T \tag{2.26} $$

which is the non-linear dynamic differential equation of motion for a rigid body with constant inertia.

Since the inertia tensor ${}^{c}I = diag(I_1,I_2,I_3)$ is of a diagonal positive definite form in F_c, a change from F_b to F_c enables to equivalently write (2.26) as

$$ \dot{\omega}_{c,1}^{ci} = \dot{\omega}_1 = \frac{I_2 - I_3}{I_1}\omega_2\omega_3 + \frac{{}^{c}T_1}{I_1} \tag{2.27.a} $$

$$ \dot{\omega}_{c,2}^{ci} = \dot{\omega}_2 = \frac{I_3 - I_1}{I_2}\omega_1\omega_3 + \frac{{}^{c}T_2}{I_2} \tag{2.27.b} $$

$$ \dot{\omega}_{c,3}^{ci} = \dot{\omega}_3 = \frac{I_1 - I_2}{I_3}\omega_1\omega_2 + \frac{{}^{c}T_3}{I_3} \tag{2.27.c} $$

Equations (2.27.a,b,c), well-known as Euler's moment equations, are used in the analysis of the flight stability conditions in the following after the introduction of an important environmental torque source, the gravity gradient effect.

2.5 Gravity Gradient Torque

A gravity gradient torque arises from the fact that the satellite is traveling in a non-uniform central force field resulting in slightly different attraction of gravity across the satellite. The following model is based on the two-body approximation, i.e. lunar and solar gravity sources are neglected, with the Earth having a spherically symmetric mass distribution, i.e. an ideal gravitational potential field. Also, the spacecraft is assumed to be rigid and small compared to its distance from the center of the Earth.

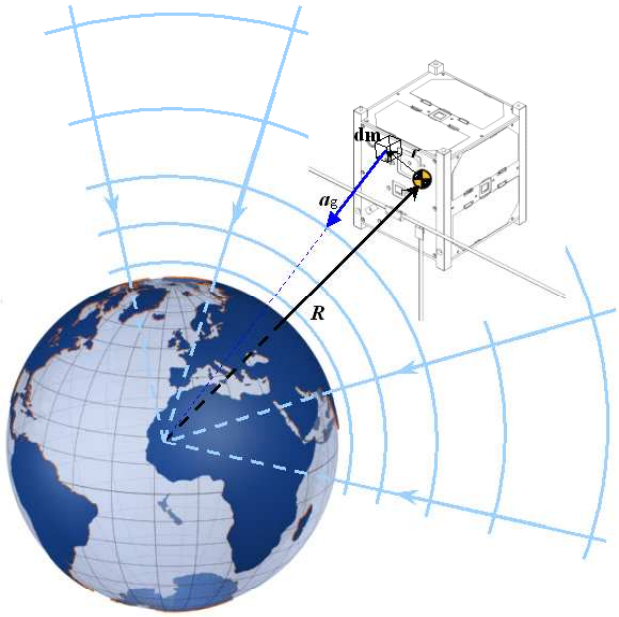

Figure 2.2: In a central force field, minuscule accelerations acting on all mass elements of a rigid body are directed towards the CG of the primary body, the Earth. This gives rise to a minute torque called 'gravity gradient torque'.

$$a_g = -GM_E \cdot \frac{R+r}{|R+r|^3} \tag{2.28}$$

$$M = \int r \times a_g \, dm \tag{2.29}$$

Note that the integral in (2.29) would evaluate to zero in a uniform gravity field or if the body was perfectly symmetric. In other terms, every asymmetric body in a central force field is subject to a gravity gradient torque; these environmental torques are so small that they are not noticed during all-day life but in the otherwise near torque free environment of a LEO picosatellite, these torques are no longer negligible.

The gravity gradient torque can be shown to be [15]

$$T_{GG} = 3\omega_0^2 \cdot \left[{}^b\hat{o}_3 \times I \cdot {}^b\hat{o}_3 \right] \tag{2.30}$$

with ${}^b\hat{o}_3$ being the local vertical (third unit base vector of the orbital frame) expressed in the body frame, which implies that the gravity gradient effect is a function of the attitude indeed. Also, by observation of (2.30), no torque is exerted about the local vertical direction. Gravity gradient torques of an asymmetric body subject to a gravitational field are conservative torques tending to align the axis of minor principal inertia with the gravity field vector. This is the reason why, in this thesis, the gravity gradient is not considered a disturbance in the original sense of the term; Compass-1 is designed for gravity gradient stability, satisfying criteria discussed in the next section, and the resulting torque will tend to align the payload boresight with the local vertical, i.e. the nadir direction. Hence, the gravity gradient effect supports the control system rather than disturbing it.

The gravity gradient torque is often expressed in the principal reference system in which some of the terms related to the products of inertia in the inertia tensor vanish. Also, this formulation is more compatible with Euler's moment equations in (2.27.a,b,c). In terms of the 3-2-1 euler angles the gravity gradient torque T_{GG} can be expressed in the following form:

$${}^cT_{GG,1} = \frac{3\mu}{2R^3}(I_3 - I_2)\sin(2\phi)\cos^2(\theta) \tag{2.31.a}$$

$${}^cT_{GG,2} = \frac{3\mu}{2R^3}(I_3 - I_1)\sin(2\theta)\cos(\phi) \tag{2.31.b}$$

$${}^cT_{GG,3} = \frac{3\mu}{2R^3}(I_1 - I_2)\sin(2\theta)\sin(\phi) \tag{2.31.c}$$

2.6 Gravity Gradient Stability

Having established the equations of motion of the rigid body in space and a torque acting on the satellite as a function of its attitude and mass properties, an interesting question is now, under which conditions the spacecraft is naturally stable. Compass-1 is designed to be stable in order to enable passive support of the attitude control system.

Applying the small angle approximation for roll φ and pitch θ, and introducing the orbital mean motion ω_0 for a circular orbit

$$\omega_0 = \sqrt{\frac{\mu_\oplus}{R^3}} \tag{2.32}$$

the gravity gradient may be linearized as

$$T_{GG,1} = 3\omega_0^2 (I_3 - I_2) \cdot \phi \tag{2.33.a}$$

$$T_{GG,2} = 3\omega_0^2 (I_3 - I_1) \cdot \theta \tag{2.33.b}$$

$$T_{GG,3} = 0 \tag{2.33.c}$$

Under the small angle assumption of (2.19.a,b,c) and with $R^{oi} = E$, the kinematics of (2.17.e)

$$\omega_c^{ci} = \omega_c^{co} + R^{co} \cdot (-\omega_0 \cdot \hat{o}_2) \tag{2.34}$$

are linearized to yield

$$\omega_c^{ci} = \begin{bmatrix} \omega_1 \\ \omega_2 \\ \omega_3 \end{bmatrix} = \begin{bmatrix} \dot{\phi} - \psi\omega_0 \\ \dot{\theta} - \omega_0 \\ \dot{\psi} + \phi\omega_0 \end{bmatrix} \tag{2.35.a}$$

and

$$\dot{\omega}_c^{ci} = \begin{bmatrix} \dot{\omega}_1 \\ \dot{\omega}_2 \\ \dot{\omega}_3 \end{bmatrix} = \begin{bmatrix} \ddot{\phi} - \dot{\psi}\omega_0 \\ \ddot{\theta} \\ \ddot{\psi} + \dot{\phi}\omega_0 \end{bmatrix} \tag{2.35.b}$$

Inserting (2.35.a) and (2.35.b) into Euler's moment equations (2.27.a,b,c) and discarding any products of euler angles or derivatives thereof finally yields the linearized homogeneous equations of motion subject to gravity gradient and in euler angle terminology.

$$I_1\ddot{\phi} + 4\omega_0^2 (I_2 - I_3)\phi - \omega_0 (I_1 + I_3 - I_2)\dot{\psi} = 0 \tag{2.36.a}$$

$$I_2\ddot{\theta} + 3\omega_0^2 (I_1 - I_3)\theta = 0 \tag{2.36.b}$$

$$I_3\ddot{\psi} + \omega_0^2 (I_2 - I_1)\psi + \omega_0 (I_3 + I_1 - I_2)\dot{\phi} = 0 \tag{2.36.c}$$

By simple inspection, (2.36.b) is a differential equation of second order, with no damping term, i.e. the pitch motion is a simple harmonic oscillator as long as

$$I_1 > I_3 \tag{2.37}$$

This is the first stability criterion; if $I_3 < I_1$ the satellite is pitch stable with a frequency of

$$f_p = \omega_0 \cdot \sqrt{\frac{3 \cdot (I_1 - I_3)}{I_2}} = \omega_0 \cdot \sqrt{3\sigma_2} \tag{2.38}$$

and an amplitude equal to the initial pitch condition $\theta(t=t_0)$; if not, the pitch equation is unstable and the satellite will swing away from the equilibrium condition when disturbed.

With the following definitions

$$\sigma_1 = \frac{I_2 - I_3}{I_1} < 1 \tag{2.39.a}$$

$$\sigma_2 = \frac{I_1 - I_3}{I_2} < 1 \tag{2.39.b}$$

$$\sigma_3 = \frac{I_2 - I_1}{I_3} < 1 \tag{2.39.c}$$

the coupled equations (2.36.a) and (2.36.c) become

$$\ddot{\phi} + 4\omega_0^2 \sigma_1 \phi - \omega_0 (1 - \sigma_1)\dot{\psi} = 0 \tag{2.40.a}$$

$$\ddot{\psi} + \omega_0^2 \sigma_3 \psi + \omega_0 (1 - \sigma_3)\dot{\phi} = 0 \tag{2.40.b}$$

From the stability analysis of the Laplace transform of (2.40.a) and (2.40.b) [14], three inequalities can be derived as conditions for stability:

$$3\sigma_1 + \sigma_1\sigma_3 + 1 > 4\sqrt{\sigma_1\sigma_3} \tag{2.41.a}$$

$$\sigma_1\sigma_3 > 0 \tag{2.41.b}$$

$$3\sigma_1 + \sigma_1\sigma_3 + 1 > 0 \tag{2.41.c}$$

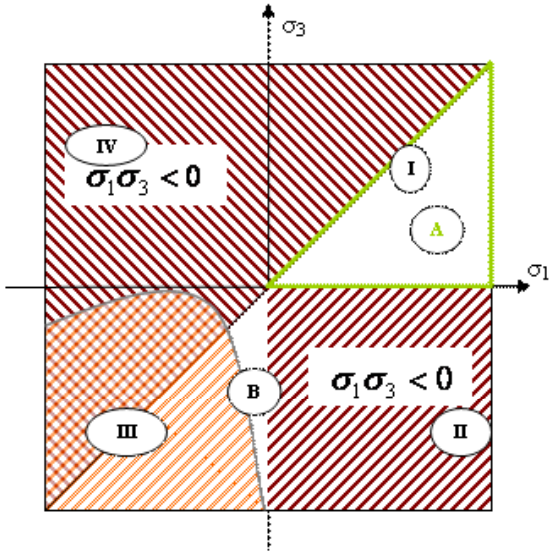

Figure 2.3: σ_x - σ_z plane showing regions of stability and instability; adapted from [14]

Figure 2.3 shows the regions of stability in the $\sigma_1 - \sigma_3$ plane resulting from conditions (2.41.a,b,c). The four quadrants are labeled I, II, III and IV. Quadrants II and IV are immediately instable, due to violation of condition (2.41.b).

From (2.39.a) it follows that

$$I_2 < I_1 + I_3 \tag{2.42}$$

With (2.37) it can be shown that

$$\sigma_1 > \sigma_3 \tag{2.43}$$

Quadrants I and III are equally divided by a line, for which $\sigma_1 = \sigma_3$; only systems with $\sigma_1 > \sigma_3$ (below the dividing line) are stable. The curve in quadrant III shows the solution to inequality (2.41.a), with unstable systems being located below the curve. This leaves only two stable regions, labeled A and B. Since σ is not usually a design parameter, the following states the implications for the principal moments of inertia I, properties which are more commonly used during the design of a spacecraft. From $\sigma_1 > 0$, $\sigma_3 > 0$, $\sigma_1 > \sigma_3$ and (2.37) it follows for subregion A that $I_2 > I_1 > I_3$ in addition to (2.42). From $\sigma_1 < 0$ and $\sigma_3 < 0$ and (2.37) for region B it follows that $I_1 > I_3 > I_2$ in addition to $I_1 < I_2 + I_3$. These conditions were derived by Beletsky in 1959 [22].

Table 2.1: Summary of stability conditions in terms of principal moments of inertia

	Subregion **A**	Subregion **B**
Primary condition	$I_2 > I_1 > I_3$	$I_1 > I_3 > I_2$
Additional condition	$I_2 < I_1 + I_3$	$I_1 < I_2 + I_3$

In typical spacecraft designs stability is achieved in region A due to the more limited margins in subregion B which impose practical difficulties on the structural design of the bus. Furthermore, subregion A stability is preferable due to a globally minimum total energy configuration; in the presence of energy dissipation this is the only stable region. Compass-1 is designed such that various degrees of freedom allow for a tuning of the mass properties within the CAD system prior to fabrication and assembly. This method of proper equipment placement is utilized in order to achieve gravity gradient stability in subregion A.

2.7 Linear Dynamics

The following section will present a complete derivation of the linearized equations of motion in terms of quaternions of a tri-inertial[2] rigid spacecraft on a circular orbit. A linear system model is essential in order to apply linear system theory and control law synthesis procedures.

The starting points for the linearization process are (2.14) and (2.26), the nonlinear kinematic and dynamic equations of motion, respectively. The objective is to find a set of equations which are linear (constant coefficients) in the state variables, i.e. to find a linear algebraic system representation of the form

$$\dot{x} = F \cdot x \tag{2.44}$$

where **F** is the plant system matrix. External disturbances presented in the next chapter have been omitted since their nature precludes a linear representation.

In most mechanical systems, the state space is twice the number of the degrees of freedom of the system. Principally, any state vector which describes the attitude and the rate of change of the attitude is valid, as these informations plus an initial condition are sufficient to unambiguously resolve a time history of the spacecraft attitude. Since attitude parametrization on Compass-1 is achieved by quaternions throughout owing to their superiorites compared with other methods of attitude parametrization as discussed above, a state vector of the form

$$x_{(6x1)} = \begin{pmatrix} q & \dot{q} \end{pmatrix}^T \tag{2.45}$$

has been selected for detailed derivation of the linear system dynamics subject to gravity gradient. This selection of state variables is unique; related work by [19], [20] and [21] describes the linear dynamics in terms of the quaternion and the body angular rates. However, the choice of quaternion and their rate of change is simplifiying the implementation of the state estimation, as will be shown in chapter 6, by erasing the need for the conversion from the quaternion rates to the angular body rates ω by application of the inverse kinematic equation of motion (2.58). Hence, the desription of the state dynamics in the here presented state variables is more closely related to the state estimation method.

Since Compass-1 is a nadir-pointing satellite, the equilibrium is chosen such that the control frame coincides with the local orbital frame at rest, i.e.

$$\bar{q}_{equi}^{co} = \begin{bmatrix} 0 & 0 & 0 & 1 \end{bmatrix}^T \text{ and } \omega_{c,equi}^{co} = \begin{bmatrix} 0 & 0 & 0 \end{bmatrix}^T \tag{2.46.a,b}$$

[2] All principal inertias are valued differently: no axial symmetries

Under the assumption of small deviations (total principal euler angle deviation $\Phi \approx 0$) from this reference, the kinematic state variables are expressed as

$$\delta\bar{q}^{co} = \begin{pmatrix} \delta q_1^{co} \\ \delta q_2^{co} \\ \delta q_3^{co} \\ \delta q_4^{co} \end{pmatrix} = \begin{pmatrix} a_1 \cdot \sin\dfrac{\delta\Phi}{2} \\ a_2 \cdot \sin\dfrac{\delta\Phi}{2} \\ a_3 \cdot \sin\dfrac{\delta\Phi}{2} \\ \cos\dfrac{\delta\Phi}{2} \end{pmatrix} \approx \begin{pmatrix} \delta q^{co} \\ 1 \end{pmatrix} \tag{2.47.a}$$

and

$$\delta\omega_c^{co} = \begin{bmatrix} \delta\omega_{c,x}^{co} & \delta\omega_{c,y}^{co} & \delta\omega_{c,z}^{co} \end{bmatrix}^T \tag{2.47.b}$$

Rewriting the dynamic equation of motion (2.26) in the control frame and considering only gravity gradient torque yields the known non-linear dynamic equation of motion

$$\underbrace{\dot{\omega}_c^{ci}}_{\text{angular. acceleration}} = \underbrace{-I^{-1} \cdot \omega_c^{ci} \times I \cdot \omega_c^{ci}}_{\text{cross coupling}} + \underbrace{I^{-1} \cdot T_{GG}}_{\text{gravity gradient}} + \underbrace{I^{-1} \cdot T_c}_{\text{control action}} + \underbrace{I^{-1} \cdot T_{dist}}_{\text{external disturbances}} \tag{2.48}$$

Eqn. (2.48) identifies various contributors to the angular acceleration in the inertial frame. The first term containing the cross product arises solely due to the fact, that the dynamics are described in a rotating frame with respect to an inertially fixed frame. It is commonly referred to as the *cross-coupling* of the spacecraft rotational dynamics. The equation of motion may be expanded by an arbitrary number of torques imposed on the rigid spacecraft structure. It would be reasonable to append three sources of torques: (i) the torque resulting from the gravity gradient effect, (ii) the internal control torque and (iii) the external net disturbance. However, for the derivation of the pure, “quasi-homogeneous” system dynamics, only the gravity gradient is considered.

$$\frac{\mathrm{d}}{\mathrm{dt}}\delta\omega_c^{ci} = \delta(\mathrm{cross-coupling}) + \mathrm{I}^{-1}(\mathrm{gravity-gradient}) \tag{2.49}$$

The three terms of (2.49) can now be linearized separately.

Linearization of the angular acceleration term

Rewriting the general addition theorem of angular velocities (2.16) in the control frame yields

$$\omega_c^{ci} = \omega_c^{co} + \omega_c^{oi} \tag{2.50}$$

The angular rotation of the orbital frame with respect to the inertial frame is governed by the circular orbital rate ω_0 about the orbital frame axis parallel to the orbit normal vector $-\hat{o}_2$. Using the kinematic relationships in (2.17.a) to (2.17.e) the following can be shown with $R^{oi} = E$.

$$\omega_c^{oi} = R^{co} \cdot E \cdot (-\omega_0 \cdot {}^i\hat{o}_2) \tag{2.51}$$

Consider a direction cosine matrix R^{co} which describes the transformation of the orbit frame into the control frame and consists of the unit base vectors of the orbital frame expressed in the control frame:

$$R^{co} = \left[{}^c\hat{o}_1 \quad {}^c\hat{o}_2 \quad {}^c\hat{o}_3 \right] \tag{2.52}$$

Since it is possible to convert from one attitude parametrization to another, this DCM can alternatively be expressed in terms of the quaternion components. Evaluating (2.11) yields

$$R^{co} = \begin{bmatrix} q_1^2 - q_2^2 - q_3^2 + q_4^2 & 2(q_1q_2 + q_3q_4) & 2(q_1q_3 - q_2q_4) \\ 2(q_1q_2 - q_3q_4) & -q_1^2 + q_2^2 - q_3^2 + q_4^2 & 2(q_2q_3 + q_1q_4) \\ 2(q_1q_3 + q_2q_4) & 2(q_2q_3 - q_1q_4) & -q_1^2 - q_2^2 + q_3^2 + q_4^2 \end{bmatrix} \tag{2.53}$$

with

$$q_i = \delta q_i^{co} \qquad \text{for i = 1,2,3,4} \tag{2.54}$$

As stated above δq_1, δq_2 and δq_3 are small numbers such that the products

$$\delta q_i^{co} \cdot \delta q_j^{co} \approx 0 \qquad \text{for i, j = 1,2,3} \tag{2.55.a}$$

$$\delta \dot{q}_i^{co} \cdot \delta q_j^{co} \approx 0 \qquad \text{for i, j = 1,2,3} \tag{2.55.b}$$

$$\delta \dot{q}_i^{co} \cdot \delta \dot{q}_j^{co} \approx 0 \qquad \text{for i, j = 1,2,3} \tag{2.55.c}$$

may be neglected as a first-order approximation. Remember that δq_4 is approximately 1 according to (2.47.a). Having made these simplifications, the linearized DCM becomes

$$R^{co} = \begin{bmatrix} 1 & 2\delta q_3^{co} & -2\delta q_2^{co} \\ -2\delta q_3^{co} & 1 & 2\delta q_1^{co} \\ 2\delta q_2^{co} & -2\delta q_1^{co} & 1 \end{bmatrix} \tag{2.56}$$

and the inertial angular velocity of the orbit frame as seen in the control frame is then

$$\omega_c^{oi} = \begin{bmatrix} 1 & 2q_3^{co} & -2q_2^{co} \\ -2q_3^{co} & 1 & 2q_1^{co} \\ 2q_2^{co} & -2q_1^{co} & 1 \end{bmatrix} \cdot \begin{pmatrix} 0 \\ -\omega_0 \\ 0 \end{pmatrix} = \begin{pmatrix} -2q_3^{co}\omega_0 \\ -\omega_0 \\ 2q_1^{co}\omega_0 \end{pmatrix} \tag{2.57}$$

By inverting the kinematic equation of motion (2.14), the angular velocity of the control frame as seen by the orbit frame can be expressed in terms of the quaternion and their rates of change [15] using the same abbreviations resolved in (2.54)

$$\omega_c^{co} = \begin{pmatrix} \delta\omega_{c,x}^{co} \\ \delta\omega_{c,y}^{co} \\ \delta\omega_{c,z}^{co} \end{pmatrix} = 2\left[\frac{q_4^2 \cdot E - q_4 q^{\times} + qq^T}{q_4} \right] \cdot \dot{q} \tag{2.58}$$

or, with $q_4 \approx 1$

$$\begin{aligned} \omega_c^{co} &\approx 2 \cdot \left[E - \begin{bmatrix} 0 & -\delta q_3^{co} & \delta q_2^{co} \\ \delta q_3^{co} & 0 & -\delta q_1^{co} \\ -\delta q_2^{co} & \delta q_1^{co} & 0 \end{bmatrix} + 0 \right] \cdot \dot{q}^{co} \\ &\approx 2 \cdot \begin{bmatrix} 1 & \delta q_3^{co} & -\delta q_2^{co} \\ -\delta q_3^{co} & 1 & \delta q_1^{co} \\ \delta q_2^{co} & -\delta q_1^{co} & 1 \end{bmatrix} \cdot \dot{q}^{co} \end{aligned} \tag{2.59}$$

It is now necessary to rid (2.59) of multiplicative state components. Under the simplifying assumptions of (2.55.a,b,c), equation (2.59) can be substantially simplified to

$$\omega_c^{co} \approx 2 \cdot \dot{q}^{co} \tag{2.60}$$

Inserting the results of (2.57) and (2.60) into (2.50) yields

$$\omega_c^{ci} = \begin{pmatrix} 2\delta\dot{q}_1^{co} \\ 2\delta\dot{q}_2^{co} \\ 2\delta\dot{q}_3^{co} \end{pmatrix} + \begin{pmatrix} -2\delta q_3^{co}\omega_0 \\ -\omega_0 \\ 2\delta q_1^{co}\omega_0 \end{pmatrix} = \begin{pmatrix} 2(\delta\dot{q}_1^{co} - \delta q_3^{co}\omega_0) \\ 2\delta\dot{q}_2^{co} - \omega_0 \\ 2(\delta\dot{q}_3^{co} + \delta q_1^{co}\omega_0) \end{pmatrix} \tag{2.61}$$

By time-derivation of the angular velocity of the control frame expressed in the inertial frame, the first linearized term of the motion model is found as

$$\dot{\omega}_c^{ci} = \begin{pmatrix} 2(\delta\ddot{q}_1^{co} - \delta\dot{q}_3^{co}\omega_0) \\ 2\delta\ddot{q}_2^{co} \\ 2(\delta\ddot{q}_3^{co} + \delta\dot{q}_1^{co}\omega_0) \end{pmatrix} \tag{2.62}$$

Linearization of the cross-coupling term

Now attention will turn to the second term of the nonlinear model, the cross-coupling

$$-I^{-1}\cdot\omega_c^{ci}\times(I\cdot\omega_c^{ci})$$

First, the cross product will be linearized using the results of (2.61) and applying

$$a\times b = a^{\times}\cdot b$$

$$\begin{aligned}
&\omega_c^{ci}\times(\mathrm{I}\cdot\omega_c^{ci}) = \\
&= \begin{bmatrix} 0 & -2(\delta\dot{q}_3^{co}+\delta q_1^{co}\omega_0) & 2\delta\dot{q}_2^{co}-\omega_0 \\ 2(\delta\dot{q}_3^{co}+\delta q_1^{co}\omega_0) & 0 & -2(\delta\dot{q}_1^{co}-\delta q_3^{co}\omega_0) \\ -2\delta\dot{q}_2^{co}+\omega_0 & 2(\delta\dot{q}_1^{co}-\delta q_3^{co}\omega_0) & 0 \end{bmatrix}\cdot\begin{pmatrix} 2\mathrm{I}_1\cdot(\delta\dot{q}_1^{co}-\delta q_3^{co}\omega_0) \\ \mathrm{I}_2\cdot(2\delta\dot{q}_2^{co}-\omega_0) \\ 2\mathrm{I}_3\cdot(\delta\dot{q}_3^{co}+\delta q_1^{co}\omega_0) \end{pmatrix} \\
&= \begin{pmatrix} -2(\delta\dot{q}_3^{co}+\delta q_1^{co}\omega_0)\cdot\mathrm{I}_2(2\delta\dot{q}_2^{co}-\omega_0)+(2\delta\dot{q}_2^{co}-\omega_0)\cdot 2\mathrm{I}_3\cdot(\delta\dot{q}_3^{co}+\delta q_1^{co}\omega_0) \\ 4\mathrm{I}_1\cdot(\delta\dot{q}_3^{co}+\delta q_1^{co}\omega_0)\cdot(\delta\dot{q}_1^{co}-\delta q_3^{co}\omega_0)-4\mathrm{I}_3\cdot(\delta\dot{q}_1^{co}-\delta q_3^{co}\omega_0)\cdot(\delta\dot{q}_3^{co}+\delta q_1^{co}\omega_0) \\ (-2\delta\dot{q}_2^{co}+\omega_0)\cdot 2\mathrm{I}_1\cdot(\delta\dot{q}_1^{co}-\delta q_3^{co}\omega_0)+2(\delta\dot{q}_1^{co}-\delta q_3^{co}\omega_0)\cdot\mathrm{I}_2(2\delta\dot{q}_2^{co}-\omega_0) \end{pmatrix}
\end{aligned} \tag{2.63}$$

Again, the assumptions of (2.55.a,b,c) yield a significantly simplified version of (2.63):

$$\begin{aligned}
\omega_c^{ci}\times(\mathrm{I}\cdot\omega_c^{ci}) &= \begin{pmatrix} 2\mathrm{I}_2\cdot\omega_0\delta\dot{q}_3^{co}+2\mathrm{I}_2\cdot\omega_0^2\delta q_1^{co}-2\mathrm{I}_3\cdot\omega_0\delta\dot{q}_3^{co}-2\mathrm{I}_3\cdot\omega_0^2\delta q_1^{co} \\ 0 \\ 2\mathrm{I}_1\cdot\omega_0\delta\dot{q}_1^{co}-2\mathrm{I}_1\cdot\omega_0^2\delta q_3^{co}-2\mathrm{I}_2\cdot\omega_0\delta\dot{q}_1^{co}+2\mathrm{I}_2\cdot\omega_0^2\delta q_3^{co} \end{pmatrix} \\
&= \begin{pmatrix} 2\delta\dot{q}_3^{co}\omega_0(\mathrm{I}_2-\mathrm{I}_3)+2\delta q_1^{co}\omega_0^2(\mathrm{I}_2-\mathrm{I}_3) \\ 0 \\ 2\delta\dot{q}_1^{co}\omega_0(\mathrm{I}_1-\mathrm{I}_2)-2\delta q_3^{co}\omega_0^2(\mathrm{I}_1-\mathrm{I}_2) \end{pmatrix}
\end{aligned} \tag{2.64}$$

Including the principal inertia to formulate the complete linearized cross-coupling term yields

$$-I^{-1}\cdot\omega_c^{ci}\times(I\cdot\omega_c^{ci}) = \begin{pmatrix} (-2\delta\dot{q}_3^{co}\omega_0-2\delta q_1^{co}\omega_0^2)\cdot\sigma_1 \\ 0 \\ (-2\delta\dot{q}_1^{co}\omega_0+2\delta q_3^{co}\omega_0^2)\cdot\sigma_3 \end{pmatrix} \tag{2.65}$$

with the inertia parameters σ_1 and σ_3 as defined in (2.39.a) and (2.39.c). Eqn. (2.65) constitutes the linearized formulation of the cross-coupling term.

Linearization of the gravity gradient term

Rewriting (2.30), the gravity gradient term in (2.48) can be written as

$$I^{-1} \cdot T_{GG} = I^{-1} \cdot 3\omega_0^2 \cdot \left[{}^c\hat{o}_3 \times I \cdot {}^c\hat{o}_3 \right] \tag{2.66}$$

Using (2.52) and (2.56) this can be simplified to

$$\begin{aligned} \mathrm{I}^{-1} \cdot \mathrm{T}_{\mathrm{GG}} &\approx \mathrm{I}^{-1} \cdot 3\omega_0^2 \cdot \begin{bmatrix} 0 & -1 & 2\delta q_1^{co} \\ 1 & 0 & 2\delta q_2^{co} \\ -2\delta q_1^{co} & -2\delta q_2^{co} & 0 \end{bmatrix} \cdot \begin{pmatrix} -2\mathrm{I}_1 \cdot \delta q_2^{co} \\ 2\mathrm{I}_2 \cdot \delta q_1^{co} \\ \mathrm{I}_3 \end{pmatrix} \\ &\approx \mathrm{I}^{-1} \cdot 3\omega_0^2 \cdot \begin{pmatrix} -2\mathrm{I}_2 \cdot \delta q_1^{co} + 2\mathrm{I}_3 \cdot \delta q_1^{co} \\ -2\mathrm{I}_1 \cdot \delta q_2^{co} + 2\mathrm{I}_3 \cdot \delta q_2^{co} \\ 0 \end{pmatrix} \\ &\approx 3\omega_0^2 \cdot \begin{pmatrix} -2\sigma_1 \delta q_1^{co} \\ 2\sigma_2 \delta q_2^{co} \\ 0 \end{pmatrix} \end{aligned} \tag{2.67}$$

Assembly of the linearized motion model

Having established the linearized terms of the non-linear equation of motion, the complete linearized plant system matrix can now be assembled from the individual results. Recalling (2.48) and discarding any torque other than the gravity gradient, the linear algebraic equation can now be written as

$$\begin{pmatrix} 2(\delta\ddot{q}_1^{co} - \delta\ddot{q}_3^{co}\omega_0) \\ 2\delta\ddot{q}_2^{co} \\ 2(\delta\ddot{q}_3^{co} + \delta\ddot{q}_1^{co}\omega_0) \end{pmatrix} = \begin{pmatrix} (-2\delta\ddot{q}_3^{co}\omega_0 - 2\delta q_1^{co}\omega_0^2)\cdot\sigma_1 \\ 0 \\ (-2\delta\ddot{q}_1^{co}\omega_0 + 2\delta q_3^{co}\omega_0^2)\cdot\sigma_3 \end{pmatrix} + \begin{pmatrix} -6\omega_0^2\sigma_1\delta q_1^{co} \\ 6\omega_0^2\sigma_2\delta q_2^{co} \\ 0 \end{pmatrix} \tag{2.68}$$

Solving (2.68) for the second time-derivative of the quaternion vector part yields

$$\delta\ddot{q}_1^{co} = (-4\sigma_1\omega_0^2)\cdot\delta q_1^{co} + (\omega_0(1-\sigma_1))\cdot\delta\ddot{q}_3^{co} \tag{2.69.a}$$

$$\delta\ddot{q}_2^{co} = (3\sigma_2\omega_0^2)\cdot\delta q_2^{co} \tag{2.69.b}$$

$$\delta\ddot{q}_3^{co} = (\sigma_3\omega_0^2)\cdot\delta q_3^{co} + (-\omega_0(1+\sigma_3))\cdot\delta\ddot{q}_1^{co} \tag{2.69.c}$$

Equations (2.69.a,b,c) constitute the final linearized equations of motion of the rigid spacecraft subject to gravity gradient only and in the vicinity of the equilibrium state defined in (2.46.a,b). The matrix representation of the linear spacecraft motion model can be finally written in the form of (2.44) as

$$\begin{pmatrix} \delta\dot{q}_1^{co} \\ \delta\dot{q}_2^{co} \\ \delta\dot{q}_3^{co} \\ \delta\ddot{q}_1^{co} \\ \delta\ddot{q}_2^{co} \\ \delta\ddot{q}_3^{co} \end{pmatrix} = \begin{bmatrix} 0 & 0 & 0 & 1 & 0 & 0 \\ 0 & 0 & 0 & 0 & 1 & 0 \\ 0 & 0 & 0 & 0 & 0 & 1 \\ -4\omega_0^2\sigma_1 & 0 & 0 & 0 & 0 & \omega_0(1-\sigma_1) \\ 0 & 3\omega_0^2\sigma_2 & 0 & 0 & 0 & 0 \\ 0 & 0 & \omega_0^2\sigma_3 & -\omega_0(1+\sigma_3) & 0 & 0 \end{bmatrix} \cdot \begin{pmatrix} \delta q_1^{co} \\ \delta q_2^{co} \\ \delta q_3^{co} \\ \delta\dot{q}_1^{co} \\ \delta\dot{q}_2^{co} \\ \delta\dot{q}_3^{co} \end{pmatrix} \tag{2.70}$$

The plant system matrix in (2.70) is sparsely occupied and the upper half has the expected property of an identity for the case of a rigid body without damping.

2.8 Summary

This chapter has introduced the definition of important spacecraft-centered reference systems used throughout this thesis. The important attitude parametrization methods used in the following chapters have been introduced and the non-linear kinematic and dynamic equations of motion have been stated. The conservative torque generated by the gravity gradient effect has been presented and the method of linearization was used to derive stability criteria binding for the Compass-1 spacecraft design. The most significant result of this chapter has been the linearization of the non-linear plant dynamics in terms of quaternions and quaternion rates in the desired nadir-pointing equilibrium attitude. Having established a linear plant model of the nadir-pointing Compass-1 spacecraft, linear control theory can be applied to derive stabilizing control laws; this will be done in chapter 6.

Chapter 3

Space Environment

An object in LEO is subject to a complex natural environment including charged particle systems, high energy radiation, presence of atomic oxygen and geophysical phenomena like gravitational and magnetic fields. Most of these environmental elements affect parts of the spacecraft in one or the other way[3] but to the attitude control system designer, influences on the vehicle's dynamics are of foremost interest.

A picosatellite at orbital altitude is the most nearly torque-free system ever created by human agency. However, various minute disturbances do act on the spacecraft structure in the form of external torques. It is the task of the attitude control system to compensate these disturbance torques which are complex functions of the spacecraft body geometry, time, position and attitude. The objective of this chapter is to present tractable models for the most significant LEO disturbances and to estimate a conservative torque level, based on worst-case assumptions, which constitutes an essential input to the selection of attitude control hardware and the sizing of the actuator elements. The disturbances considered in this chapter are

- aerodynamic drag torque
- solar radiation pressure torque
- residual dipole moment torque

In addition to the estimation of the required control authority, this chapter will also present a thorough description of the geomagnetic field, which is the main prerequisite for the proposed attitude control system.

[3] Space is a fairly hostile environment for man-made machines. However, space engineers believe that space is a much safer place than the Earth itself, because the environment is highly predictable and space hardware can be made withstanding exactly these conditions without being subject to the poking and probing hands of untrained users.

3.1 Orbit analysis

An important prerequisite for estimating the disturbance levels, the spacecraft will experience during its mission is the knowledge of the satellite orbit. Since Compass-1 is a secondary payload on a launch vehicle not yet determined at the time of writing, the mission orbit cannot be predicted with final accuracy; in order to establish a reasonable reference orbit for the system design, the orbits of the previously launched CubeSats will be investigated in the following. Table 3.1 shows the relevant orbital parameters for the CubeSats launched in June 2003 and October 2005; the information is based on TLE data obtained in December 2005.

Table 3.1: Orbit parameters of the CubeSats launched in June 2003 and October 2005 (as of December 2005)

S/C Number	27842	27844	27846	27847
S/C Name	**DTUSat**	**CUTE-1**	**AAUSat**	**CanX-1**
Inclination [deg]	98.7219	98.7226	98.7229	98.7226
RAAN [deg]	342.2087	342.6907	343.1797	343.1124
Eccentricity	$8.599 \cdot 10^{-4}$	$9.119 \cdot 10^{-4}$	$8.689 \cdot 10^{-4}$	$8.704 \cdot 10^{-4}$
Arg. Of Perigee [deg]	257.2589	269.7095	254.4612	253.508
Mean Motion [revs/day]	14.208	14.204	14.208	14.208
Period [min]	101.35	101.38	101.35	101.35
semi-major axis [km]	7200.845	7202.150	7200.842	7200.851
Perigee Alt. [km]	816.518	817.447	816.450	816.448
Apogee Alt. [km]	828.902	830.583	828.964	828.984

S/C Number	27848	28895	28892	28894
S/C Name	**XI-IV**	**XI-V**	**UWE-1**	**Ncube-2**
Inclination [deg]	98.7201	98.1833	98.1808	98.1827
RAAN [deg]	341.9563	233.2839	233.273	236.1961
Eccentricity	$9.163 \cdot 10^{-4}$	$1.9226 \cdot 10^{-3}$	$1.8521 \cdot 10^{-3}$	$1.8807 \cdot 10^{-3}$
Arg. Of Perigee [deg]	274.7686	64.8277	63.4028	57.3391
Mean Motion [revs/day]	14.202	14.593	14.593	14.594
Period [min]	101.39	98.68	98.68	98.67
semi-major axis [km]	7202.61	7073.5	7073.68	7073.17
Perigee Alt. [km]	817.875	681.765	682.444	681.732
Apogee Alt. [km]	831.075	708.965	708.646	708.338

The orbits are visualized using the Satellite Tool Kit (STK) in figure 3.1; apparent differences exist in the right ascension of the ascending node (RAAN) as well as orbit altitude. Both campaigns launched the picosatellites into a near-circular retrograde orbit of high inclination (~98°).

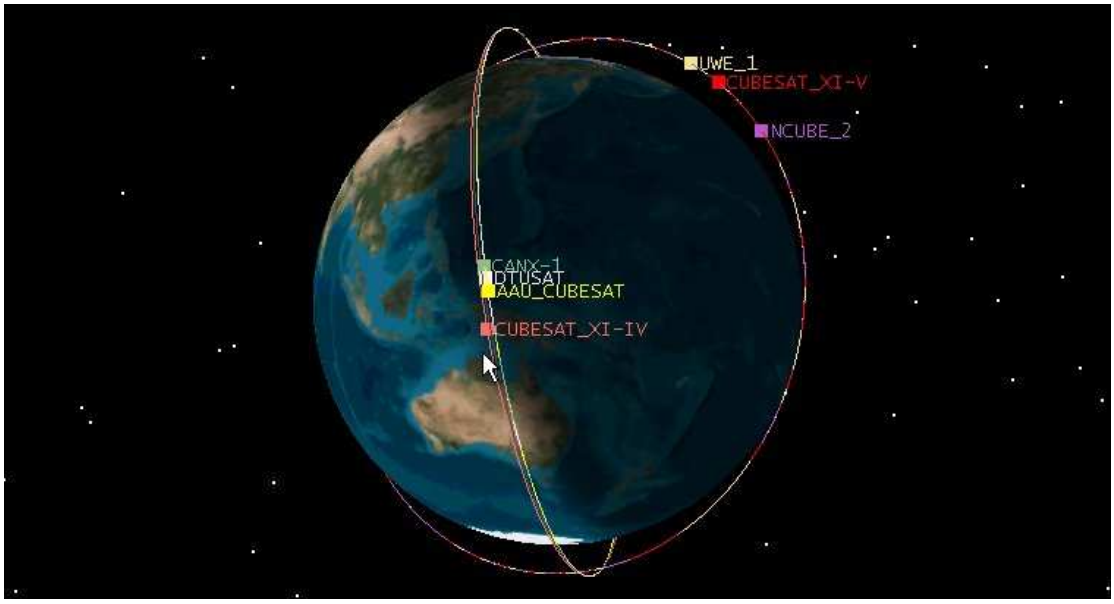

Figure 3.1: Visualization of present CubeSat orbits; generated with STK.

The figures of merrit for the assessment of the dynamical environment of Compass-1 are the altitude, inclination and eccentricity. Based on the previous CubeSat orbits, the reference orbit has the following parameters.

Table 3.2: Compass-1 reference orbit parameters

Orbit type	circular, sun-synchronous
Altitude	600 – 800 km
Radius	6978 – 7178 km
Inclination	98°
Velocity	7558 – 7452 m/s
Period	5801.06 – 6052.24 sec 96.68 – 100.87 min

3.2 Disturbance Torques

3.2.1 Aerodynamic Drag Torque

Contrary to the general notion of an ideal vaccum at LEO altitudes, satellites experience forces and torques which are a result of aerodynamic drag, since a spacecraft travels along the outer fringe of the Earth's atmosphere where the atmospheric density ρ is greater than zero. Many density profile models exist but MSISE-90 [23] is the recommended ECSS (European Cooperation for Space Standardization) standard atmosphere model, from which the main thermodynamic parameters of the atmosphere at 600, 700 and 800km and during low, mean and high solar and geomagnetic activity are listed in table 3.3.

Table 3.3: ECSS standard atmospheric density, temperature, pressure, molecular weight and scale height at 600, 700 and 800 km altitude and for different levels of solar activity [23]

Activity Level	**low**		
Altitude [km]	**600**	**700**	**800**
Temperature [K]	699.1631	699.1631	699.1631
Density [kg/m³]	$1.03 \cdot 10^{-14}$	$3.58 \cdot 10^{-15}$	$1.91 \cdot 10^{-15}$
Pressure [N/m²]	$1.09 \cdot 10^{-8}$	$6 \cdot 10^{-9}$	$3.96 \cdot 10^{-9}$
Molecular Weight [kg/mol]	5.5149	3.4648	2.8075
Scale Height [km]	71.0934	129.9408	188.1991

Activity Level	**mean**		
Altitude [km]	**600**	**700**	**800**
Temperature [K]	1011.533	1011.537	1011.538
Density [kg/m³]	$1.56 \cdot 10^{-13}$	$3.91 \cdot 10^{-14}$	$1.25 \cdot 10^{-14}$
Pressure [N/m²]	$1.01 \cdot 10^{-7}$	$3.36 \cdot 10^{-8}$	$1.58 \cdot 10^{-8}$
Molecular Weight [kg/mol]	13.0389	9.7818	6.6572
Scale Height [km]	68.1361	78.5188	101.1751

Activity Level	**extremely high**		
Altitude [km]	**600**	**700**	**800**
Temperature [K]	1622.042	1622.087	1622.093
Density [kg/m³]	$6.20 \cdot 10^{-12}$	$2.38 \cdot 10^{-12}$	$9.59 \cdot 10^{-13}$
Pressure [N/m²]	$5.31 \cdot 10^{-6}$	$2.11 \cdot 10^{-6}$	$8.84 \cdot 10^{-7}$
Molecular Weight [kg/mol]	15.7321	15.2723	14.6447
Scale Height [km]	102.6271	108.0038	111.8358

The simplest model is a scalar evaluation of the aerodynamic drag force imposed on the center of pressure with an offset from the center of gravity [24].

$$T_a = \frac{1}{2} \cdot \rho \cdot c_D \cdot A_p \cdot v_c^{\,2} \cdot \left(c_{CP} - c_{CG}\right) \tag{3.1}$$

This simple model ignores the fact that the flow regime at LEO altitudes is far from continuous. In the Earth's exosphere gas molecules are widely spaced, i.e. the molecular

mean free path length is large compared to the dimension of the CubeSat body; this type of rarefied gas flow can be best characterized by particles randomly and in a perfectly plastic manner impacting and subsequently slipping off the body's surface. The model only considers normal pressure forces, not the friction of a molecule slipping on a surface, and it does so in a manner which is typical for the continuum assumption of fluid mechanics. However, although statistical fluid mechanics yield a better approximation to the problem of aerodynamic drag on a spacecraft, the model in (3.1) is deemed to provide results of reasonable usefulness as estimate of the expected torque level.

The newtonian slipstream theory of rarefied gas dynamics predicts a coefficient of drag c_D of exactly 2.0 for a spherically shaped body; a cubic body should experience slightly higher coefficients. Hence, a c_D of 2.2 is assumed. It is further assumed that the center of pressure coincides with the cube's geometric center. It is a standard requirement that the CubeSat center of gravity (CG) must be within 2cm of the geometric center. Hence a worst-case offset between CP and CG of 0.02m is assumed.

The projected area A_p is highest if the velocity vector joins a cube vertex and the geometrical center. For this scenario, the aerodynamic area is

$$A_p = \frac{a^2}{2} \cdot \left(1 + \sqrt{6}\right), \quad \text{a = 0.1m} \tag{3.2}$$

For worst-case torque estimation, residual density for 600km and high solar activity, i.e. $\rho = 6.2 \cdot 10^{-12}$ kg/m³, and the lower orbit altitude with a circular velocity of 7558m/s are assumed. This yields a conservative aerodynamic torque of $1.34 \cdot 10^{-7}$Nm.

For simulation purposes, a model is required which evalutes the secular aerodynamic torque as a vector.

$$T_a = \frac{1}{2} c_D \cdot \rho \cdot v^2 \cdot \sum_{k=1}^{n} \vec{r}_{s,k} \times \left(\hat{n}_k^T \circ \hat{V}\right) \cdot \hat{V} \cdot A_k \text{ ,} \quad \text{n = 6} \tag{3.3.a}$$

Any general convex body shape can be divided into a finite number of n surfaces and the total aerodynamic torque is obtained by summation of the individual torque contributions. Since the geometrical configuration of Compass-1 is fairly simple, a cube with six orthonormal faces of equal area will yield results with sufficient accuracy. In (3.3.a), A_k is the area of the k-th surface, V is the normalized velocity vector in the body frame, n_k is the normal vector of the k-th surface and $r_{s,k}$ is the vector from the CG to the area center of the k-th surface. Again, in this discrete model the location of the CP inherently assumed to coincide with the geometrical centre; the location of the CG can be easily extracted from CAD models.

More realistic results can be obtained by evaluating (3.3.a) for the velocity relative to the Earth's atmosphere. If a static, Earth-fixed atmosphere is assumed, the velocity is expressed in the Earth-fixed frame of reference (ECEF, see chapter 6).

$$v_{ECEF} = A^{ECEF,ECI} \cdot \left(v_{ECI} - \left(\omega_{\oplus} \times r_{ECI}\right)\right) \tag{3.b}$$

where $A^{ECEF,ECI}$ transforms the inertial velocity into the Earth-fixed CS and $\omega_{\oplus}$ is the Earth's angular velocity of rotation about the z-axis ($\omega_{\oplus} = 7.2921 \cdot 10^{-5}$rad/sec).

3.2.2 Solar Radiation Pressure Torque

A spacecraft in LEO receives electromagnetic radiation from three major sources, (i) the sun, (ii) solar radiation reflected by the Earth, termed albedo, and (iii) the thermal infrared radiation of the Earth. For all following discussion, only the first source, i.e. direct sun radiation, is considered due to its dominance over other torques of the same nature.
The sun's electromagnetic radiation exerts a normal force on space objects, known as solar radiation pressure. This pressure originating from photonic momentum exchange causes a cyclic disturbance torque which may be modeled in a similar form as the aerodynamic normal pressure torque [24].

$$T_{sp} = \frac{S_0}{c} \cdot A \cdot (1+r) \cdot \cos i \cdot (c_{CP} - c_{CG}) \tag{3.4}$$

The solar constant S_0 is defined as the normal energy flux onto a unit area per unit time, outside of the atmosphere, at 1 AU distance to the sun. Although S_0 is labeled a constant, it varies by approximately 3.4% during a year due to the eccentricity of the Earth's orbit about the sun; an additional variability of ±0.1% arises from the sun's cyclic emission level fluctuation with a period of 11 years, known as a solar cycle. The standard values for the electromagnetic radiation of the sun are as follows [23]:

Table 3.4: Solar Constant value variation range [23]

Solar Constant at 1 AU	1371 W/m^2
Max. solar energy flux (perihel)	1428 W/m^2
Min. solar energy flux (apohel)	1316 W/m^2

Because of the great distance between the sun and a LEO satellite, the solar pressure disturbance torque is virtually independent of the orbit altitude. However, it is strongly dependent on the type of surface being illuminated. In general, solar cells are absorbers and the spacecraft body is a reflector. Typical values for the body reflectance r are ranging between 0.4 and 0.7 (0: perfectly absorbing, 1: perfectly reflecting). Since the body of Compass-1 is largely covered in antireflectance-coated solar cells, r is assumed to be 0.6 while still being conservative. The assumption for the maximum irradiated area is identical to the discussion of the aerodynamic drag. The worst-case sun incidence angle is easily identified as i = 0°. This yields a conservative solar pressure torque of $2.62 \cdot 10^{-9}$Nm.

Similar to the model of the aerodynamic torque, the solar radiation pressure disturbance can be rewritten in a more general discrete form, i.e. for a rigid body with an arbitrary geometric configuration.

$$T_{sp} = \frac{S_0}{c}(1+r)\cdot\sum_{k=1}^{n}\vec{r}_{s,k}\times\left(\hat{n}_k^T\circ\hat{S}\right)\cdot\hat{S}\cdot A_k \tag{3.5}$$

In (3.5), A_k is the area of the k-th surface, S is the normalized sun vector in the body frame, n_k is the normal vector of the k-th surface and $r_{s,k}$ is the vector from the CG to the area center of the k-th surface.

Note that the solar pressure torque is typically a non-continuous source of disturbance, since the spacecraft may not be exposed to direct sun light at all times of the orbit. It is a reasonable simplification for LEO satellites to set $T_{sp} = 0$ if the spacecraft is in umbra and $T_{sp} \neq 0$ otherwise. A simple shadow function will be presented in chapter 6 in the context of attitude estimation.

3.2.3 Residual Dipole Torque

As everyone who has used a compass needle before is well aware of, the Earth is not only surrounded by a gravity field, but also by a significant magnetic field. Scientists still have not fully agreed on the specifics of the origin of this field, but what is known for certain is that the general magnetic field is composed of a superposition of various potential field sources. These sources are (i) the main field, electrodynamically generated internal to the Earth's outer core, (ii) the crustal (lithospheric) field from local remanent or magnetically induced rocks (e.g. volcanic), and (iii) a combined disturbance field from electrical current systems in the upper atmosphere (ionoshere) and the magnetosphere, which also induces secondary electrical currents in the sea and the ground. The crustal field is largely attenuated at the altitudes of LEO satellites and, with the exception of the auroral and polar areas, disturbance field effects at LEO altitudes are small [27].

The simplest model of the geomagnetic field is that of an ideal dipole, first discovered by William Gilbert of Colchester, english physician and man of learning at the court of Queen Elizabeth I, and, in the year 1600, published in his treatise *"De Magnete, magneticisique corporibus"*[59]. Gilbert gave the first rational explanation to the mysterious ability of a compass needle to point south-north and opened the era of modern physics and astronomy, starting a century marked by great achievements of Galileo, Kepler, Newton and others. What Gilbert did not know at the time was that the Earth's dipole is both tilted and offset with respect to the Earth's axis of rotation, so that the geomagnetic poles do not coincide with the geographic poles. Additionally, the field strength is not independent of longitude; this configuration is called an eccentric dipole.

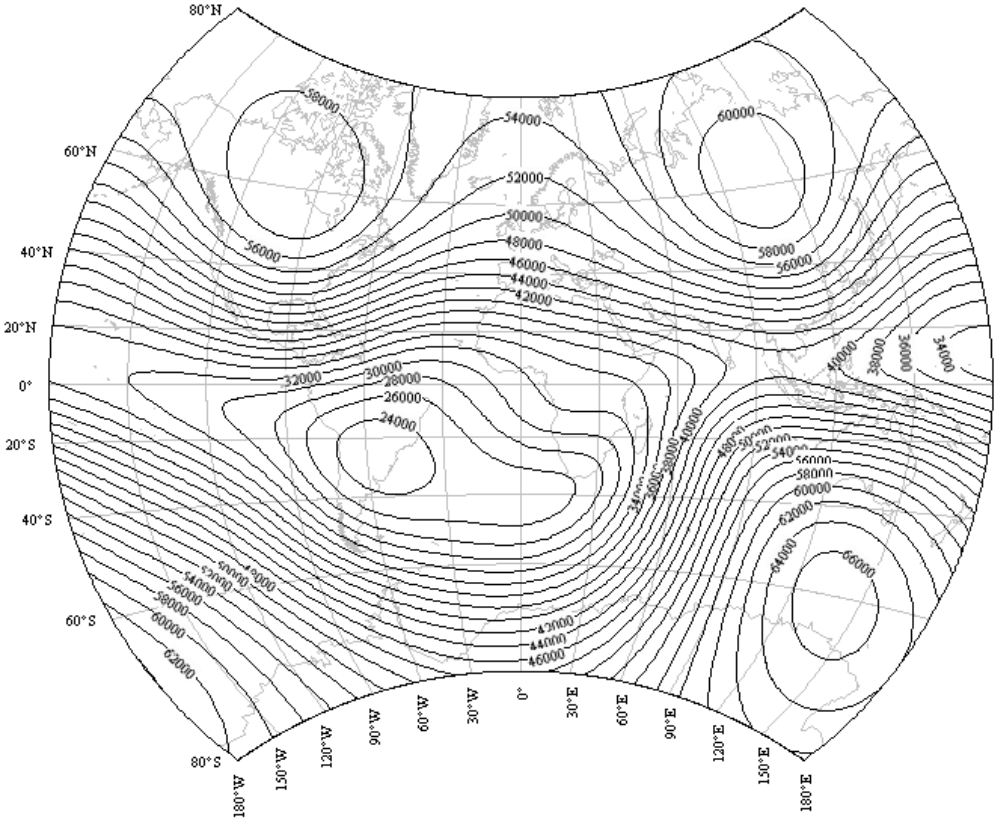

Figure 3.2: isomagnetic map of the geomagnetic field strength at sea level in Van-der-Grinten projection; contour line spacing is 2000nT [25]

The scalar field strength assuming the Earth being an ideal dipole is given by

$$B = \frac{M}{R^3} \cdot \sqrt{1+3\sin^2 \lambda_m} = \frac{B_0 \cdot R_E^3}{R^3} \sqrt{1+3\sin^2 \lambda_m} \tag{3.6}$$

Any residual magnetic field inherent to the spacecraft, whether generated by a magnetized material, e.g. ferromagnetic, or by an electrical current system, will interact with the geomagnetic field to produce a mechanical torque T_m. Magnetic fields may be represented by equipotential field lines (or shells in 3D) of a magnetic potential field. Local magnetic flux density vectors are oriented tangentially to these field lines. The strength of a magnetic field is governed by the magnetic dipole of the body generating the field. A common bar magnet is an example for a simple magnetic dipole field source; it has two poles and all magnetic field lines are connecting the poles. Deviations from the simple dipole may exist for bodies of more complex internal magnetic structure; the fields of higher order poles (quadrupole, octopole, etc.) are superimposed on the dipole field to shape a complex magnetic field structure.

Expressing the net residual magnetic field in terms of a residual dipole D, the disturbance torque imposed on the spacecraft's structure can be conservatively written as

$$T_m = D \cdot B \tag{3.7}$$

The geomagnetic flux density B becomes a periodic maximum for $\lambda_m = n\pi/2$ for n = 1,2,3…, which is located above the magnetic poles. At these positions the worst case torque can be defined as

$$T_m = D \cdot \frac{2M}{R^3} \tag{3.8}$$

Estimating the residual dipole before the spacecraft is fully integrated is difficult. Since Compass-1 is an extremely small spacecraft, a conservative residual dipole of 0.01Am² is assumed. According to [24], small (still much larger than Compass-1), uncompensated vehicles usually exhibit a residual dipole of around 1Am². Assuming the lower bound on the orbital altitude, the worst-case magnetic torque is evaluated as $4.587 \cdot 10^{-7}$Nm.

3.2.4 Total Disturbance Torque Level

Summarizing the analysis of the dynamical disturbance environment of Compass-1, the following worst-case torque contributions have been identified.

Table 3.5: Summary of the expected worst-case disturbance level

Source	Torque
Aerodynamic Drag	$1.34 \cdot 10^{-7}$ Nm
Solar Pressure	$2.62 \cdot 10^{-9}$ Nm
Residual Dipole	$4.59 \cdot 10^{-7}$ Nm
Total Disturbance Level	$5.95 \cdot 10^{-7}$ Nm

Again, the shown results depict the worst case situation, i.e. the individual torques are simply summed up as it would be the case if all torques would act on the same axis in the same direction. In reality this case is highly unlikely to happen. Torque cancellation is much more probable, resulting in a significantly lower realistic total torque. Note that the aerodynamic drag torque is classically dominant for altitudes below 500km while the residual dipole typically dominates at altitudes above 500km.

3.3 Variability of the Geomagnetic Field

The sum of magnetic main and disturbance fields is not constant over time; variations with time can be divided into two types: *temporal (reversible) variations* and *secular (irreversible) variations*. The disturbance field can temporarily vary both (i) regularly, with a fundamental period of one day, and (ii) irregularly on time scales of seconds to days. The regular variations are called *diurnal variations* and they are essentially generated by changes in ionospheric currents, or more specifically, by the ionized dayside atmosphere in altitudes of 100 to 130 km, with ions being moved into the Earth's main field by winds and tides. Irregular temporal variations include magnetic storms, invoked primarily by solar flares, which are related to the sun's periodic sun spot activity, and auroral activity, which is at a maximum in the spring and fall when the Earth is located at its equinoxes. Magnetic storms are generally more severe at high geomagnetic latitudes. The rotation rate of the sun is 27 days, which suggests that the frequency of magnetic storms follow a 27-day cycle. In addition, the activity of sunspots follows the 11-year solar cycle, so increases in magnetic storm occurence follow the same trend.

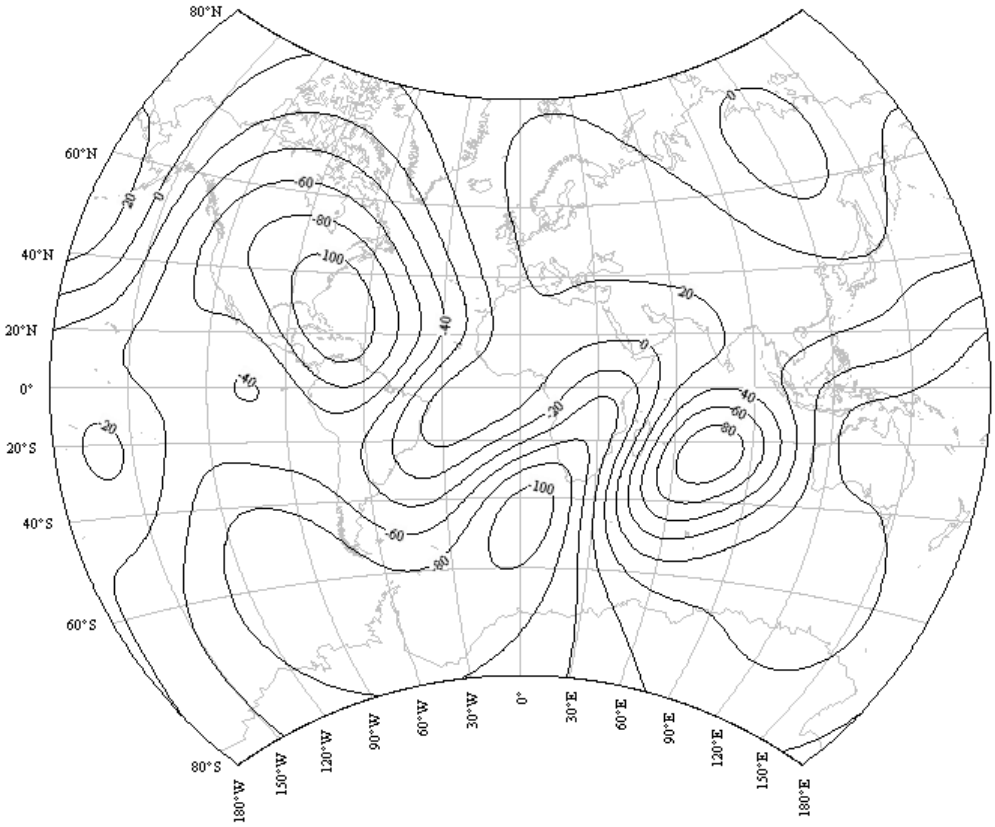

Figure 3.3: map of the secular variations of the geomagnetic field strength at sea level in Van-der-Grinten projection; contour line spacing is 20nT/year [25]

3.3.1 Monitoring Magnetic Storms

The Space Environment Center (SEC) in Boulder, Colorado, USA, provides real-time monitoring and forecasting of solar and geophysical events, conducts research in solar-terrestrial physics, and develops techniques for forecasting solar and geophysical disturbances. SEC's Space Weather Operations Center is jointly operated by the National Oceanic and Atmospheric Administration of the U.S. Department of Commerce (NOAA) and the U.S. Air Force and is an international warning center for disturbances that can affect people and equipment working in the space environment. For the specific purpose of magnetic storm warning, a severity scale, ranging from 0 (quiet) to 9 (severe storm), is commonly used. The severity is expressed by the (local) '*K-index*' and the planetary (global) 'K_p *index*'.

The K-index is a code that is related to the maximum fluctuations of horizontal components observed on a magnetometer relative to a quiet day, during a three-hour interval. The conversion table from maximum fluctuation (nT) to the K-index, varies from observatory to observatory in such a way that the historical rate of occurrence of certain levels of K are about the same at all observatories and the index becomes a globally standardized code. In practice this means that observatories at higher geomagnetic latitude require higher levels of fluctuation for a given K-index.

The official planetary K_p index, introduced by J. Bartels in 1949, is derived by calculating a weighted average of standardized K-indices from a network of 13 geomagnetic observatories [62]. It was originally designed to measure solar particle radiation by its magnetic effects. Since the observatories do not report their data in real-time, it is necessary for a monitoring center to make the best estimate based on available data. Space weather operations uses near real-time estimates of the K_p index which are derived by the U.S. Air Force 55th Space Weather Squadron. Most of the observatories are located in North America, although there is one European station also contributing at this time from Hartland, UK. A K_p of 0 to 4 indicates sub-storm severities; harmful situations arise from conditions of $K_p = 5$ and above.

3.3.2 The International Geomagnetic Reference Field

Several geomagnetic field models exist; one of those models is the World Magnetic Model (WMM) published and maintained by the British Geological Survey and other institutes [26]. The WMM is updated every five years, alike the major and most important field model, the International Geomagnetic Reference Field (IGRF). The IGRF is a mathematical description of the Earth's main magnetic field used widely in studies of the Earth's deep interior, the lithosphere, the ionosphere and the magnetosphere. The generation and maintenance of the IGRF is an international collaborative effort led by the International Association of Geomagnetism and Aeronomy (IAGA) and relies on cooperation between magnetic field modellers, institutes and agencies responsible for collecting and publishing geomagnetic field data. The IGRF incorporates data from permanent land observatories and from airborne, marine and spaceborne surveys. The following discussion of the geomagnetic field topology is based on the 10^{th} Generation IGRF model (IGRF-10) for epoch 2005 which was finalized by IAGA's Division V Working Group MOD (formerly WG V-8) in December 2004 [29]. Alike the prior version, the 9^{th} generation IGRF, it includes 195 main field model

coefficients and 80 secular variation coefficients; IGRF-8 contained main field coefficients up to degree/order 10 with precision truncated to integer nanotesla (nT) while IGRF-9/10 is a degree/order 13 model, with a precision of one tenth of a nT, reflecting the increased availability of high-quality data. The recommended period of validity of IGRF-10 is gregorian year 2005 through 2010.

3.3.3 Spherical Harmonics Field Modelling

In close analogy to the relationship between a force vector in a gravitational potential field, the magnetic vector can be expressed by the negative gradient of the geomagnetic potential field. Henry Gellibrand, first priest, then mathematician, has already shown in 1635 that the geomagnetic field is both time and position dependent (in opposition with the conviction of Gilbert). One year before his death he published his significant experimental observations in *"A discourse mathematical on the variation of the magnetical needle, together with its admirable diminution lately discovered"* [60].

Hence, the geomagnetic main field can be generally expressed as

$$\vec{B} = -\nabla U(R,\phi,\theta,t) \tag{3.9}$$

which satisfies Laplace's equation

$$\nabla^2 U(R,\phi,\theta,t) = \nabla \cdot (\nabla U) = \frac{\partial^2 U}{\partial R^2} + \frac{\partial^2 U}{\partial \phi^2} + \frac{\partial^2 U}{\partial \theta^2} + \frac{\partial^2 U}{\partial t^2} = 0 \tag{3.10}$$

in addition to Maxwell's equations. The interpretation of the Laplace equation is that the normal vectors to lines of constant U have no divergence; intuitively this means that the rate at which such vectors enter a region of space is the same as the rate at which they leave. The gradient of the geomagnetic potential U gives the direction of the geomagnetic flux density at each point in space; the fact, that these field lines are divergence free in some region simply implies that the geomagnetic main field is source-free.

It lies in the nature of the problem, that the approach of a scalar potential, approximated by an expansion of harmonic terms, described in a spherical coordinated system, is most suitable. The empirical formulation of the geomagnetic potential U is hence approximated using a method known as '*spherical harmonics expansion*'. Using this method, the scalar main field potential can be generally approximated as a truncated series expansion:

$$U = f(R,\phi,\theta,t) = a \cdot \sum_{n=1}^{k} \left[\left(\frac{R_E}{R} \right)^{n+1} \sum_{m=0}^{n} \left[g_n^m \cos(m\phi) + h_n^m \sin(m\phi) \right] P_n^m(\cos\theta) \right] \tag{3.11}$$

where R is the geocentric distance of the point of interest, θ is the co-latitude (sometimes called co-elevation)[4], measured from the geographic north pole, and ϕ is the (Greenwich) longitude. 'g' and 'h' are the model coefficients and 'P' are the Schmidt (semi-)normalized associated Legendre functions.

If only internal sources (the main field) are considered, as it is reasonable for LEO spacecraft, U is a function of (i) the location of interest, expressed in spherical coordinates and (ii) time. However, (11) does not contain direct time dependency information; the field calculated by the above coefficients is a mere 'snapshot' of the magnetic field at *epoch* t_0. Variations of the potential field with time are small, but not negligible within the epoch period of 5 years. To account for the time variations, the field coeffients are corrected by means of secular coefficients. Secular coefficents are expressed in the unit [nT/year], evolving from a linear interpolation technique of the observed secular change of a field model. Predictions of the main field for more than 5 years into the future from the time of epoch are not sufficiently accurate for general navigation purposes which is the reason why models and charts are revised in five year intervals. Combined with the secular coefficients, the main field coefficients are assumed to vary with time at a constant rate of change over the entire five-year period. See appendix D for a complete list of the IGRF-10 field model coefficients.

$$g_n^m(t) = g_n^m + \dot{g}_n^m (t - t_0) \qquad t_0 \le t \le t_0 + 5\text{years} \tag{3.12.a}$$

$$h_n^m(t) = h_n^m + \dot{h}_n^m (t - t_0) \qquad t_0 \le t \le t_0 + 5\text{years} \tag{3.12.b}$$

Much more useful is a set of equations which yields the components of the geomagnetic flux density vector directly as

$$B_r = \frac{-\partial V}{\partial R} = \sum_{n=1}^{k} \left(\frac{R_E}{R} \right)^{n+2} (n+1) \sum_{m=0}^{n} \left(g_n^m \cos(m\phi) + h_n^m \sin(m\phi) \right) P_n^m(\theta) \tag{3.13.a}$$

$$B_\theta = \frac{-\partial V}{R \cdot \partial \theta} = -\sum_{n=1}^{k} \left(\frac{R_E}{R} \right)^{n+2} \sum_{m=0}^{n} \left(g_n^m \cos(m\phi) + h_n^m \sin(m\phi) \right) \frac{\partial P_n^m(\theta)}{\partial \theta} \tag{3.13.b}$$

$$B_\phi = \frac{-\partial V}{R \sin\theta \cdot \partial \phi} = \frac{-1}{\sin\theta} \sum_{n=1}^{k} \left(\frac{R_E}{R} \right)^{n+2} \sum_{m=0}^{n} m \left(- g_n^m \sin(m\phi) + h_n^m \cos(m\phi) \right) P_n^m(\theta) \tag{3.13.c}$$

B_r is the radial component of the magnetic field (positive outward), B_θ is the co-elevation component (positive southward), B_φ is the azimuthal component of the field (positive eastward) and k is the maximum degree and order of the field model evaluation. In general, a higher degree and order results in better accuracy because localized deviations from the dipole field can be best resolved with high order spherical harmonics coefficients.

[4] co-latitude is essentially the same as latitude, only with a different origin definition; geogr. north-pole: 0°, geogr. equator: +90° and geogr. south-pole: +180°

A set of notations and definitions is used among geophysicists, which shall be briefly presented here for the sake of completeness. The geomagnetic flux density vector B is described by the orthogonal components *X* (northerly intensity), *Y* (easterly intensity) and *Z* (vertical intensity, positive downwards); total intensity *F*; horizontal intensity *H*; inclination (or dip) *I* (the angle between the horizontal plane and the field vector, measured positive downwards) and declination (or magnetic variation) *D* (the horizontal angle between true north and the field vector, measured positive eastwards). Declination, inclination and total intensity can be computed from the orthogonal components using equations (3.14.a,b,c and d).

$$D = \tan^{-1}\left(\frac{Y}{X}\right) \qquad (3.14.a)$$

$$F = \sqrt{H^2 + Z^2} \qquad (3.14.b)$$

$$I = \tan^{-1}\left(\frac{Z}{H}\right) \qquad (3.14.a)$$

$$H = \sqrt{X^2 + Y^2} \qquad (3.14.d)$$

Helpful conversions are:

$$H = F\cos I \qquad (3.14.a)$$

$$X = H\cos D \qquad (3.14.b)$$

$$Z = F\sin I \qquad (3.14.a)$$

$$Y = H\sin D \qquad (3.14.d)$$

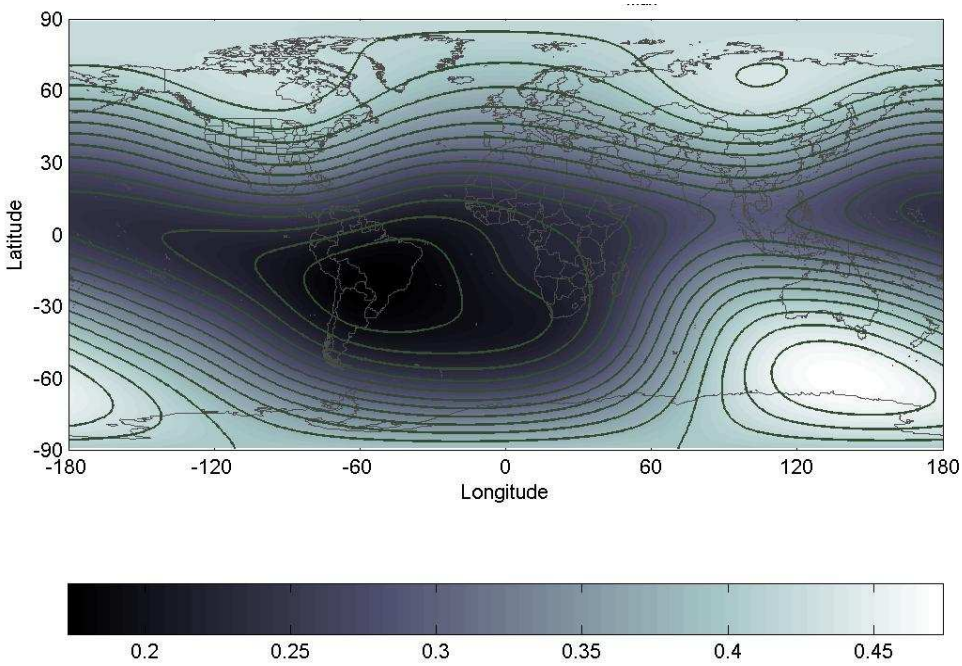

Figure 3.4: Contour Plot of the total geomagnetic flux density in Gauss[5] for an IGRF2005 model of degree and order 13, 700km altitude (R_E = 6378.135km) and 01.04.2006; note the south atlantic anomaly

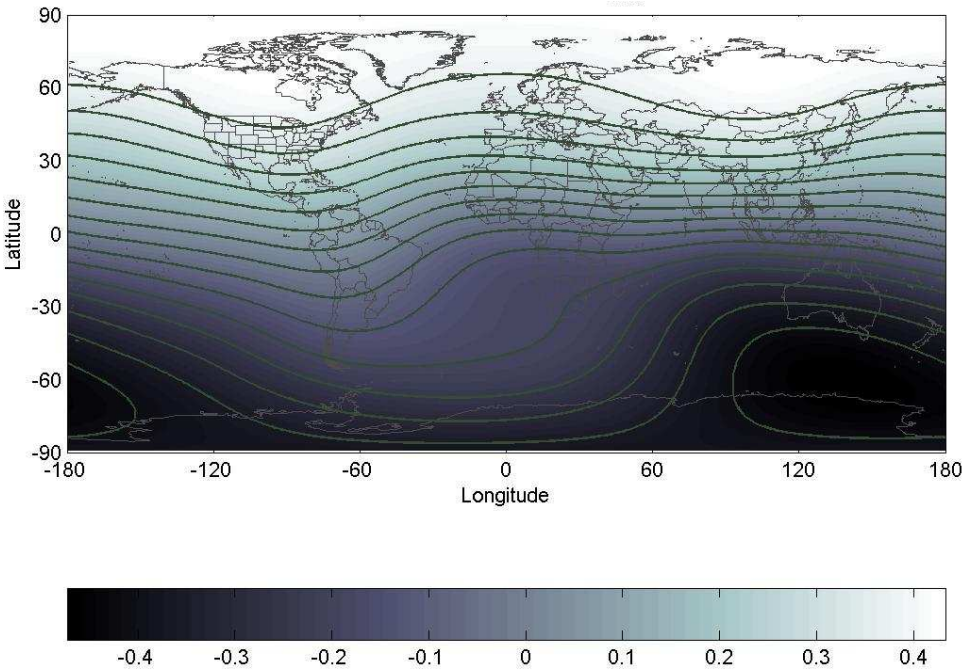

Figure 3.5: Contour Plot of the downward flux density in Gauss for an IGRF2005 model of degree and order 13, 700km altitude (R_E = 6378.135km)and 01.04.2006

[5] 1 Gauss = 1 Ørsted = 10^5 nT

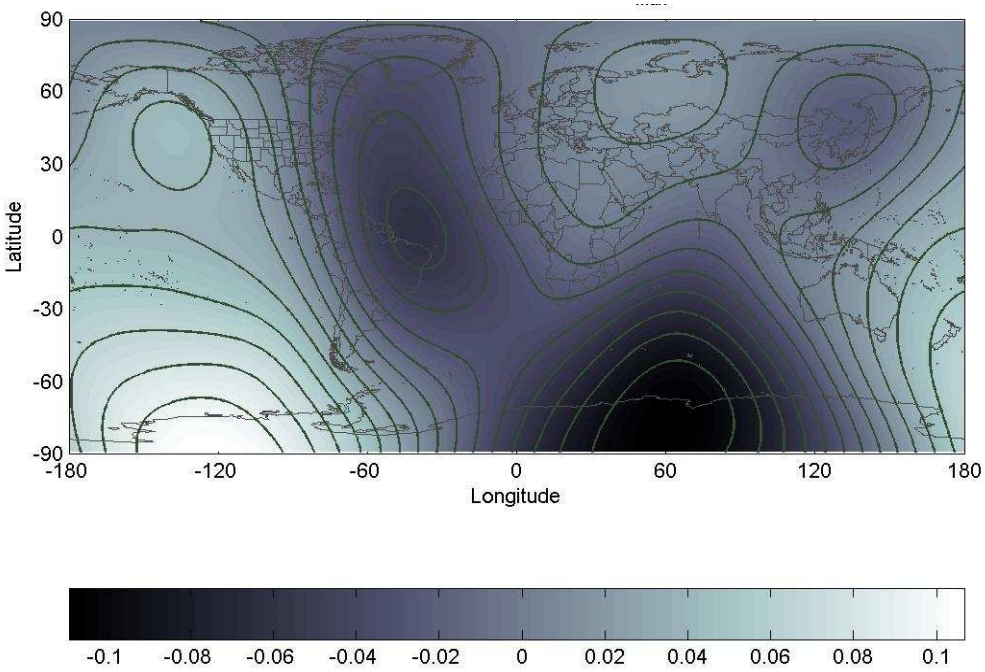

Figure 3.6: Contour Plot of the eastward flux density in Gauss for an IGRF2005 model of degree and order 13, 700km altitude (R_E = 6378.135km) and 01.04.2006

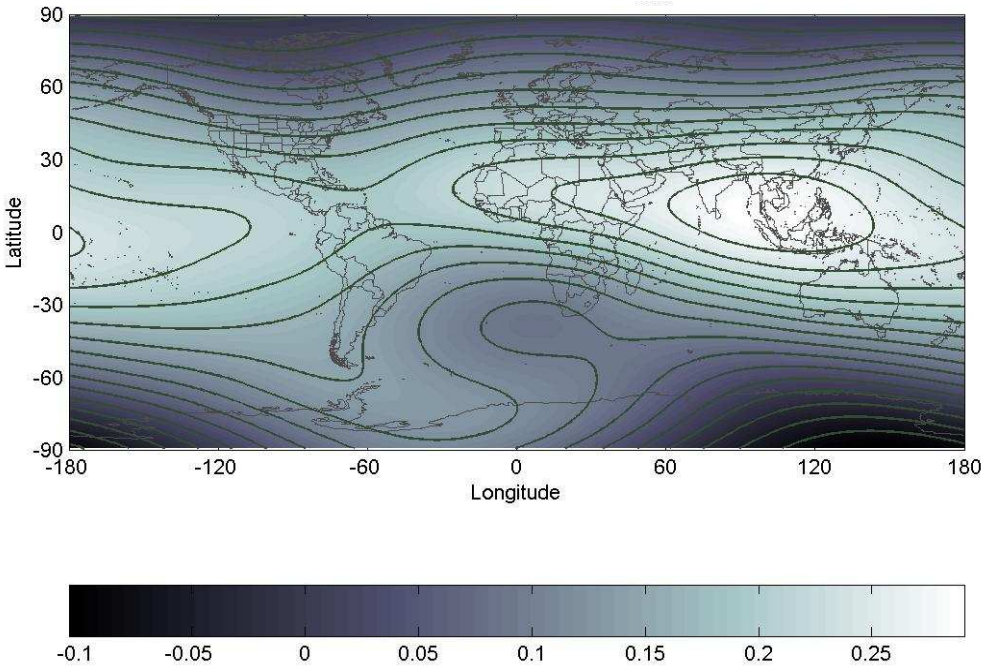

Figure 3.7: Contour Plot of the northward flux density in Gauss for an IGRF2005 model of degree and order 13, 700km altitude (R_E = 6378.135km) and 01.04.2006

Figures 3.4 through 3.7 show the total intensity and the components of the geomagnetic main field at 700km altitude according to IGRF-10. It is important to observe the maximum total field strength of 0.47 Gauss at the centre design altitude as this will be a driving quantity for the design of the attitude determination instruments.

A degree and order 1 model (only 3 gaussian coefficients) corresponds to the ideal magnetic dipole, tilted by approximately 10°. From these first coefficients of the complete model various useful information can be derived. The total dipole strength can be expressed as

$$B_0 = \sqrt{{g_1^0}^2 + {g_1^1}^2 + {h_1^1}^2} = 30036.74\text{nT} \tag{3.16.a}$$

$$M = B_0 \cdot R_E^3 = 7.79 \cdot 10^{24}\text{nTm}^3 \tag{3.16.b}$$

Hence, the flux density is app. 0.6 Gauss at sea level at the magnetic poles, as compared to the 0.47 Gauss at 700km altitude.

The coelevation of the dipole is

$$\theta_m' = \cos^{-1}\left(\frac{g_1^0}{H_0}\right) = 169.74° \tag{3.17}$$

and the east longitude of the dipole is (quadrant corrected)

$$\phi_m' = \tan^{-1}\left(\frac{h_1^1}{g_1^1}\right) = 108.22° \tag{3.18}$$

For epoch 2005.0, the geomagnetic north pole is at longitude 71.78°W and geodetic latitude 79.74°N and the geomagnetic south pole is at longitude 108.22°E and geodetic latitude 79.74°S. This yields an inclination of the magnetic equator w.r.t. the geographic equator of 10.26° at epoch.

3.4 Summary

In this chapter, the reference orbit for Compass-1 has been derived by comparison of previous CubeSat launch campaigns. For this reference orbit the disturbance torque environment has been estimated to yield the worst-case disturbance torques the spacecraft will experience during its mission and which the attitude control system must be capable of compensating. Furthermore, a thourough description of the geomagnetic main field has been presented including the very accurate, empirical spherical harmonics expansion model of IGRF.

Chapter 4

Attitude Control Hardware

The methods employed for spacecraft attitude control are manifold; however, only those which can achieve the required earth-pointing mode shall deserve a closer look here, i.e. gravity gradient stabilization and active three-axis attitude control. In general, any source of active control torques or predictable conservative torques is a potential candidate for spacecraft attitude control. The passive method of gravity gradient stabilization, although conceptually simple, bears a significant drawback for CubeSat attitude control: the gravity gradient generated by a satellite of cubic configuration is not sufficient in magnitude to stabilize the satellite within a sensible pointing envelope. Pitch and roll stability require a sizable difference in principal inertia about the $\hat{c}_3$ yaw axis and the remaining two principal inertiae; this is difficult to achieve structurally, since a deployable appendage is required. However, for nadir-pointing spacecraft the stabilizing gravity gradient effect may be condired a passive support to another, active means of attitude control. The identical CubeSats NCube-1 and NCube-2 [6] use a deployable 1.5m boom for this purpose, and the 0.5m monopole antenna of Compass-1 yields the same effect, even though less pronounced. The gravity gradient causes very little yaw stability, a fact which is of minor importance for a spacecraft with the payload boresight coinciding with the yaw axis.

In comparison to the passive gravity gradient effect, all active control methods although conceptually much more versatile and capable are complicated by the fact that they require knowledge of the satellite attitude in order to form a closed-loop control system. The active actuators of the feedback system are used to impose a controlled angular acceleration on the spacecraft in order to position the body into the desired attitude; such satellites are said to be three-axis attitude controlled. A more general concept is the management of angular momentum of the plant system to exert control torques as illustrated in (4.1).

$$T = \dot{h} = I \cdot \dot{\omega} \tag{4.1}$$

As the torque is the derivative of the angular momentum, the actuator must change the angular momentum of the spacecraft, which according to Newtons law must be constant as long as the spacecraft is not affected by external torques. As a result there are only two groups of methods to alter the attitude of the spacecraft

- By exchanging angular momentum with an external object
- By exchanging angular momentum with another part of the spacecraft

One active method belonging to the first group of attitude control strategies is by irreversably exchanging angular momentum with the momentum of an offset particle jet created by either conventional or electrical thrusters. CubeSats are not allowed to carry any volatile material such as solid or liquid propellants, but cold gas thrusters are an option. However, owing to the stringent weight restrictions no attempt to implement cold gas propulsion systems for attitude or orbit control has been undertaken in the context of picosatellites so far. Electrical thrusters are problematic on CubeSat platforms since existing designs require exceedingly large amounts of electrical power and a high voltage power bus. Micro-Electro-Mechanical Systems (MEMS) technology provides a promising approach to overcoming these technological obstacles; a Danish research team at DTU has developed a subminiature low-voltage MEMS electron emitter for picosatellites [30].

Almost every modern three-axis controlled satellite carries a set of at least three momentum / reaction wheels for attitude actuation. These usually very expensive actuators enable a spacecraft to slew into any desired attitude and maintain this orientation to a degree of accuracy which is virtually only limited by the certainty in the knowledge of the satellite attitude. Depending on the sizing of the actuators high slew rates can be achieved and sophisticated mission scenarios such as target tracking are viable without expending propellant mass. The momentum wheel belongs to the second group of actuators as the angular momentum is reversably transferred from the spacecraft to the momentum wheels. They consist of a motor and a flywheel; when the flywheel is accelerated by the motor it picks up angular momentum, which is transferred from the satellite frame on which the motor is mounted. Some momentum wheels are operated unidirectionally at a bias spin rate of half the maximum allowed rate to avoid non-linearities introduced by stiction and dead band at zero-crossing. The motor has saturation limits, i.e. a maximum spin rate of typically $\leq$ 10,000rpm and a minimum spin rate of >0rpm, and this limits the angular momentum capacity that can be transferred between the wheels and the spacecraft; momentum wheels are thus often used in conjunction with another actuation system for the purpose of ‘wheel desaturation’ or ‘momentum unloading’.

Assuming a worst-case disturbance level of $5.95 \cdot 10^{-7}$ Nm found in the previous chapter and postulating that the wheel may only be desaturated once per orbit at 800km altitude yields the following conservative momentum capacity sizing for disturbance rejection control authority.

$$h_{mw,\max} = T_{dist} \cdot P = 59.5 \cdot 10^{-8}\, Nm \cdot 6050 s = 3.6 \cdot 10^{-3}\, \frac{kg \cdot m^2}{s} \tag{4.2}$$

Among the smallest commerically available momentum wheels are Dynacon's MicroWheel200 [31] and Teldix' RSI 01 with a capacity of 50mNms and 40mNms and a mass of 770g and 600g, respectively. Both momentum wheels are designed for small LEO satellites with a mass of several tens of kilograms. Not only do these devices exceed the mass restriction of any sensible CubeSat platform but also the power and size limitations, and are thus no feasible option for CubeSat attitude control. Miniature momentum wheels for picosatellites are currently under development by a collaboration between the Technical University Berlin, Germany and the private company Astrofein GmbH, as well as the Danish Aalborg University which will implement the new actuators in their next generation CubeSat AAUSat-II [32].

The diagram in figure 4.1 illustrates the attitude control hardware layout; this chapter presents details concerning each of the hardware building blocks. A description of the GPS receiver has been omitted since it is not an integral part of the attitude control system.

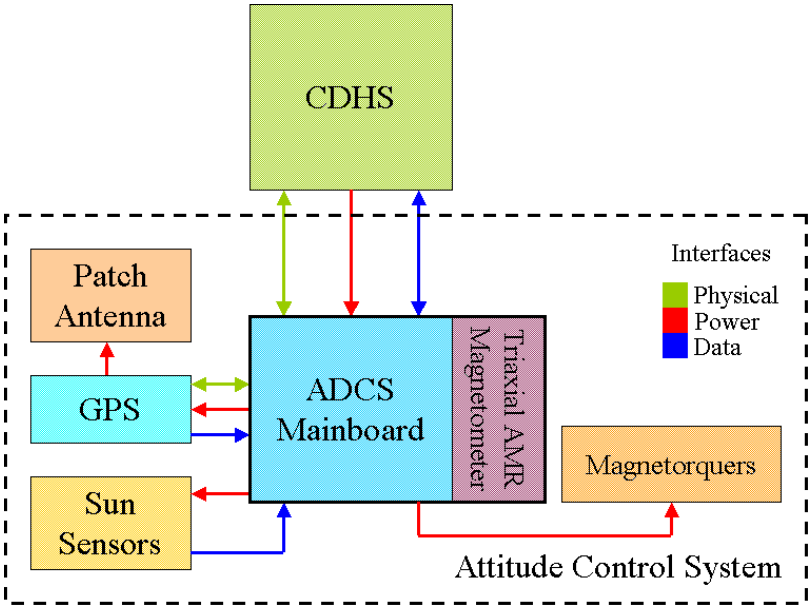

Figure 4.1: Overall Layout of the Compass-1 ADCS hardware

4.1 Magnetic Actuators

The most common actuators used in conjunction with momentum wheels for the purpose of momentum unloading are magnetic torquers. Environmental torques due to magnetic dipoles have already been presented in chapter 3; there exists one simple algebraic equation which describes the way in which a control torque is generated by the presence of a magnetic dipole *m* subject to an ambient magnetic flux density *B*.

$$\vec{T} = \vec{m} \times \vec{B} \tag{4.3}$$

As an example, the functional principle of a compass, the most significant navigational aid before the installation of the Global Positioning System (GPS), can be better understood in the light of equation (4.3). A common compass is a planar device with a gimballed needle made from a magnetized material with a strong dipole characteristic. This magnetic dipole can be understood as a vector quantity which is fixed to the needle. The interaction between this magnetic moment and the Earth's magnetic field will produce a mechanical torque which rotates the needle until its magnetic moment becomes aligned with the geomagnetic field direction (towards the magnetic north pole) where the cross product and the torque will reach the value zero. The damping introduced by the friction of the bearing, a viscous bath of water or both will then eventually lead to the needle being steadily aligned with the geomagnetic field vector, i.e. point towards magnetic north.

This highly predictable torque generation capability has inspired engineers of early spacecraft to implement passive attitude control by strapping a sufficiently strong magnetized ferromagnetic rod as well as a damping mechanism to the spacecraft structure, such that the dipole vector of the satellite will always follow the geomagnetic field lines. However, this passive magnetic control mechanism results in a vehicle motion which is incompatible with the nadir-pointing requirement of Compass-1 since the geomagnetic field vector rotates twice w.r.t. to the inertial frame or once w.r.t. to the orbital frame.

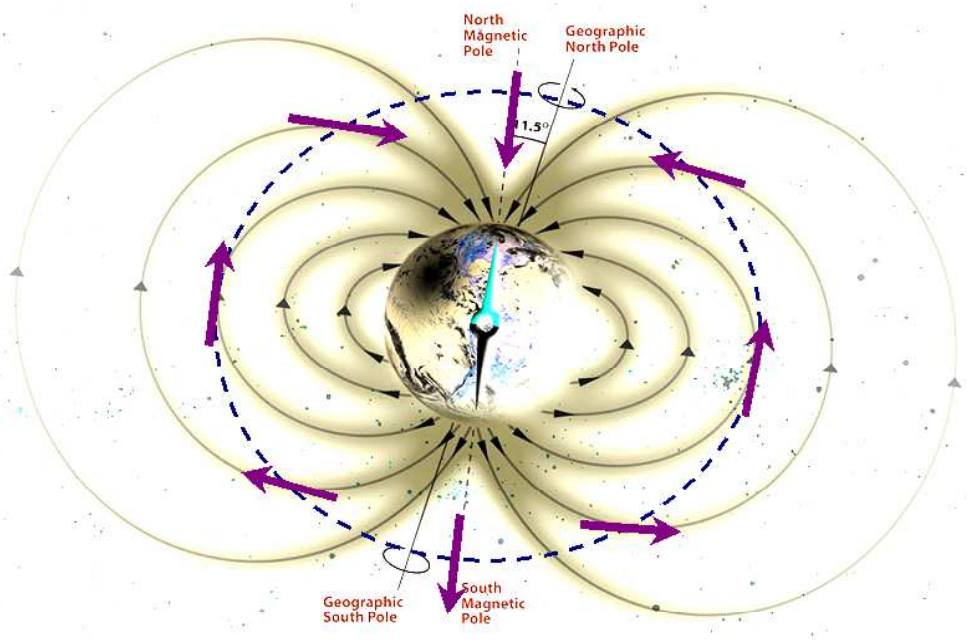

Figure 4.2: Passive magnetic control aligns a spacecraft axis of choice with the local geomagnetic field vector; this prohibits nadir-pointing attitude control.

A solution would be to suspend the magnet in a cardanic frame, but this is unnessecarily difficult to accomplish. Luckily, there exists an alternative to the permanent ferromagnet, the electromagnet. An electromagnet consists of many loops of conductors which are optionally wound around a core of high magnetic permeability. With the ferromagnetic core the

electromagnet forms an active magnetic spacecraft actuator known as a torque rod; without it, the term air coil is common.

Active magnetic control inherents a range of advantages over other attitude control approaches. Electromagnetic coil hardware is inexpensive, simple, robust, reliable and sizable. In particular the last item is important in the context of picosatellites for which suitable actuators are not readily available. The control method is perfectly vibrationless which may be an essential asset for potential scientific payloads. Also, magnetic control offers a relatively simple and reliable method for initial momentum dumping, known as the Bdot-detumbler which is treated in chapter 5. The major disadvantages that have to be attributed to active magnetic control include its inherently moderate accuracy due to a phenomenon referred to as fundamental underaction further discussed in chapter 5. A direct implication of this fundamental underactuation is that magnetic control is only an option for small satellites (up to app. 60kg) with high orbital inclinations. Furthermore, it is only feasible for LEO spacecraft due to the cubically declining magnitude of the geomagnetic field with increasing altitude.

4.1.1 Origin of magnetic torques

The following presents the origin of the electromagnetic torque produced by a rectangular air coil as implemented on Compass-1, subsequently called magnetorquer.

Particles with a charge *q* in an electric field *E* travelling through a magnetic field with flux density vector *B* experience a Lorentz force which is given as

$$F_L = q \cdot (E + v \times B) \tag{4.4}$$

Within the magnetorquers, charges in the form of a continuous current of electrons follow the direction of the electric field and stream along defined tracks, the windings of the coil. The Lorentz force can thus be considered a force which is imposed on the conducting wire material. Consider a small differential length *dl* of a wire. The differential charge *dQ* in the volume of the wire with the length *dl* can be found using the charge density in the wire ρ_n.

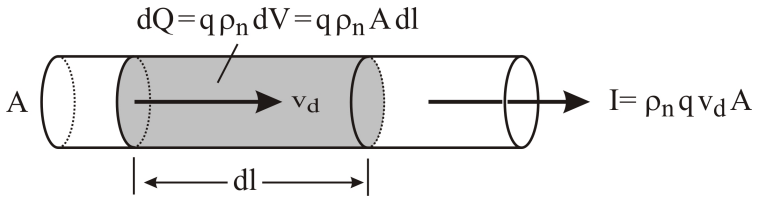

Figure 4.3: A current-carrying wire segment

The magnetic force on the differential volumetric charge dQ moving with the drift velocity v_d in a magnetic field B is:

$$\begin{aligned} d\vec{F} &= dQ \cdot \vec{v}_d \times \vec{B} \\ &= (\rho_n \cdot q \cdot \vec{v}_d \cdot A) \cdot dl \times \vec{B} \\ &= (\rho_n \cdot q \cdot v \cdot A) \cdot d\vec{l} \times \vec{B} \\ &= I \cdot d\vec{l} \times \vec{B} \end{aligned} \tag{4.5}$$

Hence, by integration, the force acting on a finite straight conductor segment is given as

$$F = L \cdot \vec{I} \times \vec{B} \tag{4.6}$$

A rectangular loop may be divided into 4 straight segments of lengths a and b. Figure 4.4 shows the forces which act on the loop segments in a general planar orientation.

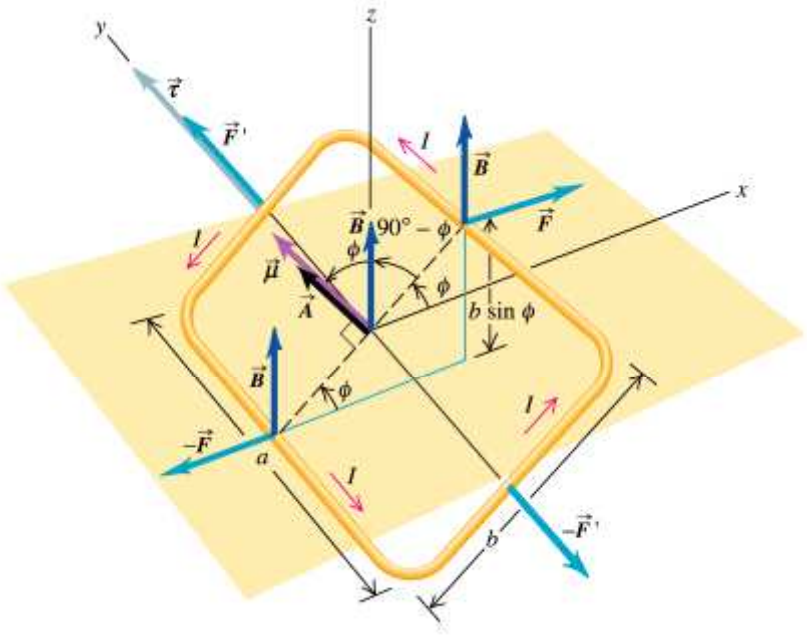

Figure 4.4: Lorentz forces on a tilted conducting loop subject to a magnetic field B; note that $\mu = m$.

Only one of the two force pairs contribute to the torque about the y-axis, while the other is in balance as a direct consequence of the orthogonality in (4.6). The scalar torque about the center of mass of the loop is

$$T = 2 \cdot F \cdot \frac{b}{2} \cdot \sin \phi \tag{4.7}$$

For the given situation, (4.6) may be simplified to

$$F = I \cdot a \cdot B \tag{4.8}$$

Inserting (4.8) into (4.7) yields

$$T = I \cdot a \cdot b \cdot B \cdot \sin\phi = I \cdot A \cdot B \cdot \sin\phi \tag{4.9}$$

Defining the magnetic moment for a single loop as

$$m = I \cdot A \tag{4.10}$$

and recognizing the basic property of the cross product,

$$|\,a \times b\,| = |\,a\,| \cdot |\,b\,| \cdot \sin\angle\,(a,b)$$

the mechanical torque may be generalized by the simple algebraic statement in (4.3). The definition in (4.10) may be equivalently generalized for a coil with a number of turns $N \geq 1$, such that

$$m = N \cdot I \cdot A \tag{4.11}$$

It follows that the mechanical torque produced by a set of three mutually perpendicular magnetorquers is

$$T = m \times B = \begin{pmatrix} N_1 \cdot I_1 \cdot A_1 \\ N_2 \cdot I_2 \cdot A_2 \\ N_3 \cdot I_3 \cdot A_3 \end{pmatrix} \times B \tag{4.12}$$

It is reasonable to design the three magnetorquers to have identical physical parameters, such that $N_1 = N_2 = N_3 = N$ and $A_1 = A_2 = A_3 = A$, leaving only the coil currents as independent variables. In that case (4.12) may be rewritten as

$$T = m \times B = N \cdot A \cdot \begin{pmatrix} I_1 \\ I_2 \\ I_3 \end{pmatrix} \times B \tag{4.13}$$

By applying different current values, distinct magnetic moment values can be produced. Thus, measuring the geomagnetic flux density with an on-board sensor, and adjusting the coil currents, mechanical torques can be regulated and the attitude of the satellite can be effectively controlled.

4.1.2 Magnetorquer Design

The parameters N and A in (4.13) are the only magnetorquer design parameters important for the treatment of attitude dynamics. However, although the face area A is determined by structural consideration, the choice of the number of turns N presents many consequential issues, which ought to be addressed by a careful design process. The following will present the design concepts with general implications using the Compass-1 magnetorquers as examples. For more detailed information regarding the specifics of the Compass-1 actuator design and magnetorquers refer to [34].

The objective is to design three identical air coil magnetorquers which are individually able to produce an average torque of 1µNm at full current, being subject to design constraints given in table 4.1. The torque requirement is derived from the need to maintain high control authority over worst-case disturbance torque levels.

Table 4.1: Magnetorquer Design Constraints

Parameter	Symbol	Value		Unit	
Maximum width	b_{max}	74		mm	
Maximum height	h_{max}	83		mm	
Allowed mass per magnetorquer	$M_{c,max}$	20		g	
Maximum power at full load	P_{max}	250		mW	
Coil Voltage at full load	U_c	4.5		V	
Minimum temperature	T_{min}	-60	213.16	°C	K
Nominal temperature	T_{norm}	20	293.16	°C	K
Maximum temperature	T_{max}	100	373.16	°C	K

With the given torque requirement it is possible to define the required magnetic moment at full load. A 600km orbit is assumed with the spacecraft being located at the magnetic equator and the magnetorquer normal being perpendicular to the field vector to yield an average estimate of $4.26 \cdot 10^{-2}$ Am² for the required magnetic moment.

$$m = \frac{T}{B} = \frac{T \cdot R^3}{M} \tag{4.14}$$

A total of four basic equations, i.e (4.15), (4.17), (4.18) and (4.11), govern the physical and electrical properties of the magnetorquers, more specifically the mass, power, resistance and the producible magnetic moment. The mass of a coil is given by the product of the total lead length, the wire cross-sectional area and the material density.

$$M_C = N \cdot C \cdot a_w \cdot \rho \tag{4.15}$$

with a_w being the wire cross-sectional area, ρ being the lead material density and the average perimeter C defined as

$$C = 2\left(b + h - 2h_c\right) \tag{4.16}$$

The dissipated electrical power is given by the ohmic law

$$P_C = U_C I_C = \frac{U_C^2}{R_C} = I_C^2 \cdot R_C \tag{4.17}$$

where the coil resistance R_c is a function of temperature.

$$R_C = \frac{N \cdot C \cdot \sigma(T)}{a_w} \tag{4.18}$$

In general this dependency is described by a linear approximation governed by two parameters, i.e. the material resistivity coefficient σ_0 and the temperature coefficient of resistivity α.

$$\sigma(T) = \sigma_0 (1 + \alpha \cdot T) \tag{4.19}$$

Using the simple relationship of coil current and magnetic moment $m = N \cdot I \cdot A$ and inserting (4.15) into (4.17) the power dissipation of a single coil can be reformulated as a function of the coil mass.

$$P_C = \frac{\rho \cdot \sigma \cdot m^2}{M_C} \cdot \left(\frac{C}{A} \right)^2 \tag{4.20}$$

Eqn. (4.20) clearly indicates that power dissipation is inversely proportional to the magnetorquer mass but directly proportional to the square of the ratio between the perimeter and the face area of the wire loops. An implication of this is that a circular coil yields the lowest power consumption for a given mass or, equivalently, the lowest mass for a given maximum available power. However, in spite of the slight loss in efficiency, for Compass-1 it has been decided to use rectangular air coils owing to a simpler structural integration into the cubical frame and a larger achievable face area. Rearranging (4.20) for the magnetic moment yields

$$m = \frac{A}{C} \cdot \sqrt{\frac{M_C \cdot P_C}{\rho \cdot \sigma}} \tag{4.21}$$

Eqn. (4.21) states that the producible magnetic moment can be maximized by minimizing the product of the material density ρ and the material resistivity σ. Both parameters are a function of the selected material. Although exotic materials which minimize this product may exist, realistic lead material candidates are copper and aluminium only. Table 4.2 lists the relevant properties for these two materials.

Table 4.2: Lead material comparison Copper - Aluminium

Parameter	Symbol	Value (Cu)	Value (Al)	Unit
Material density	ρ	8.93E-03	2.7E-03	g/mm³
Material resistivity	σ_0	1.55E-05	2.5E-05	Ωmm
Temperature coeff. of resistivity	α	3.90E-03	3.90E-03	1/K

Given the data in table 4.2 it can be concluded that weight considerations make aluminium a more favorable choice as coil wire material with a density-resistivity-product of $6.75 \cdot 10^{-2}$ Ωg/m² compared with copper which has a parameter product of 0.14Ωg/m². Since it is important to fit a large number of turns into a small volume, a low wire diameter is necessary. Formally, this can be shown by rearranging (4.15).

$$N = \frac{M_C}{C \cdot a_w \cdot \rho} \tag{4.22}$$

It is a simple fact that aluminium wire is not commercially available in as thin gauges as is copper wire. This lack of available thin aluminum wire as well as the lower cost makes copper the material of choice as magnetorquer lead material.

According to (4.18) there is a lower limit to the wire diameter, owing to the fact that ohmic resistance increases with decreasing lead cross-section. The maximum allowable ohmic resistance coincides with the maximum resistivity, which occurs at the maximum operational temperature T_{max} of the coils.

$$R_{\max} = \frac{U_{C,\max}^2}{P} = \frac{N \cdot C \cdot \sigma_{\max}}{a_{w,\min}} \tag{4.23}$$

Substituting the number of turns by (4.22) and rearranging for $a_{w,min}$ yields the minimum wire cross-sectional area.

$$a_{w,\min} = \frac{1}{U_{C,\max}} \sqrt{\frac{M_C \cdot P_C \cdot \sigma_{\max}}{\rho}} \tag{4.24}$$

The design of magnetorquer hardware is complicated by the fact that, according to the IEC 60317 standard, only discrete values for the wire diameters exist. Also, the wire needs to be electrically polyurethane insulated, i.e. enamelled, to avoid short circuits which adds mass and volume to the magnetorquer but on the other hand allows for an effective heat bonding to provide the desired structural integrity and stiffness without the need for additional expoxy resin. The results of an iterative design process based on the above design equations is shown in table 4.3.

Table 4.3: Magnetorquer Design Results

Parameter	Symbol	Value	Unit
Wire diameter (bare)	d_w	0.15	mm
Wire diameter (incl. insulation)	d	0.16..0.17	mm
Coil width	b	74	mm
Coil height	h	83	mm
Mean coil width ($b - h_c$)	b_m	69	mm
Mean coil height ($h - h_c$)	h_m	78	mm
Mean face area ($b_m \cdot h_m$)	A	5382	mm²
Mean circumference ($2(b_m+h_m)$)	C	294	mm
True mean face area	A_{true}	5205	mm²
True mean circumference	C_{true}	283.7	mm
Cross-sectional height	h_c	5	mm
Cross-sectional width	b_c	2.1	mm
Cross-sectional area ($h_c \cdot b_c$)	A_c	10.5	mm²
Number of turns	N	400	-
Total wire length ($N \cdot C_{true}$)	l	113.48	m
Coil mass (w/o insulation)	M'_c	18.56	g
Coil mass (incl. insulation)	M_c	19.20	g
Coil resistance @ -60°C	$R_{c,-60}$	89.02	Ω
Coil resistance @ 0°C	$R_{c,0}$	116.21	Ω
Coil resistance @ 50°C	$R_{c,50}$	138.87	Ω
Coil resistance @ 100°C	$R_{c,100}$	161.53	Ω
Max. Current @ -60°C	$I_{max,-60}$	50.55	mA
Max. Current @ 0°C	$I_{max,0}$	38.72	mA
Max. Current @ 50°C	$I_{max,50}$	32.4	mA
Max. Current @ 100°C	$I_{max,100}$	27.86	mA
Producible magn. mom. @ -60°C	$m_{max,-60}$	105.25	mAm²
Producible magn. mom. @ 0°C	$m_{max,0}$	80.62	mAm²
Producible magn. mom. @ 50°C	$m_{max,50}$	67.46	mAm²
Producible magn. mom. @ 100°C	$m_{max,100}$	58.00	mAm²
Max. power dissipation @ -60°C	$P_{max,-60}$	227.48	mW
Max. power dissipation @ 0°C	$P_{max,0}$	174.24	mW
Max. power dissipation @ 50°C	$P_{max,50}$	145.8	mW
Max. power dissipation @ 100°C	$P_{max,100}$	125.37	mW

4.1.3 Magnetorquer Validation

Validating the magnetorquer design by means of tests poses significant difficulties. Two standard approaches often appearing in CubeSat related documentation [32] are to (i) directly measure the produced mechanical torque or to (ii) map the magnetic field generated by the magnetorquers. Magnetorquers create torques well below the sensitivity threshold of common torque transducers making accurate measurements in a laboratory environment impossible. Mapping the magnetic field will not directly yield torque levels but the magnetic moment; inaccuracies are introducted by the fact that the magnetorquer field is superimposed with an ambient magnetic field and it may be difficult to conduct mapping of reasonable resultion on such a small DUT. Hence a test method has been conceived by the author which works around the need to measure mechanical torques or magnetic fields by rather

determining the generated magnetic dipole moment through the concept of an oscillating torsion pendulum.

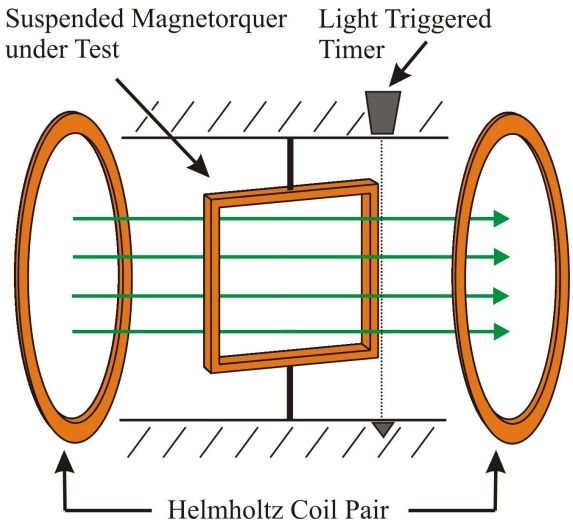

Figure 4.5: Conceptual Test setup for measuring the produced magnetic moment of a magnetorquer

Figure 4.5 shows the conceptual test setup for measuring the produced magnetic moment of a magnetorquer. The DUT is suspended along one of the two axes of symmetry which are reasonably assumed to be the principal axes of inertia by its own lead wire in a strong uniform magnetic field of known magnitude generated by a pair of Helmholtz coils. The resulting system can be characterized as a one-dimensional torsion pendulum without damping as in (4.25).

$$J \cdot \frac{d^2\varphi}{dt^2} = -k_\varphi \cdot \varphi - m \cdot B \cdot \sin\varphi \tag{4.25}$$

where k_φ is the torsional suspension stiffness. Assuming small rotational displacements φ, (4.25) may be linearized as

$$\frac{d^2\varphi}{dt^2} + \left(\frac{k_\varphi + m \cdot B}{J} \right) \cdot \varphi = 0 \tag{4.26}$$

The differential equation (4.26) has the solution

$$\varphi(t) = \varphi_0 \cdot \cos(\omega \cdot t) \tag{4.27}$$

with the oscillation period being

$$T = \frac{2\pi}{\omega} = 2\pi \cdot \sqrt{\frac{J}{k_\varphi + m \cdot B}} \tag{4.28}$$

The magnetorquer test is designed to be conducted in two sequential stages. First, with known magnetorquer inertia J, the suspension stiffness k_φ is determined by measuring the oscillation period while m = 0.

$$k_\varphi = 4\pi^2 \cdot \frac{J}{T^2} \tag{4.29}$$

In the second stage, once k_φ is determined, various coil currents may be invoked and the resulting oscillation period measured; with known suspension stiffness k_φ, magnetorquer inertia J and ambient magnetic flux density B, the corresponding magnetic moment is indirectly found by

$$m = \frac{T^2}{4\pi^2 \cdot J \cdot B} - \frac{k_\varphi}{B} \tag{4.30}$$

The accuracy of this measurement method is limited by the accuracies of three parameters, i.e. the principal coil inertia J, the period of oscillation T and the ambient magnetic flux density B. A test campaign has produced magnetic moments to within 5% relative deviation from the theoretical prediction, which can be shown to be in the order of the combined measurement accuracy of fairly generic laboratory equipment, i.e. multimeters, a helmholtz coil pair, a Hall effect magnetometer and a light barrier triggered timer.

4.1.4 Configuration

The electromagnetic coils are integrated into the structure of Compass-1 to form a set of three mutually perpendicular magnetorquers (figure 4.6). The magnetorquers are clamped and glued onto the face plates in $-b_1$, $+b_2$ and $+b_3$. Polyimide (Kapton™) tape is applied between the torquers and the anodized aluminum panels to provide additional insulation and protection against abrasion due to launch vibrations.

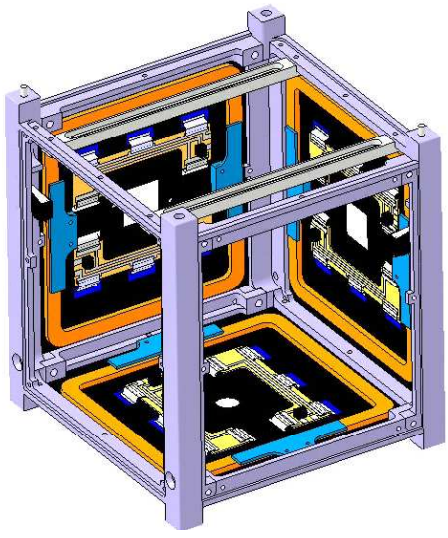

Figure 4.6: Magnetorquer configuration within the Compass-1 structure

4.1.5 The Magnetorquer as Resistance-Inductance Series

Electrically, the magnetorquers represent an inductive load, which may be comfortably characterized as a linear first-order RL circuit with the transfer function

$$H_C(j\omega) = \frac{1}{1 + j\omega\frac{L}{R}} \tag{4.31}$$

where the time constant τ_c, i.e. the time required to establish a voltage/current equal to 2/3 of the step input voltage/current function, is

$$\tau_C(T) = \frac{L}{R_c(T)} \tag{4.32}$$

and R_c is the temperature-dependent magnetorquer coil resistance.

4.1.6 Coil Self Inductance

The DC self inductance has been neither a design nor optimization variable during the magnetorquer design but has significant implications for the design of the electronics driving the magnetorquers as can be seen from (4.31). In order to obtain accurate results for the self inductance of the magnetorquers, various experiments involving a precision inductance-meter have been conducted. The results for prototype magnetorquers with parameters listed in table 4.3 are presented in table 4.4

Table 4.4: Results of Inductance Experiments (at 10kHz input frequency)

Parameter	Symbol	Value	Unit
Mean Inductance @ 10kHz	L	27.6	mH
Inductance Tolerance		±5	%
Min. Inductance	L_{min}	26.2	mH
Max. Inductance	L_{max}	29.0	mH

Predicting the self-inductance theoretically is not straight-forward. It has been found that even formulae considering the rectangular coil geometry [33] yield inductance values far above the measured values; the common assumption of the total self-inductance being proportional to the square of the number of coil turns is only valid for long coils, which the magnetorquers are not.

Highest-valued time constants τ_c arise from max. coil inductance coupled with low temperature. Table 4.5 summarizes the time-constants based on information in tables 4.3 and 4.4.

Table 4.5: Magnetorquer Time constants

Parameter	Symbol	Value	Unit
Max. time constant (@ -60°C)	τ_{max}	320.37	µs
Min. time constant (@ 100°C)	τ_{min}	160.71	µs
Mean time constant	τ	240.54	µs

4.1.7 Coil Driver Circuit

Electrically, a magnetorquer represents a load of sizable inductance similar to a DC motor load. Although the selected microcontroller (µC) is capable of sourcing up to 25mA per I/O drive, switching inductive loads directly be the µC is not recommended due to the high in-rush currents and voltage peaks typical for cycled inductive loads. Hence, driving the magnetorquers requires some interface electronics, referred to as a 'coil driver'. Each of the three coil driver channels must be capable of driving the connected magnetorquer with a µC controllable, near continous and bi-directional current level in the milli-Amps regime. In addition, all three driver channels must be capable of operating entirely independent of each other.

Extensive work, both in simulation/design and test on prototype hardware, has been done on a dicrete power stage driven by a µC controller pulse-width modulated (PWM) waveform[6] with base frequencies up to 80kHz. The CubeSat projects DTUSat [41] and AAUSat [32] utilized a discrete transistor stage in H-bridge configuration in order to effectively decouple the logic system from a power system. Either bi-junction transistors (BJT) or Field-Effect transistors (FET) may be used to construct such a discrete power device. The advantages of this type of electronics are an inherently bi-directional nature and the certainty of zero load currents while the power stage is quiescent.

The load, i.e. the magnetorquer, can either by switched on or off, with the direction of the current flow being determined by which diagonal pair of the H-bridge is cycled. When the magnetorquer is switched on, the maximum current flows; when it is off, no current flows. Intermediate current levels can then be theoretically achieved by appling a PWM waveform with variable duty cycle and high base frequency, owing to the load being inductive.

[6] Most modern microcontroller feature a hardware implementation of the PWM waveform scheme. A PWM signal is rectangular waveform defined by a period and a duty cycle; the duty cycle simply defines the fraction of the period being at logic high level. This peripheral on-chip system allows for the generation of PWM waveforms with a flexible frequency selection easily reaching up to 100kHz.

In the following, significant disadvantages of the discrete power stage as driving element of the magnetorquer current will be briefly discussed. All major drawbacks of this approach arise from this discrete nature of the circuitry. Figure 4.7 illustrates the two main problems based on realistic SPICE[7] simulations.

- Although the inductive load enables the generation of near-continuous current levels, the steady-state current remains a superposition of direct current and alternating current, i.e. $i_c = i_{DC} + i_{AC}$ (figure 4.7.a), with the AC portion being partially attenuated at higher PWM base frequencies. This could be deemed a rather aesthetic concern, but a high current load with significant transients will certainly inject undesirable noise into the power bus of the spacecraft. Also, while the current residuals may appear insignificant at high DC current levels, they become a disturbing issue at low power levels near zero, at which the magnetorquers operate for large portions of their useful life.

- With the low output impedance of a discrete H-bridge, distorting feedback-coupling from the magnetorquer onto the power stage occurs. This becomes apparent at low and high duty-cycles in terms of non-linearities in the duty cycle – current relationship (figure 4.7.b). This effectively reduces the operational range to mid-duty cycles, which results in clipping and truncation of the obtainable magnetorquer currents, if the operational range is limited to the linear region. Magnetic attitude control requires the capability of generating currents in the very low power region for most of the operational time. In particular clipping to a lower limit severly degrades the performance of the controller and may even render it useless.

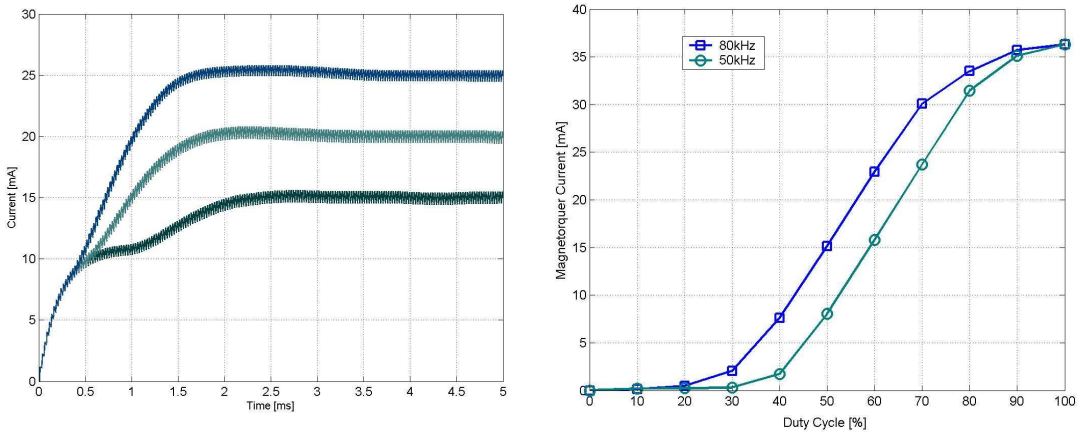

(a) (b)

Figure 4.7: Simulated magnetorquer current (a) and (b) the duty cycle – current relationship for the discrete power stage driver. Note the superimposed AC current in (a) and the non-linearity in (b).

[7] SPICE is a general purpose analog circuit simulator, which incorporates component-specific non-linear parameter models.

The reason why it is important to assume linearity over the entire operational is an implication of the fact that the current is not only a function of the duty cycle, but also of the magnetorquer temperature and, thus, resistance. In order to maintain a desired current level in the presence of temperature changes it is necessary to implement a digital µC PI feedback controller, using magnetorquer current measurements as feedback variable. It is assumed that predictable and steady current levels can only be established in the linear region of figure 10.b, and this calls for current clipping with the effect on the overall attitude control performance stated above.

The above problems with a discrete coil driver approach have inspired a re-evaluation of the coil driver task. The author has found an elegantly simple solution to the problem by constructing a common continuous programmable (i.e. voltage-controlled) current source with rail-to-rail operational amplifiers (OpAmp) as shown in figure 4.8.

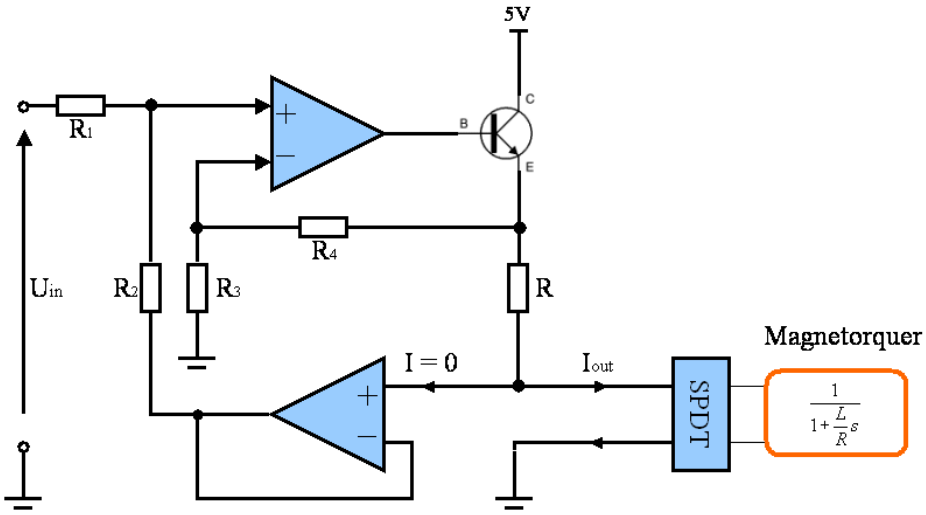

Figure 4.8: continuous programmable current source; the upper OpAmp sources the current, while the lower provides feedback.

The current source works by generating a current through R, which is identical to the load current since OpAmp inputs are high impedance devices. The upper OpAmp sources a current proportional to the differential input voltage, i.e. U_{in}, which is then amplified by a general-purpose npn BJT. This circuit containing only one OpAmp is sufficient to provide a programmable open-loop current source; but consider the lower OpAmp, which provides feedback, such that the following simple steady-state relationship holds

$$I_{out} = \frac{U_{in}}{R} \tag{4.33}$$

The idea is to keep the resistance R constant; small changes due to temperature remain but can be reduced by using a number of high stability resistors in parallel. Then the load current is a linear function of the input voltage only and is independent of the temperature-varying load itself. This continuous hardware-feedback is much more efficient and reliable than the

digital PI controller required for the discrete power stage approach. Furthermore, new magnetorquer designs can be incorporated without any changes to the electronic circuit driving the coil.

Bi-directionality of the load current is achieved by using a µC controlled single-pole dual-throw (SPDT) switch with very low contact resistance (0.5Ω) between the current source and the magnetorquer. Serial, unipolar digital-to-analog converters (DAC) are used to produce input voltages with a dynamic range of 0 to 2.5V and a resolution of 16bits. With a setup resistance value of R = 100Ω, this yields a theoretical maximum achievable current of 25mA.

Figure 4.9 shows the results of a realistic SPICE simulation for R = 100Ω and U_{in} = 1V. The values of the magnetorquer resistance has been varied between 90Ω (at minimum operational temperature) and 160Ω (at maximum operational temperature) to reflect the temperature variability of the magnetorquer resistance. The results show that a predictable steady-state current level of 10mA is established after app. 2ms. Changes of the coil resistance obviously slightly change the transient behavior, i.e. the time constant τ_c, but the loop remains stable with the settled current response unaffected by the change in resistance. The same results have been found by sweeping the coil inductance from $L_{min} \approx 26mH$ to $L_{max} \approx 30mH$. Note that the behavior of the coil driver including the magnetorquer is theoretically entirely symmetric in positive and negative current directions. Hence, all presented results for positive current flow are equivalently valid for negative current flow. Table 4.6 shows the overall magnetorquer performance including the coil driver electronics.

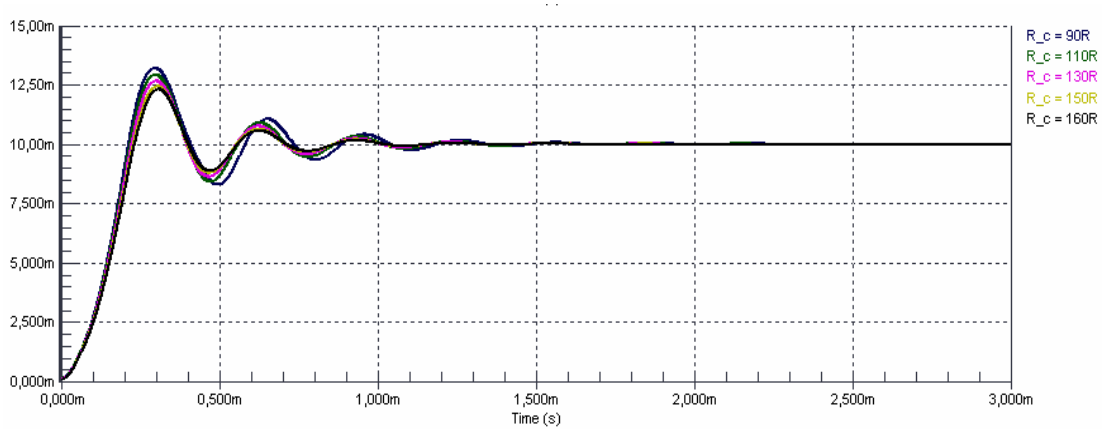

Figure 4.9: Current source performance for a parameter sweep in magnetorquer resistance between $R_{c,-60} \approx 90\Omega$ and $R_{c,100} \approx 160\Omega$ with fixed input voltage of 1V; in all cases a steady-state current of 10mA is generated.

Table 4.6: Combined Magnetorquer/Coil Driver Performance

Parameter	Symbol	Value	Unit
Setup Resistor	R	100	Ω
DAC Dynamic Range	U_{in}	2..2.5	V
Max. Current	I_{max}	25	mA
Max. magn. moment	m_{max}	52.05	mAm²
DAC Resolution	Δ_{DAC}	16	bit
Current Resolution	Δ_i	0.381	µA
Magn. moment resolution	Δ_m	0.794	µAm²

4.2 Attitude Sensors

Measuring the attitude of a body in space can be accomplished by a variety of means. For non-spinning spacecraft attitude sensors can be generally classified as (i) reference sensors, which relate the attitude of a spacecraft w.r.t. to known objects, or entities, e.g. the sun, high visual magnitude stars, the geomagnetic field, etc., or (ii) rate sensors, which measure the inertial body angular velocities, e.g. by using optical, mechanical or piezo-electrical effects. As shown in chapter 2, rate measurement requires integration in time to derive the attitude information and measurement noise and inaccuracies can introduce sizable drift to the attitude determination. Hence, a common scheme is to couple the short term accuracy benefits of rate sensors with the long term stability of reference sensors to create an attitude determination system of high overall performance. For CubeSats, only piezo-electric rate sensors appear to be viable in terms of size, mass and power consumption [13], but these devices suffer from low sensitivity.

For this reason and in order to avoid the complexity and computational burden inherent to the above scheme it has been decided to implement reference sensors only. The attitude sensors of Compass-1 are a three axis magnetometer and five analog slit sun sensors. The following section describes the selection and design of the magnetometer hardware and presents the configuration of the sun sensors.

4.2.1 Magnetometer Technologies

Virtually every spacecraft carries a device with a known response to the presence of an ambient magnetic flux, i.e. a magnetometer, for one of two primary purposes: either as an attitude sensor or as a scientific instrument (spaceborn precision magnetometer instruments play an increasing role in the generation of the major geomagnetic field models like the IGRF). A substantial number of magnetic field related physical effects is known and shaped into devices which may be most generally classified as vector or scalar magnetometers, i.e. capable of measuring field directions as well as magnitudes or of measuring scalar field intensities only; in the context of spaceborne applications, all scalar magnetometers are scientific instruments based on quantum-physical effects. Scalar devices include Proton Precession Magnetometers, which are based on the very regular precession frequency of proton spin about a disturbed field axis, Optically Pumped Caesium Vapour Magnetometers and Overhauser Magnetometers, which employ the proton precession effect in a way that

yields extremely high linearity and temperature stability. The following presents an overview of currently employed vector magnetometer technologies.

SQUIDs

Superconducting Quantum Interference Devices (SQUIDs) consist of a ring of superconducting material within which, owing to quantum physical reasons, the magnetic flux is constrained to be an integer multiple of the magnetic flux quantum ($\Phi_0 = 2{,}0678 \cdot 10^{-15}$ Wb). An ambient magnetic flux causes a quantization maintaining compensation current in the ring; detecting this circulating current enables the use of a SQUID as a magnetometer. In a DC SQUID the superconducting ring is divided by two thin Josephson junctions; a DC current sent through the SQUID creates a measurable voltage drop across the SQUID which is a function of the DC current and the compensation current. The relationship between the voltage drop and the magnetic flux is periodic in exactly one flux quantum; this implies that SQUIDs require sophisticated signal processing when measuring the magnetic fields over a wide range as it is demanded from attitude magnetometers. When the measurement range is limited to within one elementary flux quantum, SQUIDs constitute instruments of extreme sensitivity and find a variety of applications in medical engineering [63]. However, due to the problems of measurement range and the need to maintain the device in a superconducting state SQUIDs are not viable for use on CubeSat platforms.

Fluxgates

The fluxgate magnetometer is the most used spacecraft attitude sensor; a single axis of this instrument consists of a ferromagnetic core which is excited by strong a sinusoidal current waveform applied to an excitation coil. The non-linear flux curve of the ferromagnetic core distorts the flux waveform and a fourier transformation reveals three dominant frequencies in the induced flux which is picked up by a secondary pick-up coil. The amplitude of the second harmonic is proportional to the ambient DC field and is thus the measurement variable of the fluxgate magnetometer [40].

Small fluxgate magnetometers are commerically available, e.g. the 3-axis device FLC3-70 from Stefan Mayer Instruments with dimensions Ø25x50mm and integrated signal conditioning. Further advances in miniaturization are currently under development by the Institute for Microtechnology at the Technical University Braunschweig, Germany, by employing MEMS technology to produce miniature fluxgates (µMAG) with a mass of only 100mg per axis (without signal conditioning).

Hall Effect Probes

According to (4) charged particles are subject to forces due to electric and magnetic fields. In a current-carrying conducting plate of thickness d subject to a magnetic flux density *B* the magnetic contribution to the Lorentz-Force will deflect electrons until an equilibrium state is established, i.e.

$$q(E + v \times B) = 0 \tag{4.34}$$

This equilibrium state constitutes a seperation of charges which is measurable as a voltage U_H across the hall plate, i.e.

$$U_H = A_H \cdot \frac{I \cdot B}{d} \tag{4.35}$$

where is A_H is called the Hall coefficient. Hall sensors can be made from copper but semiconductor materials such as gallium arsenide or indium arsenide produce the most stable Hall coefficients. All magnetometers based on the Hall effect have in common that they are not sufficiently sensitive for applications involving the measurement of geomagnetic field intensities at LEO altitudes as required for attitude determination purposes.

The Anisotropic Magnetoresistive Effect

Soft ferromagnetic metal films anisotropically change their ohmic resistance in the presence of magnetic fields. This anisotropic magnetoresistive (AMR) effect was first observed in 1856 by english physicist William Thompson, later Lord Kelvin, but the discovery had to wait over 100 years before thin film technology has evolved to a state where integrated AMR sensors where technically feasible. The key benefit of AMR sensors from a commercial point of view is that they can be bulk manufactured on silicon wafers and mounted in commercial integrated circuit packages to produce sensors of exceptionally low cost and small outline.

Commercially available sensors are made of patterned, polycrystalline NiFe (permalloy) thin film strips deposited on a silicon wafer; the properties of the AMR thin film cause it to change resistance by 2-3% in the presence of a magnetic field. When four AMR elements are used in a Wheatstone bridge configuration highly predictable voltage outputs are produced when subjected to magnetic fields. Among a few others, the manufacturers Phillips and Honeywell offer highly integrated AMR bridges for mid-range magnetometry applications.

Other Magnetoresistive Effects

The range of magnetoresistive effects is not limited to AMR; other MR effects are the Giant Magnetoresistance (GMR), the Tunnel Magnetoresistance (TMR) and the Colossal Magnetoresistance (CMR). The Ordinary Magnetoresistance (OMR) is the smallest of all MR effects. The youngest MR effect, GMR, was discovered in 1988 and employs thin Fe/Cr layer systems to yield resistance changes of up to 50%. TMR is similar to GMR and achieves up to 40% resistance changes in changing layers of ferromagnetic metals and insulators. CMR is the strongest MR effect and appears in manganates with Perowskit structure. All MR effects can be explained by quantum-physical phenomena; dominant technical relevance must be attributed to the GMR effect (and the related so called ‘spin valve’) which is employed in modern hard disc drive heads and possibly in future magnetic RAM memory modules, known as MRAM. However, the usefulness of GMR as an attitude sensor is highly questionable since only magnetic fields in the layer plane can be measured, precluding the application as a vector magnetometer.

For the attitude control system presented in this thesis, a magnetometer based on the AMR effect has been selected. AMR sensors may not be the most sensitive devices but all attitude determination based on a magnetometer backbone has in common that its accuracy is inherently limited by the unmodeled temporal variations of the geomagnetic field discussed in chapter 3, and resolution in the order of nanoteslas is certainly sufficient. In that context and in view of the currently availably hardware, a custom-designed AMR sensor offers the benefits of having full control over the overall performance, power requirements and physical integration into the control system. At the moment, the small outlines make integrated AMR sensors the attitude sensor of choice for CubeSat applications. However, with the good progress underway in miniaturization of more sensitive devices, particularly fluxgates, may be found on future picosatellite platforms.

4.2.2 Magnetometer Design

The tri-axial magnetometer implemented on Compass-1 uses the single-axis and dual-axis Honeywell HMC1021/1022 devices as the active sensing elements. The wheatstone bridge is operated at 2.5V; accordingly adjusted key specifications are listed in table 4.7.

Table 4.7: HMC1021/1022 Specifications [35]

	min	typ	max	Unit
Bridge Voltage		2.5		V
AMR Element Resistance	800	1100	1300	Ω
Bridge Current	1.92	2.27	3.13	mA
Operating Temperature	-55		150	℃
Field Range	-6		+6	G[8]
Linearity Error (3 ±1gauss sweeps)		0.05		%FS
Hysteresis Error		0.08		%FS
Repeatability Error		0.08		%FS
Sensitivity	2.0	2.5	3.13	mV/G
Bridge Offset	-5	±1.25	5.625	mV
Bandwidth		5		MHz
Degrading Field	20			G
S/R Strap Resistance	5.5	7.7	9.0	Ω
S/R Current	0.5	0.5	4.0	A
Offset Strap Resistance	38	50	60	Ω
Offset Field	4.0	4.6	6.0	mA/G

[8] 1 Gauss (G) = 10^{-4} T = 10^{5} nT

In a wheatstone bridge configuration, changes in the bridge element resistance values are translated into a differential voltage across the bridge terminals.

$$\Delta U = U_B \cdot \left[\frac{R_2}{R_1 + R_2} - \frac{R_4}{R_3 + R_4} \right] \tag{4.36}$$

It is possible to use a straight-forward amplifier approach to amplify the terminal voltage prior to A/D conversion. However, it is known that the AMR effect is highly non-linear in the angle between the strip current and the direction of permalloy magnetization. The linear assumption is best valid in the vicinity of 45° and hence the permalloy strips are patterned in a 45° barber pole pattern to yield the optimum linearity characteristics stated in table 7. Further reduction of linearity errors is possible and has been implemented on Compass-1 but requires more complex signal path electronics; the design of this analog signal path is largely based on an existing four-axis AMR magnetometer design for the DTUSat mission [36].

The performance increasing strategy involves an integrated sensor feature called offset straps. These straps are small coils which are tightly coupled into the AMR elements. By applying an offset current to the straps, it is possible to superimpose a bias field B_{bias} of highly linear current-field relationship onto the ambient field B_{ext}. This allows for exactly compensating the ambient field such that the brigde output is constantly zero, i.e. maintains a constant operating point around which linearity is sizably improved. As a result, the measurement variable is no longer the bridge output voltage but the bias current required to balance the ambient field exposure. To accomplish this strategy, an analog PI regulator is implemented to form a closed-loop system as shown in figure 4.10.

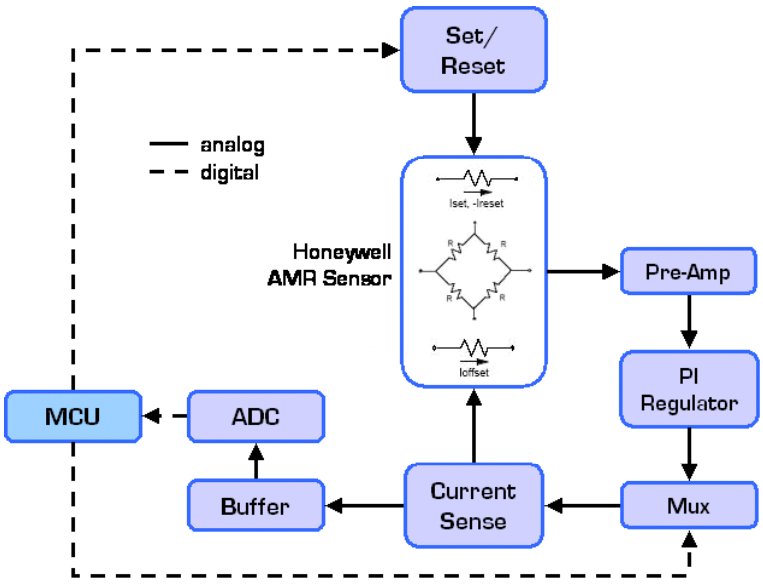

Figure 4.10: Magnetometer design overview

During nominal operation, the magnetic domains of the polycrystalline AMR elements are uniformly oriented along the easy axis, i.e. the axis of intended magnetization. Ambient fields change the orientation of the soft magnetic domains, giving rise to the linearity issue, and strong disturbing fields will actually break down the magnetization alignment in the permalloy film. The direction and magnitude of this magnetization is essential to repeatable, low noise, and low hysteresis output signals. Figure 4.11 (top) illustrates the AMR film when exposed to a strong disturbing magnetic field with the permalloy strip broken up into randomly oriented magnetic domains.

To recover the original magnetic state and restore optimal sensor performance, a strong magnetic field must be applied along the length of the permalloy film. Within tens of nanoseconds the random domains will re-align with the easy axis as shown in figure 4.11 (bottom). In addition to the offset straps, Honeywell's family of AMR sensors has a patented on-chip set/reset (S/R) strap wrapped around the bridge elements. Switching a high current pulse in excess of 400mA through the strap will momentarily create a high intensity magnetic field of 60-100 G and restore the magnetization vector and with it, the predictable magnetoresistive effect; once the original magnetization vector is restored it will maintain this state for years as long as there is no strong magnetic disturbance field present. The same effect will also take place for a pulse in the opposite direction, the reset pulse. Being able to change the direction of the easy axis by 180° implies an interesting feature which distinguishes AMR bridges from all other measurement bridges used in electrical engineering: a state switch results in a theoretically entirely symmetric reversal of bridge sensitivity.

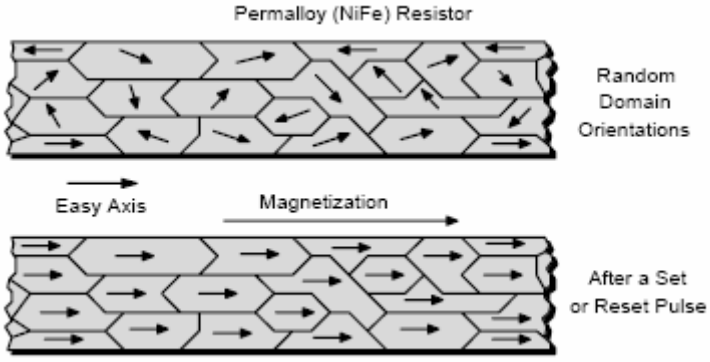

Figure 4.11: Magnetic domain orientations before and after a Set/Reset pulse

Equation (4.36) implies that the bridge output is zero in the absence of a magnetic stimulus only if

$$\frac{R_1}{R_2} = \frac{R_3}{R_4} \tag{4.37}$$

Manufacturing tolerances lead to a small mismatch in the resistive values which results in an error known as bridge offset. Being able to reverse the bridge sensitivities allows to

effectively cancel the offset which is unaffected by a state switch by using the method of digital subtraction.

$$U_{set} = S \cdot B_{applied} + U_{offset} \tag{4.38.a}$$

$$U_{reset} = -S \cdot B_{applied} + U_{offset} \tag{4.38.b}$$

$$U_{set} + U_{reset} = 2 \cdot U_{offset} \tag{4.38.c}$$

or

$$U_{offset} = \frac{U_{set} + U_{reset}}{2} \tag{4.39}$$

In the context of the PI closed-loop regulator, a state switch requires a reversal of the bias current direction. Since the operational amplifier used the implement the PI regulation is only capable of sourcing current in one direction, a µC controlled single-pole dual-throw multiplexer (mux) switch identical to the one used in the coil driver circuit is implemented between the bias current source and the offset strap.

4.2.3 Magnetometer Model

The following section presents a theoretical model of the magnetometer analog signal path using linear approximation [36]. The constants A_i are operational amplifier gains and S_i are sensor sensitivities; $\pm$ or $\mp$ indicates sign dependencies on the sensor state, with the upper sign belonging to the reset state. Equations (4.40.a) through (4.40.e) define the PI regulator's point of operation:

$$B_{tot} = B_{bias} - B_{ext} \tag{4.40.a}$$

$$U_{sensor} = \pm S_{sensor} \cdot B_{tot} + U_{offset,sensor} \tag{4.40.b}$$

$$U_{preamp} = A_{preamp} \cdot (U_{sensor} + U_{offset,preamp}) \tag{4.40.c}$$

$$U_{PI,error} = U_{offset,PI} - U_{preamp} \tag{4.40.d}$$

$$B_{bias} = \pm S_{bias} \cdot I_{bias} \tag{4.40.e}$$

It follows that

$$U_{PI,error} = \mp A_{preamp} \cdot S_{sensor} \cdot \left(-B_{ext} \pm S_{bias} \cdot I_{bias}\right) + U_{offset,loop} \tag{4.41}$$

and

$$I_{bias} = \pm \frac{B_{ext}}{S_{bias}} + \frac{U_{offset,loop}}{A_{preamp} \cdot S_{sensor} \cdot S_{bias}} \tag{4.42}$$

with

$$U_{offset,loop} = U_{offset,PI} - A_{preamp} \cdot U_{offset,sensor} - A_{preamp} \cdot U_{offset,preamp} \tag{4.43}$$

The path from the regulator loop to the analog-to-digital converter (ADC) contains a current-to-voltage gain stage (I-to-V), a buffer amplifier and the ADC itself.

$$U_{I-to-U} = -A_{I-to-U} \cdot I_{bias} + U_{offset,I-to-U} \tag{4.44}$$

$$U_{buffer} = -A_{buffer} \cdot (U_{I-to-U} + U_{offset,buffer}) \tag{4.45}$$

$$C_{ADC} = \frac{U_{buffer} + U_{offset,ADC}}{U_{LSB}} \tag{4.46}$$

$$C_{ADC} = \pm \frac{A_{buffer} \cdot A_{I-to-U}}{S_{bias} \cdot U_{LSB}} \cdot B_{ext} + \frac{U_{offset}}{U_{LSB}} \tag{4.47}$$

where U_{LSB} is set by the resolution of the ADC.

$$U_{LSB} = \frac{U_{range}}{2^n - 1} \tag{4.48}$$

The converter implemented on Compass-1 is a four-channel successive approximation register (SAR) ADC with a bit-width of 16; it has a input range of ±1.25V with a set point of 1.25V yielding a dynamic range of 2.5V and a LSB resolution of 38.15µV.

$$\begin{aligned} U_{offset} = & -\frac{A_{buffer} \cdot A_{I-to-U}}{S_{sensor} \cdot S_{bias}} \cdot \left(U_{offset,sensor} + U_{offset,preamp}\right) \\ & + \frac{A_{buffer} \cdot A_{I-to-U}}{A_{preamp} \cdot S_{sensor} \cdot S_{bias}} \cdot U_{offset,PI} \\ & - A_{buffer} \cdot (U_{offset,I-to-U} + U_{offset,buffer}) \\ & + U_{offset,ADC} \end{aligned} \tag{4.49.a}$$

or

$$\begin{aligned} U_{offset} = & \alpha_1 \cdot \left(U_{offset,sensor} + U_{offset,preamp}\right) \\ & + \alpha_2 \cdot U_{offset,PI} - A_{buffer} \cdot (U_{offset,I-to-U} + U_{offset,buffer}) \\ & + U_{offset,ADC} \end{aligned} \tag{4.49.b}$$

Equation (4.49.b) identifies a total of 6 electrical sensor offsets of which the bridge offset $U_{offset,sensor}$ is the most pronounced. The parameters A_i, S_i and U_{LSB} are variable in temperature making the offset reading according to (4.39) a function of temperature. This implies that the determination of sensor offset has to occur at intervals which are negligibly small compared with the thermal time constant of the integrated sensor.

Table 4.8: typical magnetometer model parameters

Parameter	Symbol	Value	Unit
Pre-amplifier gain	A_{preamp}	45.18	mV/mV
I-to-U converter gain	$A_{I\text{-}to\text{-}U}$	120	mV/mA
Output buffer gain	A_{buffer}	1.5	mV/mV
Bridge sensitivity	S_{sensor}	0.4	G/mV
Bias field sensitivity	S_{bias}	0.217	G/mA
Major offset factor	α_1	-331.2	mV/mV
Minor offset factor	α_2	7.33	mV/mV

The overall sensor gain factor

$$A = \pm \frac{A_{buffer} \cdot A_{I-to-U}}{S_{bias} \cdot U_{LSB}}$$

remains a function of temperature; however, assuming that the parameters have similar temperature drifts on all three axes, e.g. by using gain-defining resistors of similar temperature coefficients, it can be argued that the magnetic field vector reading is merely subject to a drift in magnitude but it is the knowledge of the direction of the magnetic field which is of primary importance as will be shown in the context of attitude determination in chapter 6. Table 4.9 lists the overall magnetometer performance parameters based on test results.

Table 4.9: Integrated 3-axis magnetometer performance overwiew.

Effective Measurement Range	> ±1	G
Relative effective range	68	%
Effective Sensitivity	828	mV/G
Resolution	≈5	nT
Offset Error	<25	nT
Linearity Error	<30	nT
Noise	15	nT_{rms}
Peak Noise	45	nT
Mean total error	60	nT
Worst-case error	100	nT

4.3 Sun Sensors

The second attitude sensor implemented on Compass-1 is a set of 5 analog two-axis sun sensors. At a spacecraft-sun distance of 1AU, the angular diameter of the sun is app. 0.53° and hence, for moderate accuracy requirements, can be considered a point source of highly collimated light. The miniature active sensor area is fabricated in MOEMS technology using manufacturing techniques common to the semiconductor industry and has been developed by a Danish postgraduate student group for the DTUSat spacecraft [37]. For the Compass-1 satellite the chip design is augmented by state-of-the-art mixed-signal microelectronics with the objective to provide front-end processing capability in order to synthesize and communicate a single sun vector in body coordinates from readings of one or more individual sensors.

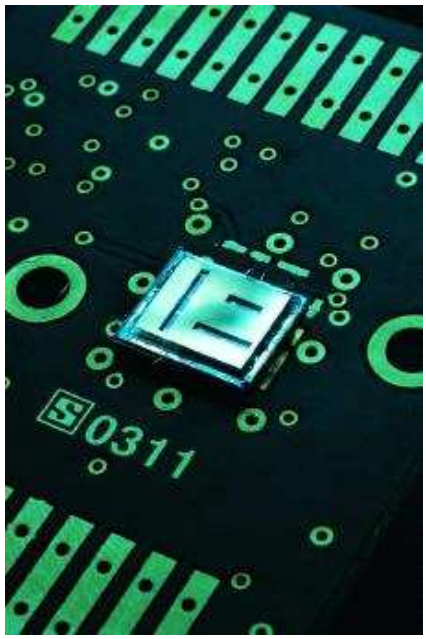

Figure 4.12: Photograph of the MOEMS analog two-axis slit sun sensor (centre) mounted on a printed circuit board (taken from [37] with permission)

The sensors are glue-mounted on the centers of the cube faces except the payload (nadir) face. The objective of the following section is to find the minimum required field of view (FOV) for complete coverage of the spacecraft celestial sphere, for now considering an imaginary sixth sensor present on the south pole. While in the two-dimensional case this angle is simply 45°, the situation changes in three dimensions. Figure 4.13 shows the geometrical situation when only 3 neighbouring sensors are considered. Due to symmetry this is sufficient to fully describe the problem at hand, which is to determine the maximum angle that a point on the sphere can be from the boresight of the closest sun sensor. This is represented by the intersection of 3 equal spherical conic sections in point P, such that the problem really reduces to finding the angle of $\gamma_1 = \gamma_2 = \gamma_3 = \gamma$ in figure 4.13. Note that the FOVs of the sensors are assumed to be conical while it is really a square field of view. However, with the cone being completely inscribed by the pyramid, the assumption of a cone, being geometrically more convenient, is a conservative one.

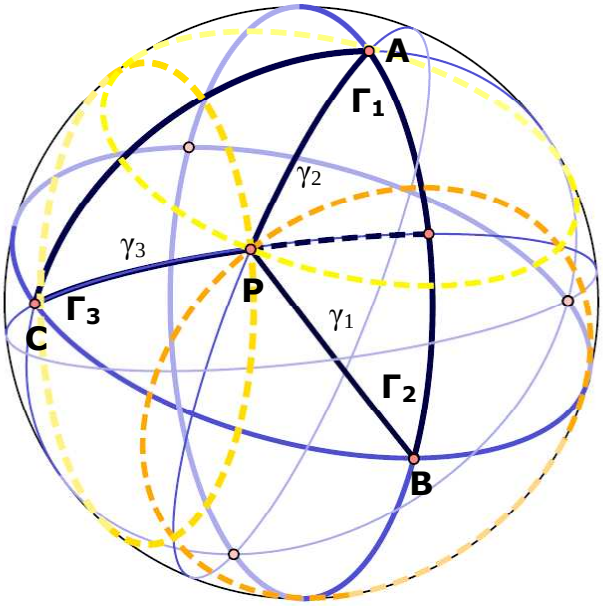

Figure 4.13: Problem definition for the minimum required FOV; all instances in this figure are located on the unit sphere.

Because the triangles APB and APC are isosceles, $\Gamma_1 = \Gamma_2 = \Gamma_3 = \Gamma = 45°$. By recognizing that the triangle APB is in fact a quadrantal spherical triangle, i.e. one having one side of $\pi/2$, the problem can be solved by applying Napier's rules for quadrantal triangles, which yields

$$\sin\Gamma_1 = \tan\Gamma_2 \tan(90° - \gamma_2) \tag{4.50}$$

or

$$\cot\gamma = \cos\Gamma \tag{4.51}$$

for $\Gamma = 45°$

$$\gamma = arc\cot\sqrt{2} = 54.73° \tag{4.52}$$

This means that the sun sensors are required to provide a FOV $\geq \pm 55°$ in order to guarantee a gapless coverage of at least the northern celestial hemisphere for the sensor configuration present on Compass-1. According to the sensor specifications [38], the sensors provide a FOV of ±70° before reflection and refraction effects render the reading useless, with the significant implication that the sun can be viewed by up to three individual sensors simultaneously at any given time.

It has been shown that the current sensor configuration can provide gapless coverage of the northern body hemisphere. However, on the payload face, a gap area must be expected. In this section the exact unobserved area will be determined in terms of a percentage gap. This investigation will assume a conservative FOV of ±60° for all sensors.

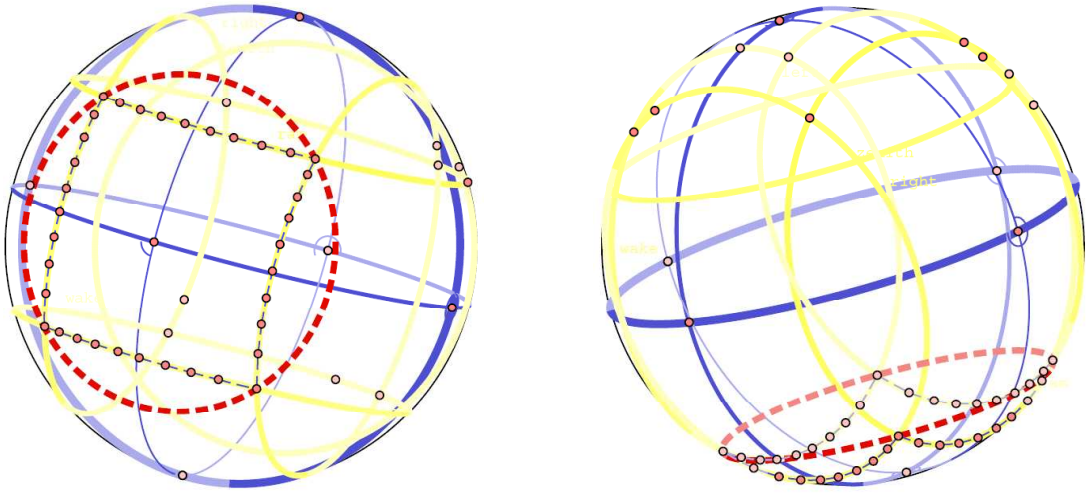

Figure 4.14: Geometry of the sensor gap; all instances in this figure are located on the unit sphere.

Figure 4.14 shows the geometry of the coverage gap on the payload side which is a spherical square delimited by the small circle segments of the sensor FOVs. The bold dashed red line shows the corresponding conic section which inscribes the gap area. This small circle is centered on the south-pole and has a radius of $\pi / 4$ (45°).

In order to determine the amount of area on which coverage is missing, it is very convenient to use the concept of *angular areas*. This area is independent of the actual radius of the celestial sphere by expressing the area in a normalized fashion such that

$$S = \frac{A}{R^2} \tag{4.53}$$

where S denotes the angular area and A the absolute area. Note that following this terminology, the angular area of a sphere is 4π steradian, irrespective of its radius. By observation of figure 4.14 and ignoring the sensor on the north-pole it becomes transparent, that the angular area of the entire sphere can be composed in the following way

$$4\pi = 4S_{cap} - 4S_{OL} + 2S_x \tag{4.54}$$

where S_{cap} is the area of the spherical cap or the area of the small circle with radius 60°, S_{OL} is the overlap area between two adjacent spherical caps and S_x is the uncovered area of interest at the south pole. This yields

$$S_x = 2 \cdot \left(\pi - S_{cap} + S_{OL}\right) \tag{4.55}$$

The absolute area of a spherical cap is [39]

$$A_{cap} = 2\pi \cdot R \cdot h \tag{4.56}$$

Finding an alternative expression for h (figure 4.15)

$$R - h = R \cdot \cos\beta \tag{4.57.a}$$
$$h = R \cdot (1 - \cos\beta) \tag{4.57.b}$$

it is possible to reformulate (4.56) as

$$A_{cap} = 2\pi \cdot R^2 \cdot (1 - \cos\beta) \tag{4.58}$$

Such that, according to (4.53), the angular area of the spherical cap becomes

$$S_{cap} = 2\pi \cdot (1 - \cos\beta) \tag{4.59}$$

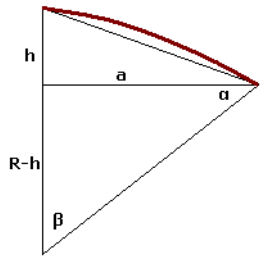

Figure 4.15: Geometry of a spherical cap

The overlapping area between two small circles with radii ρ and ε and an angular center-to-center distance α is [39]

$$\begin{aligned} S_{OL} = {} & 2\pi \\ & -2\cos\rho \arccos\left(\frac{\cos\varepsilon - \cos\rho\cos\alpha}{\sin\rho\sin\alpha}\right) \\ & -2\cos\varepsilon \arccos\left(\frac{\cos\rho - \cos\varepsilon\cos\alpha}{\sin\varepsilon\sin\alpha}\right) \\ & -2\arccos\left(\frac{\cos\alpha - \cos\varepsilon\cos\rho}{\sin\varepsilon\sin\rho}\right) \end{aligned} \tag{4.60}$$

When evaluating (4.59) and (4.60) it transpires that for an assumed FOV of ±60°, the area of a single spherical cap is exactly π. It is interesting to note that in this case, the sum of the four overlapping areas exactly equal the sum of the spherical squares on the north and south

pole. It is known from previous discussions that no gaps exist on the northern hemisphere and the remaining area on the south pole is just twice that of S_{OL}. Hence, S_x = 1.1026sr and S_{sphere} = 4π sr = 12.566sr such that it can be concluded that only 8.8% of the total celestial sphere are not observable by the sun sensor configuration. However, during the nominal nadir pointing attitude mode, the Earth will occupy a significant portion of the spacecraft southern celestial hemisphere. The geometrical relationship for a simple scenario without atmospheric refraction is shown in figure 4.16.

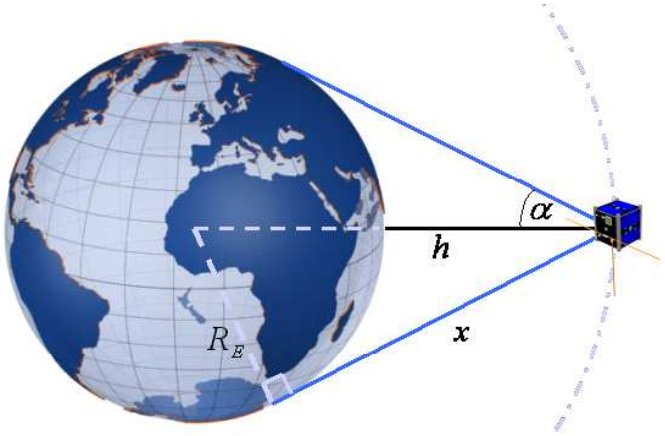

Figure 4.16: apparent radius of the Earth as seen from the orbit of Compass-1 (not to scale)

From figure 4.16 the following geometric relationships can be derived.

$$x = (R_E + h) \cdot \cos\alpha \tag{4.61.a}$$

$$\tan\alpha = \frac{R_E}{x} = \frac{R_E}{(R_E + h)\cos\alpha} \tag{4.61.b}$$

$$\sin\alpha = \frac{R_E}{R_E + h} \tag{4.61.c}$$

$$\alpha = \arcsin\left(\frac{R_E}{R_E + h}\right) \tag{4.62}$$

At an expected max. orbital altitude of 800km, the apparent radius of the Earth (α) evaluates to α = 62.68°. With (4.59) this is equivalent to 3.4sr; this is an angular area three times larger than the coverage gap of the sun sensor configuration. Hence, is has been shown that the missing sensor on the south pole theoretically does not cause any degradation of attitude determination capability during nominal attitude.

4.3.1 Measurement Geometry

Each sensor measures the sun vector in a different right-handed orthogonal sensor frame. The vector can be extracted from angular measurements in each different sensor frame. Figure 4.17 shows the measurement angles α and β for a generic sunline orientation. Note that the resulting vector component in boresight direction (z_s) is defined as unity.

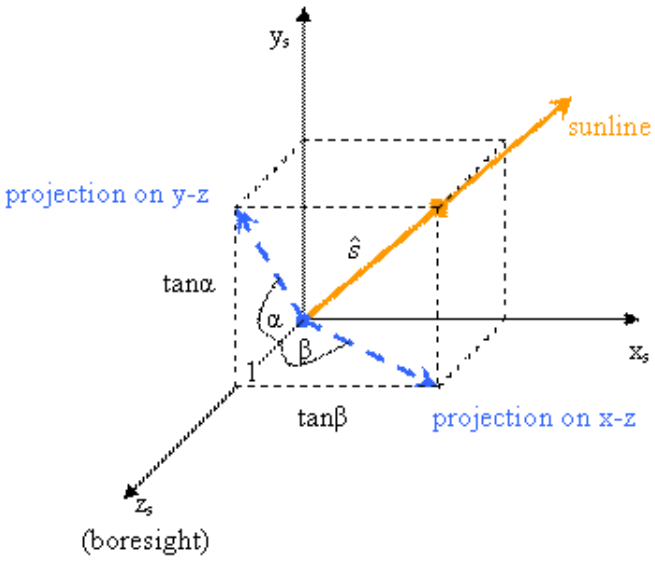

Figure 4.17: geometry of sun angles α and β

The trigonometric relations can be translated into a generic description of the unit sun vector in a local sensor coordinate triad.

$$\hat{s}_{ss} = \frac{1}{\sqrt{(\tan^2\alpha + \tan^2\beta + 1)}} \cdot \begin{pmatrix} \tan\beta \\ \tan\alpha \\ 1 \end{pmatrix} \tag{4.63}$$

Since each one of the five sensors has a different definition of the sensor frame, rotational transformation is necessary to obtain vectors expressed in the body frame.

$$\hat{s}_{b,i} = R_i^{bss} \cdot \hat{s}_{ss,i} \tag{4.64}$$

Due to the simple orthogonal relationships between all involved frames, the transformation matrices become constant permutations. These relations, however, do not account for misalignments that might happen during integration. Sensor surfaces are specifically designed to fit the plane panel surface and the integration involves the use of removable toleranced alignment pins during adhesive bonding to the panel, such that the sensors are deemed to be correctly aligned. Calibration can be used to compensate any remaining misalignment.

4.4 Microcontroller

The digital core of the attitude control system aims to derive benefits from using latest Very Large Scale Integration (VLSI) technology. The high integration density of modern microcontrollers and memory devices allows to implement capable embedded systems of high functionality consisting of only a small number of components. Modern microcontrollers are single-chip devices combining a central processor unit (CPU) with a wide range of standard interface peripherals including synchronous and asynchronous serial interfaces, inter-integrated circit (I^2C) interfaces, ADCs and pulse width modulation. Nowadays, embedded microcontrollers can be found in virtually any battery-powered consumer electronics equipment like notebooks, cameras, mobile phones etc. Functionality is flexibly added to the hardware by means of embedded software which can be conveniently coded in and compiled from high-level programming languages like C/C++. The CPUs of state-of-the-art microcontrollers are quite potent computing devices; they even support embedded real-time operating systems (RTOS) although this is not employed on the current version of the attitude control system. The extremely low power dissipation of low voltage components emerging with the rapidly growing market for battery-powered systems results in minimal requirements for space, weight, cooling, and power supply which all are limited recourses in the context of picosatellites. In this context, however, it must be ensured that the use of VLSI technology does not diminish the reliability of the embedded control system. In general, due to the optimized manufacturing processes for high volume production, the reliability of modern VLSI components already attained a very high standard. Except for the radiation problems, the environmental conditions on-board of a satellite in LEO (most notably vaccum, vibration survival and temperature) can be compared to the operating conditions assumed for industrial versions of such components.

The µC selected for the attitude control system is a recently introduced 16-bit core controller with a performance-boosting, integrated co-processor. Apart from all required digital and analog interfaces the device carries 32kB of static RAM, 512kB of Flash ROM and 4kB of EEPROM on-chip. A phase-locked-loop (PLL) allows to operate the CPU at a clock frequency of 32MHz from an external 16MHz pierce crystal. The entire digital portion of the mixed-signal embedded control system runs off a regulated 3.3V supply, resulting in a low power consumption of approximately 50mA.

The µC is directly interfaced to an external 16Mbit Flash ROM for data storage. The linear address space occupied by the 2MB of memory are accessed using a parallel, byte-wide, non-multiplexed bus, eliminating the need for time-multiplexing. The Flash volume is divided into several sections: 600kB for flight data including GPS navigation message recording and GPS almanac / ephemeris buffering and 1448kB for storage of a geomagnetic field map used for attitude determination.

4.4.1 Electronics Design

The main printed circuit board (PCB) of the ADCS engineering model (carrying the controller, memory, coil driver and magnetometer) is designed as a four-layer board of dimensions 75mm x 80mm, carrying more than 200 surface-mounted components on both board surfaces. The selection of the components is based primarily on availability and performance. Restrictions for foreign microelectronics subject to the International Traffic in Arms Regulation (ITAR) do not apply to the system design, since no component with explicit space heritage has been used[9]. Small component packages have been used throughout for an extremely high integration density. The main board has separatable interfaces for the magnetorquers, a master sun sensor and a plug-in Phoenix GPS receiver. The mechanical GPS interface is provided by a stiff aluminium frame structure while sturdy board-to-board connectors provide a redundant mechanical/electrical interface to the CDHS power and data bus.

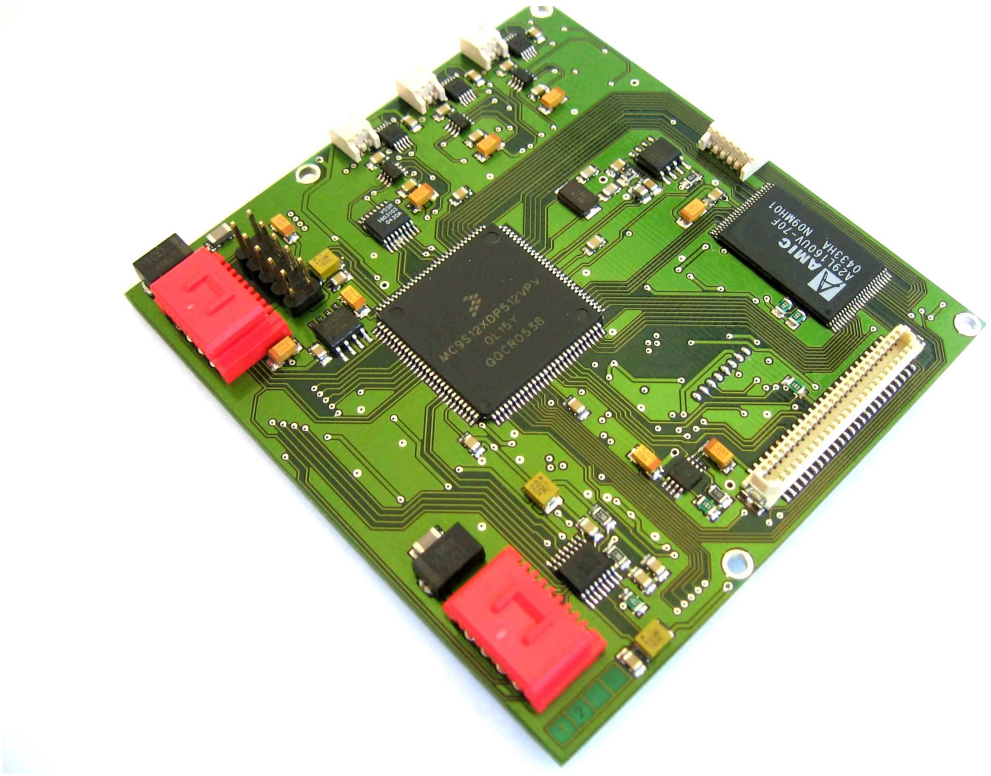

Figure 4.18: Top view of the ADCS flight spare model main board without GPS receiver; the two red plugs provide the interface with the CDHS board. The powerful microcontroller unit is placed in the center of the ADCS board. Interface provisions are three connectors to the magnetorquers (left), the board-to-board connector to the Phoenix GPS receiver (right) and one connector to the master sun sensor (top)

[9] Some microelectronics with space heritage, primarily discrete devices, are manufactured by US suppliers only and are subject to the ITAR. It is not an unusual procedure for foreign spacecraft designers to strictly avoid the use of these components, for which export restrictions may be issued by the President of the United States. For instance, this may force spacecraft equipment developers to avoid the use of MOSFETs in their designs.

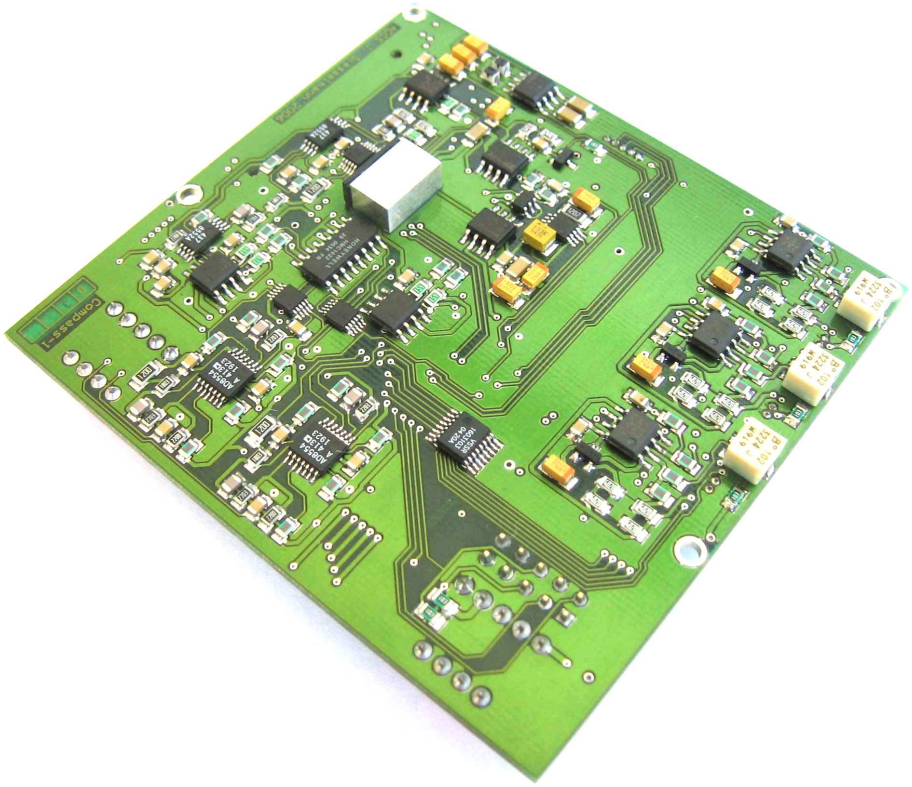

Figure 4.19: Bottom view of the ADCS flight spare model main board with complete component mount. The circuitry on the left is the analog section of the three-axis magnetometer; the three circuits on the right are the coil current drivers.

4.4.2 Reliability

As stated above, appropriate measures must be undertaken, in order to ensure survival of the hardware in the harsh space radiation environment. Low energy radiation is shielded by the aluminium cube hull with 1mm thickness. High energy ion radiation, however, penetrates the panels and may cause one of two basic radiation damage effects: (i) cumulative long-term degradation and (ii) single event effects (SEE). Cumulative degradation typically reveals itself in gradually increased power consumption and reduced performance of analog devices before complete failure. A rough estimate of the total ionization dose (TID) in LEO is app. 1krad/yr; modern microelectronics can survive various sizable levels of TID (Flash: ≈10krad, CMOS: ≈100krad) [43]. SEEs are distinguished as single event upsets (SEU) and single event latch-up (SEL); both constitute serious issues in terms of reliability. SEUs cause bit corruption in code and data memory which results in faulty data and “run-away code”, while SEL denotes the shorting of polarized regions in a semiconductor transistor cell, resulting in excessive current draw until the affected region eventually burns out [42]. In both cases, shielding is a highly inefficient solution to the problem. Components with space heritage employ the concept of fault avoidance in combination with redundancy, and this is, apart from limited redundancy perhaps, not a feasible option for picosatellite development. Here it is more sensible to employ fault tolerance by means of embedded software routines.

On Compass-1 the following measures have been applied in order achieve raised levels of fault tolerance:

- Central and local current monitoring in order to counteract SEL: the EPS monitors the current consumption of each subsystem and forces power-cycling on a subsystem experiencing SEL. In addition, current levels are monitored at several nodes local to the ADCS in order to enable more accurate, local SEL protection; SEL is known to be reversible in many cases if prompt power cycling occurs.

- Watch-dog timers in order to counteract SEU: a watch-dog timer is a free-running timer which must be reset at predetermined points within the software instruction sequence. If these resets do not occur, it is likely that bit-flips due to SEU have changed the object code and the independent watch-dog forces the controller into reset; this reverses the SEU effect, if the bit-flip occurred at a RAM location.

The problems associated with radiation damage, concerning the reliability of the system, are impossible to deny in the context of picosatellites built entirely from COTS material, but perhaps the classical notion of reliability must be reevaluated. Contrary to conventional satellites, picosatellites can be built at a very little cost *because* inexpensive COTS components are employed. Hence, it is reasonable to assume that picosatellites have a much more limited life expectancy, but on the other hand, they are much easier replaced than their conventional heavy-weight counterparts. And the success of the Japanese CubeSats, some of them operational for over 2 years and counting, so far justifies the confidence put into COTS.

4.5 Impact on the System Design

In particular in the context of magnetic control, the attitude control system imposes a few critical design constraints on the overall satellite system. The need for gravity gradient stability has been stated in chapter 2; compliance with this requirement is achieved by careful equipment placement within the cube to yield the desired relationships of the principal moments of inertia.

The same method is employed in order to match the center of gravity with the geometrical center. As will be shown in chapter 7, any remaining offset will increase the system disturbance and result in less accurate pointing.

Certainly the most extensive impact of the attitude control subsystem on the overall system is derived from the need for ‘magnetic cleanliness’, discussed in the following, final section of chapter 4.

4.5.1 Avoiding and Controlling Dipoles

For a magnetically actuated spacecraft like Compass-1 it is important that permanent magnetic field disturbances caused by the spacecraft body and stray fields generated by the electrical currents within the subsystems are minimized. Residual dipoles cause two types of effects: (i) they constitute additional loading on the attitude control system by imposing

magnetic disturbance torques on the spacecraft, and (ii) they lead to magnetic offsets in magnetometer measurements and hence degrade the attitude determination accuracy. During the design of the satellite, the following measures have been undertaken in order to avoid residual dipoles:

- Permanent disturbances have been avoided by carefully selecting the materials used in the construction of the spacecraft, in particular by avoiding iron, nickel and cobalt; only those materials with zero perming properties and a relative magnetic permeability $\mu_r \approx 1$, like aluminium Al 6061-T6, copper, PEEK and PTFE have been admitted. RF shields of COTS products, usually made from inexpensive sheet metals with perming properties, have been replaced with non-magnetic film material and all fasteners are made from non-magnetic stain-less steel. The only magnetizable parts with significant iron content found on Compass-1 are the communication antennae. The necessity for in-orbit deployment demands high elasticity making simple spring steel the obvious choice from a mechanical point of view. Tests on alternative materials with better RF properties, i.e. higher copper content, have been conducted but poor elasticity rendered them useless.

The EPS/TCS, in particular power storage and distribution elements thereof, has been identified as the main contributor to magnetic stray fields owing to the fact that this system is the spacecraft's central source node of electrical power. Battery cells (either primary or secondary) are a common commodity on any CubeSat platform. With the advent of Lithium-Ion or Lithium-Polymer (LiPo) rechargable batteries with paramagnetic lithium electrodes a single major source of stray fields remains in the electromagnetism whenever supply currents are extracted.

- Reduction and cancellation of the stray field can be best achieved in those cases where an even number of cells are combined to form the complete battery pack. Since there are 2 LiPo cells in parallel on Compass-1, cancellation of the stray field is accomplished by combining the cells back-to-back in a pair so that the stray field of one cell effectively opposes that of the other during common charge and discharge.

- The same strategy is applied to the resistive Kapton strip heater (Minco HK913-B), part of the active thermal management carried out by the EPS/TCS, which constitutes a simple current-carrying loop. It has been found that the use of 2 heaters in series with opposing polarity will not only result in parasitic dipole reduction but also in a more adequate heating power dissipation for the given supply voltage of 12V.

- EPS harnesses will at times carry substantial currents; harness twisting is known to counteract the generation of stray fields and alleviate EMC problems. For these reasons twisted-pair crimp-style cables have been used for all dedicated power connections, e.g. the photovoltaic generator harness. Since the power bus supplying the spacecraft subsystems is printed on a circuit board, this option is not available for the power bus.

4.6 Summary

This chapter has discussed the need for active attitude control on a nadir-pointing CubeSat under the supporting stabilizing influence of gravity gradient. Magnetic actuators have been selected for their benefits of hardware simplicity and scalability. The design of the magnetorquers and the DC current source electronics (coil driver) has been presented. Furthermore, the sensor suit for the ADCS has been selected with consideration of weight and size limitations; the magnetometer design has been highlighted and geometrical implications of the sun sensor configuration consisting of five individual sensors have been derived. The design results for the remaining required electronics on the ADCS mainboard have been concisely presented and important design constraints for the entire satellite system, required to enable maximum ADCS performance, have been discussed.

Chapter 5

Attitude Control

In this chapter magnetic control laws for the two control modes, i.e. detumbling and nadir-pointing, will be presented. For the detumbling mode the well-known B-dot controller is derived and a simple filtering method is presented. Nadir stabilization is accomplished by a full state feedback constant gain LQR controller for which relevant theoretical background is presented, including the stability analysis of Floquet theory for linear periodic systems.

5.1 Detumbling Controller

The separation from a launch interface like the standard P-POD and the impulsive deployment of the communication antennae will subject the CubeSat to fairly significant torques which may be regarded as very short term high level disturbance torques that occur only once in the life time of the satellite at the very beginning of the mission. As a result of these torques CubeSats like Compass-1 will experience a tumbling motion; in this context the term tumbling refers to sizable and undesired rotational velocities. Before the sensitive LQR attitude controller can be engaged these uncontrolled body rates must be dissipated. This is accomplished by a distinct control law which uses 3-axis magnetometer information only; this control law is commmonly referred to as the ‘B-dot controller’. It is a simple, reliable and well understood method for gradually decreasing the rotational kintetic energy, or the angular momentum of the spacecraft w.r.t. the magnetic field of the Earth.

The following section derives the detumbling control law starting from the main condition of monotonically decreasing rotational energy, i.e.

$$\frac{dE_{rot}}{dt} = \frac{d}{dt}\left(\frac{1}{2}\omega_b^{bi,T} \cdot I \cdot \omega_b^{bi}\right) < 0 \tag{5.1}$$

Decreasing the rotational energy during detumbling means that the scalar product of the angular velocity and the control torque must be negative

$$\omega_b^{bi,T} \cdot T < 0 \tag{5.2}$$

The control torque from the magnetic interaction of course is

$$T = m \times B \tag{5.3}$$

such that condition (5.2) equivalently means

$$\omega_b^{bi,T} \cdot (m \times B) < 0 \tag{5.4}$$

With the general rules for cross product manipulation

$$\vec{a}^{\,T} \cdot (\vec{b} \times \vec{c}) = \vec{c}^{\,T} \cdot (\vec{a} \times \vec{b})$$

and

$$\vec{a} \times \vec{b} = -(\vec{b} \times \vec{a})$$

condition (5.4) can be rewritten as

$$-\omega_b^{bi,T} (B \times m) < 0 \tag{5.6.a}$$

or

$$m^T \cdot (\omega_b^{bi} \times B) < 0 \tag{5.6.b}$$

This inequality dictates that the magnetic moment needs to have a component which is anti-parallel to the direction of ω x B. Maximum efficiency can be provided by ensuring that the entire vector is anti-parallel. In other words, the inequality can be solved by expanding (5.6.b) with a scalar gain C

$$m = C \cdot (\omega_b^{bi} \times B) \tag{5.7}$$

for which C < 0. With the main assumption of the change of the magnetic field vector being the result of the rotation of the spacecraft only, i.e.

$$\dot{B} \approx \omega_b^{bi} \times B \tag{5.8}$$

eqn. (5.7) finally becomes the B-dot detumbling control law

$$m = C \cdot \dot{B} \tag{5.9}$$

The assumption in (5.8) implies a lower limit to the momentum dumping capability of the B-dot controller. At the beginning of the maneuver the geomagnetic rate of change is small compared to the rotation of the spacecraft; the gradually decreasing rotational energy will eventually lead to a situation where this is no longer true and assumption (5.8) will turn invalid. Theoretically, the detumbling limit is achieved when the spacecraft rotation equals the geomagnetic field rate; in this situation the inertial body rates are $\neq 0$.

5.1.1 State Variable Filter

The detumbling control law in (5.9) requires the rate of change of the geomagnetic field vector. The differentiation of a noisy sensor signal causes numerical problems which is why it is common practice to utilize a first-order state variable filter to estimate the time derivative of *B*.

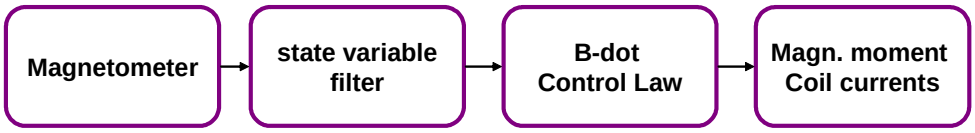

Figure 5.1: flow chart of the Bdot detumbling controller

This filter should possess the important property of filtering only high frequency noise and not affect low frequency inputs. A block diagram of a filter which behaves in that fashion is shown in figure 5.2.

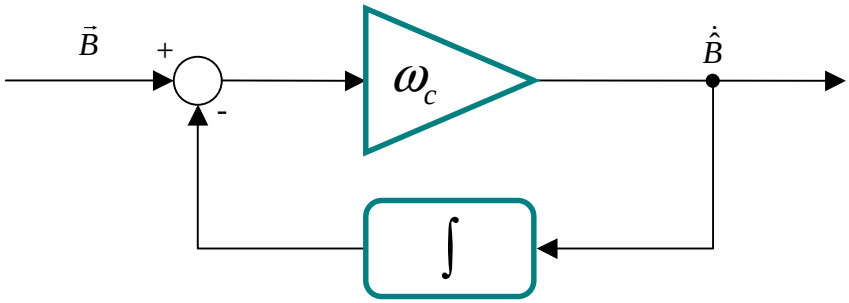

Figure 5.2: first order state variable filter block diagram

From figure 5.2 the following formulation in the Laplace domain can be easily derived

$$\dot{\hat{B}}(s) = \omega_c \cdot \left(\vec{B}(s) - \frac{1}{s} \dot{\hat{B}}(s) \right) \tag{5.10}$$

This directly yields the transfer function

$$H(s) = \frac{\dot{\hat{B}}}{\vec{B}}(s) = \frac{s\omega_c}{s + \omega_c} \tag{5.11}$$

The main property of this transfer function is that for high frequency inputs ($s >> \omega_c$) the filter behaves like a simple gain of value ω_c. For low frequency inputs ($s << \omega_c$) like the measured geomagnetic field waveform the filter is a differentiator in approximation.

The integration indicated in figure 5.2 must be performed numerically using the method of forward Euler integration. It takes the simple form

$$\hat{B}(k+1) = \hat{B}(k) + \dot{\hat{B}}(k) \cdot t_s \tag{5.12}$$

where t_s is the discrete sampling time. The forward Euler method is very simple to implement and yields adequate results in the application of detumbling a spacecraft since neither torques nor the geomagnetic field change rapidly once the satellite is free floating and divergence or time step adjustment issues do not arise. In other words, the linear approximation in between the filter updates holds valid for the duration of the detumbling maneuver.

Algorithmically, figure 5.2 can be translated as

$$e(k) = \vec{B}(k) - \hat{B}(k) \tag{5.13.a}$$

$$\dot{\hat{B}}(k) = \omega_c \cdot e(k) \tag{5.13.b}$$

$$\hat{B}(k+1) = \hat{B}(k) + \dot{\hat{B}}(k) \cdot t_s \tag{5.13.c}$$

which is a discrete representation of (5.11) at time instance k.

5.2 Attitude Controller

As shown above, active magnetic actuators provide an elegant means of dumping angular momentum. Classical satellites use this in the context of detumbling a spacecraft, as above, or in the context of wheel desaturation on three-axis momentum wheel controlled platforms. Another common application is the manipulation of the spin-axis on spin-stabilized satellites. But three-axis control using active magnetorquers only does not appear on classical platforms.

Martel, Pal and Psiaki [45] first examined the approach of using magnetic control for gravity-gradient stabilized spacecraft in 1988; they claimed that gravity gradient stabilization, along with magnetic control could provide three-axis stabilization. In 1989, Musser and Ward [46] were among the first to attempt to use a fully magnetic attitude control system for three-axis stability. They developed linear feedback control laws which use a linear quadratic regulator to obtain the value of the magnetic control torque. Wisniewski [19] developed the idea further in 1996 by using a combination of linear and nonlinear system theory to develop control laws for three-axis stabilization; linear theory was used to obtain both time-varying and constant gain controllers for a satellite with a gravity gradient boom. In addition, he developed a nonlinear controller for a satellite without appendages based on sliding mode control theory. He showed that three-axis control can be achieved with magnetic torquers only, and implemented this idea in the form of a combined active and passive attitude control system on the Danish Ørsted satellite, a 60kg microsatellite equipped with magnetorquers and an 8m deployable gravity gradient boom.

The remainder of this chapter has the objective to derive a LQR control law which is capable of stabilizing the spacecraft attitude into the desired nadir alignment. A more in-depth reference that contains the theory for much of the general material presented here is the text by Anderson and Moore [48], while the text by Kwakernaak and Sivan [49] is considered to be the classic text on the subject of LQR control.

As shown in chapter 2, there exists a homogeneous linear system equation in state space about a nadir-pointing equilibrium attitude at rest. When the system is expanded by control action and system noise in the form of unmodeled disturbance torques is neglected, the system under control has the following general time-varying linear form

$$\begin{aligned} \dot{x}(t) &= F(t)x(t) + G(t)\cdot m(t) \\ x(t) &= \begin{bmatrix} \delta q^{bo} \\ \delta \dot{q}^{bo} \end{bmatrix} \end{aligned} \tag{5.14}$$

where **F** is the 6x6 system matrix as in (2.70), **G** is the 6x3 control input matrix, sometimes referred to as the control effectiveness matrix, *m* is the control input vector $\in \nabla^3$ and *x* is the state vector $\in \nabla^6$, containing the vector components of the attitude quaternion and their rates of change, consistent with (2.70).

The cross product in (5.3) renders the control action non-linear. Linearization of the control input matrix about the equilibrium attitude is accomplished as follows: the general formulation of the control torque is

$$ {}^{c}T_{c} = {}^{c}m \times {}^{c}B = {}^{c}m \times (R^{co} \cdot {}^{o}B) \tag{5.15} $$

Substituting (2.56) into (5.15) yields

$$ {}^{c}T_{c} \approx \begin{bmatrix} 0 & -{}^{c}m_3 & {}^{c}m_2 \\ {}^{c}m_3 & 0 & -{}^{c}m_1 \\ -{}^{c}m_2 & {}^{c}m_1 & 0 \end{bmatrix} \cdot \begin{pmatrix} {}^{o}B_1 + 2{}^{o}B_2 \delta q_3^{co} - 2{}^{o}B_3 \delta q_2^{co} \\ -2{}^{o}B_1 \delta q_3^{co} + {}^{o}B_2 + 2{}^{o}B_3 \delta q_1^{co} \\ 2{}^{o}B_1 \delta q_2^{co} - 2{}^{o}B_2 \delta q_1^{co} + {}^{o}B_3 \end{pmatrix} $$

$$ \approx {}^{c}m \times {}^{o}B - 2{}^{c}m \times (\delta q^{co} \times {}^{o}B) \tag{5.16} $$

The second term of equation (5.16) is a term of second order, which must be abandoned for linearization purposes. With this simplification the control torque in the control frame simply becomes the cross product of the control dipole moment and the magnetic field vector in the orbit frame

$$ {}^{c}T_{c} \approx {}^{c}m \times {}^{o}B \tag{5.17} $$

As such, equation (5.17) simply enforces the previously applied equilibrium constraint: the control frame must coincide with the orbit frame.

Hence, the control torque portion of equation (2.48) can be written as

$$ {}^{c}I^{-1} \cdot {}^{c}T_{c} \approx {}^{c}I^{-1} \cdot {}^{c}m \times {}^{o}B \tag{5.18} $$

Augmenting (2.68) by (5.18) yields the simple control input matrix [44]

$$ G' = \begin{bmatrix} \begin{bmatrix} 0 & 0 & 0 \\ 0 & 0 & 0 \\ 0 & 0 & 0 \end{bmatrix} \\ \frac{{}^{c}I^{-1}}{2} \cdot \begin{bmatrix} 0 & {}^{o}b_3 & -{}^{o}b_2 \\ -{}^{o}b_3 & 0 & {}^{o}b_1 \\ {}^{o}b_2 & -{}^{o}b_1 & 0 \end{bmatrix} \end{bmatrix} \tag{5.19} $$

5.2.1 Fundamental Underactuation

Revisiting the cross product in the main equation (5.3) it transpires that the torque generation capability of magnetic actuation has one distinct draw-back: control torques are always perpendicular to both the magnetic moment and the geomagnetic field, i.e. the angular momentum in the direction of the field vector can not be controlled. For that reason purely magnetically actuated spacecraft are said to be fundamentally underactuated. This could be deemed a prohibitive problem, but due to the strong dipole characteristic of the Earth's main field the axis of underactuation rotates as the spacecraft travels along its orbit if a high magnetic inclination is assumed. On such orbits the field vector rotates twice w.r.t. the inertial frame and once within the orbit frame. Hence the direction of underactuation is in constant motion and, over a period of time, all rotational degrees of freedom may be manipulated, even though, at one single instance in time, the system is strictly speaking not controllable in the direction of the geomagnetic field.

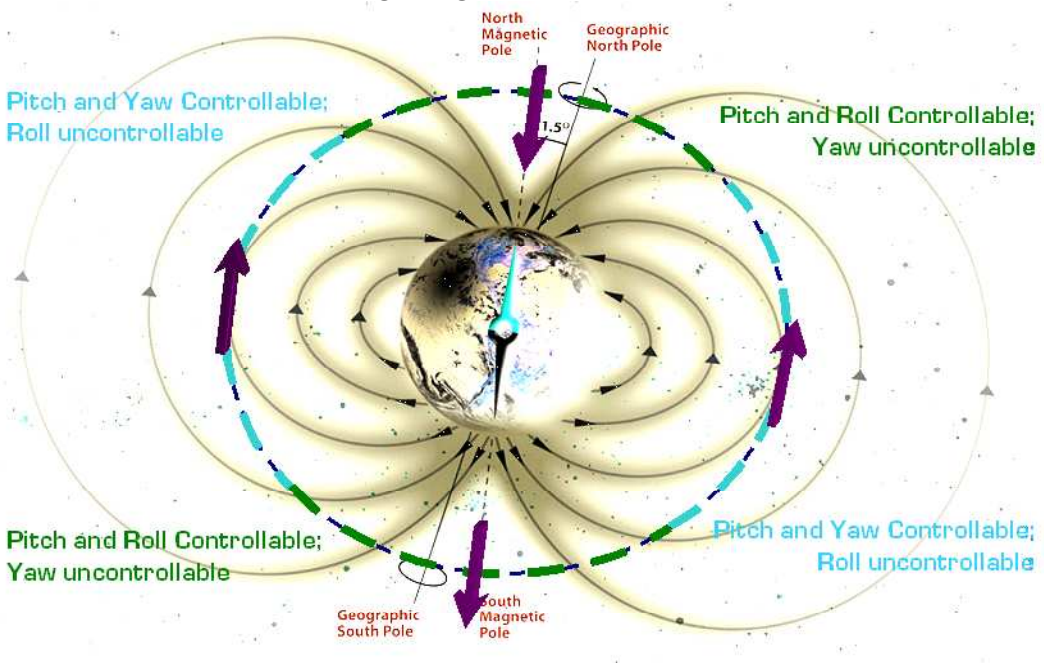

Figure 5.3: Fundamental underactuation: not all degrees of freedom may be manipulated at an instance in time but over a period of time controllability is given.

Figure 5.3 shows the simplified implications of the fundamental underactuation of magnetically actuated spacecraft. If the spacecraft is deemed to maintain an ideal nadir-pointing attitude in addition to the b_2 vector being aligned with $\hat{o}_2$, then the degrees of freedom are of course the 3 body rotational variables roll, pitch and yaw. In the equatorial regions of the magnetosphere the geomagnetic field is then aligned with the roll axis, leaving angular momentum in the same uncontrollable. Similarly, the yaw axis is uncontrollable for regions in which the geomagnetic field is parallel to the yaw axis, i.e. at the magnetic poles. In between these regions, the underactuated axis is less intuitive, as intermediate axes are uncontrollable. The rest of the chapter accounts for the fundamental underactuation, not eliminating it, in an elegant way in order to achieve higher power efficiency of the control law. This method has been first introduced by Wisniewski in [19].

5.2.2 Control Input Matrix

To accomplish this power optimality, the magnetic moment vector shall be mapped onto the manifold perpendicular to the geomagnetic field vector to form a new and unconstrained control signal *u*.

$$ {}^{c}u \mapsto {}^{c}m : {}^{c}m = \frac{{}^{c}u \times {}^{o}B}{\|B\|} \tag{5.20} $$

This is motivated by the fact that the component of the magnetic dipole moment *m* parallel to the geomagnetic flux does not contribute to the control torque because

$$ \mathrm{T} = \left(\mathrm{m}_{||} + \mathrm{m}_{\perp} \right) \times \mathrm{B} = \mathrm{m}_{\perp} \times \mathrm{B} \tag{5.21} $$

The only difference to the control input matrix in (5.19) is that the cross-product in the control torque is substituted with the double-cross-product.

$$ {}^{c}T_{c} \approx ({}^{c}u \times {}^{o}B) \times {}^{o}B \tag{5.22} $$

Applying the general rule of anti-commutativity of cross products and (AxB)xC = B(C·A) - A(C·B) the double-cross-product formulation of equation (5.22) directly translates into a new power-efficient control input matrix **G**. Since torques only affect the angular acceleration (lower half of the state vector) and the algebraic dimensions must be consistent, **G** must be augmented by a zero matrix as already done in (5.19).

$$ G = \begin{bmatrix} \begin{bmatrix} 0 & 0 & 0 \\ 0 & 0 & 0 \\ 0 & 0 & 0 \end{bmatrix} \\ \frac{{}^{c}I^{-1}}{2} \cdot \begin{bmatrix} -{}^{o}b_3^2 - {}^{o}b_2^2 & {}^{o}b_1 \cdot {}^{o}b_2 & {}^{o}b_1 \cdot {}^{o}b_3 \\ {}^{o}b_1 \cdot {}^{o}b_2 & -{}^{o}b_3^2 - {}^{o}b_1^2 & {}^{o}b_3 \cdot {}^{o}b_2 \\ {}^{o}b_1 \cdot {}^{o}b_3 & {}^{o}b_3 \cdot {}^{o}b_2 & -{}^{o}b_2^2 - {}^{o}b_1^2 \end{bmatrix} \end{bmatrix} \tag{5.23} $$

In contrast to the system matrix **F**, the control input matrix **G** is time-varying, due to the variability of the magnetic flux density *B* in the body frame. As long as the satellite maintains its nominal nadir-pointing attitude, i.e. the body frame is aligned with the orbit frame, the time-dependency of the geomagnetic field is nearly periodic. Deviations from perfect periodicity mainly result from the rotation of the Earth underneath the spacecraft orbit.

A perfectly periodic model of the magnetic field assuming a non-eccentric dipole field, no rotation and zero orbit eccentricity may be expressed as [44]

$$^{o}\vec{B}(t) = \frac{M}{R^3}\begin{bmatrix} \cos\omega_0 t \cdot \sin i_m \\ -\cos i_m \\ 2\sin\omega_0 t \sin i_m \end{bmatrix} \tag{5.24}$$

where i_m is the inclination of the orbit w.r.t. the magnetic equator, M is the Earth's magnetic dipole moment and t = 0 occurs at the ascending node crossing of the magnetic equator. Hence, the control input matrix ***G*** may be considered as of a periodic nature.

$$G(t) = G(t+T) \tag{5.25}$$

Time-invariance may be forced on the model description by averaging the periodic control input matrix.

$$\overline{G} = \frac{1}{T}\int_0^T G(t)dt \tag{5.26}$$

5.2.3 Linear Quadratic Regulation

A constant gain linear quadratic regulator (LQR) approach is applied to develop a stabilizing control law for the linear time-invariant system. The problem is stated as finding a full-state feedback (FSF) control law which minimises an infinite linear quadratic cost functional J

$$J = \int_0^\infty u^T(t)\cdot R\cdot u(t) + x^T(t)\cdot Q\cdot x(t)\cdot dt \tag{5.27}$$

where the weighting matrices ***Q*** and ***R*** are positive semidefinite and positive definite, respectively, subject to the state dynamics

$$\dot{x}(t) = F\cdot x(t) + \overline{G}\cdot u(t) \text{ and } x(0) = x_0 \tag{5.28}$$

The LQR problem statement and cost can be interpreted in the following manner: Suppose that the system is initally excited, and that the net result of this excitation is reflected in the initial state vector x_0 as an undesirable deviation from the equilibrium attitude. Given these deviations, the objective of the control can essentially be viewed as selecting a control input vector *u* that regulates the state vector back to its equilibrium as quickly as possible. If the system was fully controllable and time-invariant then it would be possible to drive the state *x*(t) to zero in an arbitrarily short period of time. This would require very large control signals in the form of magnetorquer currents which, from an engineering point of view, are unacceptable. Hence, it is clear that there must be a balance between the desire to regulate state perturbations to the equilibrium and the magnitude of the control signal needed to do

so. Minimizing the quadratic cost functional is one way to quantify this balance. Note that the quadratic nature of both terms in the cost

$$\left.\begin{aligned} u^T(t)\cdot R\cdot u(t) > 0 \\ x^T(t)\cdot Q\cdot x(t) \geq 0 \end{aligned}\right\} \text{ for u(t), } x(t) \neq 0 \tag{5.29}$$

ensures that they will be non-negative for all times t. The second term in (5.27) generates a penalty in the cost when the states that are to be kept small, are different from their desired equilibrium value of zero. Hence, the selection of **Q** defines which errors are bothersome and to which degree they are so. More general definitions of the cost functional exist but the definition in (5.27) is sufficient for the problem at hand.

It can be shown that the solution to the above problem statement is a control law of the simple form

$$u = -K\cdot x \tag{5.30}$$

or, with $R = E$ without loss of generality

$$u = -\overline{G}^T\cdot P\cdot x \tag{5.31}$$

P is the unique, symmetric, positive semidefinite steady-state solution to the algebraic Riccati equation (ARE)

$$P\cdot F + F^T\cdot P - P\cdot\overline{G}\cdot\overline{G}^T\cdot P + Q = 0 \tag{5.32}$$

The linear time-variant system under negative feedback control then has the well-known form depicted in figure 5.4.

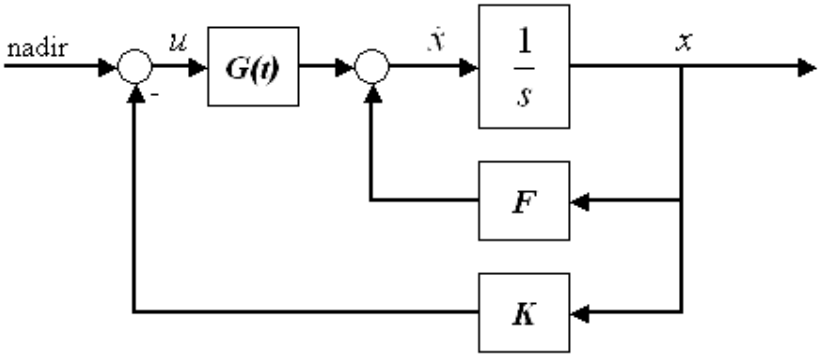

Figure 5.4: Diagram of the constant gain negative FSF LQR control loop for a linear system with periodic coefficient in G

For linear constant-coefficient dynamic systems the LQR control law has some remarkable properties. Although this type of control is complicated by the fact that full state knowledge is required for feedback the constant gain LQR is a simple and compact controller which provides uniquely optimal system response irrespective of the initial condition x_0. Furthermore, the LQR is also always guarranteed to be asymptotically stable for this class of systems [47].

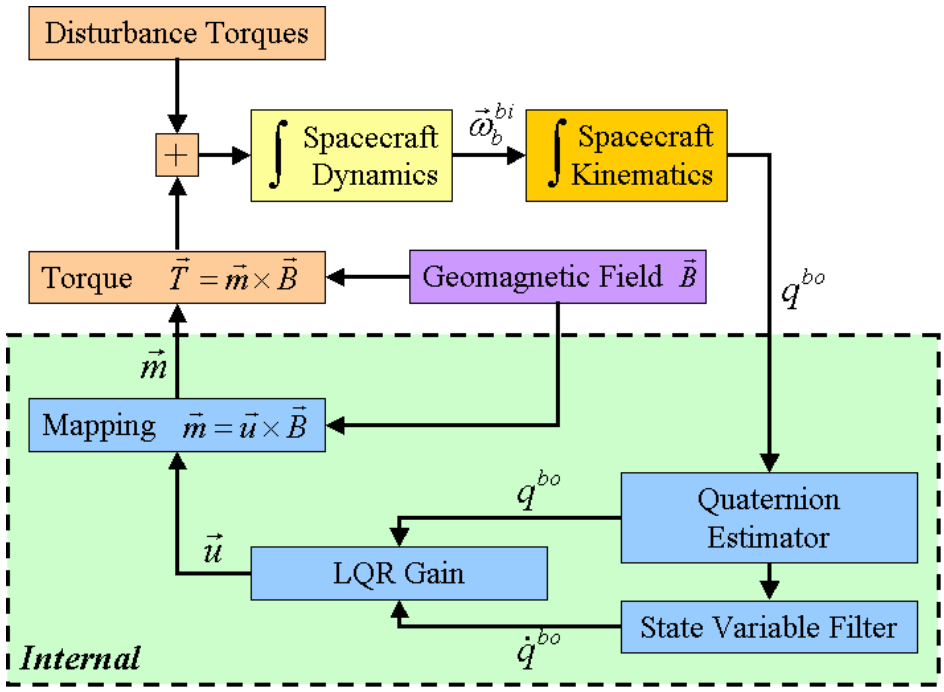

Figure 5.5: Diagram of the constant gain negative FSF LQR control loop for the non-linear dynamic system; the mapping function is applied to result in higher control efficiency.

5.2.4 Stability Analysis

Although the constant gain LQR always guarrantees closed-loop stability for constant linear systems, it does not do so for periodic linear systems. Periodic linear systems are rich of well-studied structure and closed-form theories exist for their analysis. One of the significant theories with direct application for the magnetic attitude control problem is the theory of Floquet for linear differential equations with periodic coefficients. The key result of the theory is that a linear periodic closed-loop system is asymtotically stable only if its complex characteristic multipliers belong to the open unit disk [50].

Consider a closed-loop system with periodic gain of the following form

$$\begin{aligned} \dot{x}(t) &= A_c(t) \cdot x(t) \\ A_c(t) &= F - G(t) \cdot K = A_c(t+T) \end{aligned} \tag{5.33}$$

A state transition matrix Φ relates the state vectors in time starting from an initial condition x_0 at time t_0.

$$\begin{aligned} x(t) &= \Phi(t, t_0) \cdot x(t_0) \\ x(t_0) &= x_0 \end{aligned} \tag{5.34}$$

and obeys the identities

$$\Phi^{-1}(t, t_0) = \Phi(t_0, t) \tag{5.35.a}$$

$$\Phi(t_2, t_0) = \Phi(t_2, t_1) \cdot \Phi(t_1, t_0) \tag{5.35.b}$$

$$\Phi(t_0, t_0) = E \tag{5.35.c}$$

It is useful to define an algebraic differential equation which describes the time propagation of Φ

$$\dot{x}(t) = A_c(t) \cdot \Phi(t, t_0) \cdot x_0 \tag{5.36.a}$$

$$\dot{x}(t) = \dot{\Phi}(t, t_0) \cdot x_0 \tag{5.36.b}$$

$$\dot{\Phi}(t, t_0) = A_c(t) \cdot \Phi(t, t_0) \tag{5.36.c}$$

Assume

$$\Phi(t+T, t_0) = \Phi(t, t_0) \cdot C \tag{5.37}$$

where **C** is a constant matrix. The equality in (5.37) can be shown to be valid by considering its first derivative:

$$\begin{aligned} \dot{\Phi}(t+T, t_0) &= \dot{\Phi}(t, t_0) \cdot C \\ \dot{\Phi}(t+T, t_0) &= A_c(t) \cdot \Phi(t, t_0) \cdot C \\ \dot{\Phi}(t+T, t_0) &= A_c(t+T) \cdot \Phi(t+T, t_0) \end{aligned} \tag{5.38}$$

There exists a constant matrix **R** such that

$$C \equiv e^{RT} \tag{5.39}$$

With (5.37) and (5.35.c) it follows that

$$\Phi(t_0 + T, t_0) = e^{RT} = \Psi(t_0) \tag{5.40}$$

Eqn. (5.40) shows that the state transition matrix consists of a periodically modulated exponential function. One of the fundamental results of Floquet Theory is that a linear periodic system is asymptotically stable if, and only if the *monodromy matrix* at t_0 $\mathbf{\Psi}(t_0)$ is Schur, i.e. all eigenvalues of $\mathbf{\Psi}(t_0)$, referred to as *characteristic multipliers* of $\mathbf{A_c}(t)$, belong to the open unit disk, i.e. have magnitudes less than one.

$$\begin{aligned} \det\left[E\lambda - \Psi(t_0)\right] &= 0 \\ \left|\lambda_i\right| &< 1 \end{aligned} \tag{5.41.a}$$

Alternatively it can be checked if the matrix **R** is Hurwitz, i.e. all eigenvalues of **R,** referred to as *characteristic exponents* of $\mathbf{A_c}(t)$, have only negative real parts.

$$\begin{aligned} \det\left[E\varphi - R\right] &= 0 \\ \mathrm{Re}(\varphi_i) &< 0 \end{aligned} \tag{5.41.b}$$

5.2.5 Controller Synthesis

Calculation of the Averaged Control Input Matrix

Although it is possible to numerically integrate the control input matrix in (5.23) in order to find the solution to (5.26), an analytical approach seems more sensible, recalling that a direct periodic formulation for the geomagnetic field components in $F_o \approx F_b$ exists. This analytical approach facilitates a significantly simplified controller synthesis for systems on low eccentricity orbits and is an original contribution of this thesis. Analytical integration of the periodic elements of the control input matrix in (5.23) yields to following set of solutions:

The off-diagonal integrals over one period are

$$\begin{aligned} \int_0^T b_1 b_2 dt &= -\frac{M^2}{R^6}\cos i_m \sin i_m \int_0^T \cos(\omega_0 t)dt \\ &= -\frac{M^2}{R^6}\cos i_m \sin i_m \cdot \frac{1}{\omega_0}\sin(\omega_0 t)\Big|_0^T \\ &= 0 \end{aligned} \tag{5.42.a}$$

$$\begin{aligned} \int_0^T b_1 b_3 dt &= 2\frac{M^2}{R^6}\sin^2 i_m \int_0^T \cos(\omega_0 t)\sin(\omega_0 t)dt \\ &= 2\frac{M^2}{R^6}\sin^2 i_m \cdot \frac{1}{2\omega_0}\sin^2(\omega_0 t)\Big|_0^T \\ &= 0 \end{aligned} \tag{5.42.b}$$

$$\begin{aligned}\int_0^T b_2 b_3 dt &= -2\frac{M^2}{R^6}\cos i_m \sin i_m \int_0^T \sin(\omega_0 t)dt \\ &= 2\frac{M^2}{R^6}\cos i_m \sin i_m \cdot \frac{1}{\omega_0}\cos(\omega_0 t)\Big|_0^T \\ &= 0\end{aligned} \tag{5.42.c}$$

and the diagonal integrals over one period are

$$\begin{aligned}\int_0^T -b_3^2 - b_2^2 dt &= -\frac{M^2}{R^6}\cdot\left(4\sin^2 i_m \cdot \int_0^T \sin^2(\omega_0 t)dt + \cos^2 i_m \cdot \int_0^T dt\right) \\ &= -\frac{M^2}{R^6} T \cdot \left(1+\sin^2 i_m\right)\end{aligned} \tag{5.42.d}$$

$$\begin{aligned}\int_0^T -b_3^2 - b_1^2 dt &= -\frac{M^2}{R^6}\sin^2 i_m \cdot \left(4\int_0^T \sin^2(\omega_0 t)dt + \int_0^T \cos^2(\omega_0 t)dt\right) \\ &= -\frac{5M^2}{2R^6} T \cdot \sin^2 i_m\end{aligned} \tag{5.42.e}$$

$$\begin{aligned}\int_0^T -b_2^2 - b_1^2 dt &= -\frac{M^2}{R^6}\cdot\left(\cos^2 i_m \cdot \int_0^T dt + \sin^2 i_m \cdot \int_0^T \cos^2(\omega_0 t)dt\right) \\ &= -\frac{M^2}{R^6} T \cdot \left(1-\frac{1}{2}\sin^2 i_m\right)\end{aligned} \tag{5.42.f}$$

Hence, the control input matrix is always diagonal and negative definite. For circular orbits, very good agreement between the analytical integration over one orbit and numerical integration over several orbits accounting for the rotation of the geomagnetic field with a period of one sidereal[10] day has been observed.

[10] A sidereal day is the true rotation period of the Earth (23.9344696h). The obvious discrepancy to the 24h day (called solar day) is due to the progression of the Earth on its orbit around the sun: in order for the sun to cross equal longitudes, the Earth needs to rotate slightly more than once, resulting in the slightly longer solar day.

Selection of the Weighting Matrix Q

The synthesis of a stable LQR gain also requires the selection of an appropriate weighting matrix Q. [21] proposes a nested unconstrained optimization algorithm that locally minimizes the cost function

$$f(x) = \max\left|eig(\Psi(t_0))\right| \tag{5.43}$$

by varying 6 dominant elements of the 6x6 matrix **P**.

A simpler method is proposed by [17] which defines the weighting matrix **Q** as a heuristic function of a scalar tuning variable q according to

$$Q = \begin{bmatrix} qk_1E & 0 \\ 0 & qk_2E \end{bmatrix}^T \cdot \begin{bmatrix} 0.5E & 0.5E \\ 0.5E & 0.5E \end{bmatrix} \cdot \begin{bmatrix} qk_1E & 0 \\ 0 & qk_2E \end{bmatrix} \tag{5.44.a}$$

The weighting matrix in (5.44.a) is then of the form

$$Q = 0.5 \cdot q^2 \cdot \begin{bmatrix} k_1^2 & 0 & 0 & k_1k_2 & 0 & 0 \\ 0 & k_1^2 & 0 & 0 & k_1k_2 & 0 \\ 0 & 0 & k_1^2 & 0 & 0 & k_1k_2 \\ k_1k_2 & 0 & 0 & k_2^2 & 0 & 0 \\ 0 & k_1k_2 & 0 & 0 & k_2^2 & 0 \\ 0 & 0 & k_1k_2 & 0 & 0 & k_2^2 \end{bmatrix} \tag{5.44.b}$$

Recalling the LQR cost functional (5.27) it becomes apparent that the constant parameter k_1^2 penalizes deviations in the quaternion vector, the constant parameter k_2^2 penalizes deviations in the quaternion vector rates and the parameter product $k_1 \cdot k_2$ finally penalizes the scalar combination of the quaternion and the quaternion rates. In accordance with [17] the weighting parameters have been heuristically set to $k_1 = 0.001$ and $k_2 = 0.00001$.

With the corresponding steady-state solution to the algebraic Riccati equation **P**, the LQR gain is then of the form

$$K = \begin{bmatrix} K_{1,1} & 0 & K_{1,3} & K_{1,4} & 0 & K_{41,6} \\ 0 & K_{2,2} & 0 & 0 & K_{2,5} & 0 \\ K_{3,1} & 0 & K_{3,3} & K_{3,4} & 0 & K_{3,6} \end{bmatrix} \tag{5.45}$$

5.2.6 Summary of the Design Process

The procedure for synthesising a stabilizing LQR controller for magnetically actuates spacecraft can be summarized as follows:

1. Calculate the plant system matrix **F**
2. Calculate the average control input matrix $\overline{G}$
3. Select tuning variable q
4. Calculate weighting matrix **Q**
5. Calculate the steady-state solution of the algebraic Riccati equation **P**
6. Calculate LQR gain **K**
7. Integrate the state-transition matrix over one period to find the monodromy matrix, i.e.

$$\Psi(t_0) = \int_0^T \dot{\Phi}(t, t_0) \cdot dt = \int_0^T \left(F - G(t) \cdot K\right) \cdot \Phi(t, t_0) \cdot dt$$

with the initial condition $\Phi(t_0, t_0) = E$

8. Verifiy that all characteristic multipliers belong to the open unit disk
9. Test LQR controller on a non-linear attitude dynamics model.

5.3 Summary

In this chapter the control law for magnetic detumbling and attitude stabilization have been presented. Detumbling is achieved by a Bdot controller, augmented by a discrete first-order state variable filter and nadir-pointing is achieved by an adaptation of the full state feedback constant gain linear quadratic regulator for the magnetic attitude control problem. The control law takes into account the problem of fundamental underactuation and introduces a mapping function in order to achieve higher efficiency. The magnetically actuated system is of a periodic nature and the results of Floquet theory have been presented in order to validate the stability of the synthesised controller under linearity assumptions.

Chapter 6

Attitude Estimation

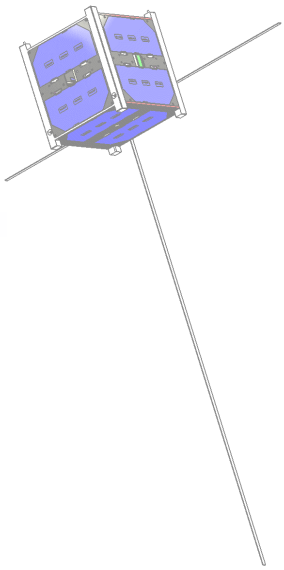

Since the LQR attitude controller requires full-state feedback, the entire attitude state needs to be synthesised by an adequate estimation technique. Compass-1 utilizes two different types of vector reference sensors in order to determine the spacecraft's orientation in space. These sensors are sun sensors and a three-axis magnetometer. A total of 5 sun sensors provide a unit sun vector, expressed in the body reference frame. The vector magnetometer returns a vector measurement of the Earth's magnetic field in a magnetometer reference frame which is also aligned with the body frame.

Determining the attitude of a satellite is equivalent to determining the rotation matrix describing the spacecraft body frame with respect to a known reference frame. Although this matrix contains 9 numbers in the three dimensional case, the attitude of the spacecraft is really defined by a minimum of three independent parameters. Since each normalized vector contains two independent pieces of information the attitude determination problem is fundamentally either under- or overdetermined when reference sensors are used; a single vector provides too little information, while a set of two vectors provide too much information. This makes any attempt to measure the attitude of a spacecraft a problem of estimation.

From the computational point of view attitude estimation is a very expensive process; In view of the limited processing recources (16bit accumulators and 32kB RAM) this highlights the need to simplifiy the process and to utilize an efficient estimator kernel. Principally, there are two types of attitude determination methods: (i) deterministic or static attitude determination and (ii) dynamic attitude determination. While the deterministic determination uses information from measurements and computation in a single instance of time only, the dynamic estimation, most notably the so-called Kalman filter in all its different appearances [51], uses present as well as past measurements to minimize an error covariance which is obtained by prediction of the dynamic state of the satellite. Kalman filters are complex algorithms which require significant amounts of memory and computing power. Neither is present on the flight processor of the presented attitude control system. Hence, static attitude estimation based on the least-squares approach is implemented on Compass-1.

The following chapter presents the QUEST algorithm as the estimation kernel and the simplifications made to the generation of the estimator input. Yet, with all the efforts made to simplify the process, the attitude estimator of the attitude control system remains the most intensive single algorithmic thread on the entire Compass-1 spacecraft.

6.1 Earth-Centred Reference Systems

A set of relevant spacecraft-centred reference systems has already been introduced in chapter 2; for the purpose of attitude determination, 2 additional reference systems, centred in the Earth's centroid, are useful.

Inertial Frame (ECI)

The ECI Frame $F_{\mathrm{ECI}} = \{\hat{\imath}_{\mathrm{ECI}}, \hat{\jmath}_{\mathrm{ECI}}, \hat{k}_{\mathrm{ECI}}\}$ is a (quasi-) inertial frame originating in the Earth's center-of-mass. It is identical in all aspects to the inertial body-centered frame described in chapter 2, except for its different origin definition. The axis labels are: $\hat{\imath}_{\mathrm{ECI}}$ points towards the vernal equinox ♈, $\hat{k}_{\mathrm{ECI}}$ points towards the (geographic) north pole and $\hat{\jmath}_{\mathrm{ECI}}$ completes the system in a right-hand sense. The ECI frame is predominantly used in its cartesian form: nearly every orbit propagation routine outputs the translational state vector in the cartesian ECI frame. Not only the spacecraft position is naturally given in the ECI frame, but also other body positions, like that of the sun or the moon.

Note that the vernal equinox is subject to the precession of the equinoxes due to dominant pertubations by the sun and the moon. The vernal equinox moves at a slow but noticeable rate of about 50 arcseconds per year. In addition, the spin axis of the Earth is subject to nutation, which also disturbs the definition of the inertial frame. Astronomers keep track of this motion and release a new definition of the inertial reference system in a regular time interval. Since the rate of change is small, an update period of 50 years is sufficient. The most recent update has been released in *epoch* 2000, the next is expected for 2050.

Earth-Fixed Frame (ECEF)

The ECI frame described above is inertial, i.e. the Earth rotates within the ECI frame with a period of 1 sidereal day. For attitude determination with a magnetometer backbone it is desirable to resolve the position of a spacecraft in a frame that is fixed to the rotation of the Earth. This frame is called Earth-Centered Earth-Fixed (ECEF) frame $F_{\mathrm{ECEF}} = \{\hat{\imath}_{\mathrm{ECEF}}, \hat{\jmath}_{\mathrm{ECEF}}, \hat{k}_{\mathrm{ECEF}}\}$ sometimes referred to as ECF. Often, the ECEF frame is used as a spherical reference, making it the only frame with predominantly spherical usage. The position of an object in this frame is parameterized by two angles and a distance from the origin. The angles are the well-known latitude λ and longitude ϕ, and the distance from the origin is referred to as the range R. The $\hat{k}_{\mathrm{ECEF}}$ axis points from the Earth's centroid to the geographic north pole. The $\hat{\imath}_{\mathrm{ECEF}}$ axis runs through the intersection of the *prime meridian* with the equatorial plane. The prime meridian is historically defined as the meridian which runs through the site of the Bristish Royal Astronomical Observatory in Greenwich near London. It is therefore also known as the *Greenwich Meridian.* The $\hat{\jmath}_{\mathrm{ECEF}}$ axis is chosen such that a right-hand orthogonal reference frame is formed.
The ECEF plays an important role whenever it is required to relate the position of the spacecraft (in the inertial frame) to an entity which is fixed to the rotation of the Earth.

Examples are spacecraft groundtracks, groundstation coverage conditions (since the groundstation moves with the Earth) and the evaluation of the geomagnetic field vector at a given position (since the geomagnetic potential field is of course fixed to the body of the Earth).

6.2 QUEST Attitude Determination

The basic attitude estimation problem that needs to be solved is to find the rotation matrix (or any other means of attitude parameterization) which transforms the reference vectors given in the reference coordinate system, i.e. the orbit frame, into the measurement vectors measured in the body frame. Mathematically that is

$$\hat{s}_b = R^{bo} \cdot \hat{s}_o \quad \text{and} \qquad \hat{B}_b = R^{bo} \cdot \hat{B}_o \tag{6.1.a,b}$$

for the sun vector and the magnetic field vector, respectively. If these measured vectors, and their modeled reference counterparts, are the only available attitude information, then it is possible to simply construct two right-handed orthonormal frames and calculate the rotation matrix directly by multiplication of the resulting direction cosine matrices (DCM), numerically taking advantage of the fact that any DCM is algebraically orthogonal. This simple algebraic method is commonly referred to as the TRIAD method and constitutes the simplest of all determination techniques. The method works by mathematically discarding one of the 4 given pieces of information, such that the problem can consequently be solved in closed form. An additional noteworthy feature of this method is the fact that the TRIAD algorithm inherently assumes one measurement vector to be more accurate than the other [54].

If the number of observations[11] N is larger than or equal to 2,

$$v_{kb} = R^{bo} \cdot v_{ko} \ , \qquad \text{k = 1, .., N} \tag{6.2}$$

then a method would be interesting that combines all available attitude information into one single, hopefully more accurate estimate. Such methods do exist; these deterministic techniques are called statistical methods, since they all try to minimize the error of an estimate in a statistical sense. This least-square problem can be formulated as: find a matrix R^{bo} which minimizes a loss function J

$$J(R^{bo}) = \frac{1}{2} \cdot \sum_{k=1}^{N} w_k \cdot \left(v_{kb} - R^{bo} v_{ko} \right)^2 \tag{6.3}$$

This function is a weighted sum of all “errors”, irrespective of their sign, between the measurement in the body frame and the corresponding reference vector, transformed from the orbit into the body frame by the sought-after rotation matrix R^{bo}. This type of minimization problem is more formally known as Wahba’s problem [53]. Note that if all measurements were perfect, *J* would be zero.

[11] In this context, an observation is a vector pair containing one measurement and one computed reference.

Minimization of J means to solve for the necessary condition. In order to avoid incorporating the quaternion constraint at this point, it is advantageous to think of the state vector *x* as the three euler angles φ, θ and ψ (roll, pitch and yaw) or x_1, x_2 and x_3.

$$F(x) = J'(R^{bo}(x)) = 0 \tag{6.4}$$

This can be done iteratively using the well-known Newton method from an initial guess x_0 until the iteration residuals drop below a defined abort threshold.

$$x_{n+1} = x_n - \left[\frac{\partial F}{\partial x}(x_n)\right]^{-1} \cdot F(x_n) \tag{6.5}$$

with

$$F = \frac{\partial J}{\partial x} = \left[\frac{\partial J}{\partial x_1}\frac{\partial J}{\partial x_2}\frac{\partial J}{\partial x_3}\right]^T \quad \text{and} \quad \frac{\partial F}{\partial x} = \begin{bmatrix} \frac{\partial^2 F}{\partial x_1^2} & \frac{\partial^2 F}{\partial x_1 \partial x_2} & \frac{\partial^2 F}{\partial x_1 \partial x_3} \\ \frac{\partial^2 F}{\partial x_2 \partial x_1} & \frac{\partial^2 F}{\partial x_2^2} & \frac{\partial^2 F}{\partial x_2 \partial x_3} \\ \frac{\partial^2 F}{\partial x_3 \partial x_1} & \frac{\partial^2 F}{\partial x_3 \partial x_2} & \frac{\partial^2 F}{\partial x_3^2} \end{bmatrix} \tag{6.6.a,b}$$

Note that the Jacobian in (6.6.b) is a symmetrical matrix. In practice, (6.6.a) and (6.6.b) must be evaluated by using the finite difference scheme for all *x*. (6.7.a) and (6.7.b) show examples for partial derivatives in x_1 and x_2, respectively.

$$\frac{\partial J}{\partial x_1} \approx \frac{J(x_1 + \delta x_1, x_2, x_3) - J(x_1, x_2, x_3)}{\delta x_1} \tag{6.7.a}$$

$$\frac{\partial^2 J}{\partial x_1 x_2} \approx \frac{\frac{\partial J}{\partial x_1}(x_1, x_2 + \delta x_2, x_3) - \frac{\partial J}{\partial x_1}(x_1, x_2, x_3)}{\delta x_2} \tag{6.7.b}$$

This iterative method is computationally very demanding, since all evaluations ought to be repeated for each iteration. The computational demand could be decreased by evaluating the Jacobian once and keeping it constant for all following iterations, but convergence may be poor. Overall, this direct method, although extremely useful for a variety of nonlinear problems cannot be deemed an efficient approach to the problem of spacecraft attitude determination.

Fortunately, there exists an analytical method for the specific nonlinear problem at hand which leads to an attitude estimate in the form of an attitude quaternion in a much more efficient way. This method is called QUEST (***qu****aternion* ***est****imator*) and is largely based on the q-method, with the very convenient modification of avoiding a computationally expensive direct solution of an eigenvalue problem [52]. Instead, the QUEST algorithm uses a cleverly constructed approximated solution which leads to estimation accuracies that are comparable with the accuracies of the q-method, at a much lower numerical expense.

The loss function in (6.3) can be expanded as follows

$$\begin{aligned} J &= \frac{1}{2} \cdot \sum w_k (v_{kb} - R^{bo} v_{ko})^T (v_{kb} - R^{bo} v_{ko}) \\ &= \frac{1}{2} \cdot \sum w_k (v_{kb}^T v_{kb} + v_{ko}^T v_{ko} - 2 v_{kb}^T R^{bo} v_{ko}) \end{aligned} \tag{6.8}$$

If all v_{kb} and v_{ko} observations are normalized unit vector, then

$$v_{kb}^T v_{kb} = v_{ko}^T v_{ko} = 1 \tag{6.9}$$

Therefore, the loss function can be rewritten as

$$\begin{aligned} J &= \sum w_k (1 - v_{kb}^T R^{bo} v_{ko}) \\ &= \sum w_k - \sum w_k v_{kb}^T R^{bo} v_{ko} \end{aligned} \tag{6.10}$$

Now the minimization of J is redefined as a maximization problem of the *gain function*

$$g(R^{bo}) = \sum w_k v_{kb}^T R^{bo} v_{ko} \tag{6.11}$$

The gain function can be reformulated as a function of an attitude quaternion defined as

$$\bar{q} = \begin{bmatrix} q^T & q_4 \end{bmatrix}^T \tag{6.12}$$

The direction cosine matrix R and the corresponding quaternion relate in the following way

$$R = \left(q_4^2 - q^T q\right) \cdot E + 2 q q^T - 2 q_4 q^x \tag{6.13}$$

Accounting for the quaternion constraint

$$\bar{q}^T \bar{q} = 1 \tag{6.14}$$

the gain function becomes of the form

$$g(\bar{q}) = \bar{q}^T \cdot K \cdot \bar{q} \tag{6.15}$$

with

$$K_{(4x4)} = \begin{bmatrix} S - \sigma E & Z \\ Z^T & \sigma \end{bmatrix} \tag{6.16.a}$$

$$B = \sum_{k=1}^{N} w_k (v_{kb} \cdot v_{ko}^T) \tag{6.16.b}$$

$$S = B + B^T \tag{6.16.c}$$

$$Z = [B_{23} - B_{32}, B_{31} - B_{13}, B_{12} - B_{21}]^T \tag{6.16.d}$$

$$\sigma = trace[B] \tag{6.16.e}$$

Adding the quaternion constraint (6.14) to a Lagrange multiplier yields a new gain function

$$g'(\bar{q}) = \bar{q}^T \cdot K \cdot \bar{q} - \lambda \cdot \bar{q}^T \bar{q} \tag{6.17}$$

Eqn. (6.17) has a stationary value when

$$K \cdot \bar{q} = \lambda \cdot \bar{q} \tag{6.18}$$

This is easily recognized as an eigenvalue problem. The optimal estimate is thus an eigenvector of the matrix K. Since K can have 4 distinct eigenvalues, it is necessary to determine which eigenvalue maximizes the gain function. Recalling (6.15)

$$g(\bar{q}) = \bar{q}^T \cdot K \cdot \bar{q} \tag{6.19.a}$$

$$g(\bar{q}) = \bar{q}^T \cdot \lambda \cdot \bar{q} \tag{6.19.b}$$

$$g(\bar{q}) = \lambda \cdot \bar{q}^T \cdot \bar{q} \tag{6.19.c}$$

$$g(\bar{q}) = \lambda \tag{6.19.d}$$

It is easily seen now, that the largest eigenvalue maximizes the gain function. Hence, the optimal quaternion estimate is the eigenvector corresponding to the largest of four eigenvalues of the matrix K.

This results is commonly referred to as the q-method. However, the direct solution of the eigenproblem is numerically intensive. The QUEST algorithm finds a numerically friendly approximation to the largest eigenvalue of K.

Recall the definitions of the original gain function (6.11) and the result of the q-method.

$$g = \sum w_k v_{kb}^T R^{bo} v_{ko} \tag{6.20.a}$$

$$g = \lambda_{opt} \tag{6.20.b}$$

This yields

$$\lambda_{opt} = \sum w_k - J \tag{6.21}$$

Since the optimization method implies that the resulting loss function J is of very small magnitude ($J \approx 0$), eqn. (6.21) simplifies to

$$\lambda_{opt} \approx \sum w_k \tag{6.22}$$

Now the eigenvalue is known but the problem remains to find the corresponding eigenvector which constitutes the approximated optimal estimate of the attitude quaternion. This can be efficiently achieved by converting the quaternion in the eigenproblem to Rodriguez parameters, defined as

$$p = \frac{\bar{q}}{q_4} = a \cdot \tan\frac{\Phi}{2} \tag{6.23}$$

Using this definition, the eigenproblem is rearranged as

$$p = \left[\left(\lambda_{opt} + \sigma\right) \cdot E - S\right]^{-1} \cdot Z \tag{6.24}$$

Calculating the inverse of the 3x3 matrix in (6.24) is computationally feasible, for instance by application of Cramer's rule. Once the Rodriguez parameter is found, it is simple to convert it back to the quaternion which is the solution to the attitude determination problem.

$$\bar{q} = \frac{1}{\sqrt{1 + p^T p}} \cdot \begin{bmatrix} p \\ 1 \end{bmatrix} \tag{6.25}$$

6.3 Generation of Reference Vectors

The QUEST quaternion estimator requires input in the form of unit vectors in the body frame, directly obtained by measurement, and reference vectors in the orbit frame. The following sections will present the individual reference models and how they are related to each other. Figure 6.1 shows the flow chart of the attitude determination process with a large portion of this process being occupied by the generation of the reference vectors. The starting point of the generation process is the knowlegde of the absolute time on which the spacecraft's position and the position of the sun depends. The parametrization of absolute time takes a number of different forms, which will not be discussed in this chapter (see appendix A for details on the Julian Calendar). With the knowledge of the satellite position, the geomagnetic reference vector can then be extracted and with the knowledge of the sun's position, the unit sun vector and the eclipse condition is obtained. Coordinate transformations are required since the models output the respective vectors in different base reference systems.

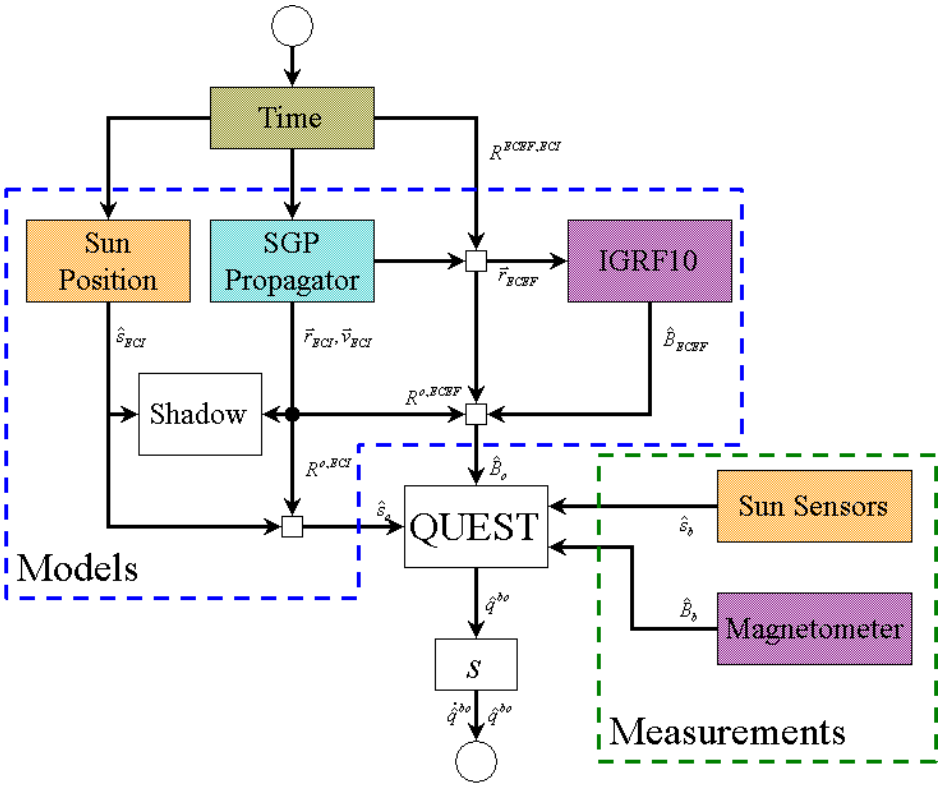

Figure 6.1: flow chart of the attitude determination process

6.3.1 Ephemeris Propagator

Although Compass-1 carries a GPS receiver which is capable of generating the required ephemeris data, the GPS system is not included in the control loop of the satellite. This is due to the receiver being declared as a payload for demonstration purposes only as well as the sizable power consumption which does not allow for the simultaneous operation of the GPS and the attitude control loop. But since the translational state is required for the generation of the attitude reference vectors a numerical alternative must be implemented.

The most obvious choices for orbit propagation are numerical integration of the equations of motion and the keplerian orbit model. However, while the numerical integration requires intensive computation and accurate models of the pertubation forces, the closed-form keplerian model lacks the long-term accuracy required in the generation of the attitude input data. There exist alternative analytical closed-form solutions to the problem of orbit ephemeris propagation which do incorporate pertubations due to zonal gravity harmonics and aerodynamic drag; these are the Simplified General Perturbation (SGP) models [55]. Starting from known mean orbital elements, SGP propagates them as oscullating elements obtained from a sum of secular and period pertubations. The SGP version 4 (SGP4) model was derived by simplification of more extensive analytical theory and utilizes a power density function for its atmospheric model. Both propagators are valid for LEO orbits with a period up to 225 minutes. Since the required computing recources are lower for the SGP algorithm while retaining reasonable accuracy, SGP is implemented on Compass-1, rather than SGP4.

As input the SGP algorithm requires the time of interest and ephemeris information stored in a Two Line Element (TLE). All active or passive LEO objects larger than about 10cm, including CubeSats, are tracked by the North American Aerospace Defence Command (NORAD) since 1958 as a response to the imminent threat of a Soviet intercontinental nuclear missile attack. In 1985 the task of satellite tracking and catalogization has been handed over to the US Space Command with a more civil set of objectives, i.e. identifying potential hazard from re-entering objects, in-orbit collision prediction etc. The Space Command uses the Space Surveillance Network (SSN) to collect observations of satellites; this network is comprised of radar sensors along 33° northern latitude in the United States for near-Earth tracking below approximately 6,000 km altitude and globally distributed electro-optical sensors for tracking deep-space objects with higher altitudes. The processed tracking data for unclassified spacecraft is regularly published via the internet in the form of TLE's (see appendix B for details on TLE's). Approximately 50% of the more than 9,000 LEO catalog objects are updated within one day. Higher update rates are done on an *as-needed* basis, e.g. for re-entering objects.

The accuracy of the TLE elements at epoch is generally in the order of a few kilometers. With the TLE as input data the SGP algorithms compute the inertial position and velocity of a satellite at an arbitrary point of time. The propagation error is depending on a number of factors, e.g. the orbit altitude and the actual aerodynamic drag. As a rule of thumb, SGP4 position errors after one week are on the order of 100 to 150km along-track compared to the total orbit length of app. 44,500km. The simpler SGP algorithm accordingly results in larger errors; a simulated comparison between SGP and SGP4 using an actual CubeSat TLE has shown that the SGP deviates dominantly in the along-track component by app. 50km after a simulated time of 2 weeks. A weekly update of the on-board TLE data is hence advisable.

6.3.2 Sun Model

The sun model calculates the sun line in the inertial reference system and determines whether the sun is obstructed by the Earth at any given time into the mission. Due to the spacecraft orbiting the Earth and the Earth itself revolving about the sun, the inertial sun vector changes minutely while the satellite travels along its orbit. However, for LEO satellites with negligible orbit radius compared to the astronomical unit these cyclic changes, in the order of few arcseconds, are well below the accuracy of the sun sensors and the required accuracy of the reference model; this enables the useful simplification of the sun model by assuming the sun line to be independent of the position of the spacecraft and hence always parallel to the vector from the Earth to the sun.

$$\hat{s}_{ECI} \approx \hat{s}_{ECI}^{Earth \to Sun} \tag{6.26}$$

The following standard algorithm describes the true motion of the Earth around the inertially fixed sun in the form of the sun orbiting the Earth being fixed in inertial space. The right ascension of the ascending node of this virtual orbit of the sun around the Earth is 0° by definition; the argument of perigee (ω) changes negligibly and is assumed constant as 282.94°. The reference epoch of this first-order model is the 1st of January 2000, 12:00:00 pm, or 2451545.0 Julian Date (JD).

$$t_{JD,2000} = t_{JD} - 2451545.0 \tag{6.27}$$

The mean anomaly of the sun is

$$M_{\odot} = 357.5277233° + 0.9856474° \cdot t_{JD,2000} \tag{6.28}$$

i.e. the first constant is the mean anomaly of the sun at epoch and the second constant is the change of the mean anomaly during a Julian Day (0.9856474° · 365.25 = 360°). The mean longitude of the sun is

$$\lambda_{\odot} = \omega + M_{\odot} \tag{6.29}$$

The ecliptic longitude of the sun introduces the correction of the sun "travelling" on an eccentric orbit.

$$\lambda_{ecliptic} = \lambda_{\odot} + 1.914666471° \cdot \sin\left(M_{\odot}\right) + 0.02° \cdot \sin(2 \cdot M_{\odot}) \tag{6.30}$$

The linear model of the ecliptic of the sun is

$$\varepsilon = 23.439291° - 3.5603559 \cdot 10^{-7}° \cdot t_{JD,2000} \tag{6.31}$$

which is close to constant. Finally the unit sun vector is given in the inertial frame as

$$\hat{s}_{ECI} = \begin{pmatrix} \cos\lambda_{ecliptic} \\ \sin\lambda_{ecliptic} \cdot \cos\varepsilon \\ \sin\lambda_{ecliptic} \cdot \sin\varepsilon \end{pmatrix} \tag{6.32}$$

6.3.3 Shadow Model

While orbiting the Earth, the spacecraft may enter eclipse conditions depending on the exact orbit parameters. While in eclipse, no attitude information can be generated by the QUEST algorithm due to the lack of sun vector readings. Hence, for reasons of power savings, it is sensible to deactivate the sun sensor hardware. It has been decided that the decision whether eclipse condition is present or not is to be made algorithmically by an adequate shadow model, rather than by sensor readings. This is simply due to the fact that once the sensor hardware is disabled, the event of re-entering direct sunlight cannot be triggered by measurement.

A fairly accurate conical shadow model is presented in [56] which is capable of distinguishing between umbra (full shadow) and penumbra (partial shadow) conditions. However, this method implies the use of trigonometric functions, which are to be avoided whenever possible owing to the high computational expense associated with the evaluation of a truncated polynomial expansion.

An alternative simplified method based on a cylindrical shadow region is presented here, which does not require the evaluation of trigonometric evaluations [57]. This model does not distinguish between umbra and penumbra; however, penumbra durations are short (on the order of 10 seconds in LEO) so that the cylindrical aproximation is sufficiently accurate for satellites on low altitude orbits.

Figure 6.2 shows the general geometry of the cylindrical shadow model. Consider a unit shadow vector u_{sh} which is antiparallel to the inertial unit sun vector; the vector u_{sh} lies on the center line of the shadow cylinder of infinite length and radius R_E.

$$\hat{u}_{sh} = -\hat{s}_{ECI} \tag{6.33}$$

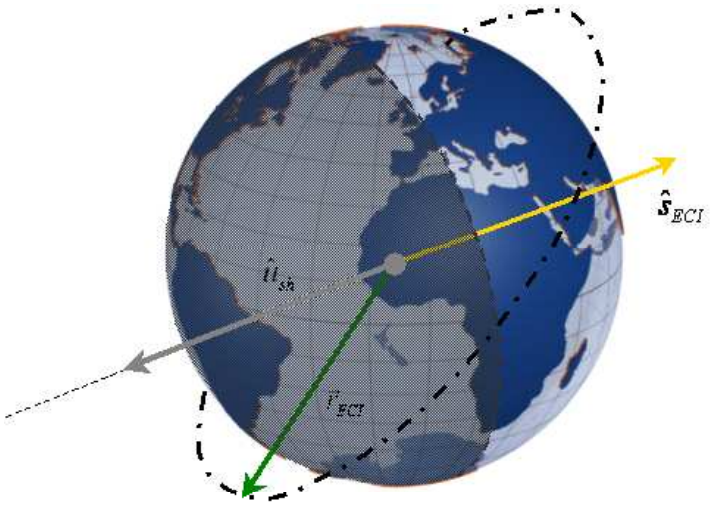

Figure 6.2: cylindrical shadow model geometry showing the terminator equally dividing the Earth's surface into a day side and a night side region.

There are now two conditions for eclipse which must be simultaneously satisfied. First, it must be determined if the spacecraft is located on the night side of the Earth by

$$\hat{u}_{sh} \cdot \hat{r}_{ECI} > 0 \tag{6.34.a}$$

If this is the case, it must then be determined if the satellite is located inside the shadow cylinder.

$$\left| R \cdot \left\| \hat{u}_{sh} \times \hat{r}_{ECI} \right\| \right| \leq R_E \tag{6.34.b}$$

Selecting R_E to be the equatorial radius is a conservative assumption and will generally result in slightly longer ecplipse durations which is advantegeous in order to avoid sun sensor measurements occuring while in penumbra.

6.3.4 Geomagnetic Reference

Evaluating the spherical harmonics IGRF model, in particular the associated Legendre functions, requires high computational capacity in terms of computing time and RAM usage. The approach implemented on Compass-1 is to essentially trade in computational load against memory capacity. Since the secular variations are small compared to the typical life time of a CubeSat, i.e. up to one year design life generally and six months specifically for Compass-1, the magnetic field can be mapped off-line as a static entity with highest possible model accuracy. The field directions required for attitude determination are then stored in memory in terms of normalized field vectors. For satellites on circular orbits a single map radius suffices; for a selected date within the mission time frame, the magnetic field is defined by a 3-dimensional array, i.e. latitude, longitude and 3 vector components. Two parameters define the actual size *z* of the array: the resolution *s*, limited by the available ROM space, and the latitude limit *i'*, given for a specific LEO orbit of inclination *i* with |90° - i'| > |90° - i|. The number of data points, evenly spaced in both directions, for a single altitude map can be predicted by:

$$z = \frac{6 \cdot 360 \cdot (90 - |90° - i'|)}{s^2} \tag{6.35}$$

The implementation on Compass-1 comprises of the geomagnetic main field spherical harmonics expansion IGRF-10 and its secular variation to full degree and order (13 and 8, respectively) evaluated in 0.5° increments in longitude and latitude at a date of interest within the mission time frame. This resolution and latitude limit yields an array size of 328 x 720 data points for a single vector component. The unit vectors are converted into the cartesian ECEF frame and formatted to the data type of 2 byte signed integers, resulting in an array size of 1383.75kB out of a total available 1448kB. The field map cannot be updated during the mission.

This predetermined approach introduces errors in the knowledge of the geomagnetic reference due to the secular variation of the main field, the variability of the radius on orbits with small eccentricities, the discretization of available data points and the formatting of the unit vectors to the integer data type. It can be reasoned that the sensitivity of the field direction, as opposed to the field strength is small with small devitations in distance. Also, the reasonably fine discretization with 0.5° increments results in a spatial resolution of ~62km (at 700km altitude); errors can be further reduced by application of linear 2D interpolation routines and this is currently employed in the flight software of Compass-1. The analysis of the latter error, due to data type conversion, is as follows:

Assume an exact unit vector *a* and the formatted unit vector *b*. The angle between these two vectors is determined by the scalar product

$$\cos\alpha = \frac{\vec{a}\cdot\vec{b}}{a\cdot b} \tag{6.36}$$

with a = 1 and $\vec{b} = \vec{a} + \delta\vec{x}$ such that

$$b = \sqrt{(a_1 + \delta x_1)^2 + (a_2 + \delta x_2)^2 + (a_3 + \delta x_3)^2} \tag{6.37.a}$$

or

$$b = \sqrt{1 + 2\vec{a}\cdot\delta\vec{x}} \tag{6.37.b}$$

because

$$a_1^2 + a_2^2 + a_3^2 = 1 \tag{6.37.c}$$

and

$$\delta x_i^2 \approx 0 \tag{6.37.d}$$

Hence the scalar product in (6.36) is

$$\vec{a}\cdot\vec{b} = a_1(a_1 + \delta x_1) + a_2(a_2 + \delta x_2) + a_3(a_3 + \delta x_3) = 1 + \vec{a}\cdot\delta\vec{x} \tag{6.37.e}$$

This yields

$$\alpha = \arccos\left(\frac{1 + \vec{a}\cdot\delta\vec{x}}{\sqrt{1 + 2\vec{a}\cdot\delta\vec{x}}}\right) \tag{6.38}$$

The integer formatting results in 4 decimals; with true rounding to the nearest integer this implies an error of $\delta x_i = \pm 5\cdot 10^{-5}$. For the given formatting, this yields errors in the order of 0.005° which is deemed sufficiently small.

6.3.5 Coordinate Transformations

As seen in figure 6.1, several coordinate transformations are required. The reference systems required for the attitude determination process are the orbit frame, the inertial ECI frame and the earth-fixed ECEF frame. Coordinate system transformations are parameterized by direction cosine matrices, owing to the fact that two of the three reference system relations can be easily constructed from the base vectors of the new system expressed in the old system, thus avoiding the need for computationally expensive trigonometric function evaluations in two of the three required DCMs. Due to the relevance of the coordinate transformation for the attitude determination process, the required DCMs are presented in the following.

The three required transformations are

$$r_o = A^{o,ECI} \cdot r_{ECI} \tag{6.39.a}$$

$$r_o = A^{o,ECEF} \cdot r_{ECEF} \tag{6.39.b}$$

$$r_{ECEF} = A^{ECEF,ECI} \cdot r_{ECI} \tag{6.39.c}$$

Recalling the definition of the reference systems and recognizing that the inertial position and velocity define the orbital plane, the base vectors of the orbit frame F_o in the ECI frame F_{ECI} can be stated as

$$\hat{o}_{3,ECI} = -\hat{r}_{ECI} \tag{6.40.a}$$

$$\hat{o}_{2,ECI} = \frac{(\vec{v}_{ECI} \times \vec{r}_{ECI})}{|\vec{v}_{ECI} \times \vec{r}_{ECI}|} = -\hat{n}_{ECI} \tag{6.40.b}$$

$$\hat{o}_{1,ECI} = \hat{o}_{2,ECI} \times \hat{o}_{3,ECI} \tag{6.40.c}$$

These base vectors are used to construct the DCM such that

$$A^{o,ECI} = \begin{bmatrix} \hat{o}_{1,ECI} & \hat{o}_{2,ECI} & \hat{o}_{3,ECI} \end{bmatrix}^T \tag{6.40.d}$$

The DCM for transformation from the ECEF frame to the orbit frame can be obtained similarly by identifying the base vectors of the orbit frame expressed in the ECEF frame.

$$\hat{o}_{3,ECEF} = -\hat{r}_{ECEF} \tag{6.41.a}$$

$$\hat{o}_{2,ECEF} = -\hat{n}_{ECEF} \tag{6.41.b}$$

$$\hat{o}_{1,ECEF} = \hat{o}_{2,ECEF} \times \hat{o}_{3,ECEF} \tag{6.41.c}$$

$$A^{o,ECEF} = \begin{bmatrix} \hat{o}_{1,ECEF} & \hat{o}_{2,ECEF} & \hat{o}_{3,ECEF} \end{bmatrix}^T \tag{6.41.d}$$

In fact, this is equivalent to

$$A^{o,ECEF} = A^{o,ECI} \cdot A^{ECI,ECEF} \tag{6.42.a}$$

with

$$A^{ECI,ECEF} = A^{ECEF,ECI\,T} \tag{6.42.b}$$

because of (6.39.a) and (6.39.c).

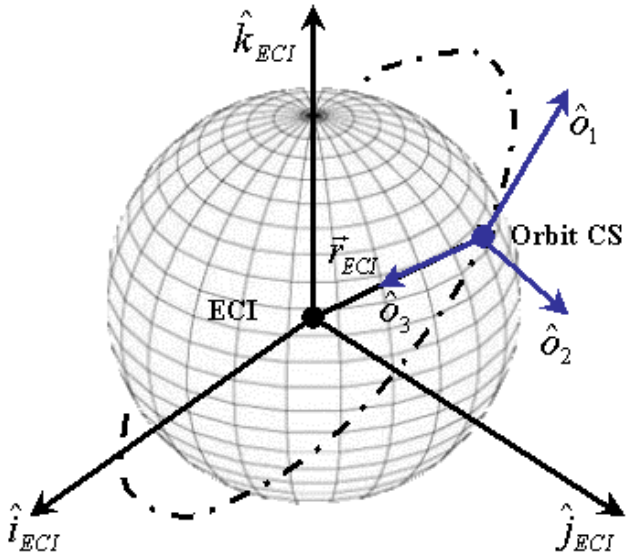

Figure 6.3: base vectors of the orbit frame in relation to the ECI frame in order to obtain the DCM for transformation from ECI to orbit (and vise versa).

The transformation from the inertial to the Earth-fixed reference system is accomplished by a rotation about the $\hat{k}_{ECI}$ axis by an angle α_G owing to the fact that $\hat{k}_{ECEF}$ and $\hat{k}_{ECI}$ coincide.

$$A^{ECEF,ECI} = \begin{bmatrix} \cos(\alpha_G) & \sin(\alpha_G) & 0 \\ -\sin(\alpha_G) & \cos(\alpha_G) & 0 \\ 0 & 0 & 1 \end{bmatrix} \tag{6.43}$$

α_G is referred to as the Greenwich Sidereal Time, or the right ascension of the Greenwich meridian or hour angle, and describes the offset angle between the prime meridian and the vernal equinox. The Greenwich Mean Sidereal Time (GMST) neglects the cyclic motion of the equinox direction due to nutation and precession of the Earth's axis of rotation and can be calculated in hours by the 24 hour modulus of

$$\begin{aligned} \alpha_G &= 6.697374558 + 0.06570982441908 \cdot JD_{prev,2000} \\ &\quad + 1.00273790935 \cdot t + 0.000026 \cdot t^2_{JC,2000} \end{aligned} \tag{6.44}$$

where t_{JC} is the Julian Century since the 2000 epoch, i.e.

$$t_{JC,2000} = \frac{t_{JD,2000}}{36525} \tag{6.45}$$

$JD_{prev,2000}$ is the epoch 2000 Julian date of the previous midnight which is obtained by subtracting 0.5 from the integer part of the epoch 2000 Julian Date and t is the fractional universal time of day.

More accurate results can be obtained by computing the Greenwich Apparent Sidereal Time (GAST), which includes the correction of the motion of the equinox due to lunar and solar pertubations. The longitude of the ascending node of the moon is

$$\Omega_{Moon} = 125.04° - 0.052954 \cdot t_{JD,2000} \tag{6.46}$$

The mean longitude of the sun λ and the obliquity of the ecliptic ε are as defined in (6.29) and (6.31), respectively. Then the nutation in longitude in hours is approximated by

$$\Delta\Psi = -0.000319 \cdot \sin(\Omega_{\text{Moon}}) - 0.000024 \cdot \sin(2\lambda_{\odot}) \tag{6.47}$$

The equation of equinoxes corrects the GMST for the shift in the position of the vernal equinox due to nutation to yield the GAST angle φ_G.

$$\varphi_G = \alpha_G + \Delta\Psi \cdot \cos(\varepsilon) \tag{6.48}$$

However, the difference between φ_G and α_G is far in the subdegree region on the order of 10^{-3} degrees. For this reason, α_G is implemented in order to find the rotation matrix in (6.43). $A^{ECEF,ECI}$ affects the knowledge of the Earth-fixed position for extraction of the geomagnetic reference, which is present in discrete form only with 0.5° increments anyway, and the definition of the orbit reference frame which affects the attitude determination accuracy overall; here, errors of a few arcseconds are deemed tolerable.

6.4 Summary

This chapter has presented the implemented process of attitude state information, suitable for application on picosatellite platforms in the context of limited computational resources. The static least-squares approach with an approximated solution to the eigenvalue problem, referred to as QUEST has been highlighted, as well as the models to generate the required reference vector input. The outputs of the estimation process is attitude information in terms of a quaternion; quaternion rates are obtained by application of a numerical differentiator. This completely defines the state information required by the LQR attitude controller. Significant computational expense has been avoided by simplifying reference models whenever feasible, and in particular by making use of a static geomagnetic field vector map stored in non-volatile memory.

Chapter 7

Simulations

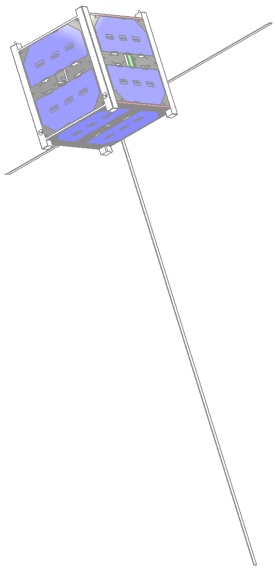

A dynamics simulation environment is an important tool for the attitude control engineer since it is often only through numerical simulation by which the non-linear and discrete nature of control systems can be accurately represented. For that reason the spacecraft dynamics and kinematics and the distinct system modes of the attitude control system of Compass-1 have been modeled numerically in MATLAB/Simulink. The dynamics model integrates the non-linear dynamic and kinematic equations of motion using the medium-order ordinary differential equation solver ODE45 with variable time step. The truth model of the satellite orbit is provided by a SGP4 ephemeris propagator while the geomagnetic main field is modeled according to IGRF10 to degree and order 13 and its secular variation to degree and order 8. The Simulink model does not consider hard real-time constraints and performs all computations in floating point arithmetics; however, hardware model blocks have been programmed in order to realistically represent the discrete and uncertain nature of sensor and actuator performance. Additionally, the system modes have been modeled to be discrete in time owing to the discrete-time nature of the digital proccessing system.

The following presents the mode implementations and the numerical simulation results thereof. The primary objective is to validate the performance of the two active system modes, i.e. detumbling and attitude stabilization control under “clean” conditions; the secondary objective is to compare the ideal system response with the performance under more realistic, discrete operational conditions.

7.1 Boundary Conditions

As input to the SPG4 propagator an orbit within the targeted design orbit of Compass-1 has been chosen. This orbit is similar to the UWE-1 CubeSat orbit, with a small eccentricity of $1.8343 \cdot 10^{-3}$, an inclination of 98.18° and an altitude of app. 700km. The TLE is:

```
1 28892U 05043C   05318.17328418  .00000229  00000-0  58313-4 0   765
2 28892  98.1816 139.4794 0018343 119.4987 240.8056 14.59254957  2614
```

The original UWE-1 orbit elements have been modified in the right ascension of the ascending node (RAAN). The RAAN angle of 139.4794° is chosen such that the eclipse time is minimized for the given inclination and epoch which results in longer solar pressure torque durations and a more complete attitude determination coverage. This sun-synchronous, dawn/dusk orbit is a realistic target orbit for Compass-1. The original UWE-1 RAAN angle is 214.6194°.

The simulation origin coincides with the epoch of the TLE, which is 53688.1732842 (MJD).

Another important prerequisite for the simulation of the spacecraft dynamics is the knowledge of the spacecraft's inertia. Since no full knowledge of the mass properties of Compass-1 has been established at the time of writing the following reasoning is used in order to estimate the moments of inertia: the general formulation of the moment of inertia with homogeneous mass distribution is given as

$$I = \rho \cdot \iiint_V r^2 \cdot dx \cdot dy \cdot dz \tag{7.1}$$

For the special case of a cube all three principal inertiae are equal (symmetric body) and are aligned with the body frame.

$$I_{1,2,3,cube} = \frac{1}{6} m h^2 \tag{7.2}$$

Hence, for CubeSats the ideal moments of inertia are $1.667 \cdot 10^{-3}$kgm². Since a sizable fraction of the mass is concentrated on the outer cube panels it is sensible to assume slightly higher values for the real moments of inertia. From the perspective of configuration including the antenna system, it is possible to deduce implications for their relation to each other. The antenna system of Compass-1 consists of 2 symmetrical dipole antennae in b_2 direction with a length of 175mm each and one monopole antenna in b_3 direction with a total length of 500mm, both mounted on the $+b_1$ face plate. Hence it is reasonable to assume that the inertiae in pitch and roll are both larger than the yaw inertia. Taking into account the CG offset of the dipole antennae for pitch motion it may be further assumed that the pitch inertia is larger than the roll inertia ($I_2 > I_1 > I_3$; $I_2 < I_1 + I_3$). This renders the spacecraft naturally gravity gradient stable. The absolute moments of inertia are adopted from [17] and are diag(0.00198, 0.0021, 0.00188)kgm².

Table 7.1: Common simulation scenario parameters (orbit and inertia)

Parameter	Symbol	Value	Unit
Roll inertia	I_1	$1.98 \cdot 10^{-3}$	kgm²
Pitch inertia	I_2	$2.10 \cdot 10^{-3}$	kgm²
Yaw inertia	I_3	$1.88 \cdot 10^{-3}$	kgm²
Semi-major axis	a	7070.8	km
Eccentricity	e	0.0018343	-
Inclination	i	98.182	°
RAAN	Ω	139.4794	°
Argument of Perigee	ω	119.496	°
True Anomaly (at epoch)	v	240.808	°
Perigee Altitude	h_p	682.444	km
Apogee Altitude	h_a	708.646	km
Period	T	5920.8	s

7.2 Detumbling Controller

7.2.1 Initial Condition

The initial condition, i.e. the initial tumbling rates at the begin of mission, are governed by the P-POD separation and the deployment of the communication antennae. Upon release the antennae unfold in less than 1 second excluding dissipation of flexible modes. Due to their mounting orientation, all release torques act in the b_1 direction; hence, antenna release torques are roll torques. The release of the dipole antennas is highly symmetrical such that the torques about their common attachment point are negligible. The only remaining torque is generated by the longer monopole antenna. Typical CubeSat designs estimate a max. expected tumbling rate upon P-POD release of 0.1 rad/sec on all three body axes [17]. Adding a margin of safety of 50% as well as the impact of antenna release on the magnitude of the roll rate yields an estimated 0.25 rad/sec in b_1, 0.15 in b_2 and 0.15 in b_3, resulting in an overall tumbling motion in excess of 3 revolutions per minute as initial condition. The initial conditions for the detumbling scenario are listed in table 7.2. The dynamics of the detumbling mode are evaluated completely in the inertial frame.

Table 7.2: Detumbling initial conditions

Initial tumbling rates	$\omega_{b,0}^{bi}$	$(0.25\ -0.15\ 0.15)^T$	rad s^{-1}
Initial tumbling	$\left\|\omega_{b,0}^{bi}\right\|$	3.131	rev/min
Initial Quaternion	$\bar{q}_0^{bi}$	$(0\ 0\ 0\ 1)^T$	-

7.2.2 Ideal Implementation

Controller Gain

The scalar gain of the detumbling control law (5.9) determines the rate at which energy is dissipated. Generally, the higher the gain, the faster will be the dissipation of kinetic energy and the higher will be the actuator load. Iterative simulation runs suggest that fairly fast energy dissipation can be achieved with gains between 2000 and 5000. Much larger gains do not result in an adequately improved behavior but require the magnetic actuators to operate at higher power levels. The simulations under ideal conditions including the gravity gradient torque as the only external torque source indicate that the detumbling maneuver requires approximately one orbital period to be completed. Other disturbances have very little impact during the detumbling mode and will only be included in the simulation of the realistic operational conditions.

In order to determine a reasonable detumbling gain a design strategy is employed which selects the control gain C in such a way that coil saturation can be excluded by design. The achievable magnetic moment is finite for a given coil design; as shown in chapter 4 Compass-1 is capable of producing a maximum magnetic moment of app. 0.052Am² at full actuator load, i.e. 25mA magnetorquer current, in a single direction. Because coil saturation, i.e. exceeding actuator limits, alters not only the magnitude but more importantly the

direction of the control action, it must be ensured that actuator saturation does not occur. It is sensible to assume that the maximum rate of change of the magnetic field occurs at the initial point of the detumbling maneuver at which $|\omega| = 0.328 s^{-1}$. At a conservative minimum orbit altitude of 600km the largest *B* vector occurs at the magnetic poles with a magnitude of $4.65 \cdot 10^{-5}$ T. According to (5.7) and using scalar terms, the detumbling gain C may be chosen according to the following conservative condition which is stated as a direct consequence of the control law in (5.9).

$$|C| \leq \frac{m_{\max}}{\omega_0 \cdot B_{\max}} \tag{7.3}$$

With the above assumptions the magnitude of the detumbling gain should be limited to 3409.4 Am²s/T. In order to alleviate the conservativeness of the assumptions leading to this value the gain is rounded up to an even C = -4000 Am²s/T for the presented implementation.

The selected gain is identical with the implementation in the related work by Renk [21], which has been found by iteratively comparing the rate at which kinetic energy

$$E_{rot} = \frac{1}{2} \omega_b^{bi,T} \cdot I \cdot \omega_b^{bi} \tag{7.4}$$

is dissipated and the accumulated current consumption

$$\int \sum_{i=1}^{3} |i_i| \cdot dt = \int \frac{\sum_{i=1}^{3} |m_i|}{N \cdot A} \cdot dt \tag{7.5}$$

for a given detumbling gain. Using this simulation-intensive empirical approach to minimizing the cost of the detumbling maneuver, Renk identified an optimum detumbling gain identical to the fast result of the above design method.

State Variable Filter Cut-off Frequency

As a rule of thumb the cut-off frequency of the first-order state variable filter in (5.11) for estimation of the geomagnetic rate of change should be chosen 5 – 10 times larger than the highest expected initial tumbling rate of the spacecraft. With an assumed initial tumbling rate of $0.328 s^{-1}$, the filter cut-off has been selected to $\omega_c = 2 s^{-1}$. Comparison between the results of simulated direct numerical differentiation and the discrete filter output has been used to validate the selection of the filter cut-off frequency. These simulations have shown that the cut-off frequency is selected large enough to allow for the low frequency input of the geomagnetic field to be correctly differentiated.

7.2.3 Results

The above continuous implementation has been numerically tested using the Simulink simulation tool over a simulated time of 0.8 orbits. The key results are shown in figure 7.1.

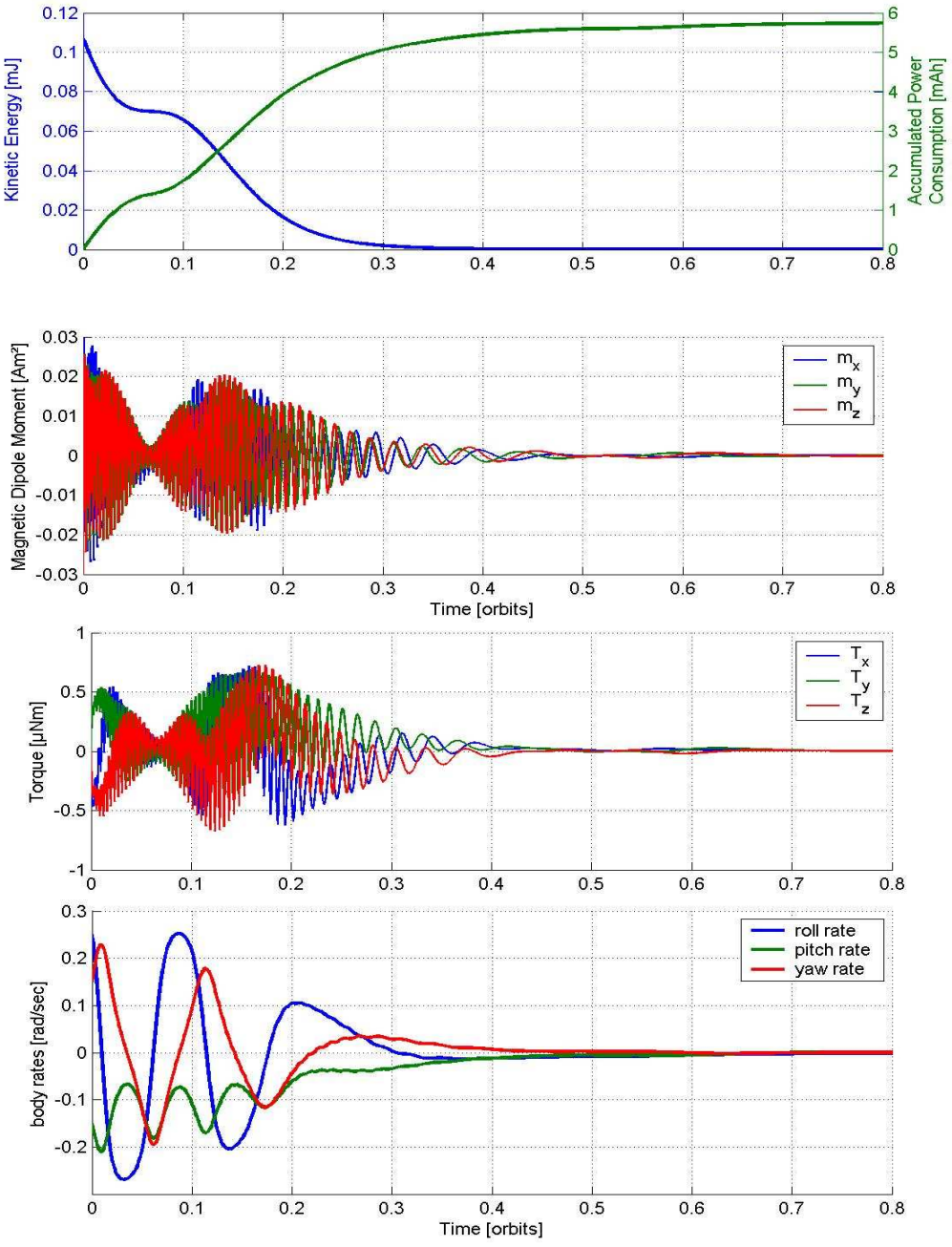

Figure 7.1: Results of the continuous detumbling mode with gravity gradient; the plots show (from top to bottom) the kinetic energy and current consumption, the magnetic dipole moment in the body frame, the torque in the body frame and the inertial body rates.

The simulation shows that the worst-case initial body rates can be dissipated to < 0.005 rad/sec after little more than half an orbit period (≈ 3500s). This is deemed well sufficient for the LQR controller to take over; it is assumed that the LQR controller can handle inertial body rates up to 0.01rad/s. Since no body rate estimation is available in the detumbling mode, the abort condition must be an elapsing timer. From the results of the continuous detumbling mode, it can be concluded that the mode must be maintained for at least 3500s after initialization in order to unload the worst-case angular momentum at the start of the mission.

It has been observed that large magnetic moments are produced during the first time steps. The reason has been identified as the finite settling time of the state variable filter after integrator initialization with an initial condition of 0. In the continuous case, the filter settles within 10 seconds; after this the magnetorquer currents do not exceed a value of app. 12mA, indicating that the chosen detumbling gain remains a conservative one.

There exists some sensitivity of the body rate history w.r.t. to the orbit orientation in the RAAN angle, owing to the different geomagnetic field geometry in the body frame for the given initial conditions but the outcome of the detumbling mode after one orbital period is always identical. The overall behavior of the Bdot controller shows high robustness w.r.t. to parameter uncertainties.

7.2.4 Realistic Implementation

After having established the performance of the continuous detumbling controller, attention will now turn towards the performance of the controller with unaltered initial and boundary conditions but under more realistic operational assumptions. The following simulation run assumes a full disturbance environment comprised of gravity gradient, aerodynamic drag, solar pressure and residual magnetic dipole; it is anticipated that the impact of the additional disturbances will be benign during detumbling. However, the discretization of the control loop and a more accurate magnetometer model subject to measurement noise and limited accuracy could alter the system performance sizably.

Environment

The environmental disturbances are modeled according to the models presented in chapter 3 and using truth models stated at the beginning of this chapter. Eclipse times during which the solar pressure is set equal to 0 is determined using the cylindrical shadow model of chapter 6. Table 7.3 shows the disturbance torque parameters valid for all following simulations.

The configuration of the spacecraft body is assumed to be ideally cubic with identical properties on each side. For the computation of the torque due to solar pressure and aerodynamic drag, a constant center of pressure (CP) is assumed to coincide with the geometrical center GC of the cube. The placement of the CG = $(5\ 0\ 0)^T$mm assumes a reasonable equipment placement within the satellite in order to reduce the impact of the diturbance environment. As will be seen later, the magnetic LQR controller is sensitive towards external torques; worst-case aerodynamic and solar pressure torques occur at a maximum displacement of the CG allowed by the CubeSat standard of 20mm, which renders the desired attitude pointing accuracy of 10° impossible to achieve.

Table 7.3: Environmental Disturbance Parameters; the simulation assumes an ideal cubic spacecraft body with identical faces and a CG at $(0.005\ 0\ 0)^T$m

Parameter	Symbol	Value	Unit
Solar Pressure			
Solar Constant	S_0	1371	W/m²
Speed of Light	c	$3 \cdot 10^8$	m/s
Reflectance	r	0.6	-
Aerodynamic Drag			
Coefficient of Drag	c_D	2.2	-
Mean Density at 700km	$\rho_{mean,700}$	$3.91 \cdot 10^{-14}$	kg/m³
Residual Dipole			
Parasitic Magnetic Dipole	m_p	$(4 \cdot 10^{-5}\ 6 \cdot 10^{-6}\ -4 \cdot 10^{-5})^T$	Am²

The direction of the parasitic net magnetic dipole moment originating from residual magnetization and stray fields inherent to the spacecraft has been chosen randomly with a magnitude equivalent to a single current-loop along the perimeter of a cube panel, carrying a DC current in excess of 5mA.

Magnetorquer Model

The control gain for the Bdot controller has been chosen such that saturation of the magnetorquers is unlikely to happen by design. However, if for some reason the requested magnetic moment m_{req} is larger than the maximum producible magnetic moment of app. 0.052Am² in any one component, a new, smaller but direction-conserving magnetic moment is calculated by the following algorithmic rule [44].

$$\beta = \max \frac{\left|\vec{m}_{req}\right|}{m_{\max}} \tag{7.6.a}$$

$$\vec{m} = \begin{cases} \vec{m}_{req} & if \beta \le 1 \\ \frac{1}{\beta} \cdot \vec{m}_{req} & if\ 1 < \beta \end{cases} \tag{7.6.b}$$

This correction method takes into account the upper bound of the control auhority by implementation. Finally, the generated magnetic dipole moment is quantized to a resolution of $7.943 \cdot 10^{-7}$Am², i.e. $I_{min} \cdot N \cdot A = 0.025A \cdot 2.082m^2 / (2^{16} - 1)$; this effectively sets the minimum producible magnetic moment equal to the resolution.

Magnetometer Model

The magnetometer has been modeled as a discrete sensor measuring the magnetic field in the body frame with a sampling time equal to the sampling interval of the detumbling controller. Random peak noise of ±40nT has been added to a periodic error of max. ±30nT with an arbitrarily chosen phase offset. The period of this error is set to one orbital period to reflect changes of the sensitivity due to temperature changes. Introducing a phase offset into this

error is certainly conservative since an in-phase error merely results in periodic changes in magnitude to which both the B-Dot controller and the QUEST attitude estimator are not particularly sensitive. The resolution of the magnetometer has been set to 5nT. Table 7.4 lists the parameters of the magnetometer model implementation.

Table 7.4: Magnetometer Model Implementation Parameters

Parameter	Value	Unit
Peak Noise	±40	nT
Phase-Offset Peak Error	±30	nT
Error Period	5920.8	s
Resolution	5	nT

Sampling Frequency

It is known that the discrete state variable filter response diverges for long update intervals making the selection of an appropriate sample interval important. Indifferent filter output has been observed for a filter update frequency of 1Hz. In order to ensure a proper margin, a filter update frequency of 2Hz has been selected resulting in a sampling period of 500ms. For the discrete case, the filter appears to settle after the first update interval but the control law is implemented to engage 5 sec after initialization of the detumbling mode.

From the perspective of implementation, another constraint of magnetic control using a magnetometer as a source of attitude information is the fact that measurements must be separated in time from the control action to avoid false magnetometer readings; this scheme is referred to as time-division multiplexing illustrated in figure 7.2.

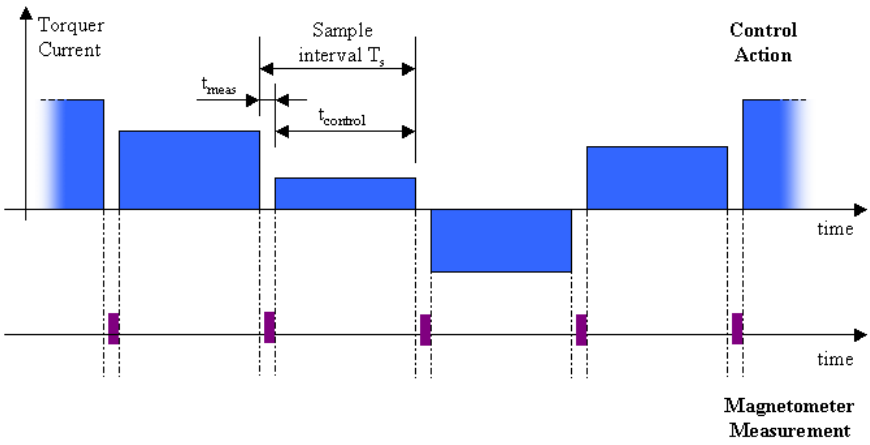

Figure 7.2: time-division-multiplexing of the control/measurement sequence

Hence the sample interval T_s is split into a measurement time and a control time, within which the control signal is held constant.

$$T_s = t_{control} + t_{meas} \tag{7.7}$$

This implies that the implementation of a magnetic control law is always of a discrete nature. In the case of the detumbling mode, 90% (450ms) of the 0.5s inteval are used for controlling and 10% (50ms) are used for measurements and processing.

7.2.5 Results

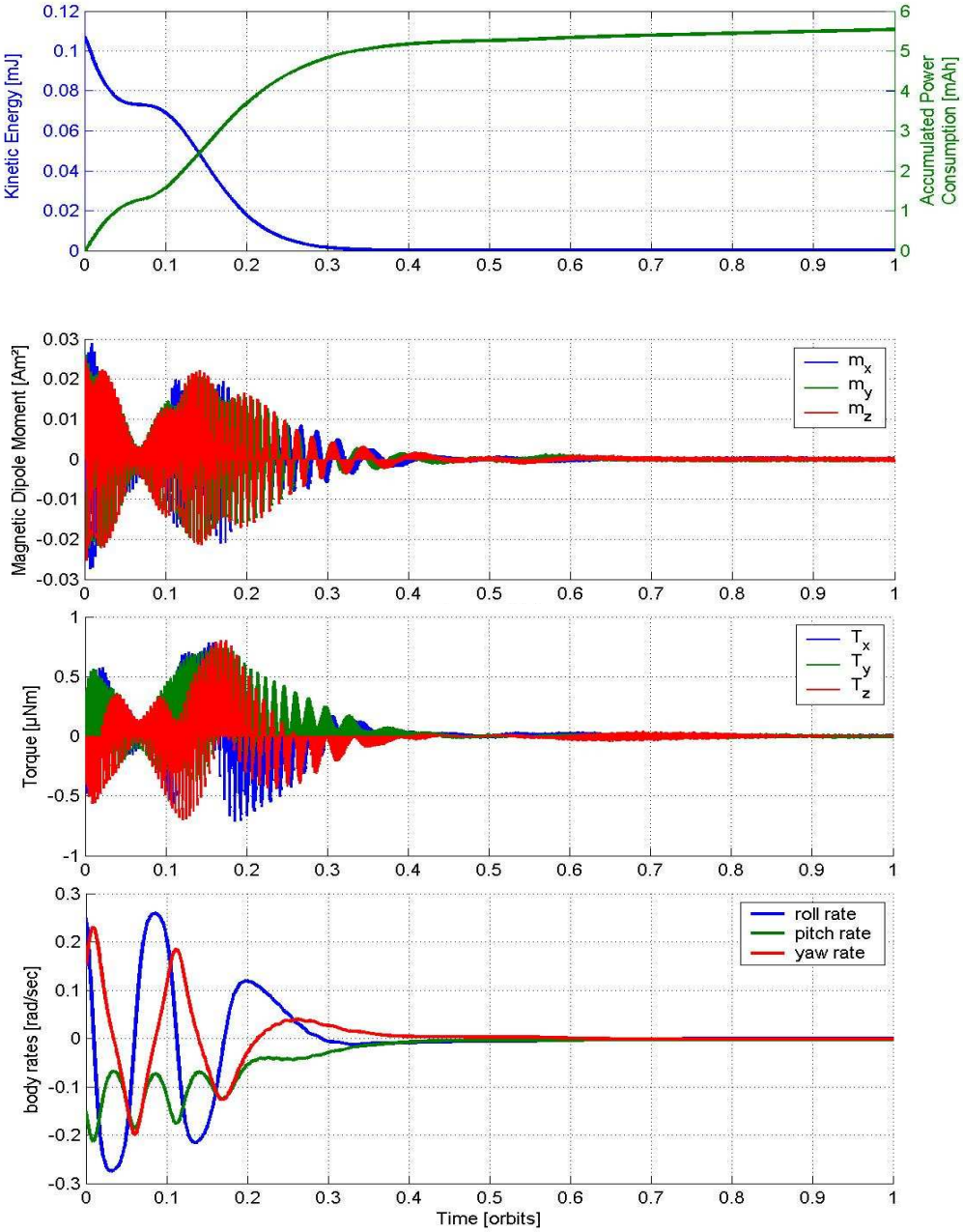

Figure 7.3: Results of the discrete detumbling mode under full disturbance environment, multiplexing and consideration of hardware models for magnetorquer and magnetometer; the plots show (from top to bottom) the kinetic energy and current consumption, the magnetic dipole moment in the body frame, the torque in the body frame and the inertial body rates.

Figure 7.3 shows the results of the realistic simulation run under full disturbance environment, multiplexing and consideration of hardware models for magnetorquer and magnetometer over a simulated duration of one full period. The results indicate very good consistency with the detumbling history under ideal conditions. Again, the body rates are reduced to < 0.005 rad/sec after 3500s; the time-division multiplexing delays the rate at which energy is dissipated insignificantly. As a direct consequence, the total power consumption is marginally reduced. The errors introduced in the magnetometer model do not affect the outcome of the detumbling mode. Based on these simulation results, the abort condition for implementation aboard Compass-1 has been defined as one full orbit revolution (≈6000s) for a safe momentum unloading from worst-case initial tumbling rates.

7.2.6 Worst-case detumbling

Finally the outcome of the worst conceivable detumbling scenario is investigated. Here, the spacecraft rotates about the roll principal axis of inertia which is aligned with the direction of the geomagnetic field such that the angular momentum of the satellite is co-directional with the magnetic field.

Table 7.5: Worst-Case Detumbling Scenario initial conditions

Initial tumbling rates	$\omega_{b,0}^{bi}$	$(0.25\ 0\ 0)^T$	rad s^{-1}
Initial tumbling	$\left\|\omega_{b,0}^{bi}\right\|$	2.39	rev/min
Initial Quaternion	$\bar{q}_0^{bi}$	$(0.075\ -0.02\ -0.053\ 0.704)^T$	-

The fundamental underaction prohibits a change in angular momentum in this situation, rendering the Bdot controller unable to reduce the kinetic energy of the spacecraft. However, as the direction of the magnetic field slowly rotates out of the angular momentum direction, the required control torques can be generated again and the detumbling controller regains control over the kinetic energy.

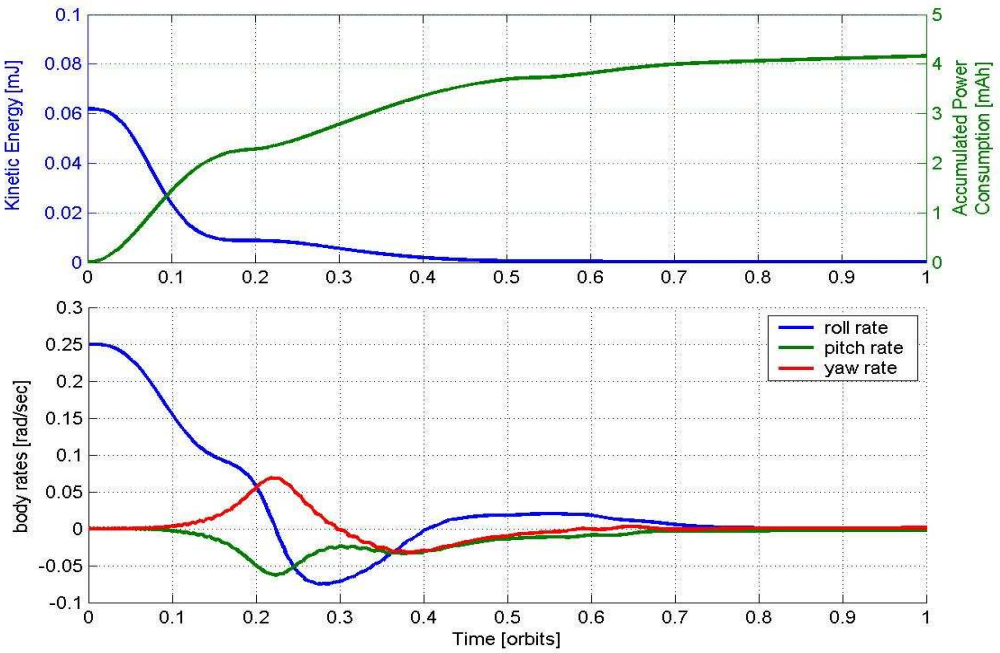

Figure 7.4: Results of the discrete worst-case detumbling mode under full disturbance environment, multiplexing and consideration of hardware models for magnetorquer and magnetometer; the plots show (top) the kinetic energy and current consumption, and (bottom) the inertial body rates.

This is confirmed by the simulation results shown in figure 7.4. Although, starting from the worst-case initial conditions, the detumbling maneuver takes app. twice as long as in the arbitrary initial conditions in table 7.2, the detumbler is capable of dissipating the kinetic energy to levels consistent with the previous simulation scenario at the abort condition; after 4500s the body rates are below 0.005rad/s, confirming the selection of the abort timer condition of one orbital period. The exact exit condition is

$$\omega_b^{bi} = (0.00068106\ -0.0020875\ 0.0011837)^{\mathrm{T}}\mathrm{rad/sec}.$$

7.3 Attitude Control Mode

7.3.1 Selection of the Tuning Parameter q

As shown in chapter 6 the stability of the LQR controller depends on the selection of the heuristic tuning parameter q. Maximum asymptotic stability is achieved by a control gain which minimizes the absolute value of the maximum eigenvalue of the monodromy matrix. Figure 7.5 shows the results of a sweep of tuning paramters in the range between 10 and 28,000 within which the linear periodic system is asymptotically stable.

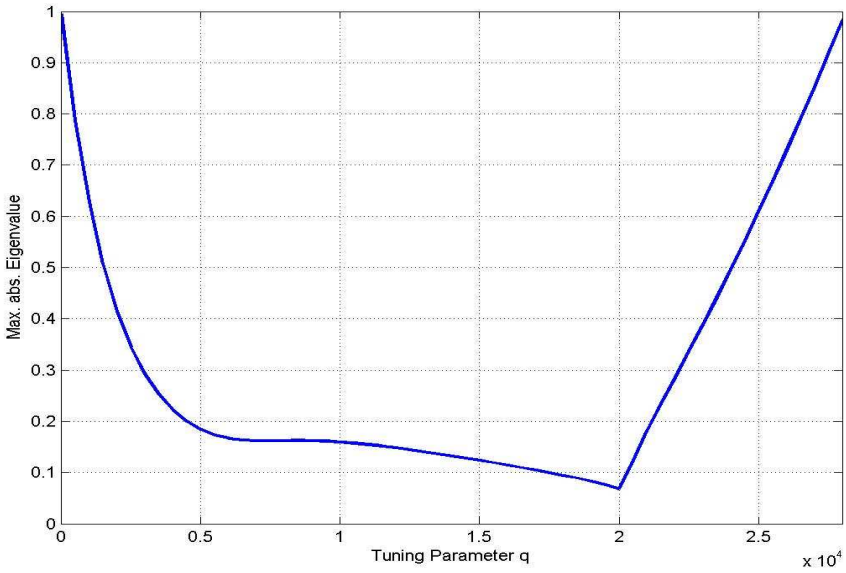

Figure 7.5: Plot of the maximum absolute eigenvalue of the monodromy matrix as a function of the tuning parameter q

The minimum of the curve in figure 7.5 is found to be at q = 20,000; this yields a maximum absolute eigenvalue of 0.0684, indicating good stability of the linear periodic system. The eigenvalues of the monodromy matrix $\Psi(t_0)$ are

$$eig(\Psi(t_0)) = \begin{pmatrix} 0.0549 + 0.0407 \cdot i \\ 0.0549 - 0.0407 \cdot i \\ 0.0148 \\ 0.0009 \\ 0 \\ 0.0001 \end{pmatrix}$$

The implemented LQR gain resulting from this selection of the parameter q is

$$K_{LQR} = \begin{bmatrix} -9.0154 & 0 & 8.9811 & -10889 & 0 & 5817.2 \\ 0 & -13.595 & 0 & 0 & -9713.1 & 0 \\ -9.0466 & 0 & -9.8674 & 1534.7 & 0 & -15067 \end{bmatrix} \tag{7.8}$$

7.3.2 Ideal Implementation

First, the controller is tested under ideal assumptions, i.e. continuous control, gravity gradient torque as only external torque, no attitude determination outage and no hardware models. The initial conditions listed in table 7.6 constitute a possible exit condition of the detumbling mode with randomly selected 30° euler angles on each axis and approximately $(3\ 0\ -3)^{T} \cdot 10^{-3}$ rad/s inertial body rates.

Table 7.6: Attitude Controller Scenario initial conditions

Initial body rates	$\omega_{b,0}^{bo}$	$\begin{pmatrix} 3.154 \\ 0.69 \\ -3 \end{pmatrix} \cdot 10^{-3}$	rad s^{-1}
Initial Rotation	$\left\|\omega_{b,0}^{bo}\right\|$	0.042	rev/min
Initial Quaternion	$\bar{q}_0^{bo}$	$\begin{pmatrix} 0.1768 \\ 0.3062 \\ 0.1768 \\ 0.9186 \end{pmatrix}$	-

The results in figure 7.6 confirm stability of the LQR controller for the non-linear system. The steady state error of the controlled system settles to subdegree accuracy after 2 orbits in the absence of non-conservative disturbances.

7.3.3 Impact of Added Disturbance

Figure 7.7 shows the results of the controller with identical initial conditions but under the influence of disturbances from solar pressure, aerodynamic drag and gravity gradient. The results illustrate the inferiority of the magnetic controller in terms of steady state accuracy resulting from the fundamental underactuation of the system; the LQR is fundamentally unable to compensate disturbance torques parallel to the geomagnetic field vector. Hence, the system under control exhibits little robustness against unmodeled disturbances. For the given mission scenario of pointing a payload axis in the nadir direction, the figure of merrit is the deviation of the body axes from the desired reference axes; of particular importance is the alignment of the z-axis (equals b_3) with the nadir direction. From figure 7.7, it can be concluded that the nadir pointing accuracy is app. 10° for the LQR gain in (7.8).

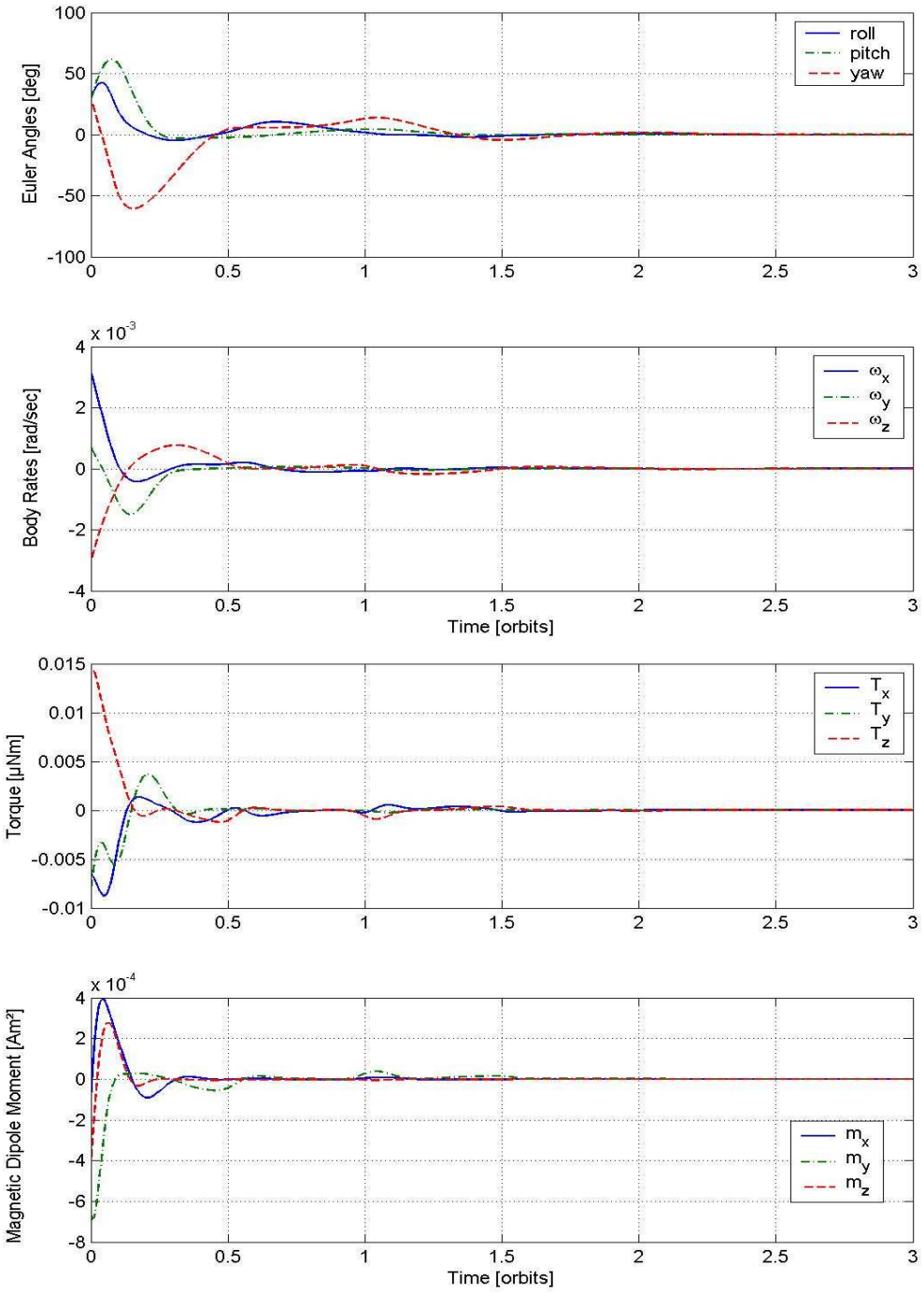

Figure 7.6: Simulation Results of the continuous LQR controller under gravity gradient influence; the plots show (from top to bottom) the attitude euler angles, the orbit body rates, the torque and the magnetic dipole moment in the body frame.

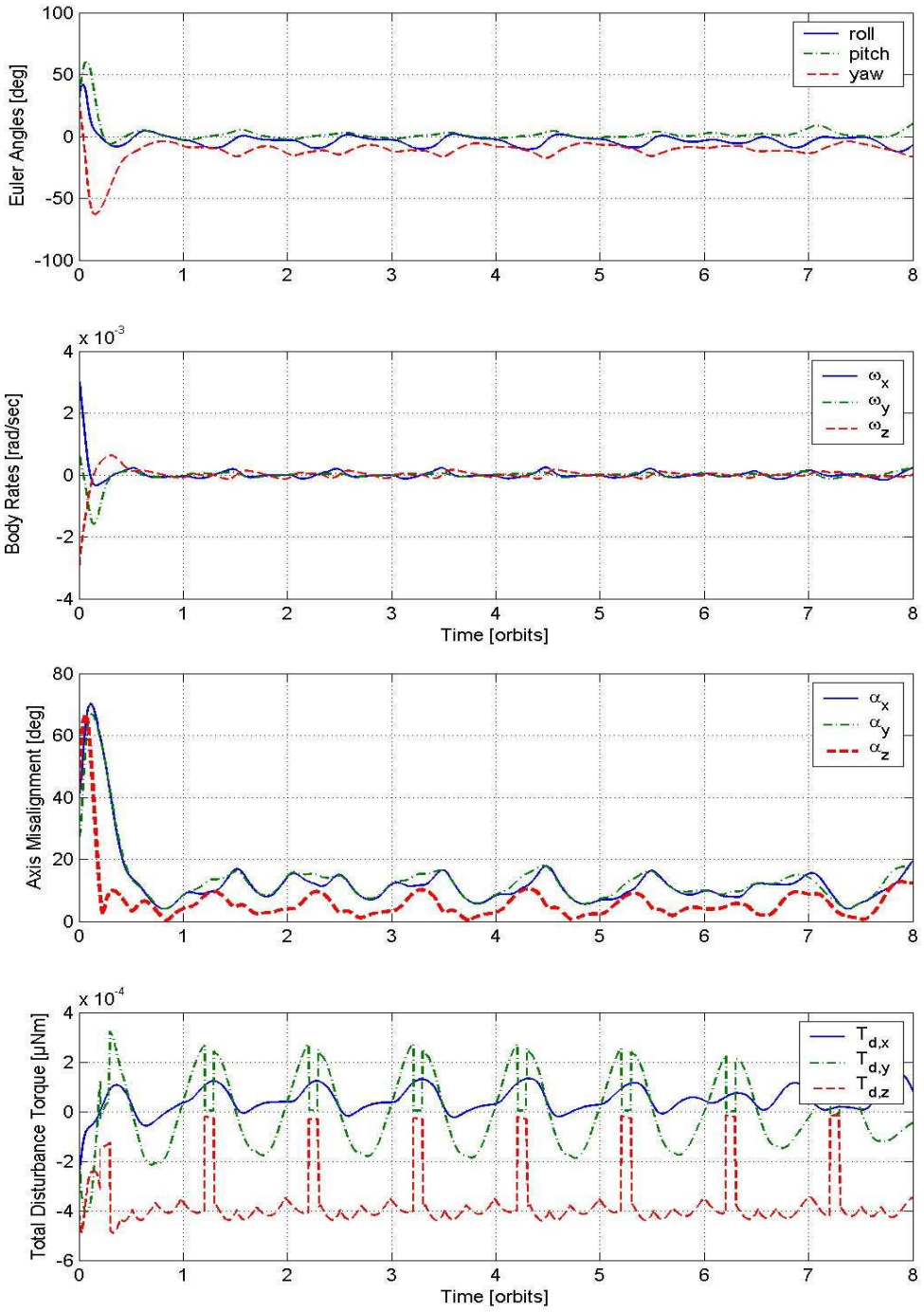

Figure 7.7: Results of the continuous LQR controller under solar pressure, aerodynamic drag and gravity gradient influence; the plots show (from top to bottom) the attitude euler angles, the orbit body rates, the misalignment between the axes of the body frame and the orbit frame and the total environmental disturbance torque in the body frame.

7.3.4 Reduction of Yaw Feedback

In order to improve the accuracy of the nadir alignment, it is advantageous to reduce the disturbance torques on the spacecraft. As figure 7.6 illustrated for the extrem case of zero non-conservative disturbance, the controller is capable of asymptotically aquiring a steady state attitude error of zero. Note that the magnitude of the aerodynamic and solar disturbance depends on the perpendicular distance of the CG and the CP. Thus, if the spacecraft is allowed to rotate into a nadir-pointing attitude which minimizes this distance, the controller is expected to exhibit less pointing error.

It is attempted to achieve this by manually tuning the LQR gain matrix. Consider the new LQR gain

$$K_{LQR} = \begin{bmatrix} -13 & 0 & 0 & -11000 & 0 & 5820 \\ 0 & -22 & 0 & 0 & -9720 & 0 \\ 0 & 0 & -6 & 1535 & 0 & -15070 \end{bmatrix} \tag{7.9}$$

The elements have been ceilling rounded to integer values to make the software implementation more compact. The entries corresponding to the quaternion rates (right 3x3 submatrix) have been slightly raised which should result in marginally improved damping behavior while the entries corresponding to the attitude quaternion (left 3x3 submatrix) have been diagonalized. The important change made to the original gain matrix in (7.8) is a decrease of the magnitude of the element corresponding to the quaternion component q_3 w.r.t. to the other quaternion components, i.e a reduction of the yaw state feedback. As a result the control authority is "less tight" on q_3 and the yaw (i.e. payload) axis is allowed to drift into larger errors than the pitch and roll axes without impacting operational pointing requirements.

For the new LQR gain with reduced yaw feedback in (7.9) the eigenvalues of the mono-dromy matrix $\Psi(t_0)$ are

$$eig(\Psi(t_0)) = \begin{pmatrix} -0.2552 + 0.136 \cdot i \\ -0.2552 - 0.136 \cdot i \\ 0 \\ 0.0001 \\ 0.0002 + 0.0001 \cdot i \\ 0.0002 - 0.0001 \cdot i \end{pmatrix}$$

The maximum eigenvalue is then of magnitude 0.2892, which is sizably larger than in the case of the original LQR gain, but still well within the stability region of the linear periodic system.

Figure 7.8 shows the simulation results for the new gain matrix with reduced yaw feedback. The nadir-pointing accuracy is improved by 2° from 10° to 8°. The results clearly show that the spacecraft has a dominant offset in the yaw euler angle while the pointing of the yaw axis is aligned well with the nadir-direction. The reason for the improved bahaviour lies in the automatic reduction in effective disturbance torques because the spacecraft is allowed to yaw into an attitude in which the control torque and the dominant solar pressure torque are in equilibrium.

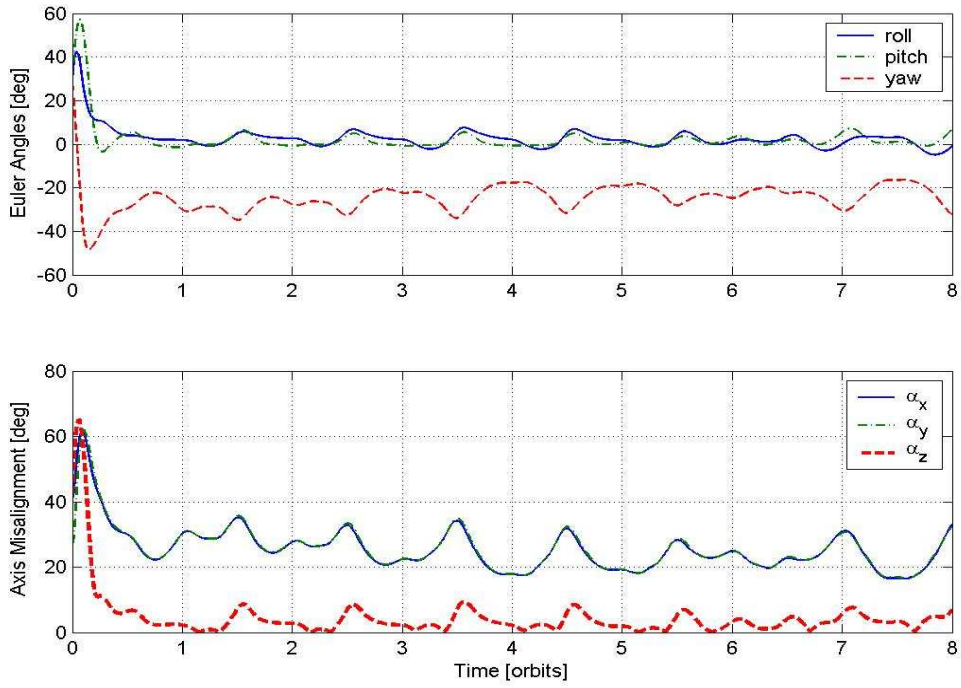

Figure 7.8: Results of the continuous LQR controller with reduced yaw feedback under solar pressure, aerodynamic drag and gravity gradient influence; CG = $(5\ 0\ 0)^T$mm

7.3.5 Sensitivity towards Orbit Parameters (RAAN)

The actual orbit parameters, in particular the RAAN angle, determine the equilibrium attitude and consequently the accuracy of the nadir alignment. This is due to the different sun vector direction in the orbital reference frame imposing different torques about the center of gravity.

Figure 7.9 shows the results for the original UWE-1 orbit parameters with a RAAN angle of 214.62°. In this orbit the steady state pointing accuracy of the yaw axis is improved by a further 2° to a value of 6° compared to the above orbit with a RAAN of 139.48°. Also, the alignment error in the remaining axes is much smaller, indicating an overall attitude which is sizably closer to the desired reference attitude. Hence, it can be concluded that there exists some sensitivity of the controller w.r.t. the choice of the orbit.

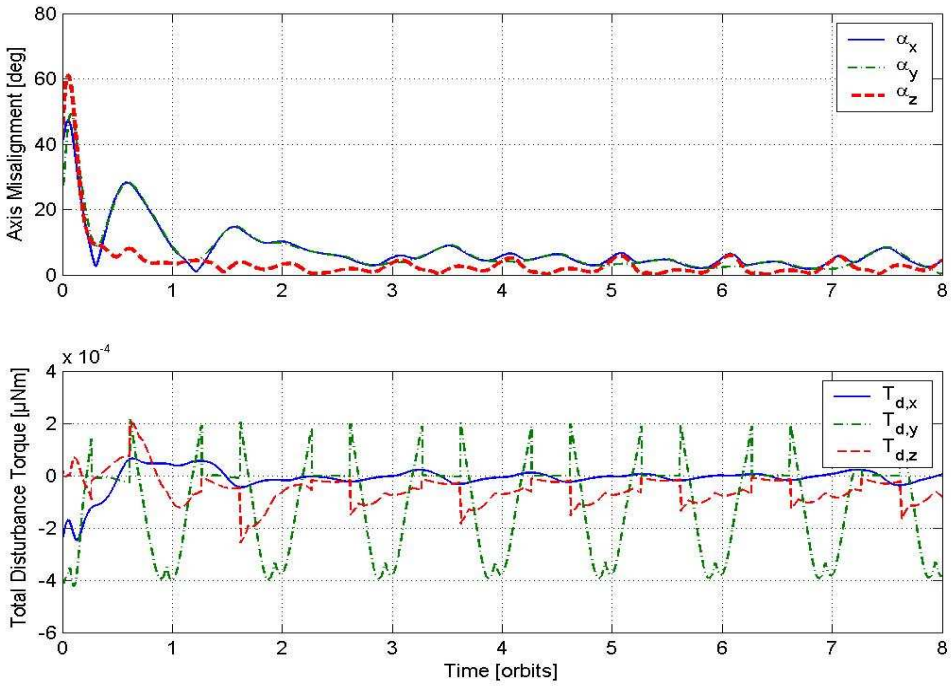

Figure 7.9: Results of the continuous LQR controller with reduced yaw feedback under solar pressure, aerodynamic drag and gravity gradient influence with altered RAAN = 214.62°; CG = $(5\ 0\ 0)^T$mm

7.3.6 Sensitivity towards the Location of the Center of Gravity

If the direction of the sun vector has an impact on the alignment performance of the controller than certainly the system must show some sensitivity w.r.t. the location of the CG. Figures 7.10, 7.11 and 7.12 show the results for different placements of the CG. For the orbit with a RAAN of 139.48° for which the sun vector has a large component in the o_2 direction, the worst behavior is expected for a CG placement on the b_1 axis because this configuration yields maximum leverage for the solar pressure force; degraded performance is also anticipated for a CG placement on the b_3 axis, because this would prohibit any disturbance equilibrium on the yaw axis (the solar disturbance torque about the yaw axis is always zero) but create disturbances in pitch and roll. The results confirm this reasoning: the best case is achieved for a CG on the b_2 axis with pointing errors below 5° at all times.

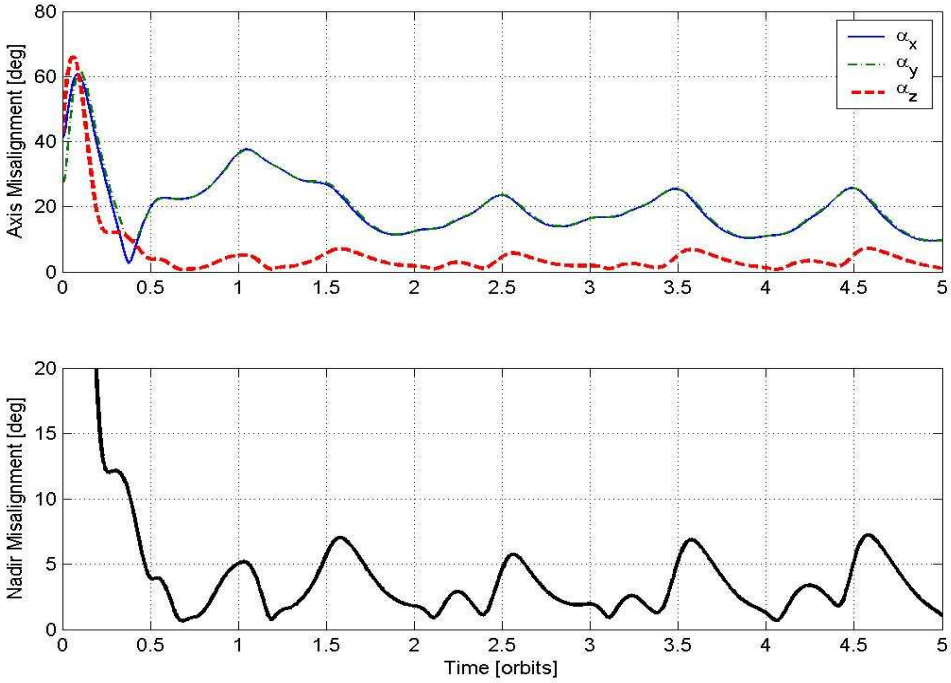

Figure 7.10: Results of the continuous LQR controller with reduced yaw feedback under solar pressure, aerodynamic drag and gravity gradient influence; CG = $(-5\ 0\ 0)^T$mm

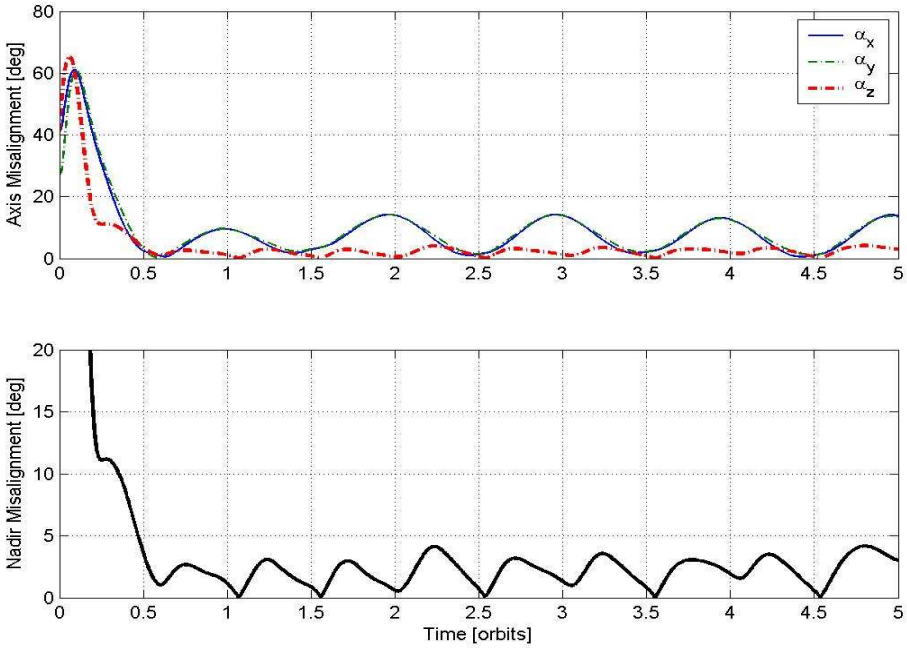

Figure 7.11: Results of the continuous LQR controller with reduced yaw feedback under solar pressure, aerodynamic drag and gravity gradient influence; CG = $(0\ -5\ 0)^T$mm

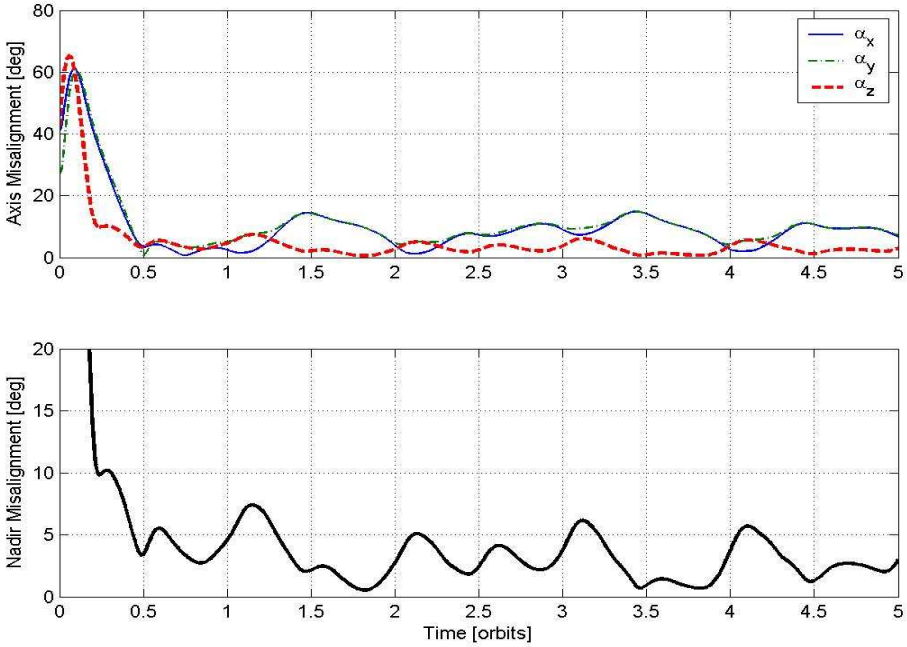

Figure 7.12: Results of the continuous LQR controller with reduced yaw feedback under solar pressure, aerodynamic drag and gravity gradient influence; CG = $(0\ 0\ -5)^T$mm

The result in figure 7.10 is qualitatively identical with the case in figure 7.8, where the CG location is in the positive b_1 direction. The only difference is that the disturbance equilibrium is established at a negative yaw angle.

7.3.7 Impact of added Residual Magnetic Dipole Disturbance

The next simulation scenario considers the full disturbance environment, i.e. solar pressure, aerodynamic drag, gravity gradient and residual magnetic dipole. The addition of the residual dipole adds a torque which is always perpendicular to the geomagnetic field vector, and hence compensatable at all times by definition. However, relatively large parasitic magnetic dipoles create considerable disturbance torques such that the accuracy is invariably degraded. Figure 7.13 shows the result for the scenario in figure 7.8 but with the addition of a parasitic magnetic dipole of $(4{\cdot}10^{-5}\ 6{\cdot}10^{-6}\ -4{\cdot}10^{-5})^{T}$Am² as in the case of the detumbling scenarios.

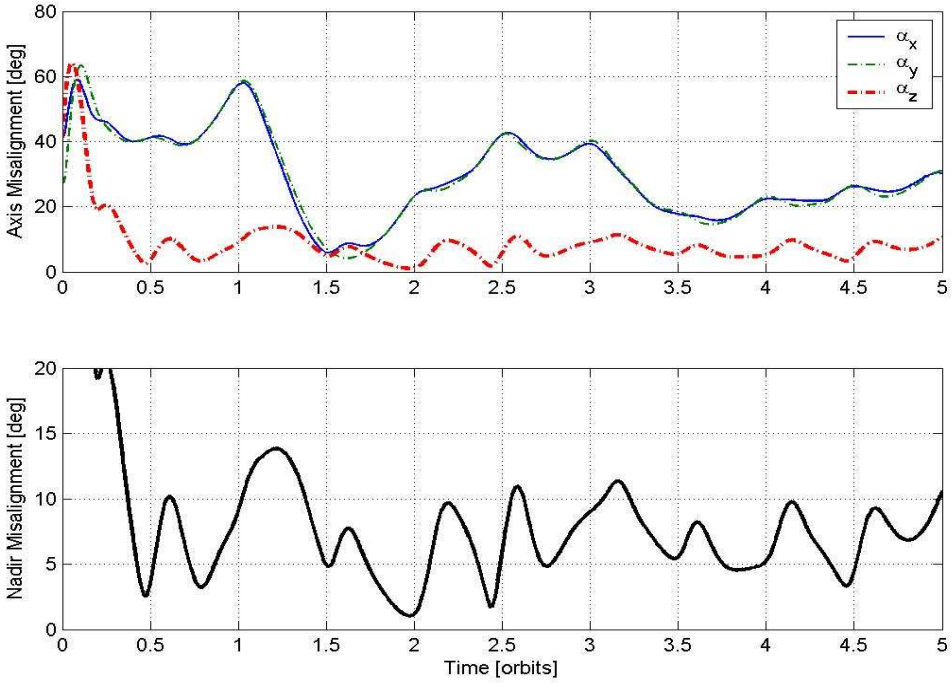

Figure 7.13: Results of the continuous LQR controller with reduced yaw feedback under full disturbance environment; CG = $(5\ 0\ 0)^{T}$mm

The results show that the continuous controller maintains a nadir alignment error of app. 10° under the full disturbance regime. Note that the effect of the parasitic dipole moment can be compensated by subtraction from the control magnetic moment if known. In that case the performance equals that of figure 7.8. Appropriate compensation methods are being investigated during the flight model integration of Compass-1.

7.3.8 The Inverted Spacecraft

The LQR controller is globally stable for initial inertial body rates up to 0.01rad/sec, not only in the vicinity of the linearization point, which has been tested by checking for stability with randomly selected upper limit initial body rates. For limit body rates of $(0.01\ -0.01\ -0.01)^T$rad/sec the controller recovers the spacecraft after app. 7 full orbital periods under ideal operational conditions.

A worthwhile case to test is that of the inverted spacecraft at rest w.r.t. the orbital frame of reference. Here, the satellite is rolled by 180° such that the b_3 axis points anti-parallel to the desired nadir direction. With the complete lack of rotation, the spacecraft is "trapped" in a stable attitude by the gravity gradient effect. Only the control torque and the remaining disturbance torque may force the satellite out of this undesired stable equilibrium and towards the required nadir pointing attitude. Figure 7.14 shows the simulation results of this scenario under full disturbance regime. The initial conditions for this case are summarized in table 7.7.

Table 7.7: Inverted spacecraft scenario initial conditions

Initial Rotation	$\left\|\omega_{b,0}^{bo}\right\|$	0	rev/min
Initial Quaternion	$\bar{q}_0^{bo}$	$(1\quad 0\quad 0\quad 0)^T$	-

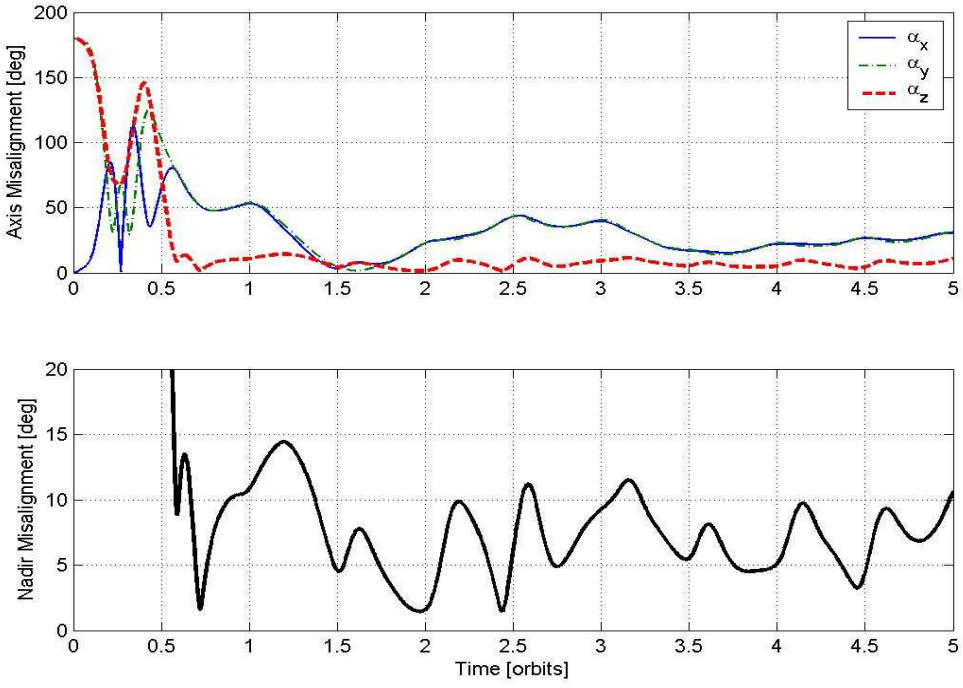

Figure 7.14: Results of the continuous LQR controller for the inverted spacecraft with reduced yaw feedback under full disturbance environment; CG = $(5\ 0\ 0)^T$mm

As the results clearly indicate, the LQR controller is able to recover the satellite from the inverted spacecraft condition. Note that after a little more than one orbit, the attitude history establishes full consistency with the result in figure 7.13, i.e. for a different initial condition.

It can be argued that the disturbance torque helps “pushing” the inverted spacecraft out of the stable gravity gradient attitude while the control torques alone cannot recover the spacecraft. However, it has been observed by simulation that the inverted spacecraft can be equally recovered in the absence of any non-conservative disturbance, indicating that the controller exerts authority on the recovery process.

7.3.9 Realistic Implementation

The following case considers a discrete LQR controller with a sampling frequency of 1Hz under full disturbance, including residual dipole, and hardware models for the magnetometer and the magnetorquers. The initial conditions have been selected as the exit condition of the realistic worst-case detumbling scenario, i.e. roll rotation about the b_1 axis aligned with B, after one orbital period plus 10% margin. The initial attitude has again be arbitrarily set to $\varphi = \theta = \psi = 30°$.

Table 7.8: Initial conditions for the realistic, discrete LQR scenarios

Initial body rates	$\omega_{b,0}^{bo}$	$10^{-3}\cdot(1.209\ -1.367\ 1.072)^T$	rad/sec
Initial Rotation	$\left\|\omega_{b,0}^{bo}\right\|$	0.02	rev/min
Initial Quaternion	$\bar{q}_0^{bo}$	$\begin{pmatrix}0.1768\\0.3062\\0.1768\\0.9186\end{pmatrix}$	-

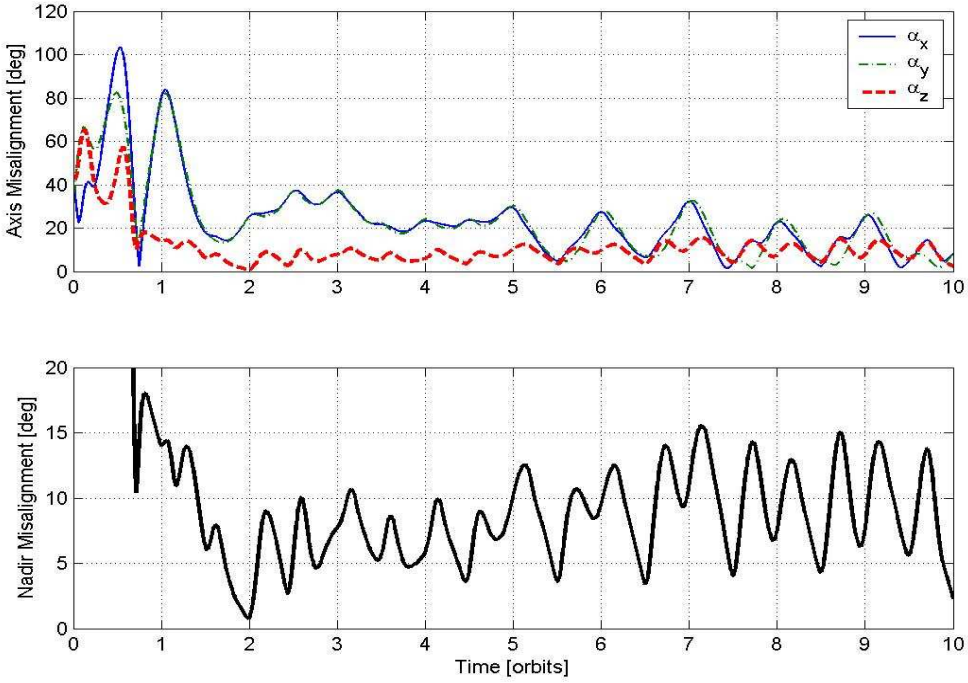

Figure 7.15: Results of the discrete LQR controller with reduced yaw feedback under full disturbance environment; CG=$[5\ 0\ 0]^T$mm

By comparison of figure 7.15 with figure 7.14 it can be concluded, that the discretization of the controller as well as the addition of hardware models does not degrade the performance of the LQR controller noticably. The settled controller yields pointing errors of 5 to 10° for 5 orbits, after which the maximum error increases to 15°. It is assumed that this drift in accuracy follows the ≈24h cycle of the Earth's sidereal rotation.

The effect of multiplexing has not been considered owing to prohibitively long simulation times. Since the multiplexed controller has less time for sustaining control torques, it is reasonable to assume, that the effect of discretization can be compensated by requesting higher control torques. Consider the scalar equality of the continuous and the multiplexed, discrete change in angular momentum, commanded by the control law.

$$dh = \int_{t_0}^{t_0+T_s} T \cdot dt = \Delta h = \int_{t_0}^{t_0+t_{control}} m \cdot B \cdot dt \tag{7.10}$$

Recall, that evaluating the scalar control torque as $m \cdot B$ is justified owing to the mapping function in the control law, which ensures that the magnetic moment is always perpendicular to the geomagnetic field. Also, for comparatively small sample intervals, and for low rotational body rates present in the nominal attitude control mode, B can be comfortably assumed constant, while m is constant by default. Assume further that T is approximately constant for small sampling times to yield

$$T_{mux} = m \cdot B = T \cdot \frac{T_s}{t_{control}} \tag{7.11}$$

which means that the applied magnetic moment should be increased depending on the fraction of the sampling period T_s which is reserved for control (i.e. $t_{control}$). It is anticipated that the measurement and processing cycle occupies app. 20% of the 1sec sampling time.

7.3.10 Impact of Attitude Determination Outage

The last scenario of the LQR control mode incorporates the fact that attitude state information is not available if

- the spacecraft is in eclipse

  AND

- the sun vector occupies the vector space in which
  no sun sensor coverage is provided

As shown in chapter 4, the sun sensor configuration of Compass-1 only provides partial sensor converage of the southern hemisphere of the satellite body. For the following scenario, no attitude information is provided if the sun is within a b_3 centered cone of half

angle β = 45°. This conservative coverage gap corresponds to the dashed, red small circle in figure 4.13 which fully inscribes the spherically rectangular gap area resulting from an individual sensor FOV of 60°.

The initial condition has been chosen such that the payoad boresight is aligned with the sun line at rest; this will produce state information outage, during which the control signal is zero, at least at the very beginning of the simulated time, and possibly at some stage into the attitude control mode.

Table 7.9: AD outage scenrio initial conditions

Initial Rotation	$\left\|\omega_{b,0}^{bo}\right\|$	0	rev/min
Initial Quaternion	$\bar{q}_0^{bo}$	$(-0.684\ 0.164\ 0.453\ 0.543)^T$	-

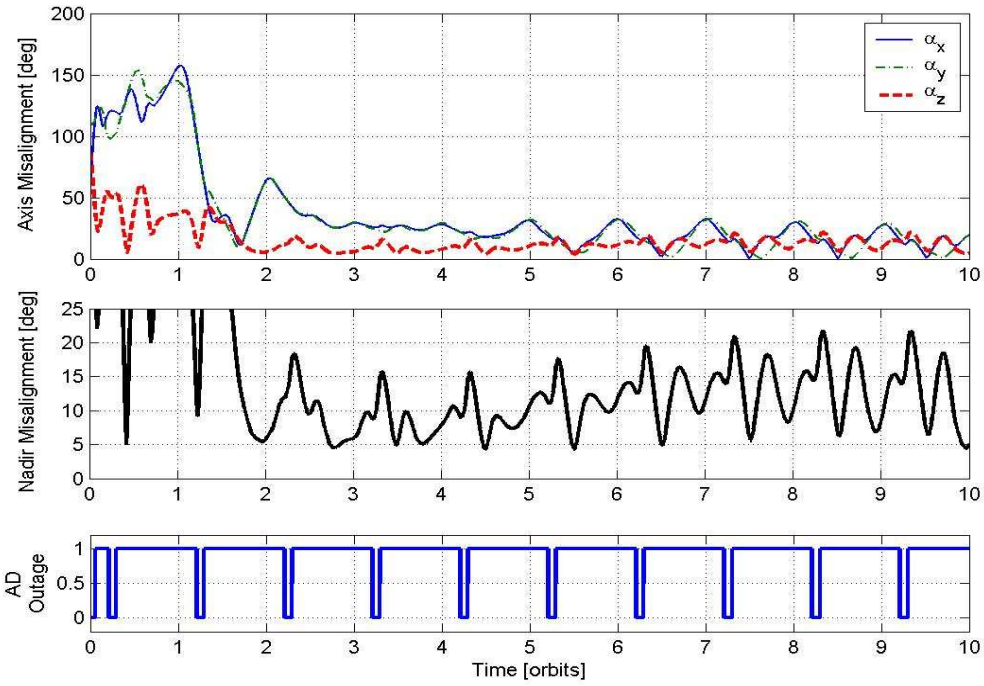

Figure 7.16: Results of the discrete LQR controller with reduced yaw feedback under full disturbance environment and with consideration of AD outages; CG=$[5\ 0\ 0]^T$mm; lack of state information occurs for signal AD Outage = 0.

From figure 7.16 it can be concluded, that partial lack of attitude information has a massive impact on the pointing performance of the controller. Peak errors can be easily correlated with the occurrence of state outage; in these intervals, the nadir error reaches peak values of app. 20° which are being quickly reduced as soon as state information becomes available again. The reason for this reduced accuracy is, of course, the environmental disturbance which governs the attitude motion of the satellite in times of AD outage, or when the spacecraft is passive.

Overall, the accuray of the presented attitude controller in a typical operational scenario is in the order of 20° peak and 12° mean.

7.4 The Passive Spacecraft

To conclude this chapter, the final scenario of interest is that of the passive spacecraft, i.e. without control torques of any kind, in order to establish a reference for the impact of disturbance torques on the free motion of the spacecraft. A full disturbance environment is considered, i.e. aerodynamic drag, solar pressure, gravity gradient and residual dipole, with the model parameters identical to the above statements.

The initial condition is the equilibrium attitude at rest as summarized in table 7.10.

Table 7.10: Passive spacecraft initial conditions

Initial Rotation	$\left\|\omega_{b,0}^{bo}\right\|$	0	rev/min
Initial Quaternion	$\bar{q}_0^{bo}$	$(0\ 0\ 0\ 1)^T$	-

The history of angular velocity (w.r.t. the orbit frame) in figure 7.17, starting from zero at t_0, clearly indicates the noticable impact of enviromental disturbances. The spacecraft picks up angular momentum in a secular non-monotonic fashion, but even after 20 orbits the inertial body rotation rates remain <0.005rad/sec, which constitutes a feasible initial condition for the LQR controller to take over. However, if the spacecraft remains passive for durations in excess of 2 days, it is safe to issue a detumbling command prior to the attitude control mode switch. This way, instability will be avoided and the controller stabilizes the satellite attitude to the desired nadir pointing orientation.

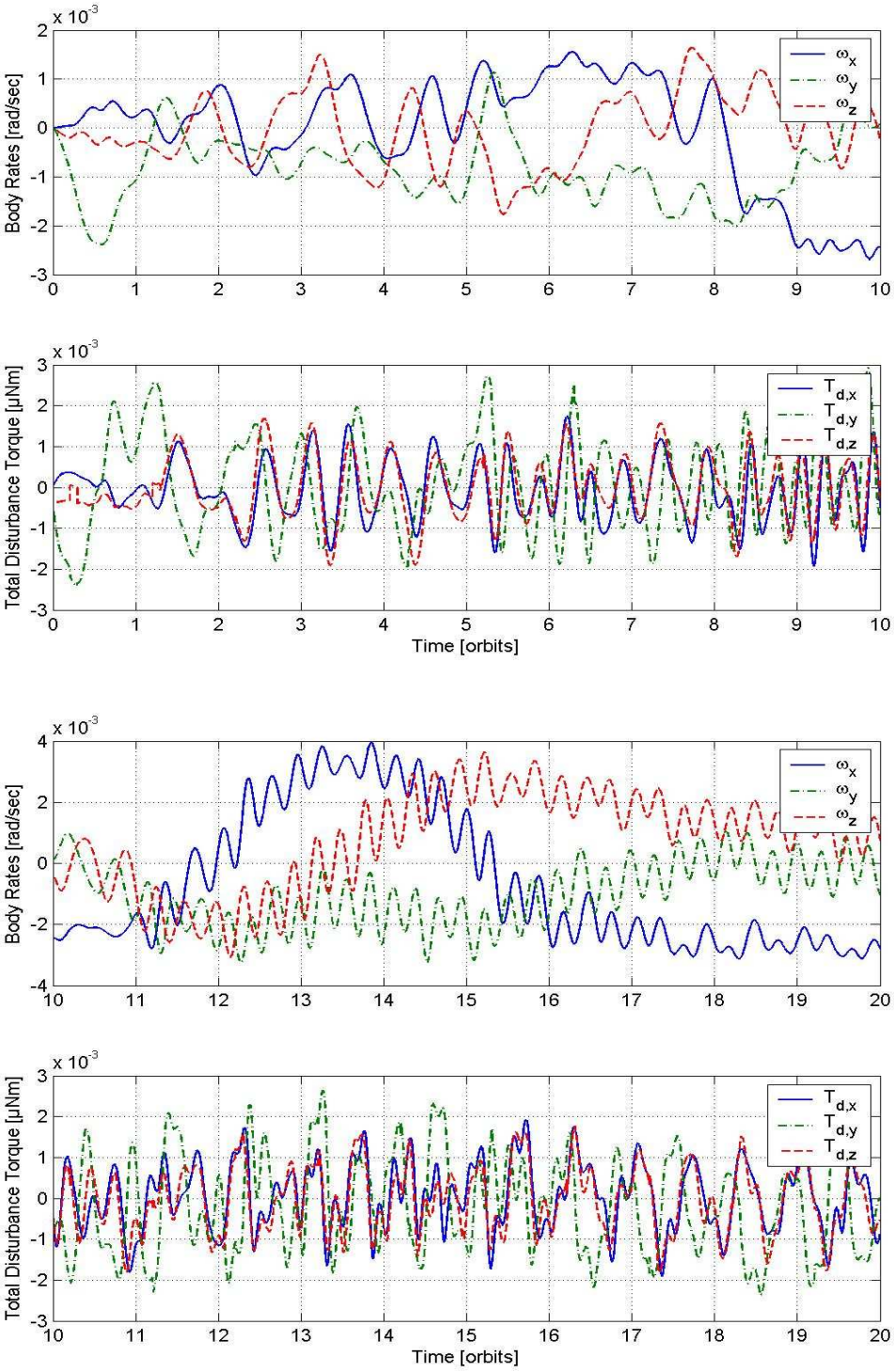

Figure 7.17: Free attitude motion of the satellite with initial condition of equilibrium at rest under full environmental disturbance for a simulated duration of 20 orbits. The upper plot shows the orbital body rates and the lower plot the total disturbance torque in the body frame.

7.5 Summary

In this chapter the implementation of the detumbling controller and the LQR attitude controller has been validated by means of non-linear dynamics simulations. The detumbling control law is capable of unloading undesired angular momentum from expected worst-case initial conditions. The abort condition implemented on Compass-1 is an elapsing timer, set to one full orbital period (≈6000s) after which the inertial body rates are robustly reduced to <0.005rad/sec.

The constant gain LQR attitude controller has been synthesised according to the procedure presented in chapter 5. This control gain provides stable system behavior for initial body rates in excess of the detumbling exit condition, but the payload pointing performance has been identified to be suboptimal, which inspired a reduction of the yaw feedback. This improves the pointing performance to app. 10° max. error. The accuracy has shown sensitivities w.r.t. the location of the CG and the actual orbit orientation. Best performance is achieved for a CG with minimum offset from the geometrical center of the cube. As for the detumbling controller, the LQR controller has been tested under realistic operational conditions, such as a discrete control loop, hardware models for the magnetometer and magnetorquers and attitude state outages. These simulations have conclusively indicated that the attitude controller maintains a mean nadir pointing error of approximately 12°, subject to a slow periodic drift. All simulations have assumed a rather significant CG offset of 5mm; it transpires that controller performance can be further improved by careful spacecraft design, including magnetic cleanliness, and further manual fine tuning of the LQR feedback gain.

Chapter 8

Conclusion

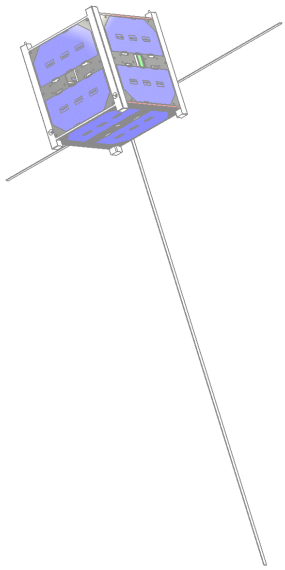

The objective of this thesis was to comprehensively establish the design of an effective attitude determination and control system for picosatellites based on purely magnetic actuation.

Starting point was the modelling of the satellite attitude dynamics and kinematics in chapter 2 and a description of the environment of the spacecraft in Low Earth Orbit, in particular the topology of the geomagnetic main field as the major resource for the control concept, in chapter 3. The hardware design comprised of a flight processor, a three-axis magnetometer, sun sensors, magnetorquers and coil drivers has been established in chapter 4 under constant consideration of the limited recources and the specific performance requirements imposed by the given attitude control task.

The constant gain attitude controller based on the Linear Quadratic Regulation approach and the stability criterion for the linear periodic system based on Floquet theory has been elaborated in chapter 5. The great advantage of this type of controller is the simplicity and efficiency of the implementation, resulting in very little software overhead. It is understood that the LQR control gain must be synthesised for a specific target orbit and spacecraft configuration in order to obtain satisfactory closed-loop behavior.

The attitude estimation process as an in important part of the feedback controller has been presented in chapter 6 under consideration of limited computing resources.

The above has established the basis for a non-linear dynamics simulation environment. In chapter 7 the implementation of the detumbling controller and the LQR attitude controller has been tested. The simulations have assumed both ideal and realistic conditions and the results have been compared.

The detumbling process efficiently reduces the angular momentum from estimated worst-case initial conditions to below 0.005rad/sec (inertial) within one orbital period. The controller has shown very good robustness against the introduction of discretization and uncertain hardware models.

The LQR controller applied to the problem of nadir pointing attitude control has shown that the achievable accuracy for payload nadir pointing is sizably depending on the disturbance regime of the spacecraft. This lack of robustness results from the fundamental underactuation of the system under control. Adequate measures can be undertaken in order to reduce the impact of disturbance torques on the spacecraft, such as proper equipment placing for CG alignment and selection of proper materials for magnetic cleanliness. In the case of incomplete disturbance removal a method for reducing the impact of disturbances has been successfully tested. In this case, however, full 3-axis attitude stabilization is not possible but the primary payload nadir-pointing requirement is satisfied to within approximately 10° accuracy.

More realistic operational conditions, such as attitude estimation outages, realistic sensor models and a discrete control loop have confirmed that the system remains functional within satisfactory performance boundaries.

8.1 Recommendations for Future Work

It would be worthwhile to investigate further improvements of the attitude determination and control system for picosatellite platforms. It transpires that active magnetic attitude control provides a weight, power and volume efficient control strategy which leaves maximum budget allocations to any potential picosatellite payload. An interesting approach would be to augment the basic control strategy presented in this thesis by additional actuator and sensor elements. Advances in reliable miniature mechanisms, for instance, would make the implementation of a pitch and roll stabilizing gravity gradient boom realistic. In addition, the yaw angle could be more accurately controlled using a single miniature reaction wheel mounted on the yaw axis. It is anticipated that such a mixed momentum wheel / magnetic control concept could produce considerably more accurate nadir alignment with sun pointing constraint.

It is also desirable to extend the sensor suit by rate sensors. Highly integrated, smart MEMS rate sensors are becoming commercially available (e.g. ADIS16xxx) to benefit the performance of the attitude estimation.

It is the opinion of the author that, in order to harness the full potential of picosatellites, a more modular, standardized system design along the lines of the Compass-1 architecture is necessary. The CubeSat standard has marked the beginning by defining (nothing more than) the launch interface. However, the system design itself is not unified, and this forces developers around to world to develop customized bus systems in time-consuming and redundant development projects. If properly coordinated, a set of standard subsystems satisfying the specific needs of general purpose picosatellite platforms could evolve to unprecedented maturity; such a standard, of course, would involve the definition of unified interfaces, which all system developers would have to adher to. The feasibility of such a

development is given by the relatively high production volume for instance for potential low-cost picosatellite constellations or swarms. When standard system modules become available, e.g. an attitude control package or a propulsion module, the system design efforts can be streamlined to between several weeks and a few months at a minimum cost, which is believed to constitute a key motivator for picosatellite applications beyond the mere ends in itself of technology demonstration.

8.2 Launch Commitment

At the time of preparing this thesis for final submission the project has entered the flight model integration phase. The promising outcome of the present research has enabled the project management to engage in concrete launch negotiations. In June 2006 the University of Applied Sciences Aachen has signed a contract with the Canadian University of Toronto, Institude of Aerospace Studies, Space Flight Laboratory (UTIAS/SFL) for a piggy-back launch in one of 5 dedicated eXperimantal Push Out Deployer (XPOD) launch containers. The launch on-board the Indian Polar Satellite Launch Vehicle (PLSV) operated by Antrix Corperation Unlimited is scheduled for June 30, 2007 and will target a circular sun-synchronuous orbit with 630km altitude, 98° degrees inclination and 10:30 ascending node; the launch is to be carried out from the Satish Dhawan Space Centre on the barrier island of Sriharikota. UTIAS/SFL is responsible for mating Compass-1 with the deployment system as well as conducting acceptance testing, final launch integration and launch coordination in compliance with the Launch Services Agreement between UTIAS/SFL and Antrix Corporation. The launch is funded by the German Aerospace Center (DLR); in retun the mission operation of Compass-1 will be partially integrated into the DLR School Lab, a division of the DLR with the aim of promoting space and other high-end technology among advanced secondary school students all over Germany. Compass-1 shares the launch vehicle with the CubeSats CanX-2, AAUSat-2, Cute1.7+APD-2, DelfiC3, SEEDS-2, and the primary payload Oceansat-2, an Earth observation satellite of the Indian Space Agency ISRO.

Provided that all subsystems perform nominally, Compass-1 could be the first actively controlled picosatellite in the history of spacecraft engineering. Downlinked engineering data will then help validating the performance of the control system to gain the required experience for potentially equipping a large number of future picosatellites with this novel attitude control technology.

Appendix A

Julian Calendar

The general purpose civil time system of modern times is the Gregorian Calender, decreed by Pope Gregory XIII in 1582, in close approximation of one tropical year, i.e. the period of the Earth's orbit around the sun. Before that decree, the common calendar of the western world has been the Julian Calender, named after its initiator Julius Scaliger, not Julius Caesar. While the Gregorian calender counts the years, months and days since its origin, defined as 1st of January 1, the Julian calendar counts the number of days since the significant origin at noon of the 1st of January, 4713 BC. Nowadays, the Julian Calendar remains the most important time system in astronomical science and thus forms an important basis for astronautical systems which depend on the knowledge of celestial features.

The Julian Date can be converted from any Gregorian Date given in years (Y) , months (M), days (D) and the universal time in hours (UT) using the following formula, where int(x) denotes a floor rounding function.

$$\begin{aligned} JD = {} & 367Y - \mathrm{int}(7(Y + \mathrm{int}((M+9)/12))/4) \\ & - \mathrm{int}(3(\mathrm{int}((Y + (M-9)/7)/100)+1)/4) \\ & + \mathrm{int}(275M/9) + D + 1721028.5 + UT/24 \end{aligned} \tag{A.1}$$

For Gregorian calendar years 1901-2099, the formula can be simplified to

$$\begin{aligned} JD = {} & 367Y - \mathrm{int}(7(Y + \mathrm{int}((M+9)/12))/4) \\ & + \mathrm{int}(275M/9) + D + 1721013.5 + UT/24 \end{aligned} \tag{A.2}$$

The Julian Calendar appears with different origin definitions. Relevant is, for instance, the Modified Julian Date (MJD) which originates at midnight November 17, 1858. MJD is a more compact time system, since it reduces the JD by two decimal digits.

$$MJD = JD - 2400000.5 \tag{A.3}$$

Another important JD origin is that of the current epoch for all celestial features, noon, January 1 2000, which corresponds to JD 2,451,545.

$$JD_{2000} = JD - 2451545 \tag{A.4}$$

Appendix B

NORAD Two Line Elements (TLE)

The US Space Command/NORAD compiles orbit data for each known object in space for the purpose of ephemeris propagation. These data sets, called TLE, follow a strict format, which shall be presented here. TLE data sets of unclassified spacecraft are freely accessible via the internet as ACII text files at the URL http://celestrak.com/. Figure 1 shows an example of a TLE with field descriptions.

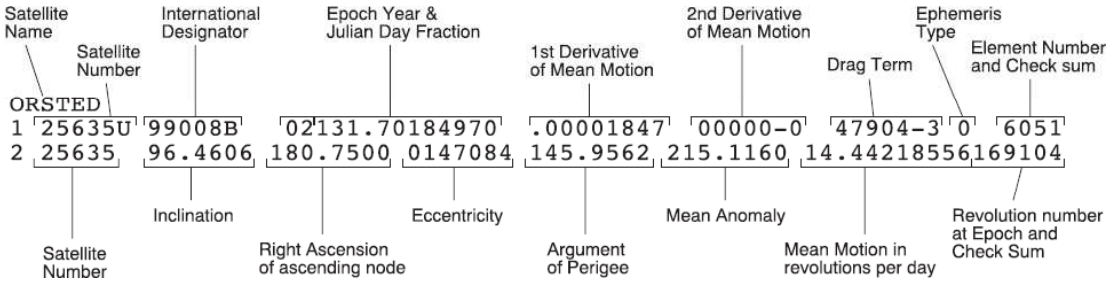

Figure B.1: examplary TLE with field descriptions; line 0 contains the official 24-character (max.) object name

L1	Column	Description
	01	Line Number of Element Data
	03-07	Satellite Number
	08	Classification (U = unclassified)
	10-11	International Designator (Last two digits of launch year)
	12-14	International Designator (Launch number of the year)
	15-17	International Designator (Piece of the launch)
	19-20	Epoch Year (Last two digits of year)
	21-32	Epoch (Day of the year and fractional portion of the day)
	34-43	First Time Derivative of the Mean Motion
	45-52	Second Time Derivative of Mean Motion (decimal point assumed)
	54-60	B* drag term (decimal point assumed)
	63	Ephemeris type (standard = 0)
	65-68	Element number
	69	Checksum (Modulo 10)
		(Letters, blanks, periods, plus signs = 0; minus signs = 1)

L2	Column	Description
	01	Line Number of Element Data
	03-07	Satellite Number
	09-16	Inclination (i_0) [°]
	18-25	Right Ascension of the Ascending Node (Ω_0) [°]
	27-33	Eccentricity (e_0) (decimal point assumed)
	35-42	Argument of Perigee (ω_0) [°]
	44-51	Mean Anomaly (M_0) [°]
	53-63	Mean Motion (n_0) [revs/day]
	64-68	Revolution number at epoch [revs]
	69	Checksum (Modulo 10)
		(Letters, blanks, periods, plus signs = 0; minus signs = 1)

The checksum is obtained by adding all digits, ignoring any other character exept the minus sign, which has a value of one. The correct checksum is then the least-significant decimal digit of the result expressed in ASCII code.

In addition to assuming an implicit decimal point, the last two characters of the 2nd derivative of the mean motion and the drag term denote an exponential function, e.g. 47904-3 is decoded as $0.47904 \cdot 10^{-3}$.

Appendix C

Simulation Environment

The following eight pages contain the graphical Simulink “source code” of all major hierachical blocks used in the simulation campaign. Some script type functions are represented by Matlab Function blocks and will not be reproduced here. Most of these algorithms can be derived from the models given in the main text of this thesis.

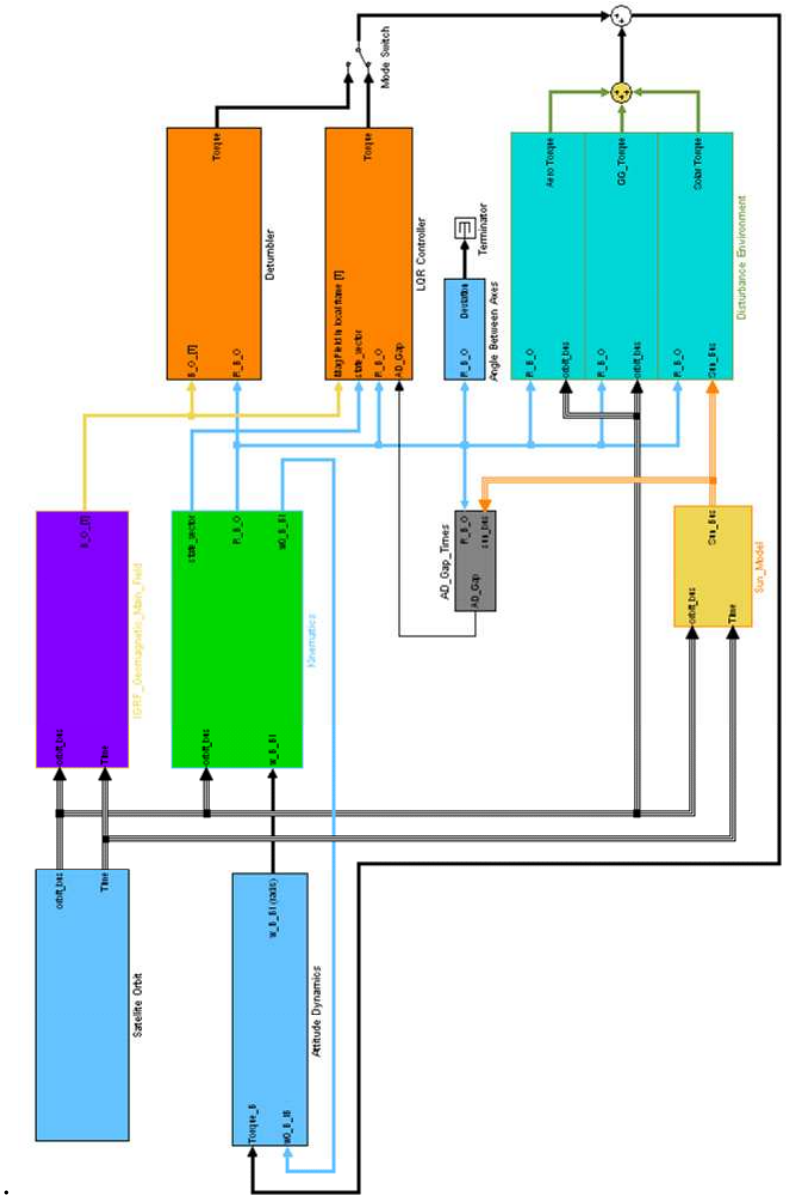

Figure C.1: Top-Level Block diagram of the Simulink simulation model; wide lines indicate non-scalar signals, thin parallel lines indicate a multitude of possibly non-scalar signals.

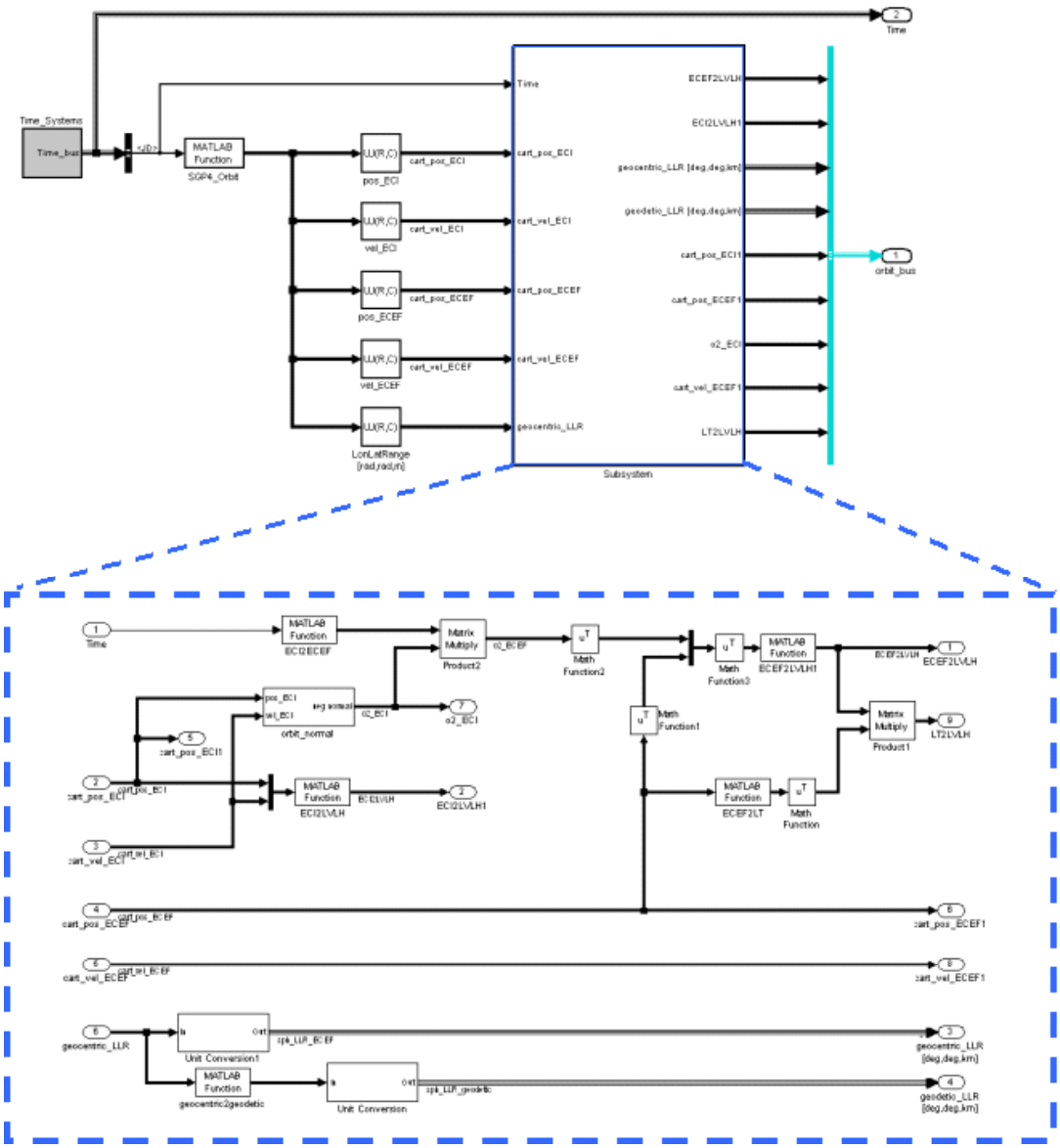

Figure C.2: The Satellite Orbit Block

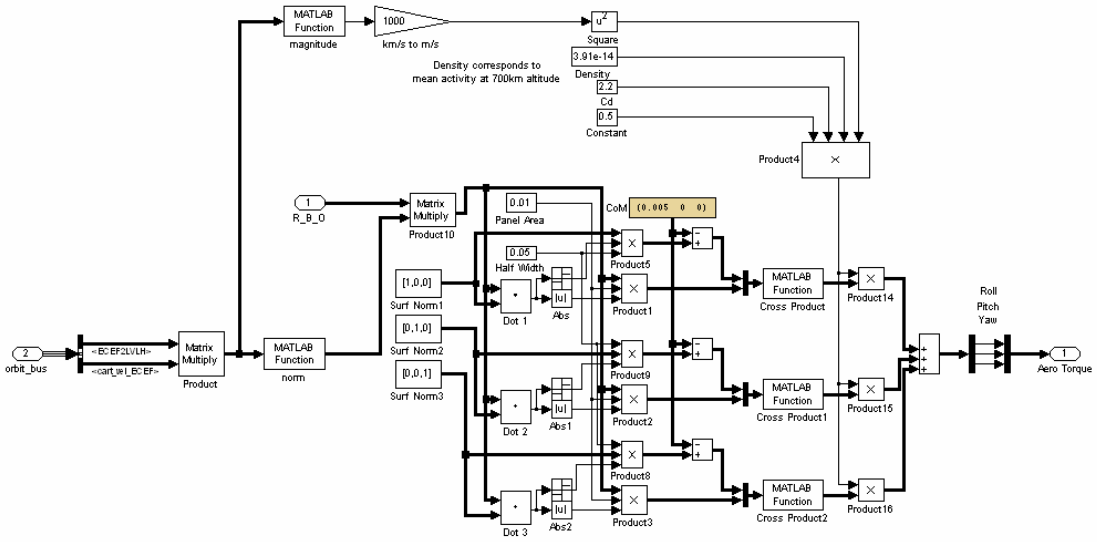

Figure C.3: The Aerodynamic Drag Torque Block

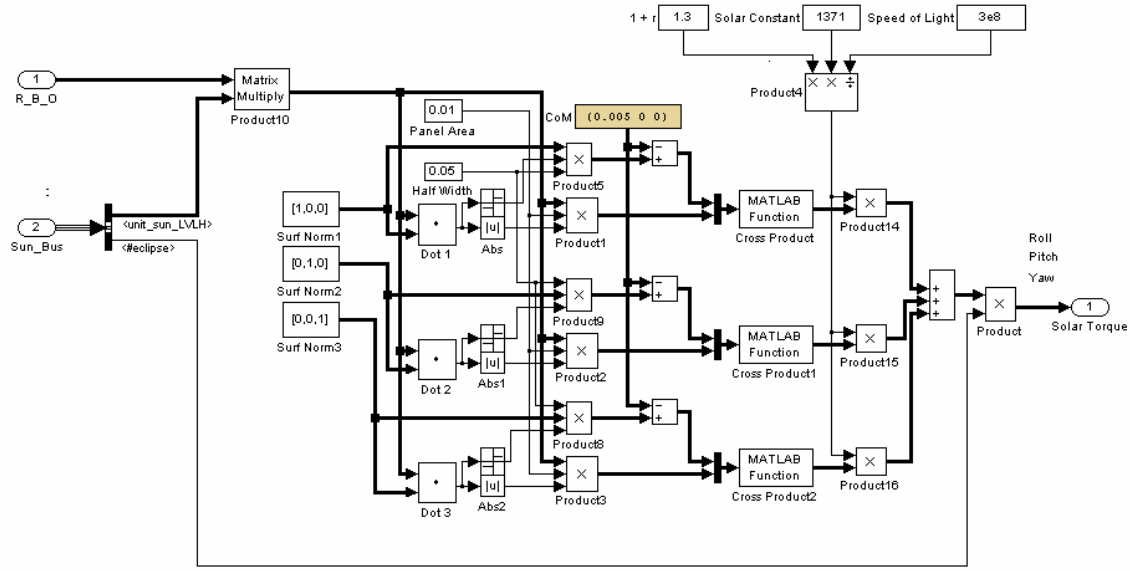

Figure C.4: The Solar Pressure Torque Block

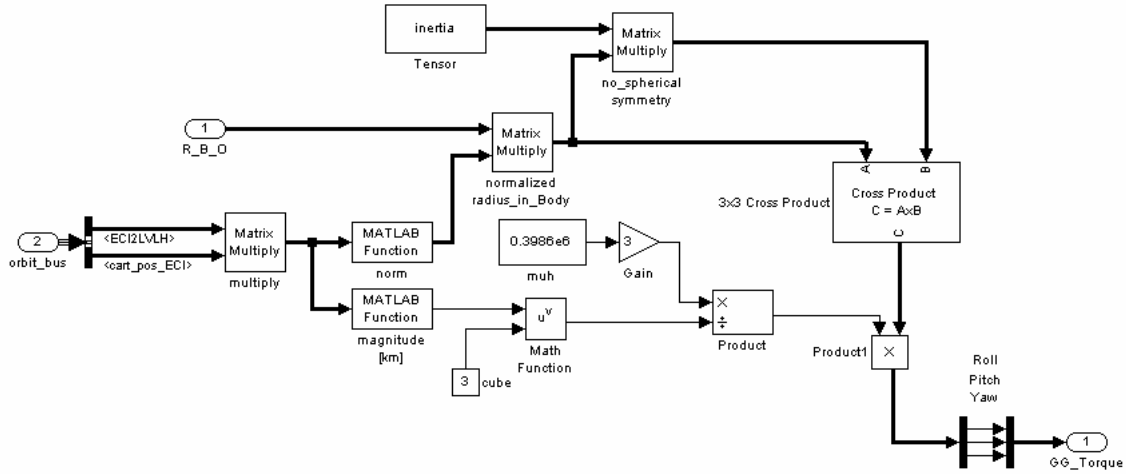

Figure C.5: The Gravity Gradient Torque Block

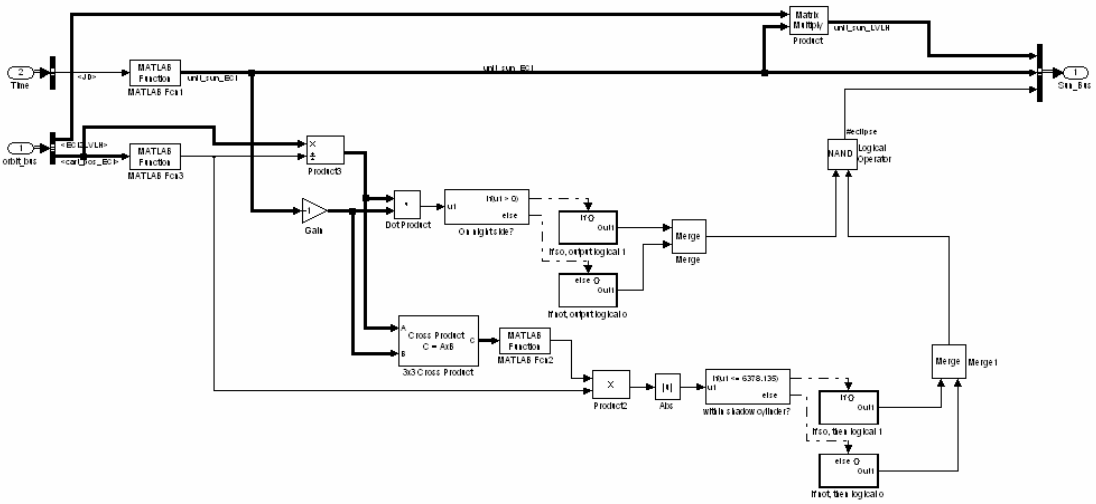

Figure C.6: The Sun Model and Shadow Model Block

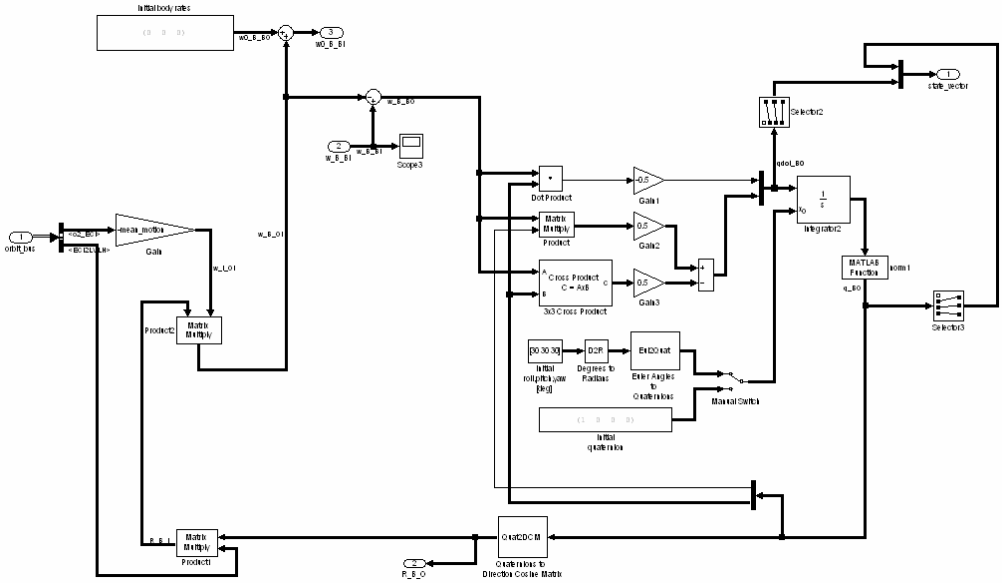

Figure C.7: The Attitude Kinematics Block

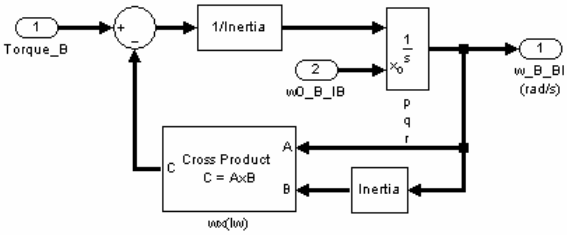

Figure C.8: The Attitude Dynamics Block

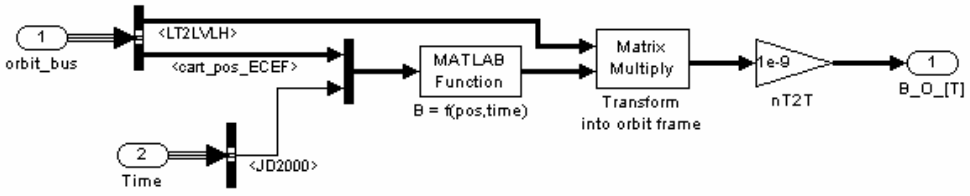

Figure C.9: The Geomagnetic Field Model Block

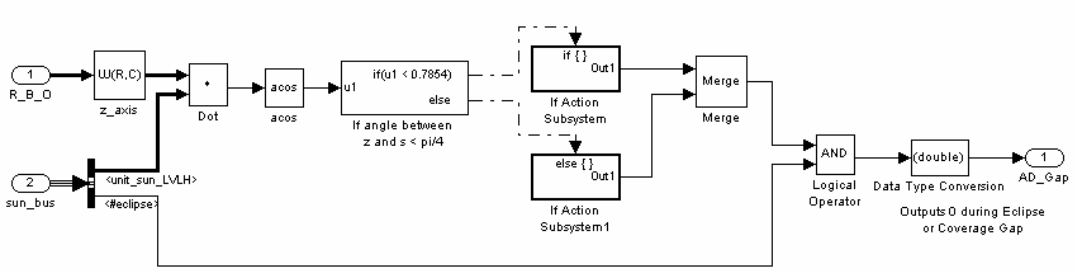

Figure C.10: The Attitude Determination Outage Block

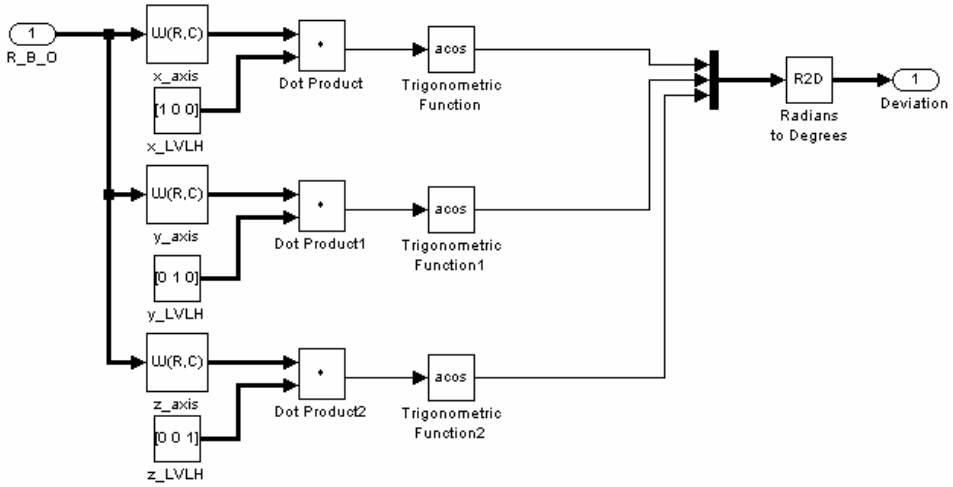

Figure C.11: The Axes Deviation Block

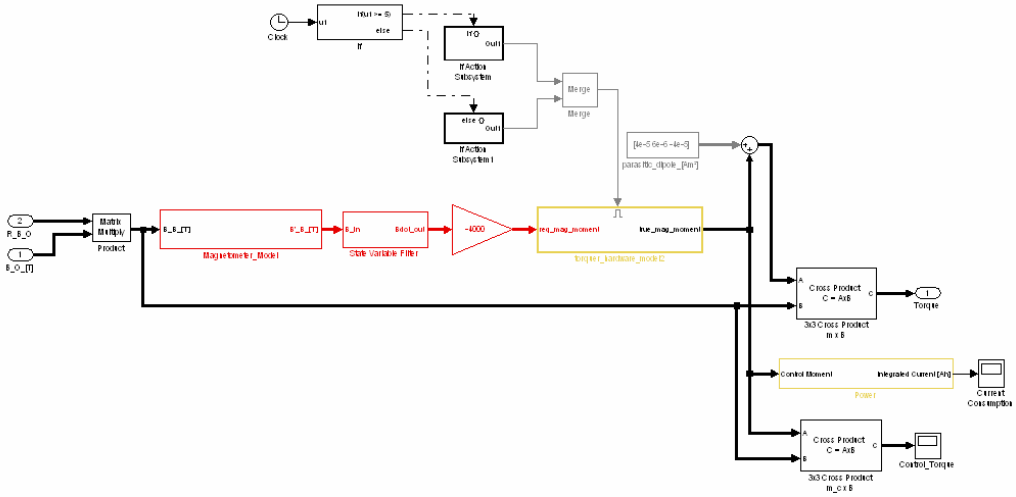

Figure C.12: The Detumbling Controller Block; different colors indicate different discretization levels; black is always continuous.

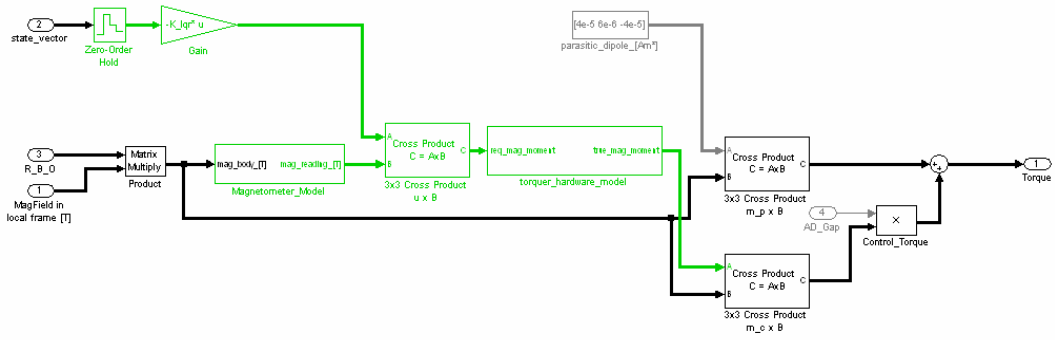

Figure C.13: The LQR Controller Block

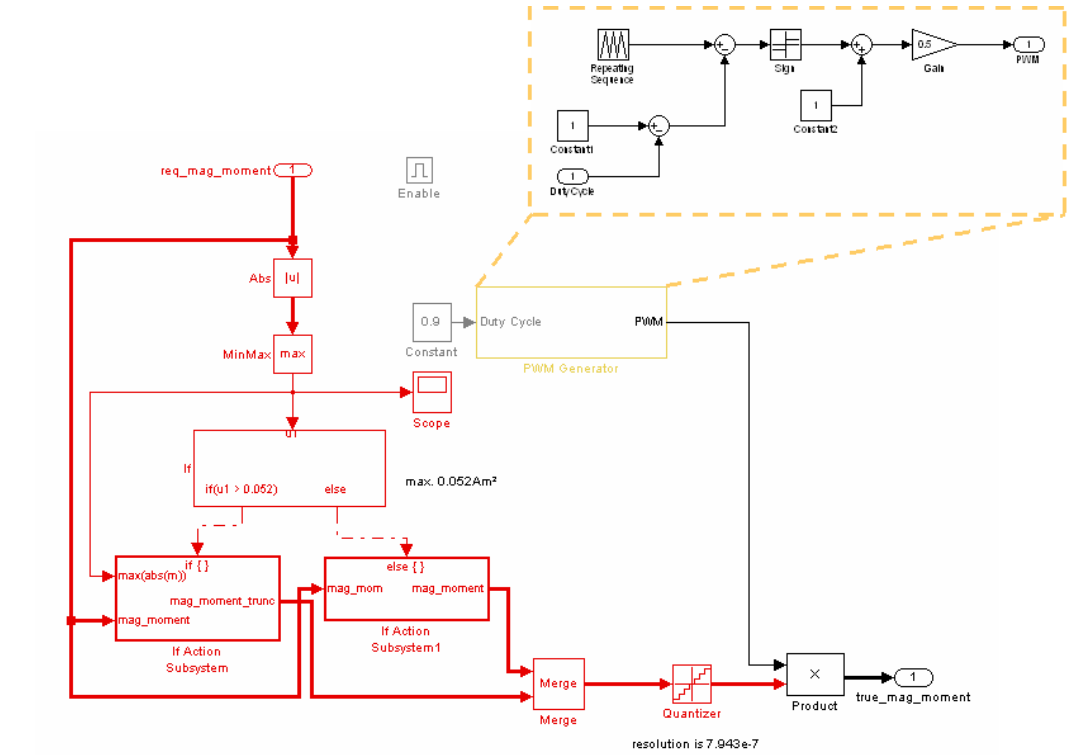

Figure C.14: The Magnetorquer Hardware Model Block

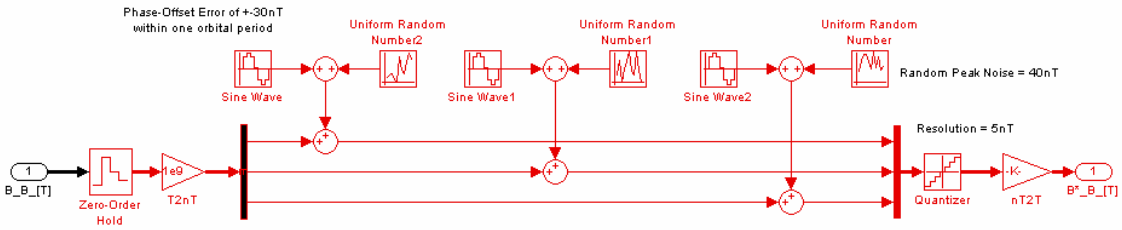

Figure C.15: The Magnetometer Hardware Model Block

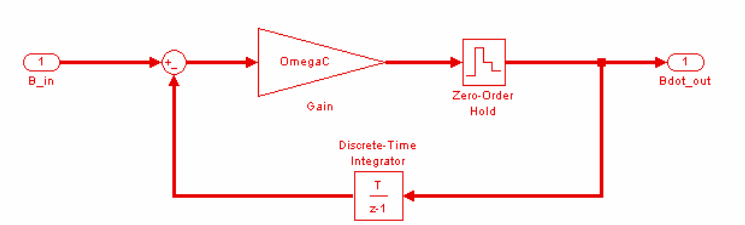

Figure C.16: The Discrete State Variable Filter Block

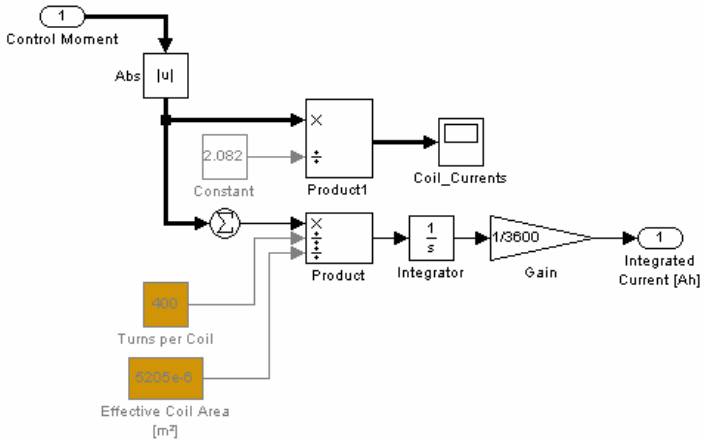

Figure C.17: The Accumulated Power Consumption Block

Appendix D

IGRF-10 Model Coefficients

The following lists the full set of spherical harmonics expansion coefficients of the recent international geomagnetic reference field (IGRF-10), valid from epoch 2005 to 2010. The model coefficients and utility source code can be freely downloaded in various file formats from the URL http://www.ngdc.noaa.gov/IAGA/vmod/igrf.html.

n	m	g_n^m	h_n^m	$\dot{g}_n^m$	$\dot{h}_n^m$
1	0	-29556.8	0.0	8.8	0.0
1	1	-1671.8	5080.0	10.8	-21.3
2	0	-2340.5	0.0	-15.0	0.0
2	1	3047.0	-2594.9	-6.9	-23.3
2	2	1656.9	-516.7	-1.0	-14.0
3	0	1335.7	0.0	-0.3	0.0
3	1	-2305.3	-200.4	-3.1	5.4
3	2	1246.8	269.3	-0.9	-6.5
3	3	674.4	-524.5	-6.8	-2.0
4	0	919.8	0.0	-2.5	0.0
4	1	798.2	281.4	2.8	2.0
4	2	211.5	-225.8	-7.1	1.8
4	3	-379.5	145.7	5.9	5.6
4	4	100.2	-304.7	-3.2	0.0
5	0	-227.6	0.0	-2.6	0.0
5	1	354.4	42.7	0.4	0.1
5	2	208.8	179.8	-3.0	1.8
5	3	-136.6	-123.0	-1.2	2.0
5	4	-168.3	-19.5	0.2	4.5
5	5	-14.1	103.6	-0.6	-1.0
6	0	72.9	0.0	-0.8	0.0
6	1	69.6	-20.2	0.2	-0.4
6	2	76.6	54.7	-0.2	-1.9
6	3	-151.1	63.7	2.1	-0.4
6	4	-15.0	-63.4	-2.1	-0.4
6	5	14.7	0.0	-0.4	-0.2
6	6	-86.4	50.3	1.3	0.9
7	0	79.8	0.0	-0.4	0.0
7	1	-74.4	-61.4	0.0	0.8
7	2	-1.4	-22.5	-0.2	0.4
7	3	38.6	6.9	1.1	0.1
7	4	12.3	25.4	0.6	0.2
7	5	9.4	10.9	0.4	-0.9
7	6	5.5	-26.4	-0.5	-0.3
7	7	2.0	-4.8	0.9	0.3
8	0	24.8	0.0	-0.2	0.0
8	1	7.7	11.2	0.2	-0.2
8	2	-11.4	-21.0	-0.2	0.2
8	3	-6.8	9.7	0.2	0.2
8	4	-18.0	-19.8	-0.2	0.4
8	5	10.0	16.1	0.2	0.2
8	6	9.4	7.7	0.5	-0.3
8	7	-11.4	-12.8	-0.7	0.5
8	8	-5.0	-0.1	0.5	0.4

n	m	g_n^m	h_n^m
9	0	5.6	0.0
9	1	9.8	-20.1
9	2	3.6	12.9
9	3	-7.0	12.7
9	4	5.0	-6.7
9	5	-10.8	-8.1
9	6	-1.3	8.1
9	7	8.7	2.9
9	8	-6.7	-7.9
9	9	-9.2	5.9
10	0	-2.2	0.0
10	1	-6.3	2.4
10	2	1.6	0.2
10	3	-2.5	4.4
10	4	-0.1	4.7
10	5	3.0	-6.5
10	6	0.3	-1.0
10	7	2.1	-3.4
10	8	3.9	-0.9
10	9	-0.1	-2.3
10	10	-2.2	-8.0
11	0	2.9	0.0
11	1	-1.6	0.3
11	2	-1.7	1.4
11	3	1.5	-0.7
11	4	-0.2	-2.4
11	5	0.2	0.9
11	6	-0.7	-0.6
11	7	0.5	-2.7
11	8	1.8	-1.0
11	9	0.1	-1.5
11	10	1.0	-2.0
11	11	4.1	-1.4
12	0	-2.2	0.0
12	1	-0.3	-0.5
12	2	0.3	0.3
12	3	0.9	2.3
12	4	-0.4	-2.7
12	5	1.0	0.6
12	6	-0.4	0.4
12	7	0.5	0.0
12	8	-0.3	0.0
12	9	-0.4	0.3
12	10	0.0	-0.8

n	m	g_n^m	h_n^m
12	11	-0.4	-0.4
12	12	0.0	1.0
13	0	-0.2	0.0
13	1	-0.9	-0.7
13	2	0.3	0.3
13	3	0.3	1.7
13	4	-0.4	-0.5
13	5	1.2	-1.0
13	6	-0.4	0.0
13	7	0.7	0.7
13	8	-0.3	0.2
13	9	0.4	0.6
13	10	-0.1	0.4
13	11	0.4	-0.2
13	12	-0.1	-0.5
13	13	-0.3	-1.0

Appendix E

Compass-1 and ADCS Pictures

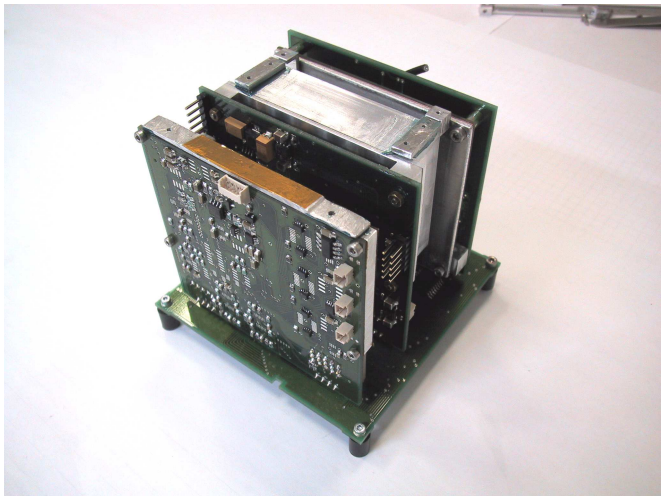

Engineering Model of the electronics package of Compass-1. All subsystems are plugged into the CDHS motherboard. The central structure is the Lithium Polymer battery box; the ADCS main board is in the foreground.

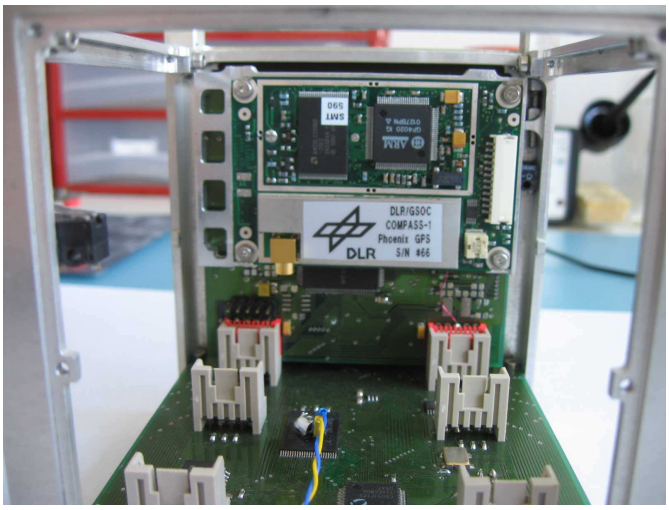

GPS Flight hardware mounted onto an ADCS test board. The integration in the cube structure is done in such a way that the ADCS electronics (including GPS) occupies a mere fraction of the total volume. The engineering model of the structure and the CDHS has undergone vibration and thermal vacuum testing; hence the temperature sensor on the flash unit of the CDHS.

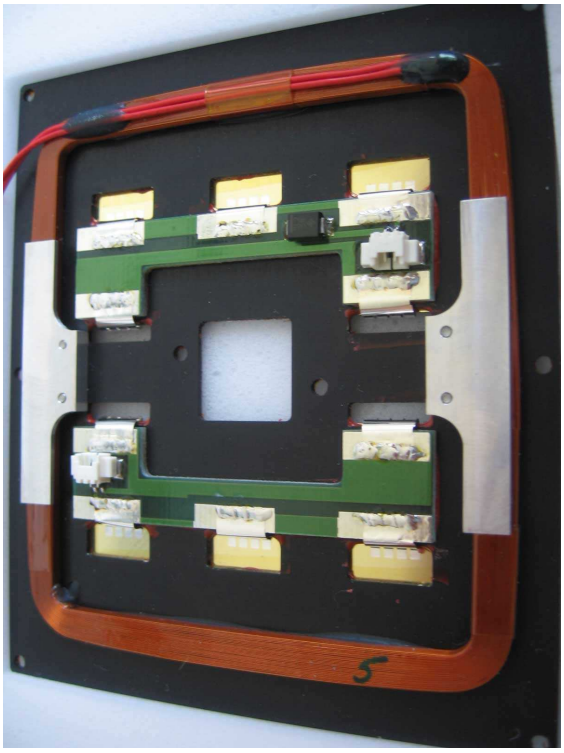

Flight model of a magnetorquer coil mounted on a side panel. The assembly space in the center of the panel (in between the solar cell interface assembly) is reserved for the sun sensor electronics.

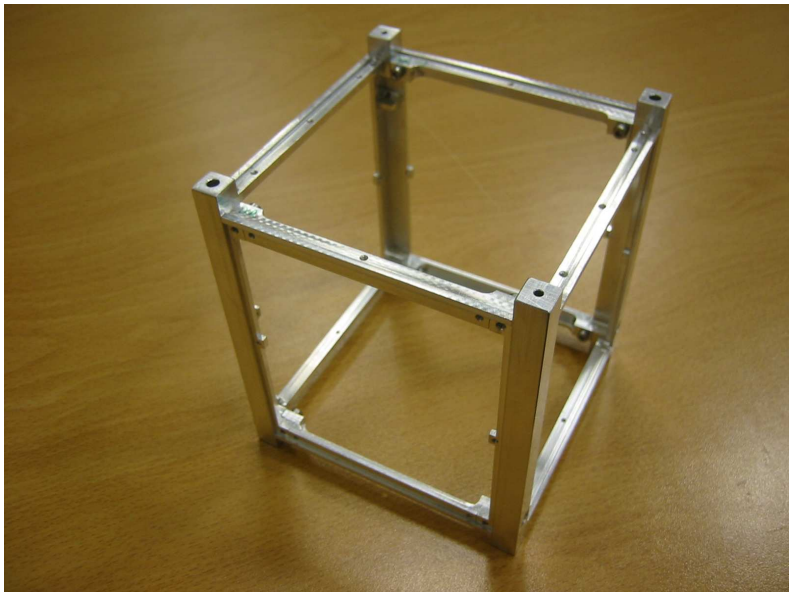

Engineering model of the main structure made from 6061-T6 aerospace grade aluminium.

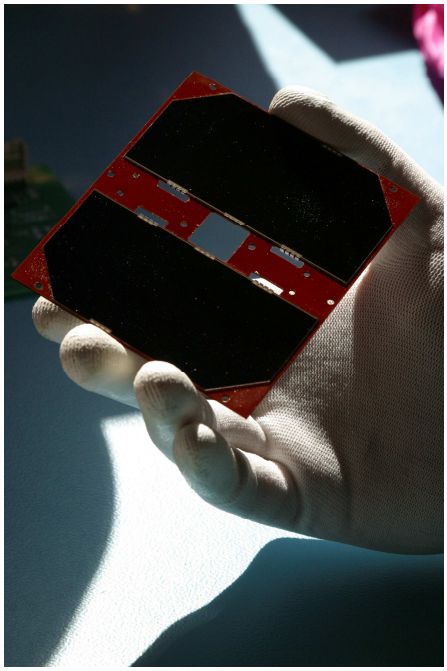

The high-efficiency triple-junction solar generators adhesively mounted on the outside of a cube panel. The space qualified adhesive is a red paste, giving the panel its crimson finish.

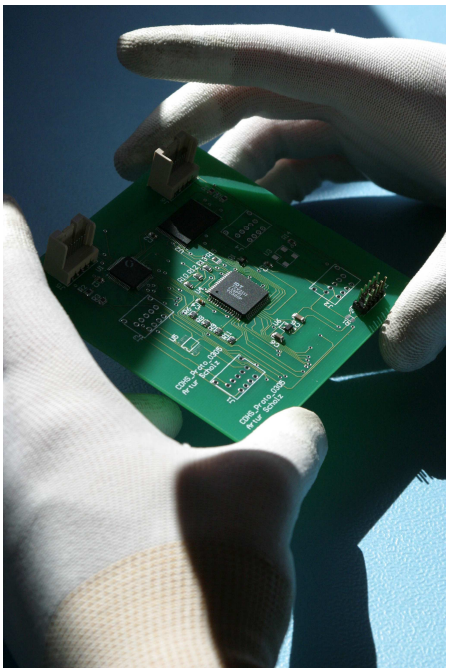

Assembly of the CDHS engineering model.

Bibliography

[1] Christopher, A. Kitts and Robert, J. Twiggs, "Low Cost Space Missions for Education and Technology Research", in *Proceedings of the 21st International Symposium on Space Technology and Science*, Omiya, Japan, May 1998

[2] Brieß, K., Montenegro, S., et al., "Demonstration of Small Satellite Technologies by the BIRD mission", *Proceedings of the 16th Annual AIAA/USU Conference on Small Satellites*, Logan, Utah, USA, Aug. 2002

[3] Bashbush, V., "Characterization of the Internal and External Environments of the CubeSat P-POD and Test Pod", Master's thesis, California Polytechnic State University, Jan. 2004

[4] Stras, L. N., Kekez, D. D., Wells, G. J., Jeans, T., Zee, R. E., Pranajaya, F. M., and Foisy, D. G., "The Design and Operation of The Canadian Advanced Nanospace eXperiment CanX-1", *Proceedings of the 21st AMSAT-NA Space Symposium*, Toronto, Canada, Oct. 2003

[5] Barza, R., Aoki, Y., Schilling, K., "UWE-1, A Student Built Pico-Satellite", *Proceedings of the 6th International Workshop on Research and Education in Mechatronics*, Annecy, France, June 30-July 1, 2005,

[6] Riise, Å.-R., Samuelsen, B., Sokolova, N., Sæther, E. T., Otterstad, J., Eide, E., et al., "NCube: The First Norwegian Student Satellite", *Proceedings of 17th Annual AIAA/USU Conference on Small Satellites*, Logan, Utah, USA, Aug. 2003

[7] Strobl, G., Dietrich, R., et al., "Advanced GaInP/Ga(In)As/Ge Triple Junction Space Solar Cells", *Proceedings of the 3rd World Conference on Photovoltaic Energy Conversion*, Osaka, Japan, May 2003

[8] Scholz, A., "Command and Data Handling System Design for the Compass-1 Picosatellite", *Proceedings of the 5thIAA Symposium on Small Satellites for Earth Observation*, Berlin, Germany, April 2005

[9] Hammer, M., Klotz, R., "Compass-1 Picosatellite: Structures & Mechanisms", *Proceedings of the 56th International Astronautical Congress*, Fukuoka, Japan, Oct. 2005

[10] Calpoly and Stanford University, *CubeSat Design Specifications Document, Revision VIII*, 2003, accessed on 06.12.2005 <http.//cubesat.calpoly.edu/documents/cubesat_spec.pdf>

[11] Scholz, A., Gießelmann, J., "CubeSat – Technical Aspects", *Proceedings of the 55th International Astronautical Congress*, Vancouver, Canada, Oct. 2004.

[12] Montenbruck, O., et. al., "A Miniature GPS Receiver for Precise Orbit Determination of the Sunsat 2004 Micro-Satellite", *ION NTM 2004*, San Diego, California, United States, Jan 2004

[13] Nakaya, K., et al., "Tokyo Tech CubeSat: CUTE-1 – Design & Development of Flight Model and Future Plan", Laboratory for Space Systems, Tokyo Institute of Technology, Japan, 2003

[14] Sidi, M. J., *Spacecraft Dynamics and Control – A practical engineering approach*, Cambridge Aerospace Series, 1997

[15] Hughes, P. C., *Spacecraft Attitude Dynamics*, John Wiley & Sons, USA, 1986

[16] Wiesel, W., *Spaceflight Dynamics*, McGraw-Hill Series in Aeronautical and Aerospace Engineering, USA, 1989

[17] Graversen, T., Frederiksen, M.K., Vedstesen, S.V., "Attitude Control System for AAU CubeSat", Master's thesis, Department of Control Engineering, Aalborg University, June 2002
[18] Lam, T. Y., "Hamilton's Quaternions", University of California, Berkeley, USA, 2002
[19] Wisniewski R., "Satellite Attitude Control Using Only Electromagnetic Actuation", Ph.D. thesis, Aalborg University, Department of Control Engineering, Dec. 1996.
[20] Makovec, K., "A Nonlinear Magnetic Controller for Three-Axis Stability of Nanosatellites", Master's thesis, Virginia Polytechnic Institute and State University, July 2001
[21] Renk, F., "Attitude Control for a Micro-Satellite Using only Magnetic Coils and Target Pointing for Multiple Satellites", Graduate thesis, Australian Centre for Field Robotics, University of Sydney, 2005
[22] Beletsky, V.V., "Libration of a Satellite", *Transactions: Artificial Satellites of the Earth*, Moscow, USSR Academy of Sciences, Issue 3, pp.13-31, 1959
[23] ECSS-E-10-04A, Space Environment, ESA-ESTEC, Noordwijk, The Netherlands, 2000
[24] Wertz, J.R., Larson, W.J., (eds.), *Space Mission Analysis and Design*, 3rd ed., Space Technology Library, Kluwer Academic Publishers, 1999
[25] Korhonen, K., "Geomagnetic Models and the IGRF-Applet", Master's thesis, Geophysical Research Division of the Finnish Meteorological Institute, 2000
[26] Macmillan, S., Quinn, J. M., *The Derivation of World Magnetic Model 2000*, Technical Report WM/00/17R, British Geological Survey, Geomagnetism Series, 2000
[27] Rauschenbakh, B., Ovchinnikov, M., McKenna-Lawlor, S., *Essential Spaceflight Dynamics and Magnetospherics*, Space Technology Library, Kluwer Academic Publishers, 2003
[28] Holme, R., Olsen, N., et al., "CO2: A CHAMP magnetic field model", *Proceedings of the First CHAMP Science Meeting*, Springer Verlag, 2003
[29] International Association of Geomagnetism and Aeronomy (IAGA), Division V, Working Group 8, "International Geomagnetic Reference Field – the tenth generation", *Earth Planets and Space*, vol.57, pp.1135-1140, 2005
[30] Hales, J. H., "Analysis and Development of MEMS based Electrical Propusion System for Space Applications", Master's thesis, Department of Micro and NanoTechnology, Technical University of Denmark, Aug. 2004
[31] Robert, E., Zee, P., Stibrany, "Canada's First Microsatellite - An Enabling Low-Cost Technology for Future Space Science and Technology Missions", 2000
[32] Pedersen, D., et al., *Attitude Control System for AAUSat-II*, Technical Report, Institute of Electronics, Aalborg University, 2004.
[33] Grover, F. W., *Inductance Calculations: Working Formulas and Tables*, Dover Publications, Inc., New York, 1946
[34] Aydinlioglu, A., "Design, Development and Production of Electromagnetic Coils for Attitude Control of a Picosatellite", Diploma thesis, Astronautical Department, University of Applied Sciences Aachen, 2006.
[35] Honeywell HMC1021/1022 Linear Magnetic Field Sensors Datasheet, 2003, Honeywell Solid State Electronics Centre, accessed on 10.02.2006 www.magneticsensors.com

[36] Krogsgaard, K., *DTUSat Magnetometer Development*, Technical Report, Technical University of Denmark, Aug. 2003
[37] Pedersen, M., Hales, J. H., *Linear Two-Axis MOEMS sun sensor*, Technical Report, Department of Micro and NanoTechnology, Technical University of Denmark, Aug. 2004.
[38] Pedersen, M., Hales, J. H., Fléron, R., "Linear Two-Axis MOEMS Sun Sensor and the Need for MEMS in Space", *Proceeding of the 54th International Astronautical Congress*, Bremen, Germany, 2003
[39] Wertz J. R., (ed.), *Spacecraft Attitude Determination and Control*, Kluwer Academic Publishers, Dordrecht, 1978
[40] Korth, H., "Untersuchung der physikalischen Eigenschaften eines Vektormagnetometers mit Netzbandkern", Diploma thesis, Institut für Geophysik und Meteorologie, Technische Universität Carolo-Wilhelmina, Braunschweig, 1998
[41] Lorentzen, T. *Attitude Control and Determination System for DTUSat1*, Technical Report, Technical University of Denmark, Department of Automation, 2002
[42] LaBel, K.A., Moran, A.K. et. al., "Current Single Event Effect Test Results for candidate Spacecraft Electronics for NASA", *IEEE Radiation Effects Data Workshop Record*, pp. 19-27, NASA/GSFC, Code 735.1, Greenbelt, 1996
[43] Markgraf, M., Montenbruck, O., *Total Ionizing Dose Testing of the Orion and Phoenix GPS Receivers*, Technical Note, DLR, 2004
[44] Psiaki, M.L., "Magnetic Torquer Attitude Control via Asymptotic Linear Quadratic Regulation", *Journal of Guidance, Conrol and Dynamics*, Vol.24, No.2, pp.386-394, 2001
[45] Martel, F., Pal, P.K., Psiaki, M.L., "Active Magnetic Control System for Gravity Gradient Stabilized Spacecraft", *Proceedings of the 2nd Annual AIAA/USU Conference on Small Satellites*, Utah, Sep. 1988
[46] Musser, K.L., Ward, L.E., "Autonomous Spacecraft Attitude Control using Magnetic Torquing Only", Proceedings of the *Flight Mechanics/Estimation Theory Symposium*, NASA Goddard Space Flight Center, Greenbelt, MD, Publication, pp. 23-38, May 1989.
[47] Levine, W.S., (ed.), *The Control Handbook*, CRC Press, Florida, 1996
[48] Anderson, B.D.O., Moore, J.B. , *Optimal Control: Linear Quadratic Methods*, Prentice Hall, Englewood Cliffs, NJ, 1990
[49] Kwakernaak, H., Sivan, R., *Linear Optimal Control Systems*, John Wiley & Sons, New York, 1972
[50] Mohler, R.R., *Nonlinear Systems*, Vol. Dynamics and Control, Prentice Hall, Englewood Cliffs, NJ, 1991
[51] Gelb, A., (ed.), *Applied Optimal Estimation*, MIT Press, 1974
[52] Choukroun, D., "Novel Methods for Attitude Determination using vector observations", PhD Thesis, Technion – Israel Institute of Technology, Maifa, May 2003
[53] Wahba, G., "A Least-Squares Estimate of Satellite Attitude", Problem 65-1, *SIAM Review*, vol. 7, no. 3, pp. 409, July 1965
[54] Hall, Ch., *Attitude Determination and Control*, Lecture notes, Department of Aerospace and Ocean Engineering, Virginia Polytechnic Institute and State University, 2003
[55] Hoots, F.R., Roehrich, R.L., *Models for Propagation of NORAD Element Sets*, Spacetrack Report no.3, 1988

[56] Montenbruck, O., Gill, E. , *Satellite Orbits – Models, Methods, Applications*, Springer, 2000
[57] Vallado, D.A. , *Fundamentals of Astrodynamics and Applications*, second edition, McGraw-Hill, New York, 2001
[58] Quakefinder Homepage, URL: http://www.quakefinder.com/quakesat.htm , accessed on 27.03.2006
[59] Short Text on William Gilbert in Wikipedia, the free encyclopedia, URL: http://en.wikipedia.org/wiki/William_Gilbert, accessed on 28.03.2006
[60] Text on Henry Gellibrand in Wikipedia (German), URL: http://de.wikipedia.org/wiki/Henry_Gellibrand, accessed on 28.03.2006
[61] Aydinlioglu, A., Hammer, M., "Compass-1 picosatellite: magnetic coils for attitude control", Proc. of the 2nd International Conference on Recent Advances in Space Technologies, RAST, Istanbul 2005
[62] Bartels, J., "The technique of scaling indices K and Q of geomagnetic activity", *Ann. Intern. Geophys. Year 4*, 215-226, 1957
[63] Text on Superconducting Quantum Interference devices (SQUID) in Wikipedia, the free encyclopedia, URL: http://en.wikipedia.org/wiki/SQUID, accessed on 28.03.2006